

ABSTRACT

Title of dissertation: Development of a dual-tip millikelvin
Josephson scanning tunneling microscope

Anita Roychowdhury, Doctor of Philosophy, 2014

Dissertation directed by: Professor Christopher J. Lobb
Department of Physics

In this thesis, I first describe the design and construction of a dual-tip millikelvin STM system. The STM is mounted on a dilution refrigerator and the setup includes vibration isolation, rf-filtered wiring, an ultra high vacuum (UHV) sample preparation chamber and sample transfer mechanism.

Next I describe a novel superconducting tip fabrication technique. My technique involves dry-etching sections of 250 μm diameter Nb wire with an SF_6 plasma in a reactive ion etcher. I present data taken with these tips on various samples at temperatures ranging from 30 mK to 9 K. My results demonstrate that the tips are superconducting, achieve good spectroscopic energy resolution, are mechanically robust over long time periods, and are atomically sharp.

I also show data characterizing the performance of our system. This data is in the form of atomic resolution images, spectroscopy, noise spectra and simultaneous scans taken with both tips of the STM. I used these to examine the tip-sample stability, cross talk between the two tips, and to extract the effective noise temperature (~ 185 mK) of the sample by fitting the spectroscopy data to a voltage noise model.

Finally, I present spectroscopy data taken with a Nb tip on a Nb(100) sample at 30 mK. The enhanced spectroscopic resolution at this temperature allowed me to resolve peaks in the fluctuation-dominated supercurrent at sub-gap voltages. My analysis indicates that these peaks are due to the incoherent tunneling of Cooper pairs at resonant frequencies of the STM's electromagnetic environment. By measuring the response of the STM junction to microwaves, I identified the charge carriers in this regime as Cooper pairs with charge $2e$. The amplitude of the response current scales as the square of the Bessel functions, indicating that the pair tunneling originates from photon assisted tunneling in the incoherent regime, rather than the more conventionally observed Shapiro steps in the coherent regime.

DEVELOPMENT OF A MILLIKELVIN DUAL-TIP
JOSEPHSON SCANNING TUNNELING MICROSCOPE

by

Anita Roychowdhury

Dissertation submitted to the Faculty of the Graduate School of the
University of Maryland, College Park in partial fulfillment
of the requirements for the degree of
Doctor of Philosophy
2014

Advisory Committee:

Professor Christopher J. Lobb, Chair/Advisor

Professor Frederick C. Wellstood, Advisor

Professor James R. Anderson, Advisor

Professor Bruce Kane

Professor Ichiro Takeuchi

© Copyright by
Anita Roychowdhury
2014

Dedication

To my loving husband, Shane.

Acknowledgments

None of the work described in this thesis would have been possible without the support and guidance of my advisors Professors Chris Lobb, Fred Wellstood, and Bob Anderson. In particular, I would like to thank Dr. Lobb for his advice and constant encouragement during my time in graduate school, Dr. Wellstood for his invaluable ideas and meticulous attention to detail, and Dr. Anderson for his moral support, friendship, and numerous bike rides. I would also like to thank Michael Dreyer for his expertise in electronics, UHV systems, and for teaching me everything I know about building and running an STM. Other colleagues that I have worked closely with on parts of this project and whose knowledge I have greatly benefitted from, include Mark Gubrud, Dan Sullivan, and Rami Dana. I am grateful to Dr. Bruce Kane for supporting the mK STM effort, and to Dr. Takeuchi for agreeing to be on my thesis committee.

I would like to acknowledge help and technical support from many LPS staff members and postdocs: Gyorgy Porkolab for helping me develop the Nb tip fabrication technique (Chapter 4), Toby Olver and Steve Brown for teaching me my way around the clean room, Dan Hinkel for his help with the SEM, and Ben Palmer and Zach Keane for advice on trouble-shooting our dilution refrigerator. The rest of the clean room staff have also been always available to help, and accommodated my using the RIE for 3-4 hours at a time.

The millikelvin STM system could not have been built without the expertise and effort contributed by our machinists Nolan Ballew, Bill Donaldson, John Sugrue,

Don Crouse, George Dearstine, and (late) Peter Kruzen. Russell Frizzell deserves special mention for his technical advice on several aspects of my work, and for providing many hours of entertainment.

Other LPS colleagues that I would like to thank for their generosity and for entertaining lunch-time discussions on everything from physics and cleanroom equipment to politics, evolution, and inner-city education are Victor Yun, Dongheon Park, Mihaela Ballarato, Vince Ballarato, Yongzhang Leng, and Charlie Kraft. I have benefited greatly in my years at LPS from being around a number of bright and friendly graduate students including Vitaley Zaretsky, Moe Khalil, Bahman Sarabi, Pavel Nagornykh and Sergiy Novikov.

I would also like to thank Dr. Joe Stroschio, Yves Noat and Ofer Naaman, all of whom have been happy to give me advice over email on various aspects of my experiment based on their extensive experience in the field.

I am grateful for many friends who have made my experience of graduate school extremely enjoyable. In this category I should mention Meghan Driscoll and Mark Kegel who have been excellent friends and housemates for the last 5 years, and Meem Mahmud and Nick Setzer, whose friendship and support I have always relied on. Other friends that have made these past few years memorable include Yigit Subasi, Michel deMessieres, Candace Pfefferkorn, Can Guven, Serap Guven, Joyce Coppock, Baladitya Suri, Remington Reid, Jennifer Elle, Jupiter Bagaipo and Sonya Weisburd. It is unfortunately, impossible to remember everyone, and I apologize to those I've inadvertently left out.

I would like to acknowledge financial support for this project from the Labo-

ratory for Physical sciences and NSF DMR-0605763.

I am extremely grateful for my parents and sister who supported me through graduate school and in pretty much every decision I have made. Finally, I am deeply thankful for my husband Shane, who transferred here to be with me, and has helped me over the years with everything from debugging LaTeX and fixing graphics for talks to driving me to the lab in the middle of numerous nights to check on my experiment.

Table of Contents

List of Figures	ix
List of Abbreviations	xii
1 Introduction	1
2 Scanning Tunneling Microscopy: Theoretical Foundations	7
2.1 STM operation and experimental setup	8
2.2 Tunneling basics	10
2.3 Constant current and constant distance imaging	12
2.4 Scanning tunneling spectroscopy	14
2.4.1 N-I-N tunneling	15
2.4.2 S-I-N tunneling	19
2.4.3 S-I-S tunneling	21
2.5 Cryogenic temperatures	23
3 Design and Implementation of the Millikelvin Dual-Tip STM	25
3.1 Introduction	25
3.2 System design	26
3.3 Dilution refrigerator: working principle and operation	28
3.4 System overview	31
3.5 The dual-tip STM	33
3.6 Vibration isolation	41
3.7 The ultra high vacuum (UHV) subsystem	42
3.8 Wiring	49
3.9 Cryogenic filters	51
3.10 Operation	54
3.11 Conclusions	55
4 Fabrication of Superconducting Nb Tips	57
4.1 Introduction	57
4.2 Motivation	57
4.3 Reactive ion etching tip fabrication technique	60

4.4	Characterization	65
4.5	Performance	69
5	Characterization and Performance of Dual Tip STM	85
5.1	Introduction	85
5.2	Topographic images taken with the STM	88
5.3	Effective temperature of our mK STM	89
5.3.1	Voltage noise and effective temperature	95
5.4	Stability and noise characteristics	104
5.5	Simultaneous imaging mode	107
5.6	Magnetic field	108
5.7	Conclusions	108
6	Fluctuation-Dominated Tunneling in Ultra-Small Junctions	110
6.1	Introduction to Josephson junctions	110
6.2	Josephson junction dynamics	113
6.3	The RCSJ model	115
6.4	Shapiro steps	120
6.5	The electromagnetic environment	123
6.6	Classical phase diffusion in ultra-small junctions	124
6.7	The Caldeira-Leggett model	129
6.8	$P(E)$ theory	131
6.8.1	Overview	131
6.8.2	Supercurrent peaks due to environmental resonances	134
6.8.3	Photon-assisted incoherent tunneling of Cooper pairs	141
6.9	Conclusions	146
7	Measurements of Photon-Assisted Incoherent Cooper Pair Tunneling in a Josephson STM	147
7.1	Introduction	147
7.2	Resonant tunneling	148
7.3	Photon assisted quasiparticle tunneling	152
7.4	Photon assisted incoherent pair tunneling	152
7.4.1	The incoherent vs. coherent junction response to microwaves	154
7.4.2	Incoherent pair tunneling: Microwave amplitude dependence	155
7.4.3	Incoherent pair tunneling: Microwave frequency dependence	165
7.5	Conclusions	170
8	Conclusions	172
8.1	Summary	172
8.2	Future work	173
8.3	Measuring the gauge-invariant phase difference on a superconducting sample	174
8.4	Phase stabilization to produce a true supercurrent in a Josephson STM	175
8.4.1	Reducing the quantum mechanical uncertainty in the phase	176

8.4.2	Proof of principle experiment	180
8.4.3	Reducing thermally induced phase diffusion	181
8.5	Implementation of the phase STM	186
8.6	Conclusions	188

List of Figures

2.1	STM schematic	9
2.2	Energy band diagram depicting N-I-N tunneling	16
2.3	Energy band diagram depicting S-I-N tunneling	20
2.4	Energy band diagram depicting S-I-S tunneling	22
3.1	Dilution refrigerator schematic	29
3.2	System overview	32
3.3	STM cross-section	35
3.4	STM components	36
3.5	STM assembly	38
3.6	System overview	44
3.7	Sample transfer	46
3.8	Collapsible transfer rod	47
3.9	Clamping mechanism of transfer rod	48
3.10	Dilution refrigerator details	50
3.11	Cryogenic filters	52
4.1	Reactive ion etcher	63
4.2	Niobium STM tips	67
4.3	Topographic STM image and dI/dV curve taken with Nb tip	70
4.4	STM images of Au(111) and Au(100) single crystals taken with Nb tips	72
4.5	Temperature dependence of dI/dV curves taken with Nb tip	73
4.6	Topography and slice of conductance map on a Bi_2Se_3 sample	75
4.7	Conductance map slices measured with a Nb tip on a Bi_2Se_3 sample	76
4.8	Conductance map slices measured with a Nb tip on a Bi_2Se_3 sample	77
4.9	Conductance map slices measured with a Nb tip on a Bi_2Se_3 sample	78
4.10	Conductance map slices measured with a Nb tip on a Bi_2Se_3 sample	79
4.11	Conductance map slices measured with a Nb tip on a Bi_2Se_3 sample	80
4.12	Conductance map slices measured with a Nb tip on a Bi_2Se_3 sample	81
4.13	Conductance map slices measured with a Nb tip on a Bi_2Se_3 sample	82
4.14	Phase diffusive dI/dV curve taken with a Nb tip on a Nb(100) sample	84

5.1	Topography and current images taken with STM at 30 mK	90
5.2	Effective temperature fit to dI/dV data	93
5.3	Temperature dependence of dI/dV data taken with a Nb tip and Bi ₂ Se ₃ sample	94
5.4	Fit to voltage noise model	98
5.5	Temperature dependence of dI/dV curves taken with a Nb tip and Nb sample	99
5.6	Temperature dependence of dI/dV curves taken with a Nb tip and Nb sample	100
5.7	Atomic resolution topographic images with both STM tips	101
5.8	Spectral density: inner tip	102
5.9	Spectral density: outer tip	103
5.10	Outer tip scan with various inner tip configurations	105
5.11	Inner tip scan with various outer tip configurations	106
5.12	Superconducting gap dependence on magnetic field	109
6.1	Circuit schematics for equivalent current-biased and voltage-biased configurations.	117
6.2	Tilted washboard potential	119
6.3	Sketch of $I-V$ curves of overdamped and underdamped Josephson junctions	121
6.4	Phase-diffusive supercurrent $I-V_b$ characteristic	128
6.5	Circuit schematic of finite transmission line	136
6.6	$I-V$ curves generated for different resistances R_L and R_∞	139
6.7	$I-V$ curves generated for different resistances R_L and R_∞	140
6.8	$I-V$ curves generated for different circuit resonant frequencies	142
6.9	$I-V$ curves corresponding to one and three environmental modes ($k =$ 1 and $k = 3$).	143
6.10	Gray scale plot of supercurrent response to microwave radiation . . .	145
7.1	Topographic image of Nb(100) sample	149
7.2	$I-V$ and dI/dV measurements in a Nb-Nb STM junction depicting resonant tunneling	151
7.3	dI/dV vs. V for 5.6 GHz microwaves, taken for increasing microwave amplitudes	157
7.4	False color plots of conductance data measured at 5.6 GHz microwave frequency, at increasing amplitudes	159
7.5	False color plots of conductance data measured at 5.6 GHz microwave frequency, at increasing amplitudes	160
7.6	dI/dV vs. V for 8.5 GHz microwaves, taken for increasing microwave amplitudes	162
7.7	False color plots of conductance data with outer STM tip and $f = 8.5$ GHz	163
7.8	False color plots of conductance data measured with inner STM tip and $f = 8.5$ GHz.	164

7.9	False color plot showing frequency dependence of the STM junction's supercurrent response to microwaves.	166
7.10	Conductance data and fits to theory for (a) $V_{ac} = 0$ V and (b) $V_{ac} = 25$ V for $f = 4.3$ GHz.	167
7.11	Conductance data and fits to theory for microwave frequencies (a) $f = 4.4$ GHz and (b) $f = 4.5$ GHz.	168
7.12	Conductance data and fits to theory for microwave frequencies (a) $f = 4.7$ GHz, and (b) $f = 5.0$ GHz.	169
8.1	dc SQUID used for test experiment and corresponding data	182

List of Abbreviations

AFM	Atomic force microscope
BCS	Bardeen, Cooper and Schrieffer
IVC	Inner vacuum can
LDOS	Local density of states
N-I-N	Normal-insulator-normal
RCSJ	Resistively and capacitively shunted junction model
RGA	Residual gas analyzer
RIE	Reactive ion etcher
SEM	Scanning electron microscope
SET	Single electron transistor
S-I-N	Superconductor-insulator-normal
S-I-S	Superconductor-insulator-superconductor
SQUID	Superconducting quantum interference device
STM	Scanning tunneling microscope
STS	Scanning tunneling spectroscopy
UHV	Ultra high vacuum

Chapter 1: Introduction

The scanning tunneling microscope [1] is essentially a mobile tunnel junction that can produce atomic resolution images and probe the local density of states of conducting samples with extremely fine precision. At ultra-low temperatures, an STM can not only achieve sub-Angstrom spatial resolution, but can provide unprecedented spectroscopic energy resolution. The combination of the two makes it a unique and extremely powerful surface analysis tool that can be used to image materials ranging from noble metals to doped semiconductors, superconductors, and most recently topological insulators.

STM studies of the local properties of superconductors are particularly interesting when the material has a short coherence length, resulting in varying superconducting properties at atomic length scales. Thus, Hess was the first to use an STM to image a vortex lattice in NbSe₂ [2] and many other such studies followed [3, 4]. Other groups used STMs to study high T_c superconductors, including MgB₂ [5–7], BSSCO [8–13] and the effect of atomic impurities on local superconducting properties of high T_c materials [11, 14–16].

Nearly all of the STM studies on superconductors to date have probed the quasiparticle density of states using normal metal tips made of W, Pt-Ir, or Au.

A tool that could instead provide spatially resolved information on the superconducting condensate by directly probing it using tunneling Cooper pairs, could prove particularly useful in studying superconductors with locally varying superconducting properties. A “Josephson STM” which tunnels quasiparticles at high biases and Cooper pairs at low or zero bias, would combine the spatial resolution of an STM with the tunneling properties of a Josephson junction.

There have been several proposals to exploit the physics of a Josephson STM [17–19]. There has also been work on developing techniques to fabricate superconducting STM tips [20–24] and studies have been reported using such tips on superconducting materials between 2.1 and 4 K [21, 25–31]. However, phase diffusion is a serious limitation in all such experiments. Phase diffusion occurs in ultra-small Josephson junctions due to thermal noise [32] and quantum uncertainty [33], causing the supercurrent to be highly suppressed. Simultaneously acquiring information on the atomic scale, while maintaining a measurable pair tunneling current has therefore proved extremely difficult to achieve in STM SIS junctions. Meanwhile, new materials with interesting superconducting properties or phases are still being discovered [34–38]. Hence there remains a need for tools that can directly study superconductivity in such materials, as well as in the high- T_c materials for which the underlying mechanism producing superconductivity is still not understood.

Theoretically, a very low STM junction temperature is favorable for obtaining a measurable supercurrent, especially at the relatively high junction resistances typical of a scanning STM junction. A Josephson STM that could operate at millikelvin temperatures could also provide enhanced spectroscopic resolution, and offers the

potential to uncover new physics that is inaccessible at higher temperatures. Furthermore, a Josephson STM that could provide spatially resolved phase sensitive information could provide new insights into superconductivity.

In this thesis, I report progress towards the realization of a dual-tip mK Josephson STM. I discuss both the classical and quantum physics of ultra-small junctions, and also present data that demonstrates Cooper pair tunneling in our millikelvin STM. This thesis is organized with the first third describing the design and characterization of the dual-tip STM and millikelvin system, the second third focusing on the physics of ultra-small junctions, and the final part focusing on my measurements on the dual-tip system.

In Chapter 2, I introduce the theoretical foundations of scanning tunneling microscopy, including a description of the two main imaging modes. I also present the relevant theory for interpreting scanning tunneling spectroscopy data. Since my goal was to build a Josephson STM, I compare tunneling from a normal conducting STM tip into a normal conducting sample (N-I-N), to tunneling from a superconducting STM tip into a normal sample, and tunneling from a superconducting STM tip into a superconducting STM sample. Finally, I present our motivations for undertaking the arduous project of building a millikelvin STM system.

In Chapter 3, I describe the design and implementation of the millikelvin dual-tip STM. I begin by discussing the dual-tip STM design and assembly in detail. The most unusual feature of our instrument is that it has two tips that can independently scan a sample while operating at millikelvin temperatures on a dilution refrigerator. I include a general explanation for the operation of our dilution refrigerator and

describe the modifications that were made to accommodate our STM. Details of the wiring and filtering are also provided. I also describe the UHV sample preparation chamber and our novel *in situ* sample transfer mechanism that allows us to exchange samples while the STM remains cold. Finally I discuss operation of the system.

In Chapter 4, I present a novel fabrication technique for making sharp and mechanically robust superconducting Nb tips. I discuss our motivation for developing this method, and discuss the physics and relevant parameters chosen for the etch. I also present data characterizing the Nb tips and demonstrating their performance. These results show that the tips are superconducting, atomically sharp, and mechanically robust over long time periods (~ 12 hours) even at relatively low junction resistances.

In Chapter 5, I present data acquired with the instrument to calibrate the system and evaluate its performance. This includes atomic resolution images with both tips, simultaneous scans, and spectroscopy indicating that the actual temperature accessible to the instrument is less than 100 mK. I also show that the effective noise temperature is approximately 200 mK by fitting spectroscopy data taken for a range of temperatures to a voltage noise model. To characterize the performance of the two tips in the simultaneous imaging mode, I also present images and noise power spectra for each of the tips for various configurations of the other tip. Finally, I demonstrate the operation of our magnet dewar via measurements of the superconducting gap of Nb as a function of magnetic field strength.

Having described and characterized the dual tip STM system as well as the fabrication and performance of superconducting STM tips, the rest of the thesis fo-

cuses on the physics of ultra-small junctions, and measurements I made that exploit this physics and the spectroscopic energy resolution of the system.

In Chapter 6, I provide a theoretical overview of the dynamics of ultra-small Josephson junctions such as that formed by a superconducting tip and sample in our STM. I first introduce the general physics of Josephson junctions, and the well known RCSJ (resistively and capacitively shunted junction) model that is used to provide an intuitive and quantitative picture of junction dynamics. I then discuss the electromagnetic environment that the junction is embedded in, and the effect this has on the dynamics of the junction, according to the quasi-classical theory for thermally induced phase diffusion in ultra-small junctions. The second half of this Chapter focuses on the quantum $P(E)$ theory that treats both the electromagnetic environment and the junction embedded in it. The $P(E)$ theory predicts that under the right conditions, one can observe the incoherent tunneling of Cooper pairs at non-zero voltages. This theory also predicts that the application of microwaves to the junction results in photon-assisted tunneling of incoherent Cooper pairs, rather than the Shapiro steps that arise from a coherent junction response.

In Chapter 7, I present measurements taken with a Nb STM tip on a Nb(100) sample at 30 mK. The data is in good qualitative agreement with what one expects from $P(E)$ theory. By coupling microwaves to the STM and characterizing the junctions response as a function of microwave amplitude, I also observed photon-assisted tunneling of incoherent Cooper pairs. The data and simulations (using the theory described in Chapter 6) show close agreement. Furthermore, the spacing between the peaks in this data revealed that the charge carriers responsible for the

current at low biases in my STM S-I-S junction are Cooper pairs. I also present measurements of the junction response to microwaves as a function of microwave frequency, rather than amplitude, as well as fits of some of the spectroscopy curves to theory.

Finally in Chapter 8, I conclude by summarizing my main findings and then discuss my contributions towards building a superconducting phase STM. I discuss the proposal by our group to reduce phase diffusion due to quantum mechanical uncertainty in the phase and connect this to reducing thermally induced phase diffusion as observed in our STM. I also discuss the feasibility of this project in terms of the experimental parameters and basic physics and technology involved in realizing such an instrument.

Chapter 2: Scanning Tunneling Microscopy: Theoretical Foundations

The Scanning Tunneling Microscope (STM), first described in 1981 by G. Binnig and H. Rohrer [39], is a remarkably powerful surface analysis tool capable of probing the local density of states of a sample on the atomic scale. It has also served as inspiration for a host of new scanning probe techniques that were developed in the decades since its invention, including the atomic force microscope (AFM) [40], the magnetic force microscope (MFM) [41], the scanning near-field optical microscope (SNOM) [42], the scanning gate microscope (SGM) [43] and the spin-polarized STM [44]. All of these techniques involve a probe that is raster scanned very close to the surface of a sample, allowing variations in a signal to be measured on the atomic scale. The type of probe determines the particular signal and physics that can be studied.

In this Chapter, I first describe the standard STM setup and operation, and introduce the basic working principle of the instrument. I then describe the various STM operation modes and discuss the relevant theory for each of them with a particular focus on spectroscopy using superconducting tips. Finally I discuss the desirability of cryogenic temperatures since this is central to the rest of my thesis.

2.1 STM operation and experimental setup

Figure 2.1 shows a schematic of the general setup used to run an STM (I describe my specific STM setup in Chapter 3). The STM tip is attached to a piezo with x , y and z electrodes. In our case, this piezo is a hollow cylindrical tube with $\pm x$ and $\pm y$ electrodes on opposing quadrants of the outer surface of the tube (see Fig. 2.1). A single z electrode is on the inside of the hollow tube. When a voltage difference is applied to the x piezo electrodes, for example, one side shear expands, while the side of the tube with the opposite polarity shear shrinks. This causes the tube to bend and the tip to trace out a small portion of an arc. Applying the opposite voltage difference causes the tube to bend in the opposite direction. By applying appropriate x or y voltages, the tip can raster scan the sample. The z -piezo causes the tube to shrink away from the sample, or expand towards it, in response to the polarity and magnitude of the voltage applied to it. This controls the fine- z motion of the scanner as the tip scans the sample.

Before a tunneling current can be established, the tip must first be brought within tunneling distance of the sample via a coarse approach mechanism, in our case a Pan-style stick-slip walker [45]. The tip typically “walks” a distance of 1-4 mm during approach. In order to generate a tunneling current, a bias voltage is applied, usually to the sample with the tip grounded. Once the tip is within tunneling distance of the sample, a current on the order of 1 nA is detected through the tip, and the coarse approach is stopped when it matches a user-defined set point. This tunneling current is amplified and converted to a voltage by a trans-impedance

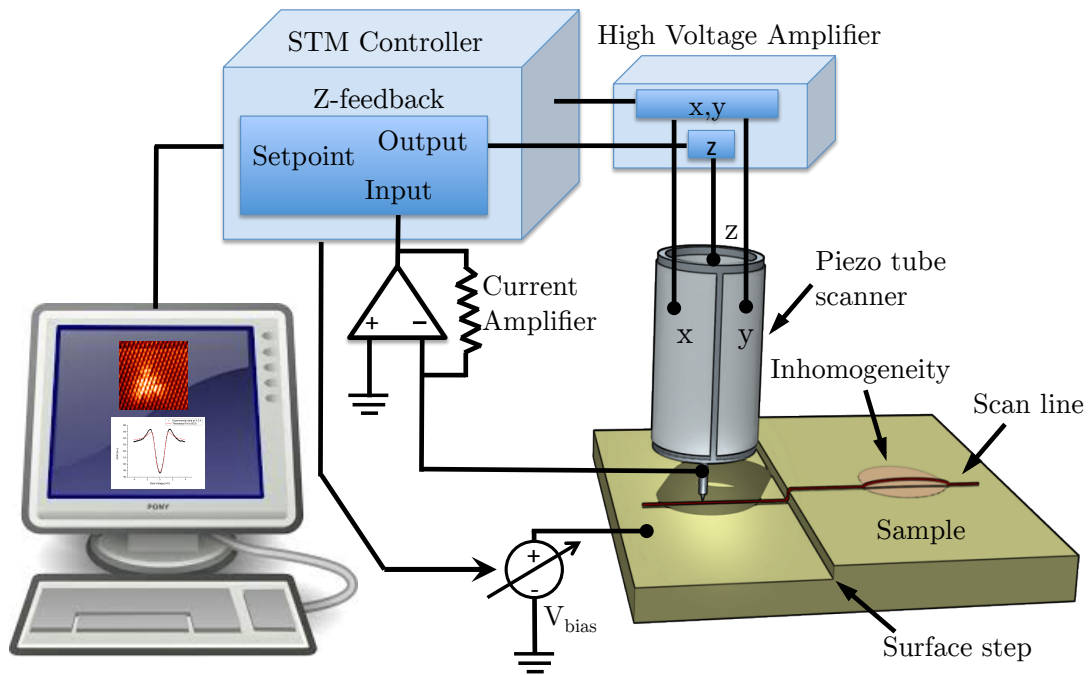


Figure 2.1: Simplified schematic of a typical STM setup. The bias voltage, set point current, and other feedback loop parameters (time constant, gain) are user-defined via the computer connected to the control unit. The x , y , and z piezos of the tube scanner are connected to a high voltage amplifier that in turn is connected to the STM controller. The tip current signal is amplified and converted into a voltage before being fed into the controller. For this input, the controller generates a feedback output that controls the z -piezo voltage to keep the tip a fixed distance above the sample.

amplifier with a resistance in the 0.1-1 G Ω range. This voltage is fed to the control electronics, which compares it to the set point and generates an error signal that is then fed back to the z -piezo to keep the tip-sample separation constant. The principle of quantum tunneling is thus crucial to the operation of an STM and the fundamental theory is introduced in the next Section.

2.2 Tunneling basics

The basic physics underlying the STM is the principle of quantum tunneling of electrons through a potential barrier [46]. When a sharp conducting tip is brought within a distance of ~ 1 nm of a conducting sample, the tip and sample form an ultra-small tunnel junction. The tunneling probability can be calculated by matching a plane wave solution to Schrodinger's equation inside the sample to an exponentially decaying wave-function inside the barrier. For a uniform, square barrier in one dimension, one finds

$$|\Psi(z)|^2 = |\Psi(0)|^2 e^{-2z\sqrt{2m(U-E)/\hbar^2}} \quad (2.1)$$

where $\Psi(0)$ is the amplitude of the wave function at the surface of the sample, z is the barrier width, U is the barrier height, m is the electron mass in its rest frame, and \hbar is Planck's constant. When a voltage V_b is applied across the STM tip and sample, and the barrier is a vacuum gap, then we may write equation Eq. (2.1) as

$$|\Psi(z)|^2 = |\Psi(0)|^2 e^{-2z\sqrt{2m(\phi_t+\phi_s-eV_b)/\hbar^2}} \quad (2.2)$$

where ϕ_t and ϕ_s are work functions of the tip and sample respectively, and the height of the barrier may be roughly approximated as the average work function of the tip

and sample.

An expression for the the electron tunnel current between two electrodes (labelled by μ and ν subscripts) with a bias voltage applied between them, was first developed by Bardeen in 1961 [46] and is given by

$$I_{\text{T}} = \frac{4\pi e}{\hbar} \sum_{\mu\nu} |M_{\mu\nu}|^2 (f(E_{\mu}) - f(E_{\nu})) \delta(E_{\mu} - E_{\nu} - eV_{\text{b}}) \quad (2.3)$$

where $f(E, T) = 1/(1 + \exp(E/k_{\text{B}}T))$ is the Fermi function at temperature T and E is energy measured from the Fermi energy. $M_{\mu\nu}$ is a matrix element that describes the overlap of the wave functions between the two electrodes and is given by

$$M_{\mu\nu} = -\frac{\hbar}{2m} \int (\psi_{\mu}^* \nabla \psi_{\nu} - \psi_{\nu} \nabla \psi_{\mu}^*) d\vec{S} \quad (2.4)$$

where the integration is over any surface S lying entirely within the vacuum gap separating the two electrodes. If we assume the system is 1-dimensional, and use the local density of states (LDOS) for the STM tip and sample, $\rho_{\text{tip}} = \sum_{\mu} |\psi_{\mu}|^2 \delta(E_{\mu} - E)$ and $\rho_{\text{sample}} = \sum_{\nu} |\psi_{\nu}|^2 \delta(E_{\nu} - E)$, the tunnel current may be written as

$$I_{\text{T}} \approx \frac{4\pi}{\hbar} |M|^2 \int_{-\infty}^{\infty} [f_{\text{tip}}(E) - f_{\text{sample}}(E + eV_{\text{b}})] \rho_{\text{tip}}(E - eV_{\text{b}}) \rho_{\text{sample}}(E) dE. \quad (2.5)$$

Here I have assumed that the tunneling matrix element M is independent of energy, and is given by

$$|M|^2 = \exp\left(-2z \sqrt{\frac{m}{\hbar^2}} \left(\frac{\phi_{\text{t}} + \phi_{\text{s}}}{2}\right)\right). \quad (2.6)$$

From Eqs. (2.5) and (2.6) it can be seen that the tunnel current depends exponentially on z . This exponential dependence of the tunnel current on the tip-sample separation is exploited in an STM to create an extremely sensitive probe

of the topography and the local density of states (LDOS) of a conducting sample. The exponential dependence is also critical to keeping the tip at a constant but extremely close distance from the sample by maintaining a constant tunnel current.

2.3 Constant current and constant distance imaging

The two main modes of imaging a sample with an STM are the constant current and constant distance modes. In the constant current mode, variations in the z -piezo voltage are recorded as a function of the tip's x - y position as it raster scans the sample. The tunnel current is held constant by a feedback circuit which compares the measured value to a set point defined by the user, and adjusts the voltage on the z -piezo accordingly. The feedback loop has an integrator with a time constant that must be adjusted by hand to suit the sample being studied. Careful adjustments of the feedback parameters are required to achieve good images in the constant current mode. A feedback that is too slow results in the tip being unable to follow the sample topography accurately, and it might cause the tip to bump into protruding features and lag over “cliffs.” A feedback that is too fast causes an underdamped response, and feedback oscillations. Such oscillations are difficult to distinguish from tip instabilities or coupling between the tip and mechanical oscillations in wires somewhere in the circuit.

For a metallic surface, constant current images generally reflect surface topography, although analyzing and interpreting the data in a precise manner is difficult. The essential problem in comparing an image to theory is the need to calculate the

tunneling matrix element in Eq. (2.4). To do this integration, explicit expressions for the tip and sample wave functions Ψ_μ and Ψ_ν are needed. The 1-dimensional approximation discussed above is easily calculable but not very realistic.

In 1985, Tersoff and Hamann [47] described an approach that improved on the 1D approximation. They used first order perturbation theory and a simple model of a spherically symmetric and atomically sharp tip to calculate the tunneling matrix element. For small bias voltages, at low temperatures, and taking only elastic tunneling into account, they wrote the tunnel current as

$$I = \frac{32\pi^3 e^2 \phi^2}{\hbar} \rho_{\text{tip}}(E_F) e^{-2\kappa R} \sum_{\nu} |\Psi_{\nu}(r_0)|^2 \delta(E_{\nu} - E_F) \quad (2.7)$$

where ϕ is the effective height of the local potential barrier, $\kappa = (2m\phi)/\hbar$ is the spatial decay constant in the barrier, R is the effective tip radius, and r_0 is the center of curvature of the tip. Also, $\rho_{\text{sample}}(E_F, r_0) = \sum_{\nu} |\Psi_{\nu}(r_0)|^2 \delta(E_{\nu} - E_F)$, is the LDOS of the sample at the Fermi level. Using this expression, images obtained in the constant current mode may be interpreted as contour maps of constant surface LDOS at E_F . However, we note that in general the current signal cannot be interpreted to represent solely the electronic structure of the sample, and a full treatment would involve de-convolving the tip states from those of the sample. Again, this is an extremely difficult problem since the precise structure and composition of a tip is not usually known.

An STM may also be used to image in the constant height mode. In this mode, the tip is raster scanned over the surface at a constant height without any z feedback, and the resulting variations in tunnel current are recorded and transformed into an

image. Since the tip-sample separation is typically on the order of 1 nm or less, very small features on the sample can result in the tip crashing into it. Thus, this method of imaging is typically only used to study atomically flat terraces of cleaved or single crystal samples.

Both the constant current and constant height modes have their advantages. For example, overviews of large areas (1-3 μm) with unknown topography are usually obtained using the constant current mode, whereas small atomically resolved images are usually easier to obtain using the constant height mode. Both modes are typically used to calibrate the piezo scanner of a new STM: images of atomic steps on a single crystal with known lattice constants taken in the constant current mode provide z -calibration, and the atomic lattice imaged in the constant height mode provides x and y calibrations.

2.4 Scanning tunneling spectroscopy

In the spectroscopic mode the STM tip is parked at a chosen point of a topographic image, the feedback circuit turned off, and the bias voltage V swept between two user defined values. The tunneling current I is recorded as a function of voltage, at specific user defined values. At the same time, a lock-in amplifier is used to measure the conductance dI/dV . In principle dI/dV could be found by numerical differentiation of the I - V curve, but the lock-in technique provides a better signal-to-noise ratio.

Scanning tunneling spectroscopy (STS) involves the simultaneous recording of

a topographic image and spectroscopy data. In this mode the tunnel current is first recorded at a user-defined fixed bias voltage, after which the feedback loop is turned off and the bias voltage swept. The I - V and dI/dV vs. V data are then recorded. The feedback loop is then turned back on, the tip moved to the next pixel, and the procedure repeated. Obtaining atomically resolved spectroscopic data in this way is arguably the most powerful capability of an STM, as it allows mapping of the LDOS of a sample on the atomic scale.

2.4.1 N-I-N tunneling

The simplified energy band model shown in Fig. 2.2 provides an intuitive picture of how dI/dV conductance data may be interpreted. This 1-dimensional model shows two normal metal electrodes representing the tip and sample. The two electrodes are separated by a vacuum gap. The distribution of quasiparticles depends on the temperature of the system and is determined by the Fermi function. At 0 K, as shown in the figure, the Fermi function reduces to a step function with all states occupied by quasiparticles up to the Fermi energy. In the absence of an external voltage, the Fermi energies line up (Fig. 2.2(a)). When a voltage bias, V is applied to the sample, the Fermi energies are shifted by eV with respect to each other, allowing tunneling from occupied states in one electrode to unoccupied states in the other (see Fig. 2.2(b)).

If a positive bias potential V is applied to the sample, the net quasiparticle

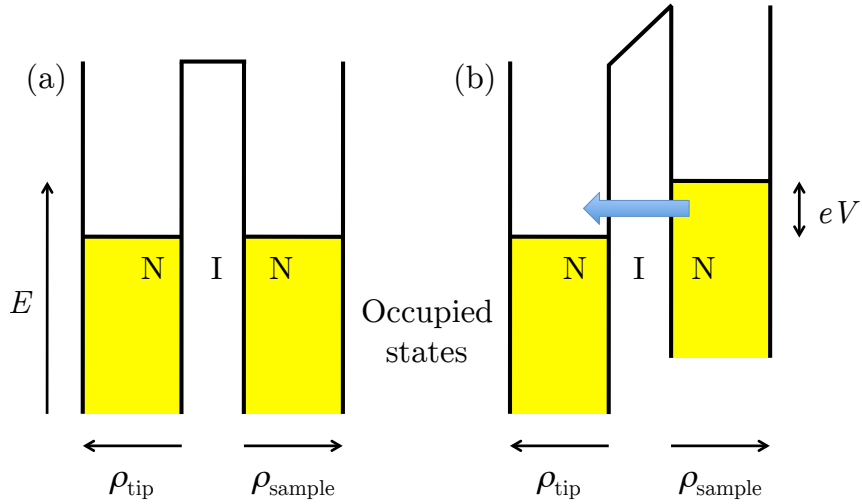


Figure 2.2: Band diagram depicting N-I-N tunneling at temperature $T = 0$ for (a) $V = 0$, and (b) $|V| > 0$, where V is the negative bias voltage applied to the sample, and the tip is grounded. The y -axis depicts the energy E of quasiparticle states. Quasiparticles from occupied states (yellow) from the sample tunnel into unoccupied states in the tip only when the applied voltage bias shifts the Fermi level of one with respect to the other.

tunnel current flowing to the STM tip from the sample can be written as [46, 48]

$$I(V) = \frac{4\pi e|M|^2}{\hbar} \int_{-\infty}^{\infty} [f_{\text{tip}}(E) - f_{\text{sample}}(E + eV)] \rho_{\text{tip}}(E)\rho_{\text{sample}}(E + eV)dE, \quad (2.8)$$

where $|M|$ is the average value of the tunneling matrix element, assumed to be independent of energy, f_{tip} and f_{sample} are the electron energy distribution functions in the electrodes which reduce to the Fermi distribution in thermal equilibrium, and ρ_{tip} and ρ_{sample} are the local electronic density of states (LDOS) of the tip and sample at the point of contact.

If the tip and sample are both normal metals, and the Fermi energy for both can be treated as approximately constant, we can write [48]

$$I = (4\pi e|M|^2\rho_{\text{sample,n}}(0)\rho_{\text{tip,n}}(0)/\hbar) \int_{-\infty}^{\infty} [f(E) - f(E + eV)] dE, \quad (2.9)$$

where $\rho_{\text{tip,n}}(0)$ and $\rho_{\text{sample,n}}(0)$ are the density of states of the tip and sample respectively at the Fermi energy. In the limit of small applied bias voltage ($eV \ll k_{\text{B}}T$), the integral reduces to eV , and we can write

$$I = G_{\text{n}}V \quad (2.10)$$

where the tunnel conductance in the junction's normal state is

$$G_{\text{n}} = 4\pi e^2|M|^2\rho_{\text{sample,n}}(0)\rho_{\text{tip,n}}(0)/\hbar \quad (2.11)$$

Since M depends exponentially on the tip-sample separation, the tunneling current I will depend exponentially on z .

While Eq. (2.10) is useful for simple metals, many STM studies are conducted on materials with a LDOS that depends on energy. It is these materials that are

interesting to probe through spectroscopic tunneling measurements. In general, Eq.

(2.8) can be rewritten in the form

$$I = \frac{G_n}{e\rho_{\text{tip},n}(0)\rho_{\text{sample},n}(0)} \int_{-\infty}^{\infty} [f(E) - f(E + eV)] \rho_{\text{tip}}(E) \rho_{\text{sample}}(E + eV) dE, \quad (2.12)$$

where $\rho_{\text{tip},n}(0)$ is the density of states of the tip at the Fermi energy when the tip is in the normal state. If we assume that the density of states of the tip is constant, *i.e.*, $\rho_{\text{tip}}(E) = \rho_{\text{tip},n}(0)$, we may write

$$I = \frac{G_n}{e\rho_{\text{sample},n}(0)} \int_{-\infty}^{\infty} [f(E) - f(E + eV)] \rho_{\text{sample}}(E + eV) dE \quad (2.13)$$

Typically dI/dV is difficult to compute from Eq. (2.13) at non-zero temperatures. Conductance (dI/dV) data at such temperatures is therefore nontrivial to interpret. However, if we consider the limit $T \rightarrow 0$, the Fermi function $f(E)$ becomes $1 - \Theta(E)$, where $\Theta(E)$ is the Heaviside step function. In this case, Eq. (2.13) reduces to

$$\begin{aligned} I &= \frac{G_n}{e\rho_{\text{sample},n}(0)} \int_{-\infty}^{\infty} [\Theta(E + eV) - \Theta(E)] \rho_{\text{sample}}(E + eV) dE \\ &= \frac{G_n}{e\rho_{\text{sample},n}(0)} \left(\int_{-eV}^{\infty} \rho_{\text{sample}}(E + eV) - \int_0^{\infty} \rho_{\text{sample}}(E + eV) dE \right) \\ &= \frac{G_n}{e\rho_{\text{sample},n}(0)} \int_{-eV}^0 \rho_{\text{sample}}(E + eV) dE \end{aligned} \quad (2.14)$$

If we shift the variable of integration, we can write

$$I = \frac{G_n}{e\rho_{\text{sample},n}(0)} \int_0^{eV} \rho_{\text{sample}}(E) dE \quad (2.15)$$

The conductance, dI/dV , is now easy to calculate by applying the first fundamental

theorem of calculus.

$$\begin{aligned}
G &= \frac{dI}{dV} = \frac{G_n}{e\rho_{\text{sample},n}(0)} \frac{d}{dV} \int_0^{eV} \rho_{\text{sample}}(E) dE \\
&= \frac{G_n}{e\rho_{\text{sample},n}(0)} e\rho_{\text{sample}}(eV) \\
&= \frac{G_n \rho_{\text{sample}}(eV)}{\rho_{\text{sample},n}(0)}
\end{aligned} \tag{2.16}$$

Thus we have

$$\frac{dI}{dV} \propto \rho_{\text{sample}}(eV). \tag{2.17}$$

We can see from Eq. (2.16) that it is extremely preferable to perform spectroscopy measurements in the $T \rightarrow 0$ limit, as they provide a way to directly probe the LDOS of a sample. This is in fact the primary motivation behind designing STM systems such as ours that operate at millikelvin temperatures.

2.4.2 S-I-N tunneling

Figure 2.3 shows a band diagram illustrating tunneling between a superconducting tip and normal sample. In this case we can write

$$\frac{dI}{dV} = \frac{G_n}{e} \int_{-\infty}^{\infty} f(E + eV) N_{\text{sample}}(E + eV) N_{\text{tip}}(E) dE, \tag{2.18}$$

where G_n is given by Eq. (2.11), and the normalized density of states for the tip and the sample are given by $N_{\text{sample}}(E + eV) = \rho_{\text{sample}}(E + eV)/\rho_{\text{sample},n}(0)$ and $N_{\text{tip}}(E) = \rho_{\text{tip}}(E)/\rho_{\text{tip},n}(0)$. For a tip made from a BCS s -wave superconductor, $N_{\text{tip}}(E)$ is given by [49]

$$N_{\text{tip}}(E) = \text{Re} \left[\frac{|E|}{\sqrt{E^2 - \Delta^2}} \right]. \tag{2.19}$$

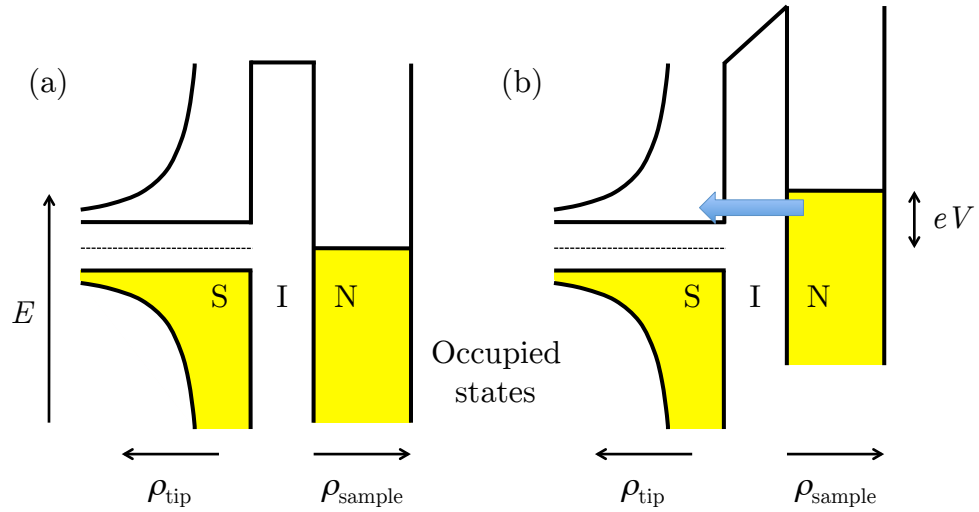


Figure 2.3: Band diagram depicting S-I-N tunneling at temperature $T = 0$ for (a) $V = 0$, and (b) $|V| > \Delta_{\text{tip}}/e$, where V is the negative bias voltage on the sample. The y -axis depicts the energy of quasiparticle states, E . Quasiparticles from occupied states (yellow) from the sample tunnel into unoccupied states in the tip only when the applied voltage bias shifts the Fermi level of one with respect to the other by an energy larger than the gap energy.

From the above equations and Fig. 2.3(b), one can see that the singularity at $E = \Delta$ in the density of states of the tip provides a way to resolve variations in the sample LDOS when the bias voltage is swept.

If either the tip or the sample is superconducting, spectroscopy measurements provide a way to probe the LDOS and electron distribution of the other electrode. For temperature $T > 0$, a conducting sample with an approximately constant density of states, and a superconducting tip, Eq. (2.18) reduces to

$$\frac{dI}{dV} \propto \left. \frac{df}{dE} \right|_{E=eV} N_{\text{tip}}(eV) \quad (2.20)$$

where $df/dE = -\text{sech}^2(E/k_{\text{B}}T)/2k_{\text{B}}T$, and $N_{\text{tip}}(eV)$ has singularities at $eV = \pm\Delta$. Thus the effect of temperature is to broaden the conductance data in a quantitatively predictable manner. In principle, this can provide an estimate for the temperature of the electrons in the non-superconducting electrode. In Chapter 6, I describe how we have used conductance measurements to obtain an estimate for the temperature of our STM junction at the base temperature of the dilution refrigerator.

2.4.3 S-I-S tunneling

Figure 2.4 shows a band diagram for quasiparticle tunneling in a junction composed of two superconductors. At $T = 0$, for superconducting materials with superconducting gaps Δ_1 and Δ_2 , a bias voltage of $V = (\Delta_1 + \Delta_2)/e$ has to be applied before quasiparticles from the occupied states of one electrode line up with

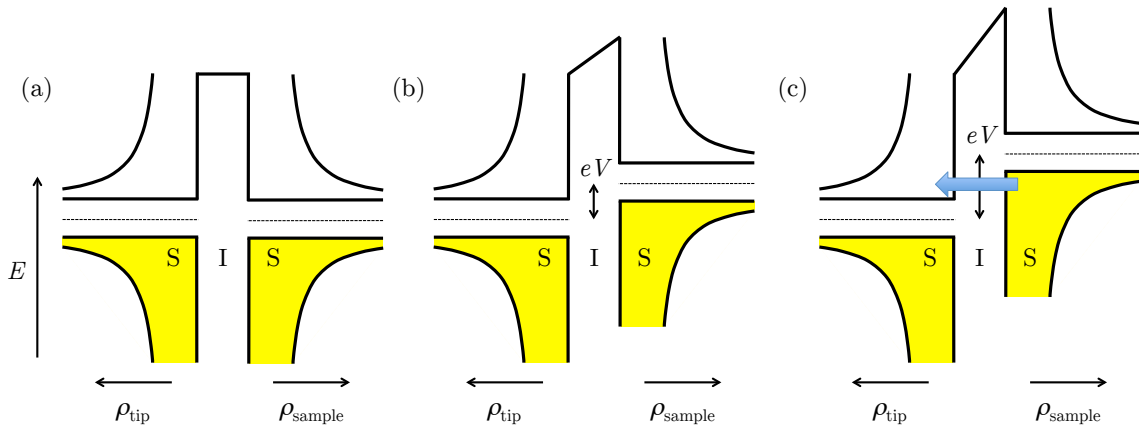


Figure 2.4: Band diagram depicting S-I-S tunneling at temperature $T = 0$ for (a) $V = 0$, (b) $\Delta_{\text{tip}}/e < |V| < (\Delta_{\text{sample}} + \Delta_{\text{tip}})/e$, and (c) $|V| > (\Delta_{\text{tip}} + \Delta_{\text{sample}})/e$. V is the negative bias voltage on the sample. The y -axis depicts the energy E of quasiparticle states. In (b), tunneling does not occur despite a positive bias voltage because quasiparticles in the occupied states of the tip DOS are not lined up with available unoccupied states in the sample DOS. Quasiparticles from occupied states (yellow) from the sample tunnel into unoccupied states in the tip only when the applied voltage bias shifts the Fermi level of one with respect to the other by an energy larger than the sum of the gaps.

available states in the other electrode. The quasiparticle current can be written as:

$$\begin{aligned}
 I &= G_n \int_{-\infty}^{\infty} [f(E + eV) - f(E)] N_{\text{sample}}(E + eV) N_{\text{tip}}(E) dE \\
 &= G_n \int_{-\infty}^{\infty} [f(E + eV) - f(E)] \frac{|E + eV|}{\sqrt{(E + eV)^2 - \Delta_1^2}} \frac{|E|}{\sqrt{E^2 - \Delta_2^2}} dE
 \end{aligned}
 \tag{2.21}$$

The expression for dI/dV is clearly more complicated than for S-I-N tunneling, and the effects of tip and sample are harder to deconvolve. However, such an S-I-S junction is interesting because the STM tip and sample form a Josephson junction. In addition to quasiparticle tunneling, one might therefore expect a supercurrent consisting of Cooper pairs to tunnel from the tip to the sample at 0 V [50]. In addition, one might expect to observe Andreev reflections due to electrons and holes combining at energies smaller than the gap to form Cooper pairs [51].

While most STM experiments on superconductors involve measurements of the quasiparticle density of states, a Josephson STM could directly probe the superconducting condensate of a sample on the atomic scale. Unfortunately, the realization of such an instrument is more complicated than one might naively expect due to a combination of engineering difficulties and constraints imposed by the physics of ultra-small junctions, as I describe in Chapter 6.

2.5 Cryogenic temperatures

There were three main reasons for undertaking the construction of the millikelvin STM system that is described in this thesis. The most straightforward reason follows directly from Section 2.4 above. When both the tip and sample are

normal metals, the Fermi function reduces to a delta function in the low temperature limit, and STS measurements may be used as a direct probe of the LDOS of the sample. Higher temperatures smear spectroscopy, obscuring fine spectroscopic features.

Second, a cryogenic scanning tunneling microscope is an extremely sensitive tool for probing physics associated with extremely small energy scales. Examples are the physics of single atomic spins [52, 53], single atom defects [54, 55], and macroscopic quantum states such as superconductivity that are manifest only at cryogenic temperatures. While superconductivity is of specific interest, there are many other physical phenomena for which millikelvin temperatures are desirable.

The final reason for building a mK STM is specific to our goal of building an STM that tunnels Cooper pairs in addition to quasiparticles. In particular, we wanted to build a dual-tip STM that can image the gauge-invariant phase difference of superconductors on the atomic scale [19], as I describe in Chapter 8. The basic idea is that a superconducting tip and sample form an ultra-small Josephson junction, the physics of which is determined primarily by three competing energy scales. These are the Josephson energy $E_J = \hbar I_c / 2e$, where I_c is the critical current of the junction, the capacitive energy $E_C = e^2 / 2C$, and the thermal energy $E_T = k_B T$. For typical STM parameters $C = 1$ fF and $I_c \approx 1$ nA, we find $E_J / k_B \approx 0.25$ K, and $E_C / k_B \approx 1$ K. In order to prevent thermal noise $k_B T$ from dominating the dynamics of the junction, we need to operate at temperatures much less than E_C / k_B and E_J / k_B , for example in the 50-150 mK regime.

Chapter 3: Design and Implementation of the Millikelvin Dual-Tip STM

3.1 Introduction

Since the invention of the scanning tunneling microscope (STM) [39], numerous systems have been built that operate at cryogenic temperatures [45, 56–62]. Cryogenic temperatures not only provide the potential for achieving finer energy resolution, but also open up the possibility of exploring otherwise inaccessible phenomena such as superconductivity and a wide range of solid state quantum effects. In the 1990’s a variety of 4 K STMs [59, 63–66] were developed and used to perform pioneering studies at the atomic scale. Since then, several groups have successfully implemented STM’s on single shot ^3He refrigerators [45, 60, 67–69] and dilution refrigerators [60–62, 70–73].

The advantage of using a dilution refrigerator instead of single shot cooling methods is that the former can supply significant cooling power continuously to an experiment, without a set time limit, at a stable temperature. Cooling power can be critical to millikelvin STM experiments due to the heat load from the STM’s several high voltage wires and moving piezos. Furthermore, some types of STM data can

take days to weeks to acquire. Temperature variations induce thermal drifts in the piezos that are extremely undesirable while taking such data.

Despite the impressive science being conducted by the systems mentioned above, there are still relatively few instruments that operate reliably at sub-Kelvin temperatures. This is mainly due to the inherent difficulties in constructing a system that operates at ultra-low temperatures, in ultra-high vacuum, with the mechanical stability necessary for STM measurements. In this Chapter, I describe details of the design, construction and operation of our dual-tip millikelvin STM. I start with general design principles and an overview of our system. I follow this with a description of our dual-tip STM, and a brief description of the principle of operation of a dilution refrigerator. I then discuss design considerations specific to our instrument such as our UHV sample preparation and transfer mechanism, vibration isolation, filter design, wiring choices, and materials used. Finally, I describe the operation of our system.

3.2 System design

Designing an STM that can operate at millikelvin temperatures involves satisfying several stringent requirements. First, the STM tip and sample obviously need to be cooled to mK temperatures. Although dilution refrigerators routinely reach millikelvin temperatures, achieving such temperatures in an STM is non-trivial. The high voltages necessary for the coarse approach motor and piezo tube scanner generate substantial heat that must be carried away and sunk at upper stages of the

fridge. In order to strongly thermally couple the STM body to the mixing chamber, some groups have resorted to making the STM body out of high purity silver [61, 62], to ensure good thermal conductivity in the entire temperature range. Although our STM head is machined out of MACOR, we have taken several other measures, discussed below, to ensure thermalization of the STM junction to the temperature of the mixing chamber.

Another critical requirement is the mechanical stability of the STM junction. Vibration isolation is critical to the operation of an STM because the tunnel current I depends exponentially on the tip-sample spacing z , *i.e.* $I = I_0 e^{-z/z_0}$. Typically the current changes by an order of magnitude when the spacing is changed by 0.1 nm which gives $z_0 = 0.23$ nm. A small change δz in z leads to a change in current $\delta I = (I/z_0)\delta z$. Hence to stabilize a 1 nA current to 10 pA requires $\delta z \leq 2.3$ pm. This illustrates the extreme stability required for the tip/sample spacing.

Our dilution refrigerator requires a host of attached pumps in order to operate and these can produce substantial vibrations. In addition, the continuous ^3He circulation can introduce unavoidable low-frequency mechanical noise. For our system, we require voltage resolution of 10 μV or better, and current resolution as fine as 1 pA. Voltage noise carried down through the wires smears signals and raises the effective temperature of the STM junction. Our strategies for filtering both mechanical and electrical noise are described in Sections 3.6 and 3.9.

Finally, samples must be kept in vacuum at a pressure of 10^{-11} Torr or better to prevent contamination of the surface. Ideally it should be possible to clean or cleave a sample and transfer it to the STM without breaking vacuum.

3.3 Dilution refrigerator: working principle and operation

A dilution refrigerator works by exploiting the phase separation that occurs when a mixture of two stable isotopes of helium (^3He and ^4He) is cooled below its tri-critical point at 0.86 K. One of the phases is ^3He rich, while the other (the dilute phase) is ^4He rich, and the enthalpy of ^3He is different in the two phases. When ^3He passes through the phase boundary from the ^3He rich phase to the dilute phase, the internal energy of the ^3He rich phase is reduced. This is analogous to evaporative cooling. The phase boundary exists all the way down to 0 K—*i.e.*, the ^3He equilibrium concentration in the ^4He -rich phase is non-zero even at 0 K. So in principle, there is no lower limit to the temperature that can be attained by the “evaporative” cooling of ^3He . Continuous cooling requires using a pump to continuously remove the ^3He atoms from the dilute phase and returning ^3He to the ^3He -rich phase.

Figure 3.1 shows a schematic of a dilution refrigerator. The refrigerator has several thermal stages that are maintained at different temperatures. The top-most is the 1K stage which is cooled by the 1K pot. The condenser is attached to the pot and is responsible for condensing the mixture (primarily ^3He) that is output from the room temperature circulation pump. The “still” stage is continually pumped on to pull ^3He from the dilute phase and also cools the incoming mixture to 600 mK. The “cold plate” sits in the middle of the heat exchangers between the still and mixing chamber and lacks active cooling power, but typically settles at a temperature of ~ 150 mK. Finally, the mixing chamber stage, contains the ^3He - ^4He phase boundary

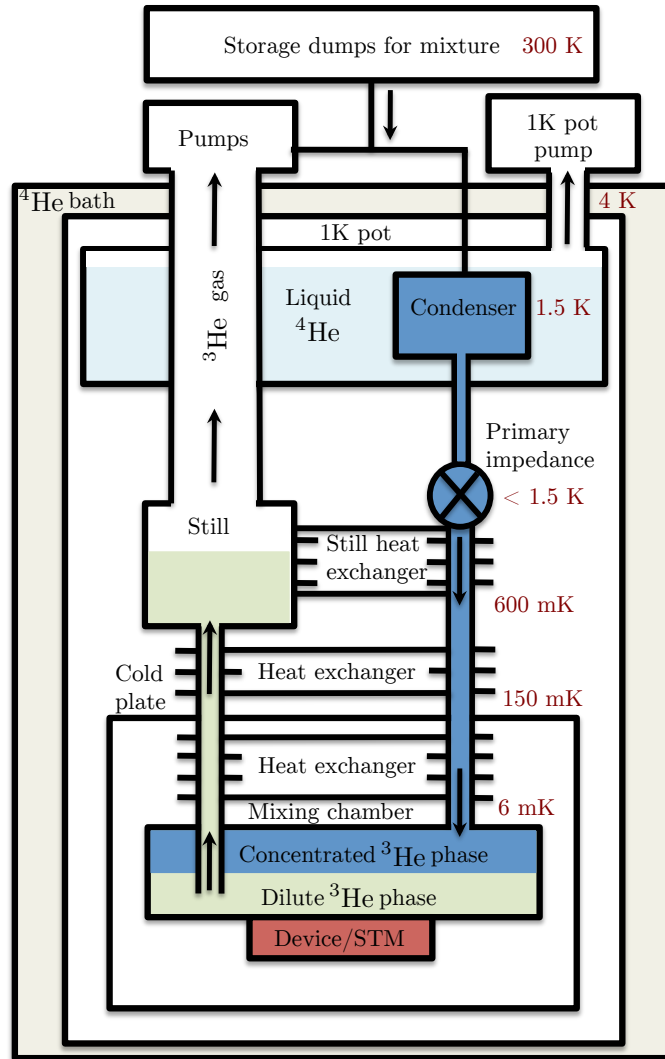


Figure 3.1: Schematic of the dilution refrigerator for the dual tip mK STM system.

and cools the mixture to $\sim 6\text{-}30$ mK. An outer dewar containing liquid ^4He functions as a ~ 4 K bath and reservoir for the 1K pot. While the refrigerator is not being operated, the warm $^3\text{He}/^4\text{He}$ mixture is stored in the “dump” at room temperature.

The inside of the refrigerator is first cooled to 77 K from room temperature by filling the outer dewar with liquid N_2 and introducing a small quantity of exchange gas, typically ^3He into the vacuum space between the dilution refrigerator unit and the dewar. Once the refrigerator has cooled to 77 K, the liquid N_2 is replaced by liquid ^4He . It is helpful if the exchange gas condenses at a temperature lower than 4K, as this aids in coupling the 4K ^4He bath to the the dilution refrigerator. Once the inside of the refrigerator has cooled to 4.2 K, the exchange gas is pumped out, and the circulation of the mixture is begun. The dilution refrigerator operation is controlled from the front panel of the main control unit; this unit directly controls all of the valves in the gas handling unit. We also used a Labview VI to operate the refrigerator automatically.

While circulating the mixture, it is first passed through cold traps kept in a 77 K nitrogen bath. The traps contain activated charcoal and are designed to condense and absorb vapors of unwanted impurities such as N_2 , O_2 or other gases present in the mixture. This is particularly important when using an oil-based scroll pump in the circulation path, as small quantities of hydrocarbons make their way into the mixture. In practice, care must be taken to pass the mixture through the cold trap at a rate of < 200 $\text{cm}^3/\text{minute}$ to ensure that the mixture is adequately cleaned. In the next step of the cycle, the mixture flows through a 4.2 K trap that is inserted in the dewar, to capture any residual impurities, such as H_2 , that were not

captured by the 77 K traps. The cold traps need to be periodically cleaned to avoid clogging. This is done by valving them off from the rest of the system and gently heating them to $\sim 100^\circ$ C, while simultaneously pumping away any released gas. A residual gas analyzer (RGA) attached to the pump is very useful for determining the composition of impurities, and for identifying small leaks.

Next, the mixture makes its way to the condenser inside the 1K pot where it is cooled to ~ 1.5 K. The 1 K pot is a small cylindrical copper chamber, connected to the ^4He bath through a fine capillary tube that forms a flow impedance. Pumping on the pot causes it to suck liquid ^4He into its body, and evaporation of the liquid produces cooling to ~ 1.2 K. The mixture next makes its way to a heat exchanger on the still (~ 0.6 K). In the main body of the still, outgoing ^3He is pumped out of the mixture by the main circulation pump. After passing through the still heat exchanger, incoming mixture is cooled even further when it passes through several coils of a heat exchanger that couples the input mixture flowing down to the colder mixture flowing up from the mix to the still. Finally, the incoming mixture reaches the mixing chamber where the phase boundary is maintained. The mixing chamber is the coldest part of the cryostat with the greatest cooling power, and the STM assembly is rigidly clamped to it.

3.4 System overview

Figure 3.2 shows an overview of our system. A UHV sample preparation and transfer system sits on an optical table directly above a ^3He - ^4He dilution refrigerator

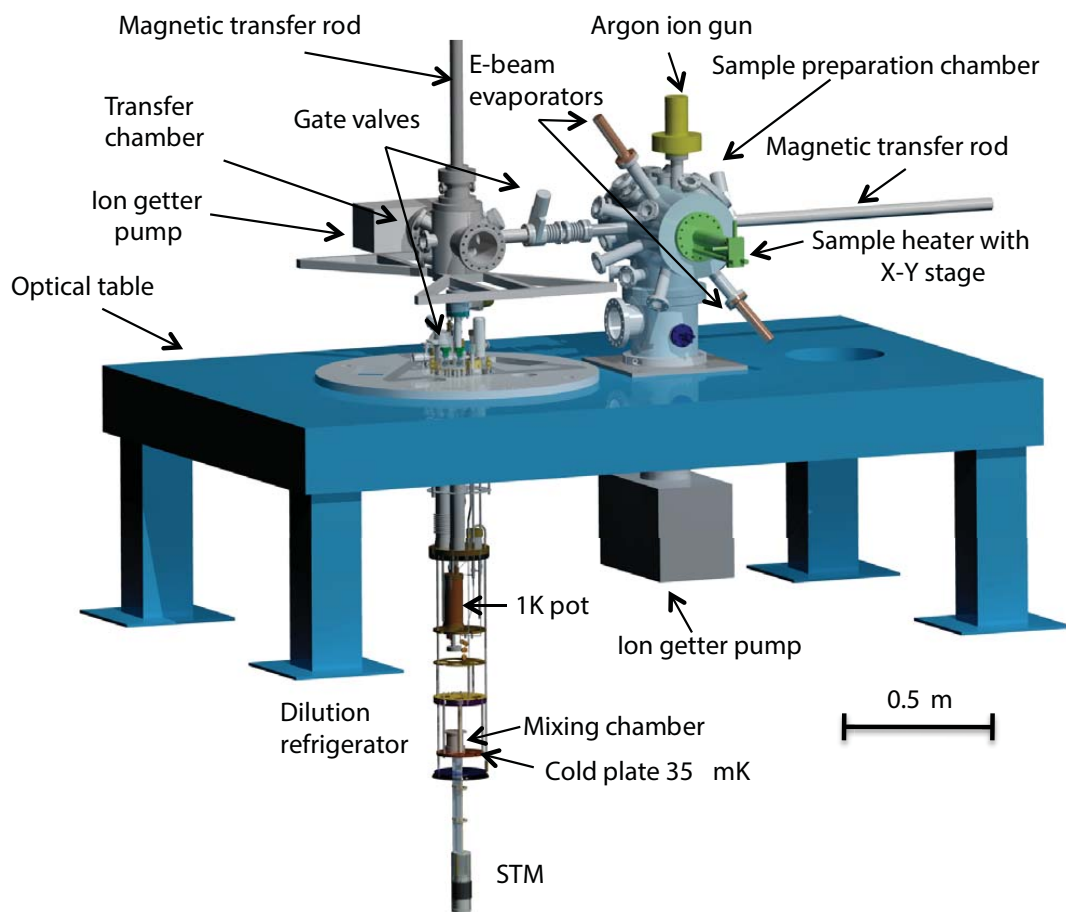


Figure 3.2: Overview of dual tip mK STM system. The dewar and radiation shields that surround the dilution refrigerator are not shown.

that has the STM assembly mounted to the mixing chamber. A vertical sample transfer rod runs along the central axis of the refrigerator to enable top loading of samples from the UHV system into the microscope. The dilution refrigerator is a customized Oxford Instruments Kelvinox with a cooling power of 400 μW at 100 mK and a no-load base temperature of 6-7 mK. The operating base temperature for our STM however is 30-35 mK due to a thermal heat-load of about 30 μW from the system wiring. Radiation shields clamped to the mixing chamber and the still (0.7 K) prevent black-body radiation from higher stages from reaching the STM. A custom made super-insulated liquid-helium cryostat [74] provides a 4 K bath. This dewar is interchangeable with a custom made 13.5 Tesla superconducting magnet dewar with a LHe capacity of 140 liters [75]. The magnet is a high field (vertical bore) solenoid system, with a rated field of 13.8 T, and a rated current of 99.8 A. The entire setup sits inside a copper and steel-walled rf shielded room with a nominal attenuation of 100 dB or greater from 1 kHz to 10 GHz.

3.5 The dual-tip STM

Our dual-tip STM is a modified version of an STM design by Pan *et al.* [45]. The main difference is that we have double the number of parts in order to allow the independent operation of two STM tips (see Fig. 3.3). Key aspects of Pan's design are its emphasis on mechanical rigidity and the use of materials that are matched as closely as possible to minimize stress from thermal expansion. In our case, this was achieved by making the main STM body from a single 94 mm long Macor cylinder

with an outer diameter of 50.8 mm and an inner diameter of 35.6 mm.

Figures 3.3(b) and 3.3(c) show details of our STM design. The sample stud (11) is loaded from the top, and the two tips approach the sample from below. The “inner” tip (1) is attached to the center or “inner” piezo tube (4), and the “outer” (off-center) tip (2) to the “outer” piezo tube (3). The tips are side-by-side, about 1 mm apart while the piezo tubes are concentric and share a common axis (see Fig. 3.2(b)). Each piezo tube is epoxied onto a Macor scanner holder. The large outer scanner (3) operates in a hole in a large sapphire prism (6). The small scanner tube (4) is located above the corresponding small sapphire prism (7) rather than within it.

The coarse approach mechanism is driven by six shear piezo stacks for each tip (see Fig. 3.3(b)). Four large stacks (5) are epoxied to the inside of the outer Macor STM body (10) and two to a Macor piece (14) held in place by a Cu-Be spring plate (13). Likewise, four small stacks (8) are epoxied onto the smaller inner Macor body, and two to a small Macor piece (15) held in place by a small Cu-Be spring plate (16).

Figure 3.4 shows the main components used to build the dual-tip STM before it was assembled. Figure 3.4(a) shows the main Macor STM body, and the components of the tip, scanner and walker components for the outer tip. Figure 3.4(b) shows the small Macor STM body, and the tip, scanner and walker components for the inner tip.

Figure 3.5 show the STM in various stages of assembly. In Fig. 3.5(a), we can see piezo stacks glued onto the large and small Macor bodies. The large piezo stacks

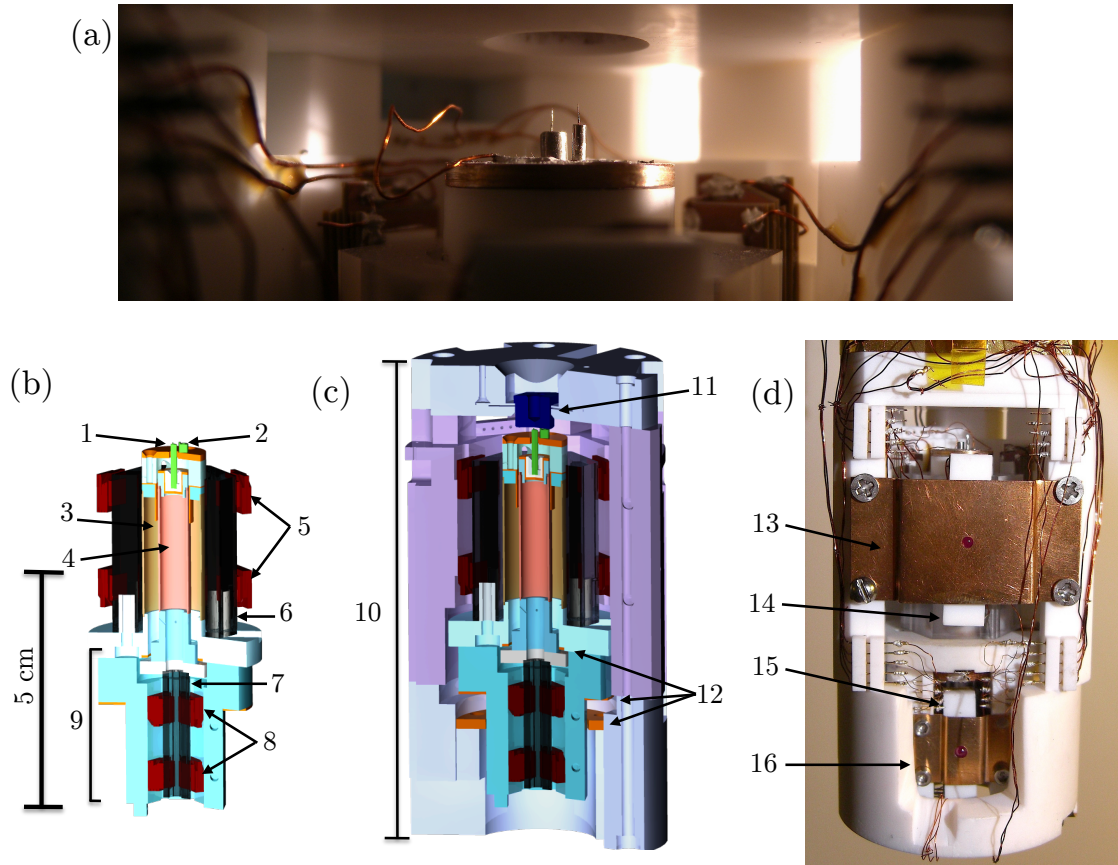


Figure 3.3: (a) Close-up photograph of STM tips, (b) inner and outer tip assemblies, (c) cross section view and (d) photograph of the STM. The figures show the inner tip (1), outer tip (2), large piezo scanner (3), small piezo scanner (4), large piezo stacks (5) and (14), large sapphire prism (6), small sapphire prism (7), small piezo stacks (8) and (15), inner tip (9), outer Macor body (10), sample stud (11), capacitance plates (12) and Cu-Be spring plates (13) and (16).

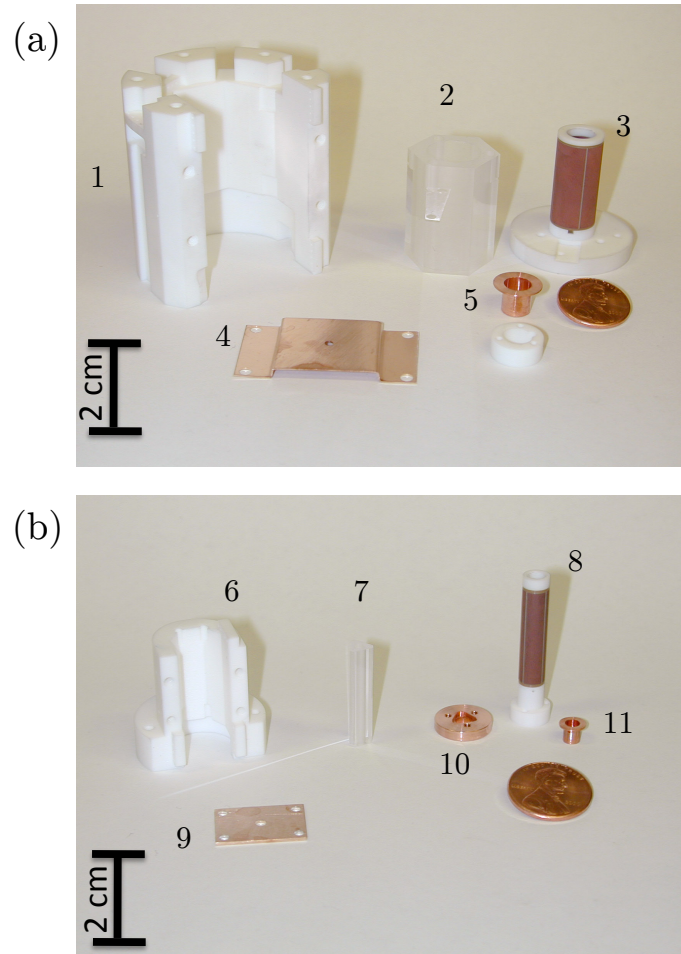


Figure 3.4: Some of the components used to build the dual-tip STM. (a) Macor main STM body (1) that forms part of the coarse approach for the outer tip, the large sapphire prism (2), the large tube scanner assembly (3), the large CuBe spring plate (4), and the copper and Macor parts of the tip cup for the outer tip (5). (b) Small Macor STM body (6), the small sapphire prism (7), the small piezo tube scanner assembly (8), the small CuBe spring plate (9), a Cu piece that attaches the small prism to the large piezo scanner (10), and the small Cu tip cup (11).

and large sapphire prism are responsible for the coarse approach for the outer tip which carries the inner tip assembly with it as well (see Fig. 3.5(c)). The small piezo stacks along with a small sapphire prism allow the inner tip to approach the sample independently. Amorphous aluminum oxide pads epoxied onto the stacks are placed in contact with sapphire prisms. The friction between these pads and the sapphire prisms is controlled by the tension of the screws against the Cu-Be spring plates.

The coarse approach uses a stick-slip motion of the piezo legs against the sapphire prisms [45]; voltage is applied to one leg at a time, which slides it backward while the static friction from the other five hold the prism in place. When all six legs have slid, the voltages on all of them are ramped down simultaneously, resulting in the prism moving forward by one step. This entire process is repeated at 60 Hz.

For first approach, I position the two tips with the inner tip just behind the outer tip (out of tunneling range), and then drive the large piezo walker so that both tips are carried forward and the outer tip makes contact with the sample first. I then retract the outer tip, and approach with the small piezo motor until a tunneling current is detected with the inner tip.

With this arrangement, our outer walker carries the weight of the inner walker (see Fig. 3.5(c)). I found that the standard design with four piezos per stack [45] was not strong enough to reliably approach the sample at mK temperatures. This was especially the case after we lost one or two of the connections to arcing due to the layer of ^3He exchange gas that adsorbed to the surface. In order to address this problem, I rebuilt the walker with six piezos per stack to incorporate redundancy even if a few of the piezo connections are lost due to arcing. I also redesigned the new

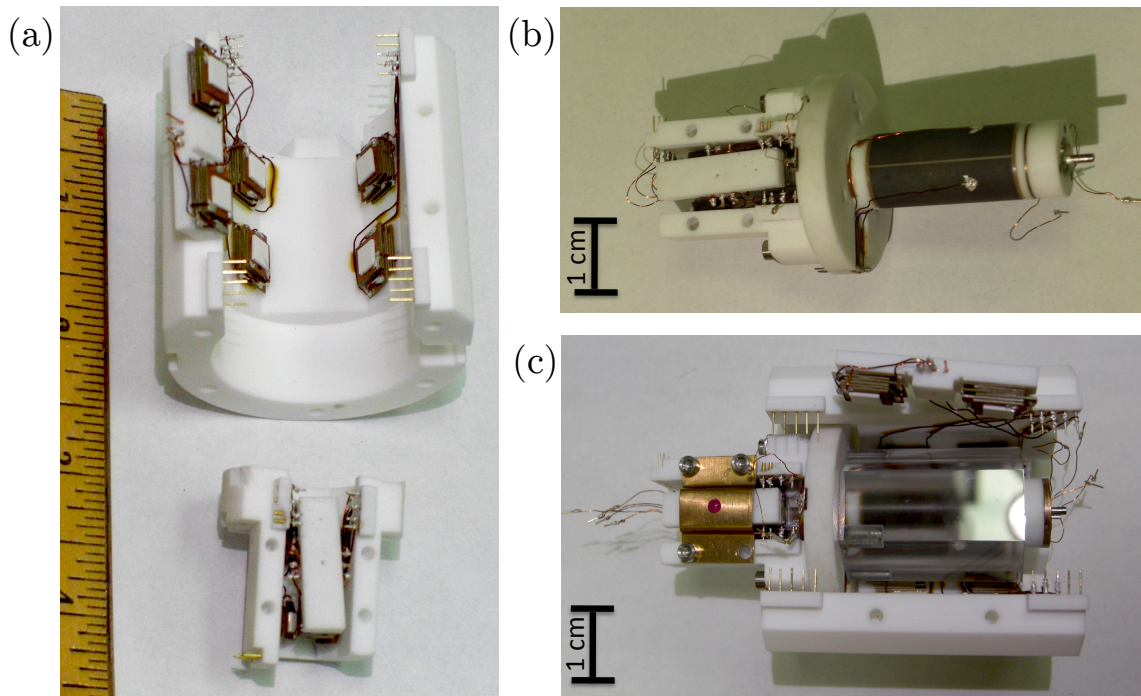


Figure 3.5: Photographs of STM while it was being assembled. (a) The large walker with 6-stack piezos and wiring, and the rebuilt small walker with 4-stack piezos. (b) STM with the small coarse approach walker attached to the large piezo tube scanner assembly. (c) STM with sapphire prism around the large tube scanner. The small Cu-Be spring plate completes the small coarse approach walker. The large CuBe spring plate and the end pieces that complete the Macor body are not shown.

stacks to have “wings” (see Fig. 3.5(a)) that tripled the distance between ground and high voltage connections, making short circuits less likely. The wings also make it easier to repair the connections if necessary.

As a final precaution against arcing, I painted a thin layer of GE varnish around the stacks, and over the connections to prevent conduction through ^3He gas adsorbed to the surface. Although GE varnish is typically avoided in UHV environments due to outgassing, I decided that the benefits in this case outweighed the costs, especially since outgassing is negligible at cryogenic temperatures. I tested the breakdown voltage of varnish up to 500 V, before and after several thermal cycles of being dipped in liquid N_2 . The varnish held up to these tests, but might eventually develop cracks after repeated thermal cycling. It should probably be redone every 15 months or so.

Testing of the six-piezo stacks at various voltages through their whole range of motion revealed that they walked about twice as fast as our four-piezo setup. The small walker for the inner tip carries less weight and four piezos per stack were sufficient. I note that the tight space makes wiring the small stacks challenging, and the prototype developed shorts after a couple of years of use. Our later design for the small walker uses replaceable piezo stacks epoxied onto copper plates that are screwed onto the small Macor body.

During operation, I monitor the relative position of each scanner-tip assembly by means of a capacitance sensor connected to capacitance plates mounted on the body (12), the small scanner section, and the large scanner section (see Fig. 3.3(c)). A capacitance bridge [76] was used to measure the capacitance, which ranges from

≈ 11 pF to 19 pF on the outer coarse approach mechanism, over the coarse motion range of 24 mm. On the inner coarse approach mechanism, the capacitance ranges from 1.8 pF to 6 pF over the maximum coarse motion range of 8 mm. I also note that at cryogenic temperatures the maximum lateral scan range of the inner tip piezo tube scanner is ≈ 1 μm while the lateral scan range of the outer tip piezo tube scanner is ≈ 2 μm .

The Macor STM body is bolted rigidly to the mixing chamber plate of the dilution refrigerator via a Cu flange and three L-shaped Cu bars. The lowest internal vibrational modes of the mixing chamber plate were stiffened with the help of additional braces [77]. The STM body is enclosed in a Au-plated Cu can for electrical and heat shielding. This can is surrounded by a 150 mK heat shield, which is in turn enclosed by the inner vacuum can (IVC) and the LHe dewar.

One of the tip-scanner-walker subsystems of the microscope is controlled by an RHK Technology STM control system [78]. It has a maximum piezo voltage of 220 V and runs in analog feedback. This subsystem uses an IVP-300 RHK trans-impedance amplifier with a conversion factor of 1 nA/V to maintain the tunnel current. The other tip-scanner-walker subsystem is controlled by a Thermomicroscopes SPM control system (now obsolete), with a digital feedback electronic control unit, and a maximum piezo voltage of 220 V. A variable gain trans-impedance amplifier monitors the tunnel current [79].

3.6 Vibration isolation

The STM must be kept as vibrationally isolated as possible—ideally with the tip-to-sample distance stable to better than 5 picometers (pm) in order to resolve atomic scale features in topographic images and fine scale structures in spectroscopy.

We chose a Pan-style design [45] for the STM head because it is resistant to vibrational noise. Vibration isolation of the entire system is achieved by mounting the refrigerator on an optical table with a pneumatically damped air suspension system (see Fig. 3.1) [80]. The nominal isolation efficiency is 97% at 5 Hz and 99% at 10 Hz, with a resonance frequency of 0.8-1.7 Hz for the vertical mode. The horizontal mode has an isolation efficiency of up to 90% at 5 Hz and 95% at 10 Hz with a resonance frequency of 1-2 Hz [81]. Another potential source of vibrations is whistling in the 1 K pot, as liquid ^4He is drawn in through the siphon. To eliminate whistling, the pot was custom-made to a larger size, allowing data to be taken for 1.5 days between fillings.

To reduce vibrations from the rotary circulation pumps, we placed them on large rubber pads in an adjacent room. The pipes from these pumps go through a sand box and vertical and horizontal aluminum bellows for additional vibration isolation. Pumping line connections to the top of the optical table present a critical vibration isolation problem. We use bellows in a “sideways T design” [77] to minimize the transfer of pressure variation from the pumping lines to the table. The T-bellows box rests on a rubber pad and has 113 kg of Pb added to it.

3.7 The ultra high vacuum (UHV) subsystem

An ultra high vacuum sample preparation and transfer mechanism is an extremely desirable feature for a low-temperature STM for several reasons. First, it allows the exchange of samples without breaking vacuum, or having to warm the system to room temperature. This also facilitates our standard procedure for cleaning the STM tip via high voltage field emission against an Au(111) single crystal, and then exchanging it out for a more interesting sample of our choice. Second, the exposure of any sample to air, even for a few seconds, results in the adsorption of a thin layer of water and other contaminants on the sample's surface. Upon cooling, this layer freezes in place and impedes one's ability to scan and interpret atomic scale features on the sample surface.

At this point I should note that with our dilution refrigerator based STM, there is an additional complication from adsorbed gases. During operation, I use a very small quantity of ^3He during cool down, to couple the inside of the refrigerator, including the STM to the 4 K ^4He bath in the dewar. This exchange gas is pumped out before starting circulation of the ^3He - ^4He mixture. However, if we cool the system with the sample placed in the STM, some residual ^3He nevertheless remains adsorbed on the sample surface. In fact, a thin layer of ^3He atoms will collect on all of the STM surfaces, including the piezo stacks used for the coarse approach mechanism. This film can lead to an arc discharge between the high-voltage piezos in the coarse approach motor, weakening its power or preventing the tip from approaching the sample. This has led other mk STM groups to replace the exchange gas with a

heat switch [61], or pre-cooling loop [62]. In our case, since we had already bought and installed our refrigerator as well as all of the STM wiring and filtering, we addressed this problem by making a minor modification to the STM head, described in Section 3.5. It is also undesirable to condense the exchange gas on the sample surface. Our *in situ* transfer mechanism allows us to insert the sample into the STM after pumping out the exchange gas. This prevents the accumulation of ^3He atoms on the sample surface.

Figure 3.6 shows a photograph of our UHV subsystem, which consists of a preparation chamber and a transfer chamber that are separated by a gate valve. Each chamber has its own ion getter [82], titanium sublimation pumps [83], and ion gauge [84]. The system is roughed out using a detachable turbo pump [85] backed by an oil-free scroll pump [86] and can be baked to 150°C using heater tape. A load lock allows the introduction of samples into the preparation chamber. Samples are mounted on sample studs that fit into the STM and can be moved throughout the UHV system on a transfer plate using a magnetic transfer rod.

The sample preparation chamber has a residual gas analyzer [87], two electron beam evaporators [88], and an argon ion sputter gun [89]. The sample stage in this chamber is attached to an XYZ manipulator [90]. Samples may be heated to 600°C by a resistive heater or by a direct current heater [91]. The preparation chamber also has a room temperature STM for examining samples before we transfer them into the mK STM.

As we noted above, a very desirable feature in a low-temperature STM is the ability to exchange samples without having to warm the system to room temper-

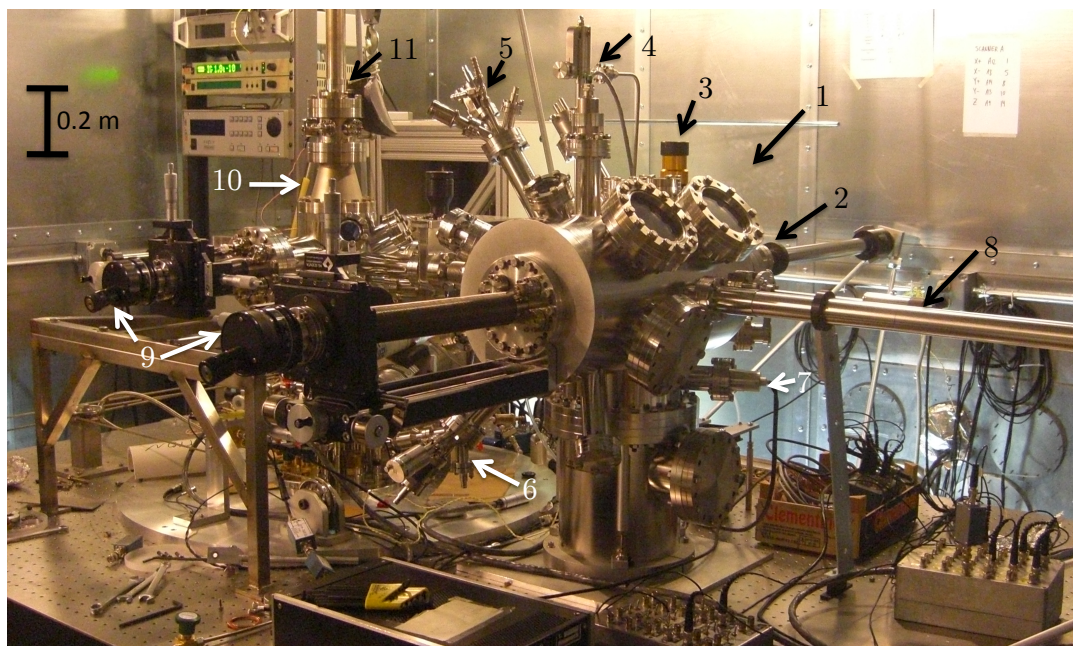


Figure 3.6: Photograph of the UHV subsystem used to prepare and transfer samples into the STM. It consists of the sample preparation chamber (1), with a load lock (2) and gate valve (3). The argon ion gun (4) and e-beam evaporators (5) and (6) are used to prepare the samples. Nitrogen is bled into the chamber during venting via a nozzle (7). A magnetic transfer rod (8) is used to introduce samples into the transfer chamber (10). Each chamber is equipped with an XYZ manipulator (9) to adjust the position of a sample holder. Finally, the sample is transferred into the STM via a collapsible sample transfer rod (11).

ature. Our design allows for top loading of samples via a 3 cm diameter access shaft in the dilution refrigerator. Figure 3.7(a) shows the sample transfer rod with a sample stud attached to it as it is being lowered through the central shaft of the dilution refrigerator. The top-loading system uses a collapsible rod that fits inside a 4' long magnetic transfer rod [Fig. 3.7(a) and 3.8(a)]. The collapsible rod has an outer tube made from a 0.5" diameter thick-walled aluminum tube with a slot cut along almost the entire length. Inside the slot there is a brass pin that is attached to a thin-walled stainless steel tube. The lower end of the inner tube is fitted with a sample exchange fork [91] for engaging the sample stud and a guide piece. The brass pin can be locked in place at either end of the outer tube. The locks have an L-shaped cut [Fig. 3.8(b) and 3.8(c)] and are operated by a short wobble stick while the pin is held in place by a clamping mechanism.

Figure 3.9 shows the two spring-loaded clamp arms. The springs force the clamping arms open while a pulley system is used to close them. The clamps are operated by a push/pull feedthrough hooked into a steel rope loop running around the pulleys. Each arm has a short spike. The spikes fit into counter bores on the brass pins in the inner stainless steel tube. This arrangement allows the inner rod to be held in place while the outer rod is moved between the upper and lower latching positions, allowing transfer of the sample from the transfer chamber to the mixing chamber.

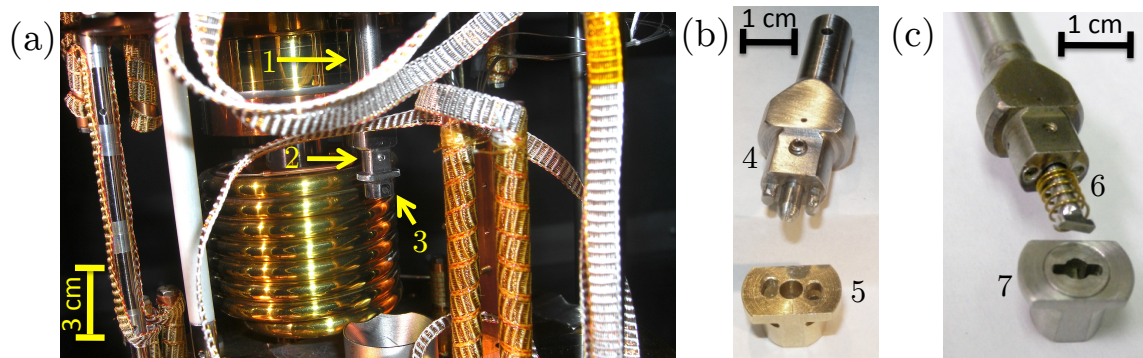


Figure 3.7: (a) Sample transfer tube (1) with sample grabber (2) and sample stud (3) as the sample is being inserted through the central shaft of the dilution refrigerator. (b) and (c) Two different sample grabber designs (4) and (6) that lock into sample studs (5) and (7) respectively.

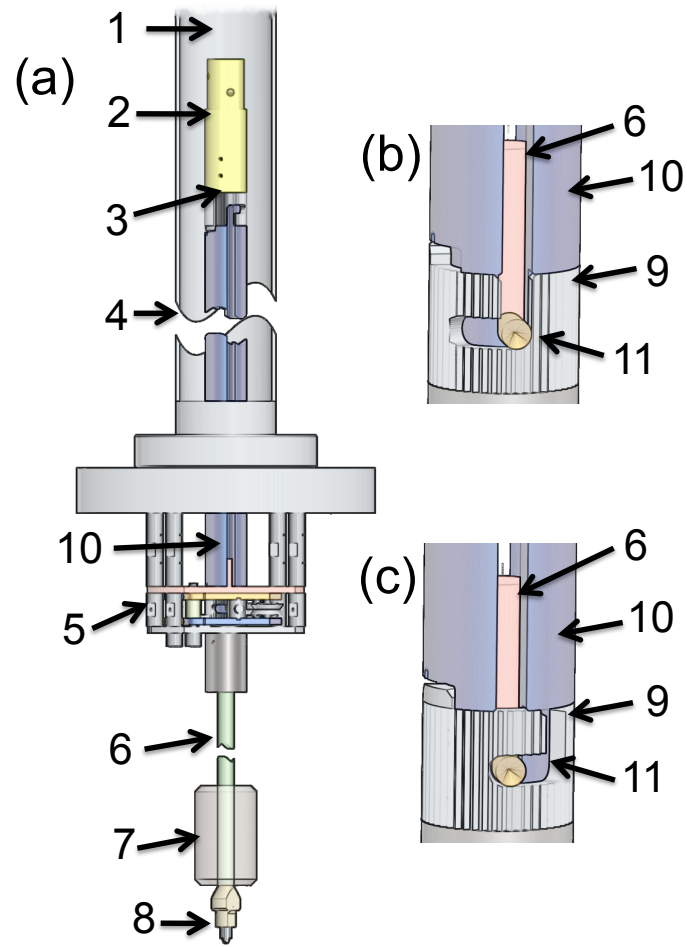


Figure 3.8: (a) Overview of collapsible transfer rod. (b) Locking mechanism in the open and (c) closed position. (1) Shell of magnetic transfer rod, (2) coupler, (3) upper lock, (4) outer rod, (5) clamp with lower lock inside, (6) inner rod, (7) guide piece, (8) sample grabber, (9) lock, (10) outer shaft, (11) slot in outer shaft showing brass pin mounted on inner rod.

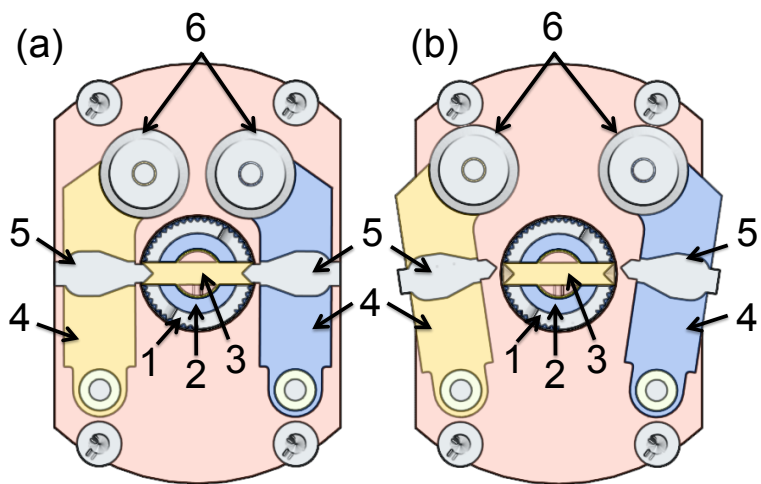


Figure 3.9: Transfer rod clamping mechanism in the (a) closed and (b) open position.

(1) lock, (2) outer shaft, (3) brass pin mounted on inner rod, (4) clamp arm, (5) spike and (6) pulley system.

3.8 Wiring

The two main kinds of wires in our system are (1) “signal wires” for the two STM tips, sample, and capacitive sensors, and (2) “drive wires” for the piezo drives and thermometry [77].

To achieve good energy resolution for tunneling spectroscopy, the signal wires must be shielded and filtered to prevent heating and smearing of non-linear electrical tunneling characteristics by broad-band noise. The length of each wire (see Table 3.1) was chosen so that heat leaks between stages were not too large. Since the body of our STM is made from Macor, which is thermally quite insulating, we used Cu wires from the STM to the mixing chamber stage to carry away heat generated during coarse approach and tunneling measurements. The wire insulation must work with tunneling resistances that range up to $100\text{ G}\Omega$, and must be able to withstand several hundreds of volts applied during field emission in order to clean the tip.

Figure 3.10 shows details of the wiring and filtering on each stage of our dilution refrigerator. One potential source of noise in our system is microphonic pickup on the signal wires for the tips. To reduce this pickup we used semi-rigid coax for all signal wires inside the vacuum space of the cryostat (see Fig. 3.10(a)). This also provides good shielding against rf pickup and allows us to use rf-tight connectors. To minimize thermal load between stages, we used CuNi microcoax (see Table 1). The coax was clamped to 3.35 cm long Cu posts at the 600 mK still stage, and 7.5 cm long posts at the 150 mK stage (see Fig. 3.10(b)). At the mixing chamber, these lines are connected to bronze powder filters [77] by SSMC connectors.

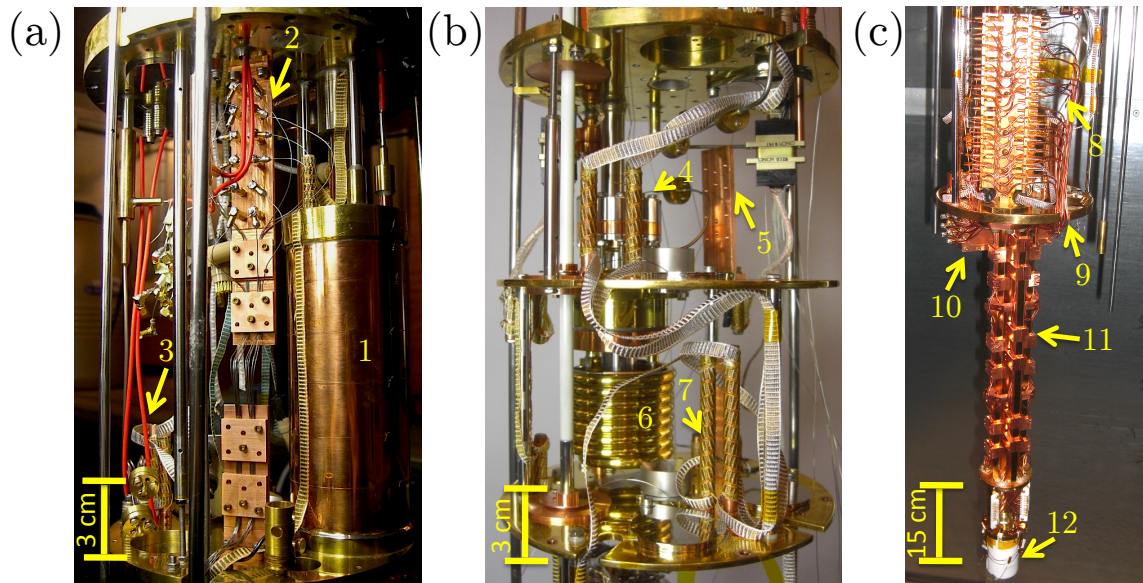


Figure 3.10: Photographs of (a) the 1K pot stage, (b) the still stage and cold plate, and (c) the mixing chamber stage and STM. The 1 K pot (1) was custom built to 1.5 times the normal size. Copper heat sinks ((2) and (5)) for the NbTi microcoax signal wires are tightly bolted to each stage of the dilution refrigerator. Cylindrical heat sinks ((3) and (7)) for the loom wires are also tightly bolted to each stage. Figure 3.7(b) also shows the still (4) and continuous heat exchangers (6). Copper coax wires (8) were used for good thermal coupling between the mixing chamber stage (9) and the STM (12). The signal wires pass through bronze powder filters (10) that are tightly bolted to the mixing chamber stage. All of the Cu coaxial wires are heat sunk by clamps (11) that tightly press the wires against the Au-plated Cu extension rods.

As shown in Fig. 3.10(c), from the mixing chamber filters to the STM, the signal lines are semi-rigid coax with Cu shielding, and a Ag plated Cu inner conductor to allow heat to be conducted away from the STM tip, sample, and piezos.

Four woven wiring looms [93], each with 12 twisted pairs of ≈ 100 μm diameter wire were used for the thermometry and piezo wiring. From 300 K to 1.4 K, two Constantan wiring looms were used as they provided a low heat load and resistances that varied only slightly with temperature. From 1.4 K to the mixing chamber, we used two CuNi-clad NbTi looms that were superconducting below 9 K. The Nb-Ti loom can be seen in the close up photograph of the still stage and cold plate in Figure 3.10(b). These lines were connected to the STM via semi-rigid coax as was done for the signal wires. The looms are wrapped around copper heat sinks at each stage on the refrigerator. To ensure adequate thermal anchoring, 40 mm tall heat-sink posts were used at the 4 K, 1.4 K, and 0.6 K stages, and 75 mm tall posts were used at the 150 mK shield stage and mixing chamber.

3.9 Cryogenic filters

To prevent external rf and microwave interference from reaching the STM, the signal wires are filtered with low pass π -filters on entry into the shielded room and at the top of the cryostat. We also used bronze powder filters on the signal wires at the mixing chamber stage (see Fig. 3.11(a)). The CuNi microcoax used for the signal wires also provides some filtering. The cable length of 1 m from room temperature to 4 K, and 1 m from 4 K to the mixing chamber, provides a total attenuation of

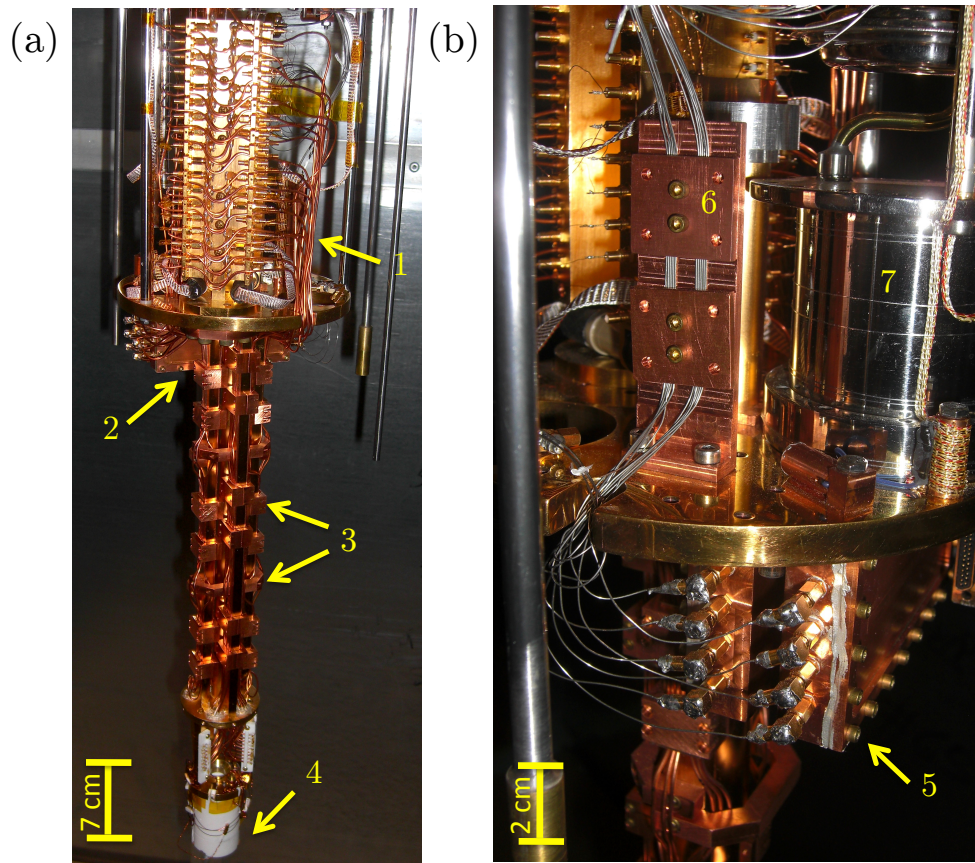


Figure 3.11: (a) Photographs of the mixing chamber stage showing the Au plated Cu box (1) designed to accommodate filters for all the non-signal lines, bronze powder filter boxes (2), heat sinking clamps (3) to ensure thermalization of the STM to the mixing chamber temperature, and the STM (4). (b) Photograph of the powder filter boxes (5), with CuNi micro-coaxial wires leading into them. Rectangular Cu heat sinks (6) are used to ensure thermalization of the coaxes to the mixing chamber (7).

about 39 dB at 1 GHz and 120 dB at 10 GHz [95].

The bronze powder filters we used were based on the design by Miliken *et al* [96] which in turn are based on the original powder filters built by Martinis *et al.* in the 1980's [97]. The principle of operation of these low-pass filters relies on a combination of the skin effect, and the large surface area to volume ratio of the metal powder. Eddy currents are created on the surface of each metal grain, causing dissipation in the metal powder/epoxy mixture. The length scale associated with the surface currents is the skin depth, $\delta = \sqrt{\rho/\pi f \mu}$, where ρ is resistivity, f is frequency, and μ is the magnetic permeability of the metal. The power dissipated is proportional to ρ/δ . Hence, the larger the surface area to volume ratio of the metal powder, the greater the dissipation at high frequencies. Figure 3.11(a) and (b) show the CuNi micro-coax signal lines leading into the copper boxes that house the bronze powder filters which are clamped beneath the mixing chamber stage. Each filter used 5.0 m of 50 μm Cu-clad NbTi wire. The wire was wound in four sections with alternating chirality around rods made from Stycast 2850 FT to minimize magnetic coupling between the filters. The rods were cast in drinking straws, which were slit lengthwise and peeled off after the epoxy was cured for ~ 24 hours. They were then cut to length (7.9 cm), and small holes were drilled into each end to fit brass connectors that mate to pins connected to the wiring. Finally, the rods were weighed to ensure the absence of air bubbles and embedded in an 80% bronze powder/20% epoxy composite. Two Cu boxes of four filters each were made (see Fig. 3.11(b)).

During development of these filters, a prototype developed short circuits at

voltages > 100 V. We found that the problem was between the bronze powder in the composite and the brass connectors. To fix this problem, we modified the design to include a < 1 mm thick insulating layer of Stycast 2850 epoxy that separated the bronze powder/epoxy mix from the connectors. This design had breakdown voltages up to 500 V, even after shocking them by dropping the Cu filters into liquid N₂. The measured attenuation of the filters scales approximately as \sqrt{f} with about 35 dB attenuation at 100 MHz [77].

3.10 Operation

Samples are mounted on copper, stainless steel, or molybdenum sample studs that can be changed *in situ*. A sample can be attached to the holder with silver epoxy or held in place by an L-shaped clamping arm. I used etched W and Nb wires as STM tips [98]. The tips cannot be changed *in situ*—the microscope has to be warmed to room temperature and the vacuum can vented in order to replace a tip.

After STM tips are installed, the vacuum can is evacuated to $\sim 10^{-7}$ Torr. I then fill the dewar with liquid N₂ and bleed ³He exchange gas into the inner vacuum can (IVC). Overnight cooling brings the STM to 77 K. The nitrogen is then siphoned out and slowly replaced with liquid helium. After cooling to 4.2 K in about a day, the exchange gas is then pumped out, the 1K pot filled, and standard operation of the dilution refrigerator begins.

After reaching a base temperature of 30-35 mK, we insert a sample of single crystal Au(111) or Au(100), and clean each tip using high voltage field emission.

This is done by turning off the z -feedback loop, retracting the tip a few nm away from the sample surface, and ramping the tip-to-sample voltage up to 80-100 V. The current is ramped up until the tip-to-sample current jumps to 0 A, indicating that a piece of the tip has fallen off. After cleaning, the I - V curve for each tip is examined to ensure we have a stable, sharp and metallic tip. The gold sample is then exchanged via the sample transfer system for other samples of interest. Sample exchange takes 12-15 hours, including about 3 hours spent pre-cooling the rod at the top plate and about 3 hours pre-cooling at the 1 K stage.

Once the STM is cold, and an interesting sample is put into the STM, I have taken data for 5-6 months without needing to warm up the system. Data taken with the STM is presented and discussed in detail in Chapter 4 and 7.

3.11 Conclusions

In this chapter, I described in detail the design and construction of the main components of our millikelvin STM system including the dual-tip STM, the dilution refrigerator, and details of the wiring. Building the system was a challenging endeavor that occupied myself, Mark Gubrud and Michael Dreyer for several years and constituted the majority of my work for this thesis.

Table 3.1: Wiring for dual-tip mK-STM

Temp. range	Wire type and Length [m]	Dimensions O.D. [mm]	Resistance [Ω /m]	Capacitance [pF/m]	10 GHz Atten. [dB/m]	No.
300 K – 10 K 10 K – MXC	CuNi coax [92] ~ 2 m	CuNi 0.08 PTFE 0.26 CuNi 0.40	wire 75 shield 5.2	96.2	61	12
300 K – 10 K 10 K – 1.4 K	Constantan loom [93] (twisted pairs) ~ 3.5 m	Constantan 0.10 polyester 0.12	66	~50	~100	48
1.4 K – MXC	CuNi-clad NbTi loom [93] (twisted pairs) ~ 1 m	NbTi 0.05 CuNi 0.08 polyester 0.10	52	~50	~100	48
MXC-STM	Cu coax [94] ~ 0.7 m	Cu 0.29 PTFE 0.94 Cu 1.19	wire 0.26	96.1	3.7	48

Chapter 4: Fabrication of Superconducting Nb Tips

4.1 Introduction

In this Chapter, I describe a reactive ion etching technique for fabricating ultra sharp superconducting Nb tips. I also examine the performance of these tips via atomic resolution images, temperature dependent spectroscopy and a conductance map. My results indicate that the tips are superconducting, mechanically stable and atomically sharp. Furthermore, the the tips display excellent spectroscopic energy resolution at mK temperatures. The tips are fabricated *ex situ* and could be used in a range of STM setups. The tip radius of curvature is often the limiting factor in field emission techniques [99, 100], atom manipulation techniques [52, 53] and STM based lithography [54, 55, 101–104]. My recipe offers a way to fabricate batches of multiple ultra-sharp probes that may be used for diverse applications.

4.2 Motivation

STM tips are typically fabricated out of normal metals such as Pt-Ir or W, for which wet etching techniques yield atomically sharp tips with minimal surface oxidation [105, 106]. Such tip materials also have an approximately constant density

of states (DOS) near the Fermi level. Thus the tunneling conductance dI/dV versus the bias voltage V between the tip and sample provides a direct measurement of the local DOS of the sample.

By using a superconducting STM tip rather than a normal metal tip, one can obtain enhanced spectroscopic resolution due to the singularity at the gap edge in the superconducting DOS [17, 23, 31, 107]. Enhanced resolution is important in observing many phenomena, including superconducting gap anisotropy and multi-band superconductivity. In contrast, a normal metal tip is subject to thermal or Fermi broadening (see Chapter 2). Furthermore, superconducting STM tips can directly probe the superconducting condensate on the atomic scale [19, 24, 29, 108]. Finally, the study of topological insulators using STM techniques has been of recent interest [109]. For example, it has been predicted that Majorana bound states may be supported by the state induced by the proximity effect between an s -wave superconductor and a topological insulator [110–112]. Scanning tunneling spectroscopy (STS) of the topological insulator surface state with a superconducting tip would enable us to explore arrangements of superconductor/topological insulator interfaces.

Despite their potential advantages, it has proven challenging in practice to reproducibly fabricate superconducting tips that are mechanically robust and sharp enough to obtain atomic resolution. Common superconducting elements such as Al and Pb oxidize quickly in air. Materials such as MgB_2 and high- T_c superconductors are brittle and difficult to work with due to surface degradation. Despite these difficulties, some progress has been made using a variety of techniques. One approach is to mechanically stretch a Nb wire in UHV until it breaks at a designated weak point

[24]. Another approach involves repeatedly indenting a tip into a sample made of a superconducting material until a relatively sharp tip is formed [23, 60, 113]. The main disadvantage of such methods however, is that they require UHV tip exchange capabilities or an *in-situ x-y* stage, approaches that are difficult to use in a scanning probe microscope that is mounted on a dilution refrigerator.

Superconducting tips based on the proximity effect have also been fabricated by depositing a layer of a Pb on a conventional Pt-Ir tip, and protecting it by a thin layer of Ag to prevent oxidation [28, 114]. This method renders a UHV environment unnecessary, but such tips have yet to yield atomic resolution topographic images. Small crystals of high- T_c superconductors have been successfully used as STM tips by attaching them to the end of a PtIr wire [5, 22, 29, 31]. This method has yielded stable superconducting tips with good spatial resolution. However, the anisotropic wave function of these superconductors renders spectroscopic information about the sample more complicated to deconvolve than an *s*-wave BCS density of states.

I chose to make our tips from Nb for several reasons. Nb is a conventional *s*-wave superconductor with a transition temperature $T_c = 9.3$ K. This allows us to operate up to a relatively high cryogenic temperature. Also Nb has much slower growing oxides than Al and this allows for *ex situ* fabrication. Furthermore, Nb is more mechanically robust than Pb, which one expects should allow for better imaging. Finally, techniques for patterning thin film and bulk Nb are well known from the fabrication of superconducting microelectronics circuits and rf cavities [115, 116].

4.3 Reactive ion etching tip fabrication technique

Since the ultimate goal of our project is the realization of a Josephson STM that can image the gauge-invariant phase difference between arbitrary points on superconducting surfaces [19], it was important to develop a reproducible technique for fabricating sharp and robust superconducting tips. In particular, since two such tips would ultimately have to be connected by a superconducting wire, it was important that the bulk of the tips be superconducting. This constraint meant that we could not use some of the most successful superconducting tip fabrication techniques developed in the last decade, including those that involve attaching a superconducting micro-crystal to the end of a metallic non-superconducting holder [23, 24, 60, 113].

I first attempted to etch Nb tips using conventional wet etching techniques [105, 117], that are commonly used in making W tips. For the wet etch, I used concentrated (30%) HCl as the electrolyte, and a Pb counter electrode. I immersed one end of a 0.25 mm Nb wire of 99.99% purity in the electrolyte, and covered the immersed portion almost entirely with a sleeve, exposing only a narrow (~ 1 mm) region to the electrolyte. I applied an ac voltage of 30 V for ~ 1 hour, and reduced it by 2 V every 30 minutes until the voltage was 2 V. The Cl^- ions etched the tip isotropically in the exposed region. As the exposed wire narrowed, it was stretched downwards by gravity pulling on the sleeve-protected wire beneath. Once I had reached 2 V, I switched to a dc voltage of 2 V and waited until the etched sections of the wire narrowed enough that the weight of the wire beneath it caused it to drop

off. The dc voltage at the end was important as it left behind a smooth and sharp tip. This tip fabrication technique is routinely used in making atomically sharp STM tips out of tungsten [105]. The main drawback of using this method with Nb, was that the long etching times (> 12 hours) in ambient conditions resulted in significant oxidation of the tips while etching. Tungsten tips by comparison can be etched in 20-30 minutes. Although the resulting Nb tips were sharp, the tip apex was typically brittle and insulating due to oxide growth during several hours of exposure to the etching solution.

I tried to reduce the etch time by increasing the voltage used, but I was unable to shorten it to much less than 10 hours, even with quite high voltages (~ 150 V). I should also note that wet etch recipes for fabricating STM tips typically involve lowering the ac voltage as the etch progresses and switching to a DC voltage for the final stage, in order to produce a well-defined and sharp tip [117]. So there is a trade-off between speeding up the process and producing a finer tip.

Another way to reduce the etch time would have been to use an electrolyte containing more electronegative ions, *i.e.* HF rather than HCl. However, I did not try using HF but instead I thought it might be possible to etch the tips using fluorine ions in the plasma generated by a reactive ion etcher (RIE), as long as I could produce an anisotropic etch that would sharpen the tips. Furthermore, using an RIE seemed likely to eliminate the problem of oxidation. In an RIE, the etch would take place in a vacuum with a controlled pressure of etching gas of $\sim 10^{-4}$ Torr, a vast improvement over ambient conditions. Furthermore, it had the potential to eliminate the need for constant oversight necessary during a wet etch to watch

for the drop off. It took me a few weeks to develop a recipe for etching Nb tips that were suitable for STM use.

Figure 4.1(a) shows a photograph of the Plasma-Therm 790 series RIE used to etch the tips, and Fig. 4.1(b) shows a schematic of a cross section through the RIE chamber. The RIE has a non-load-locked reaction chamber within which a plasma is sustained by applying a few hundred watts of rf power at 13.56 MHz. The power is applied to two parallel plates, with the upper plate grounded (see Fig. 4.1(b)). This plate is made from aluminum and has a dense array of fine channels to uniformly deliver SF₆ into the reaction chamber. The bottom plate has a custom-fitted solid graphite cover over the RF powered aluminum electrode underneath, and is electrically isolated from the chamber.

A blocking capacitor is connected in series between the bottom electrode and the RF source to allow control of the dc self-bias that builds up on the bottom electrode. The rf power ionizes the gas molecules to create a plasma. The plasma consists of cations, anions, and radicals that recombine to produce a characteristic glow from the plasma. Some of the electrons generated from ionization of the gas strike the chamber walls and are conducted to ground. The plasma is thus left with a small net positive charge. The bottom electrode or cathode, develops a large negative charge, or dc self-bias because the electrons that strike it are prevented from escaping to ground by the blocking capacitor. The upper electrode, or anode, is grounded. It should be noted that the plasma is positively charged with respect to both plates.

The typical base pressure of the reaction chamber is $\approx 50 \mu\text{Torr}$. The operating

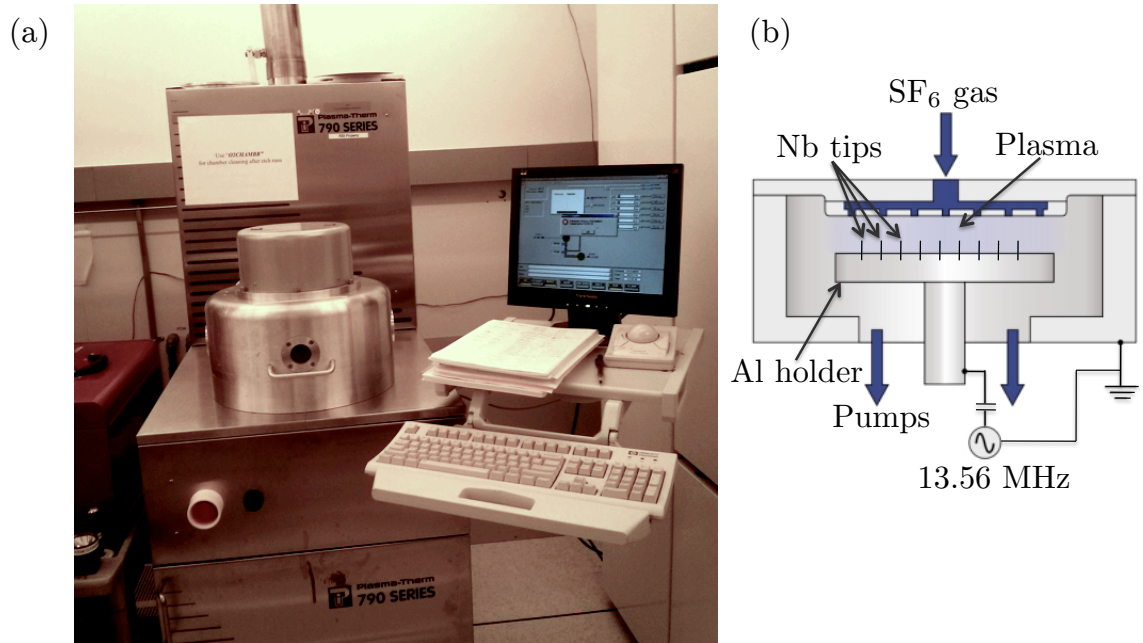


Figure 4.1: (a) Photograph of the RIE system used to etch the Nb tips, showing the main vacuum chamber, the pipe that carries the gases into it from above, and the computer that controls the process [118]. (b) Schematic of a cross section of the RIE chamber. The gas used to etch the substrate/tips enters the vacuum chamber through several fine channels at the top of the chamber. 13.56 MHz rf power is applied to the bottom electrode (cathode). A plasma is formed between the two electrodes and the substrate/tips to be etched are placed on an aluminum holder on the cathode.

pressure can be chosen in the 5-500 mTorr range, and the dc self-bias voltages can be chosen from approximately 10-600 V. The gas pressure controls the rate at which the gas is introduced into the chamber and there is an interdependence between the gas pressure and DC self-bias.

Samples to be etched are typically placed on the bottom electrode or cathode which attracts positive ions from the plasma. Ions drift towards the sample, and are accelerated across the 0.01-10 mm wide Child-Langmuir (steady-state) sheath that forms immediately around the substrate or anything immersed in the plasma [119, 120]. Nearly all of the potential is dropped across this sheath, which is formed to counteract further electron losses to the surface. The sheath width depends on the plasma parameters—*i.e.* pressure, power, and frequency of the oscillating electric field.

Most applications of the RIE involve samples that are wafers, which have an essentially two dimensional geometry. In this case, the ions accelerate vertically downwards across the sheath, and sputter the substrate at normal incidence, producing an anisotropic mechanical etch; the ions etch the sample by a combination of mechanical sputtering and chemical interactions with the substrate material. The ion energy ranges between a few to several hundred electron volts, and is inversely proportional to the plasma pressure, which in turn determines both the self-bias and the mean free path of the ions. At low pressures (0.05-90 mTorr), the mean free path is longer, the self-bias voltage higher, and mechanical sputtering dominates [121]. In this case, the energy with which the ions strike the substrate is maximized. When a combination of anisotropic mechanical sputtering and isotropic chemical etch is

desired, the 100-200 mTorr range is chosen along with a gas whose ions react chemically with the substrate. For primarily chemical etching, a pressure much higher than 100 mTorr is necessary [121]. Although there exists a vast repertoire of literature on matching gases with materials for chemical etching, the precise mechanism involved in a particular process can be difficult to pin down.

To etch my Nb tips, I placed 50 mm long pieces of bare 250 μm diameter Nb wire vertically in an SF_6 plasma generated by the reactive ion etcher [118]. Multiple tips were etched simultaneously, held in holes drilled in a 12 cm \times 12 cm \times 2 cm Al block (see Fig. 4.1(b)). Aluminum was chosen for the tip holder because SF_6 does not etch Al. The tips were glued rigidly into the Al holder with Fujifilm OiR 906 10 photoresist cured for 10-15 minutes at 150 $^\circ\text{C}$. I found that this prevented the formation of split, double or triple tips.

I spent several weeks tweaking the etch parameters and experimenting with recipes that included a brief O_2 plasma etching step. The recipe I converged on uses no O_2 , an SF_6 flow rate of 10 scm^3 , a pressure of 100 mTorr, and an applied rf power of 150 W. The resulting dc self bias potential is typically around 52 V.

4.4 Characterization

Figure 4.2(a) shows an SEM image of a Nb tip at the end of the etch. All of the wire has been etched away except for a 600-800 μm long tapered conical apex. The base of the tapered region is defined by the photoresist and Al holder. The aspect ratio of the cone was controlled primarily by the plasma gas pressure,

which determines the ratio of isotropic to anisotropic etch rates [121]. Pressures lower than 100 mTorr resulted in more anisotropic etching due to the longer mean free paths of the ions. The precise geometry of the tip apex varied somewhat from tip to tip, and for use in the STM, I chose tips that appeared to be sharp and mechanically sound.

Figures 4.2(b) and 4.2(c) show that the surface of the etched tip appears rough at the 10 μm scale and at the 1 μm scale. Typically the etch conditions result in a fairly isotropic etching process, except for geometry dependent variations in the local electric field and sheath properties. The sharp spiked microstructures seen in Fig. 4.2(b) and 4.2(c) are evidence for self sharpening on the Nb surface, which can occur when the Child-Langmuir (steady state) sheath width is much larger than the radius of curvature [122]. For our parameters, the expected sheath width that forms conformally around the wire is typically 0.1-1 mm, which is indeed much larger than the 10-100 nm tip radius. Since nearly all of the potential is dropped across this sheath, its structure around the cathode significantly affects the ion trajectories and impact angles, resulting in geometry dependent etch rates that vary locally. Analysis of complex cathode geometries suggest that the ion impact rate and angle in the vicinity of protrusions on the surface of the wire create a self sharpening effect [122–124].

A well known and prohibitive problem with fabricating STM tips out of superconducting elements such as Al and Pb, is that they oxidize rapidly in air, preventing tunneling. Our experience with Nb indicates oxidation of Nb tips leave hopping states in the oxide layer that are activated at room temperature, but inaccessible

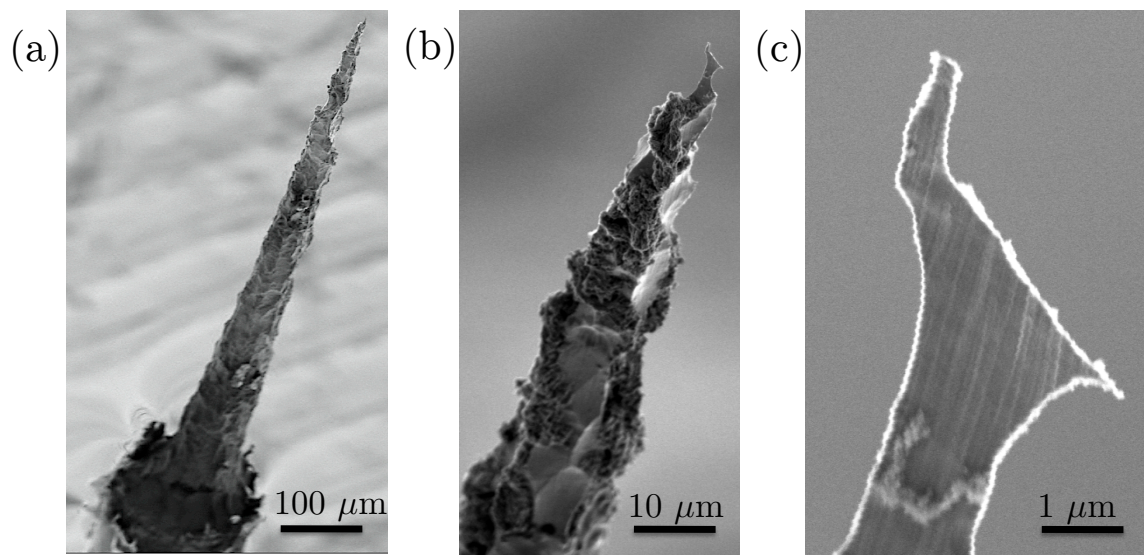


Figure 4.2: Scanning electron microscope images of a single Nb tip fabricated in a reactive ion etcher at length scales (a) 100 μm , (b) 10 μm and (c) 1 μm .

at cryogenic temperatures. If the Nb tip apex is oxidized it becomes essentially insulating and such a tip would crash into a conducting sample if it was used in an STM. To avoid this problem during the first coarse approach, we clean our tips via field emission against an Au single crystal, until the oxide layer is thin enough for electrons to tunnel through during the initial approach at low temperatures.

If a tip is exposed to air for too long, the oxide layer grows too thick to successfully approach the sample. Studies on Niobium oxides have primarily document their growth in air on Niobium thin films [125]. We cannot assume that these results will hold for our STM tips which possess an entirely different geometry. Hence I devised a simple experiment to determine how long the tip could be in air at room temperature before the oxide layer was too thick to allow an initial approach on Au.

For these tests I fabricated Nb tips in the clean room, transferred them immediately to our STM and approached an Au sample at room temperature in air. I - V curves were taken every 12 hours or so after the initial approach. The I - V curve typically started off showing a conducting tip, but the conductance decreased gradually over the next couple of days. I examined two tips in detail and in both instances the conductance of the tips became too small to measure by the 4th measurement, ~ 40 hrs after the tips were made. From this I concluded that we could safely transfer the tips from the RIE to our STM, test them at room temperature and then pump down to UHV within a few hours without risking the formation of a prohibitively thick oxide layer.

Since our STM has a sample exchange mechanism but no tip exchange mechanism (see Chapter 3), our tips needed to be in place when we cooled down and

ideally we wanted to use a tip for extended periods of time without having to warm the system up. Since I was able to make 15 (or more) tips simultaneously, there were always several sharp tips to choose from. In practice I was able to successfully take data with two Nb tips in the dual-tip system, continuously over several months at 4.2 K and at mK temperatures. Some of this work is described below and in Chapter 7.

4.5 Performance

Although the fine-scale geometry of our Nb tips is non-standard, the tips have yielded good topographic and spectroscopic STM data. In our STM setup we typically use field emission to clean the tip, which removes part of the tip. This is done by turning off the z -feedback loop, retracting the tip a few nm away from the sample surface, and ramping the tip-to-sample voltage up to 80-100 V. The current is ramped up until the tip-to-sample current jumps to 0 A, indicating that a piece of the tip has fallen off. The high corrugation on the etched Nb surface increases the chance of the remaining tip possessing a sharp tip apex, thus extending the usability of our tip. In practice we have used up to 25 or 30 field emissions on a single Nb tip, over a period of up to 6 months.

To test the resolution and stability of our tips, I used them in an STM to examine single crystals of Au(111), Au(100), Nb(100), and the topological insulator Bi_2Se_3 . Figure 4.3(a) shows an atomically resolved topographic image of a Bi_2Se_3 sample, indicating that the Nb tip used was both mechanically stable and atomically

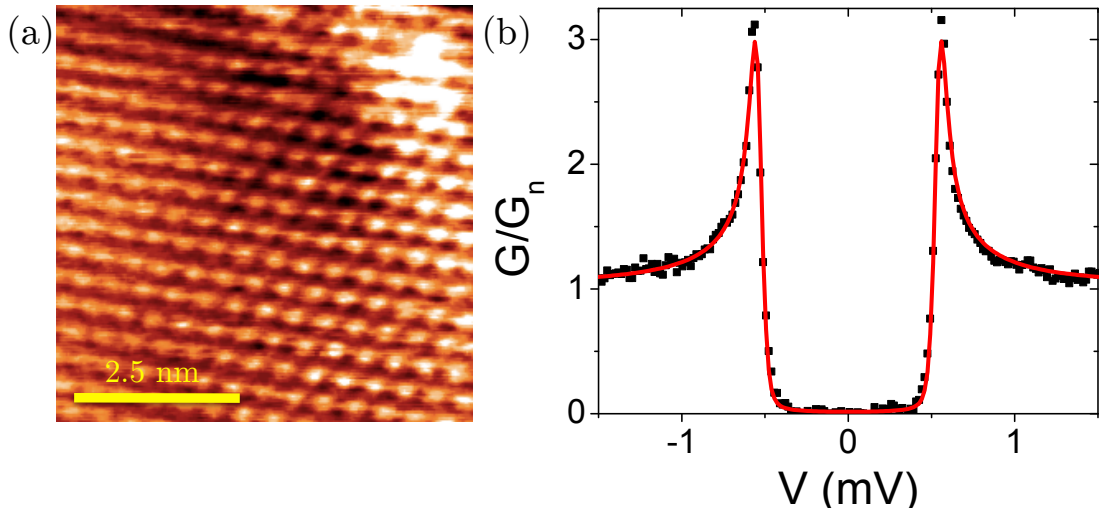


Figure 4.3: (a) Unfiltered atomic resolution image taken with a Nb tip on a Bi₂Se₃ sample at 35 mK. (b) Plot of normalized conductance G/G_n vs. tip-to-sample voltage V for the Nb tip and Bi₂Se₃ sample shown in (a). Black points are measured data and red curve is fit to Eq. (4.1) with energy gap $\Delta = 0.54$ meV, temperature $T_{\text{eff}} = 184$ mK, and $\Gamma \approx 10^{-5}$ meV.

sharp. Figure 4.3(b) shows a measurement of dI/dV on this sample. This data was taken using a millikelvin STM at 30 mK. The red curve in Fig. 4.3(b) shows a good fit to

$$\frac{dI}{dV} = G_n \int_{-\infty}^{\infty} g(E + eV) N_{s,\text{tip}}(E) dE \quad (4.1)$$

where G_n is the normal conductance, $f(E)$ is the Fermi function at energy E , $g(E) = -\partial f/\partial E$, and the normalized local density of states of the tip is $N_{s,\text{tip}}(E)$. For a superconducting tip with a BCS density of states, an energy gap Δ , and a finite quasiparticle relaxation rate Γ [126],

$$N_{s,\text{tip}}(E) = \text{Re} \left[\frac{|E - i\Gamma|}{\sqrt{(E - i\Gamma)^2 - \Delta^2}} \right]. \quad (4.2)$$

Our tips typically exhibit gap values that vary from 0.54-1.4 meV, comparable to the variation seen in other Nb STM tips [20]. We attribute this to finite size effects such as diffusion of O₂ into the atomically sharp tip apex.

Figure 4.4 shows topographic images of atomic reconstructions on surfaces of Au(111) and Au(100) single crystals scanned at 4.2 K and 1.5 K respectively. Figure 4.4(b) was scanned by the outer tip of the dual-tip STM attached to the dilution refrigerator [127]. The atomic reconstructions, step edges and presence of single atoms show that the tip used are atomically sharp and mechanically robust.

A series of dI/dV curves measured on this sample between 1.5 K and 9 K are shown in Fig. 4.5. The temperature was varied by applying power to the mixing chamber of the dilution refrigerator, while extracting the He³-He⁴ mixture from it. A RuO_x thermometer at the mixing chamber supplied with the dilution fridge was used to record the temperature. The evolution of the superconducting gap with

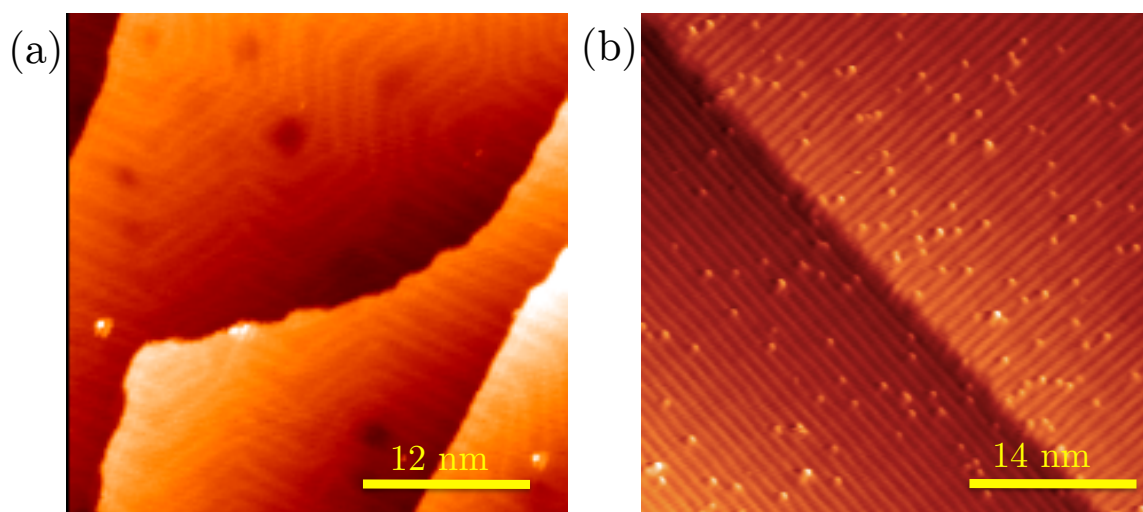


Figure 4.4: Topographic images of (a) Au(111) at 4.2 K taken with a Nb tip showing the Herringbone reconstruction [128, 129], and (b) Au(100) sample at 1.5 K showing a striped reconstruction [130].

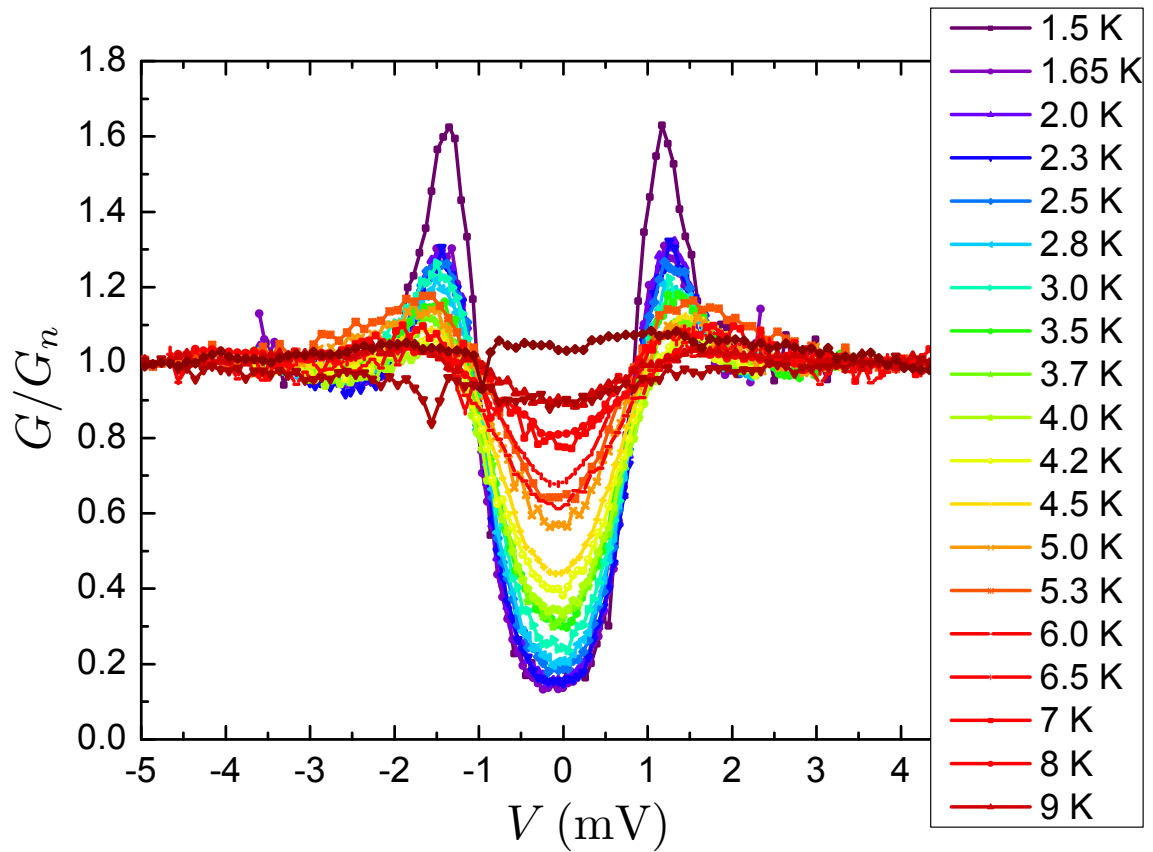


Figure 4.5: Plots of a series of normalized conductance G/G_n vs. bias voltage V , taken with a Nb tip on the Au(100) sample from Fig. 4.4(b). The legend indicates the temperatures at which each curve was obtained.

temperature is consistent with BCS theory.

Figure 4.6 shows a scanning tunneling spectroscopy map taken with a Nb tip on a Bi_2Se_3 sample at 4.2 K. In addition to topography (Fig. 4.5(a)), a spectroscopy (dI/dV vs. V) curve was taken at each point of the image, with the bias voltage being swept from -8.5 to 6.5 mV. Figure 4.5(b) shows a sample frame for $V = -8.5$ mV, and Figs. 4.6-4.13 show several more constant voltage conductance frames. This data clearly shows the tip is sensitive to spatial variations in the conductance. The singularity at the gap edge of the tip enables the Nb tip to resolve very small spectroscopic features at extremely small bias voltages. This conductance map was taken over a 12 hour period, and at resistances as low as $5 \text{ M}\Omega$, indicating that the tips are robust. I stress here the importance of tip stability (while remaining atomically sharp) at close proximity to the sample surface because at cryogenic temperatures it is the primary limiting factor in an STM's ability to obtain spatially resolved conductance information with high energy resolution.

Finally, Fig. 4.14 shows a series of dI/dV curves taken on a bulk Nb(100) sample at 30 mK at different tunneling resistances. The Nb tip and sample form an ultra-small Josephson junction. For this plot the bias voltage was swept between -1 mV and 1 mV, well below the superconducting gap for a Nb-Nb junction. As expected, there is a small phase diffusive "supercurrent" at finite voltages [114]. Examination of the plot also reveals prominent sub-gap features in the zero bias conductance peak of the phase diffusive "supercurrent." These features are fairly reproducible at different tunnel resistances, as well as with different tips at different

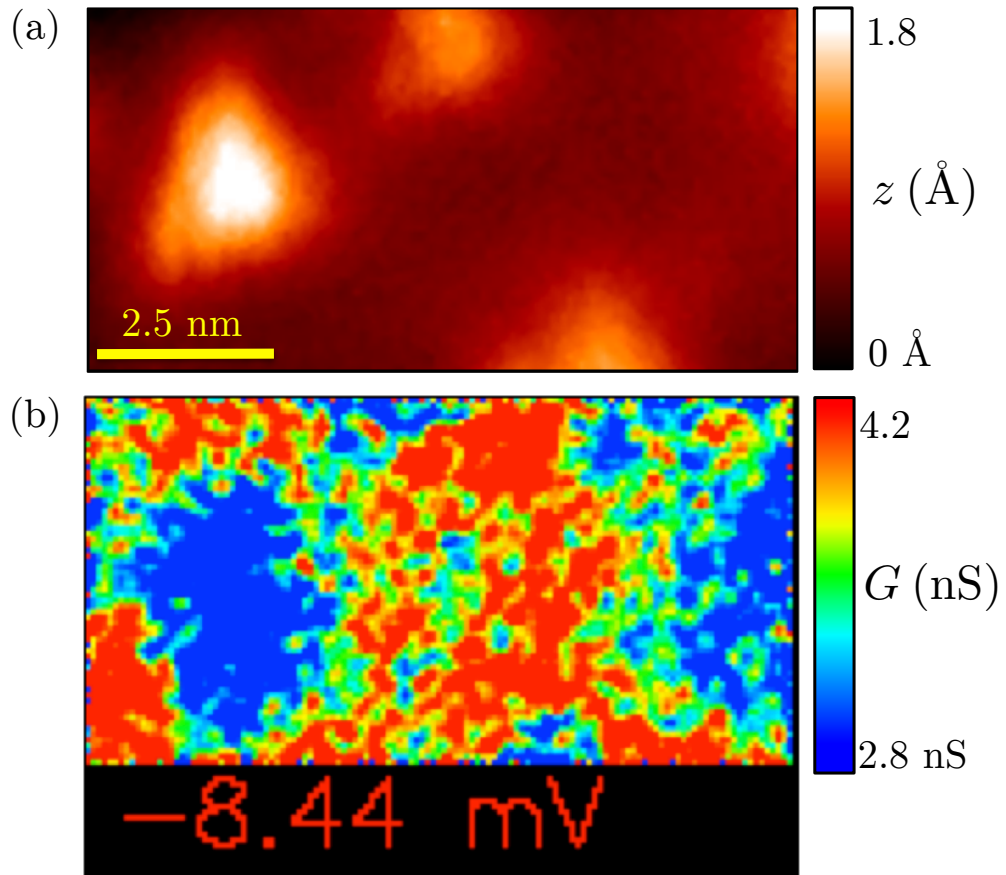


Figure 4.6: Topographic and spectroscopic images taken with a Nb tip on a Bi_2Se_3 sample at 4.2 K. (a) Topography in the vicinity of triangular Bi_2Se_3 defects caused by the replacement of single Se atoms with Bi. (b) A single slice (at $V = 8.5$ mV) of a conductance map of the region shown in (a).

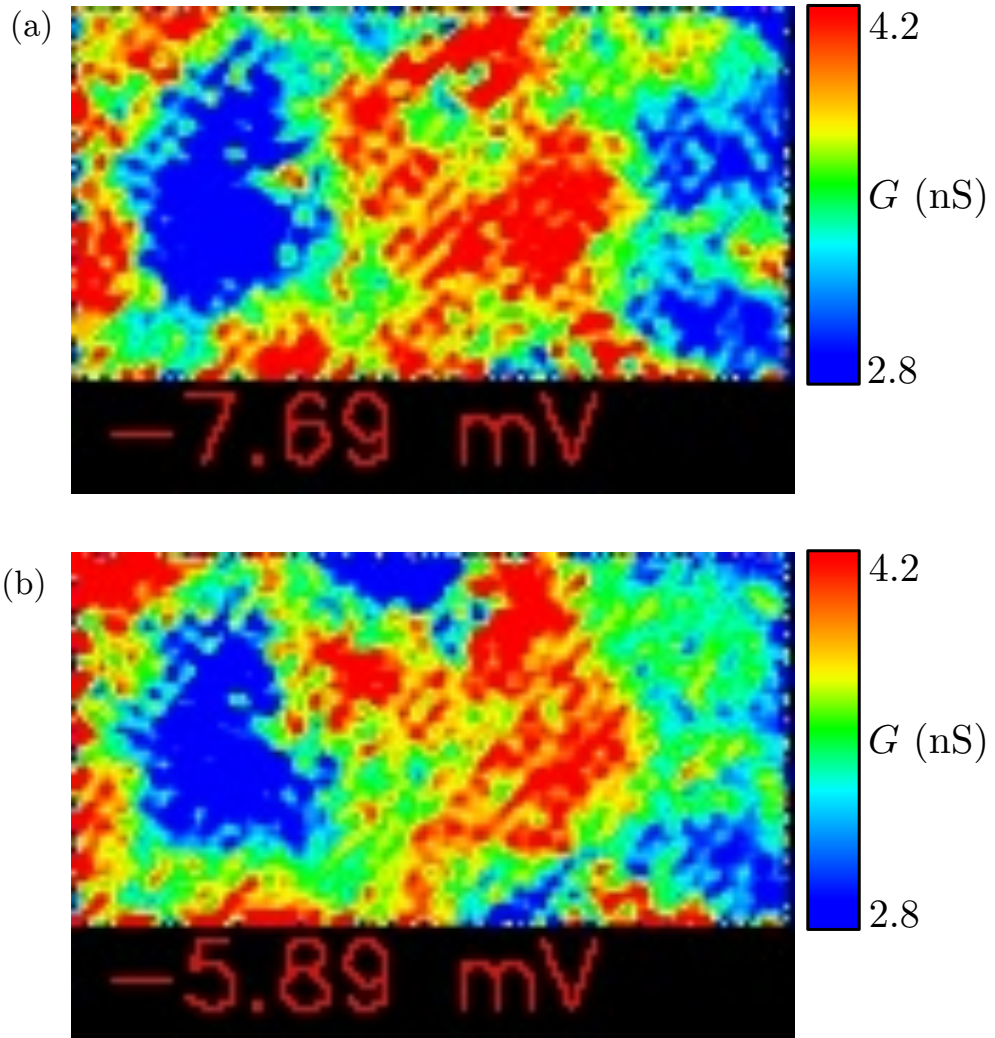


Figure 4.7: Slices of a conductance map at (a) $V = -7.69$ mV and (b) $V = -5.89$ mV of the region shown in Fig. 4.6(a)

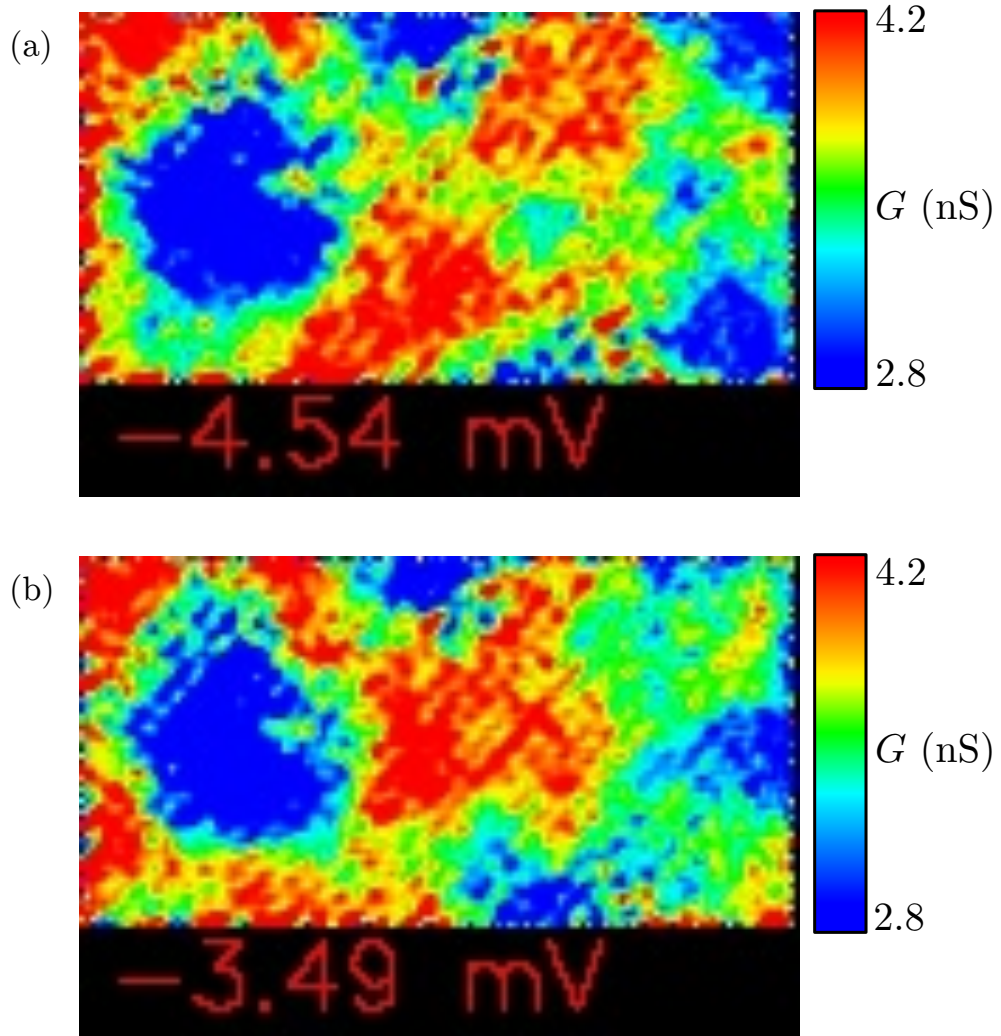


Figure 4.8: Slices of a conductance map at (a) $V = -4.54$ mV and (b) $V = -3.49$ mV of the region shown in Fig. 4.6(a).

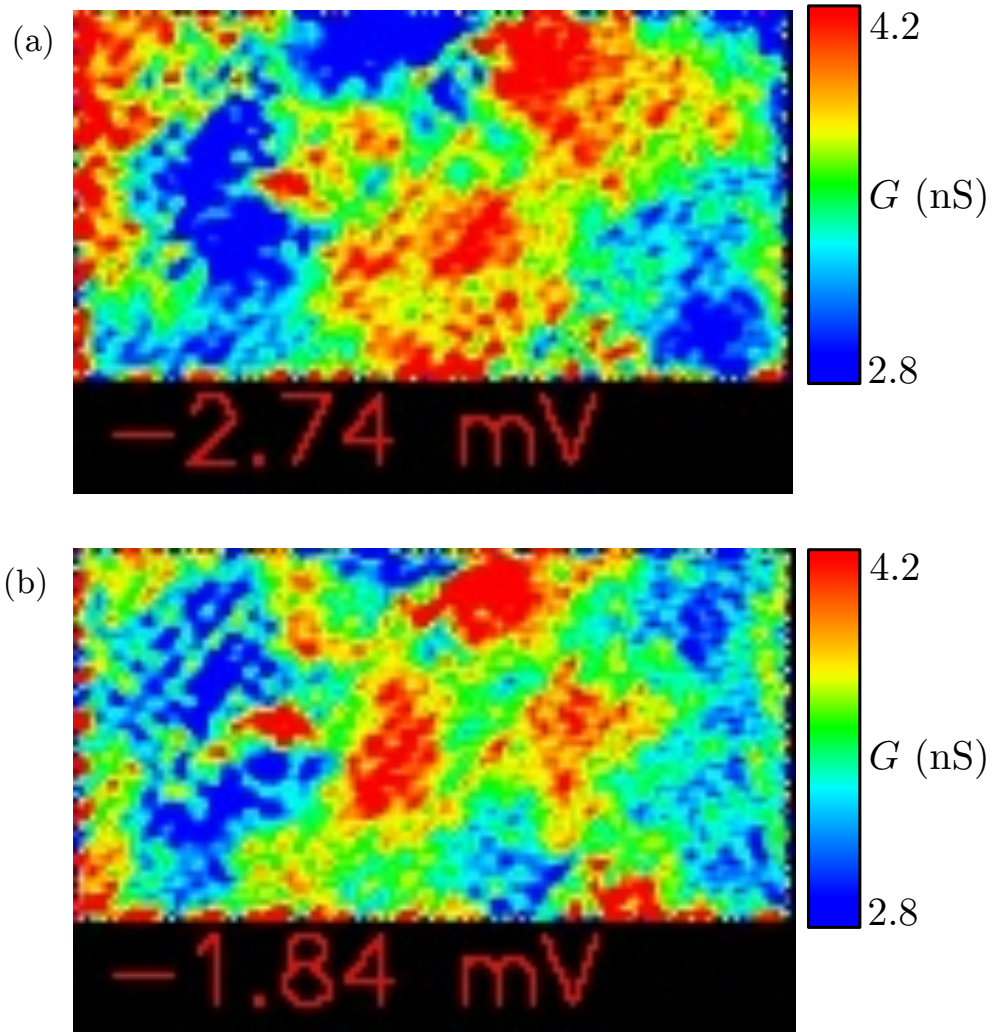


Figure 4.9: Slices of a conductance map at (a) $V = -2.74 \text{ mV}$ and (b) $V = -1.84 \text{ mV}$ of the region shown in Fig. 4.6(a).

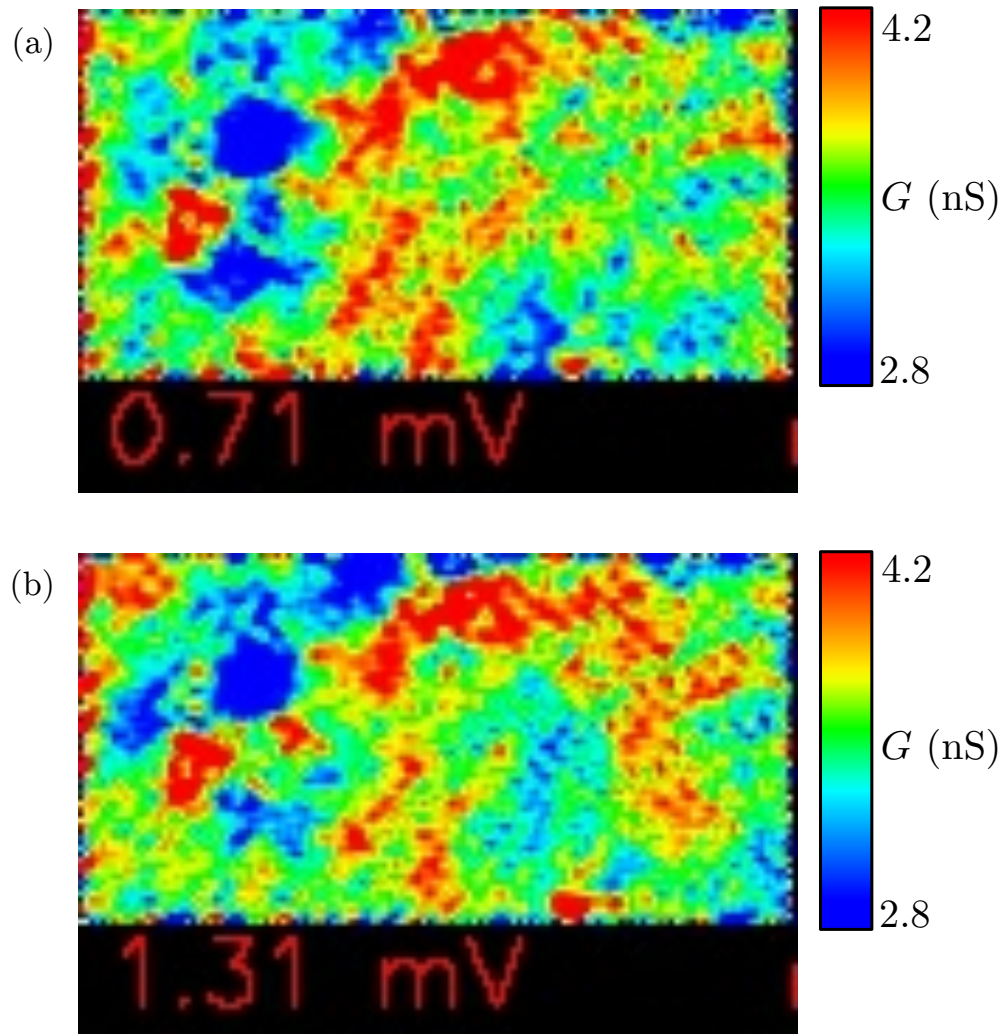


Figure 4.10: Slices of a conductance map at (a) $V = 0.71$ mV and (b) $V = 1.31$ mV of the region shown in Fig. 4.6(a).

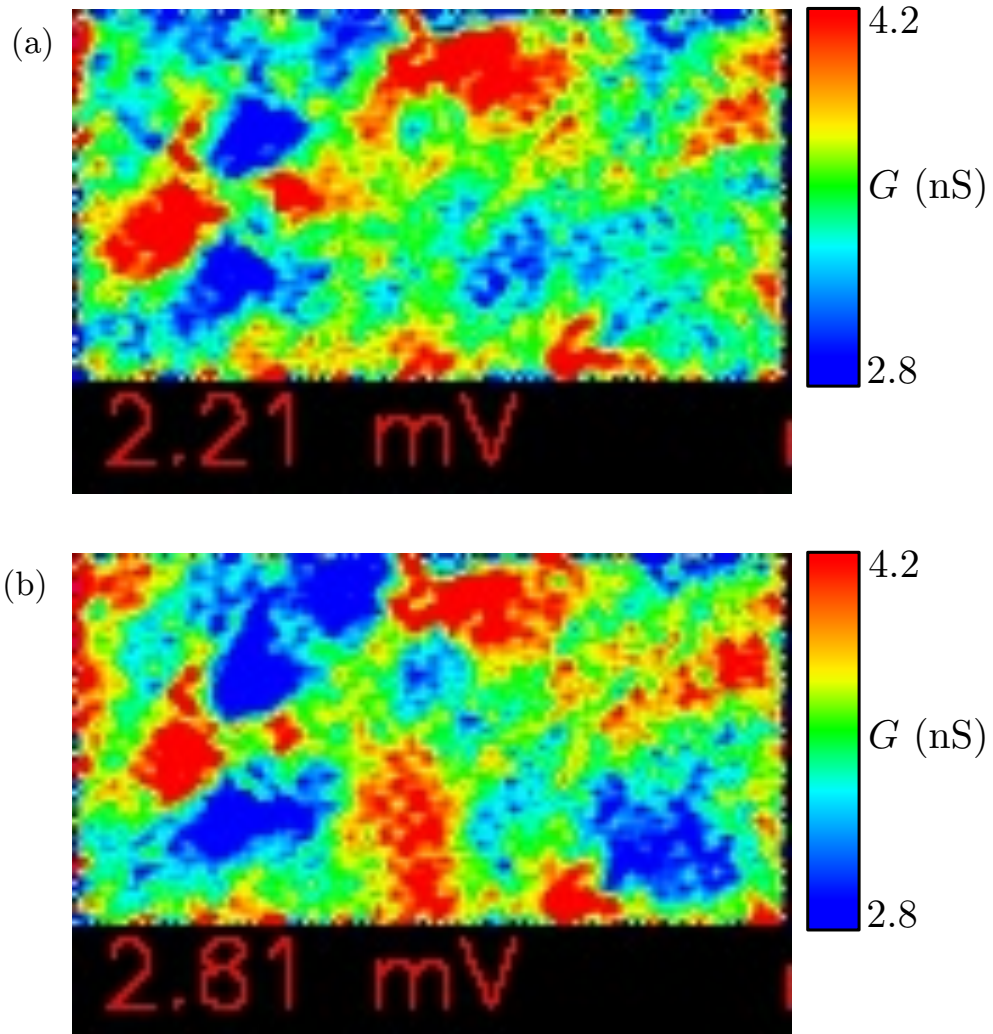


Figure 4.11: Slices of a conductance map at (a) $V = 2.21 \text{ mV}$ and (b) $V = 2.81 \text{ mV}$ of the region shown in Fig. 4.6(a).

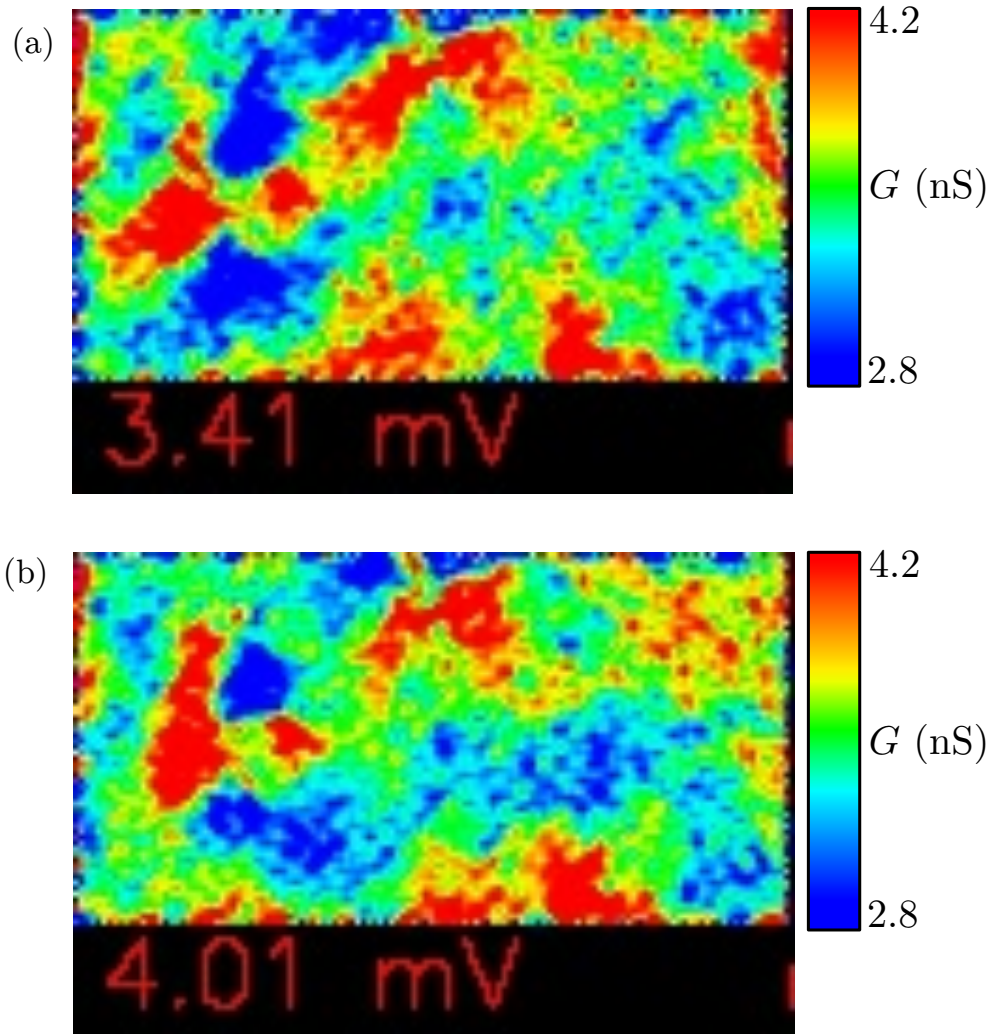


Figure 4.12: Slices of a conductance map at (a) $V = 3.41 \text{ mV}$ and (b) $V = 4.01 \text{ mV}$ of the region shown in Fig. 4.6(a).

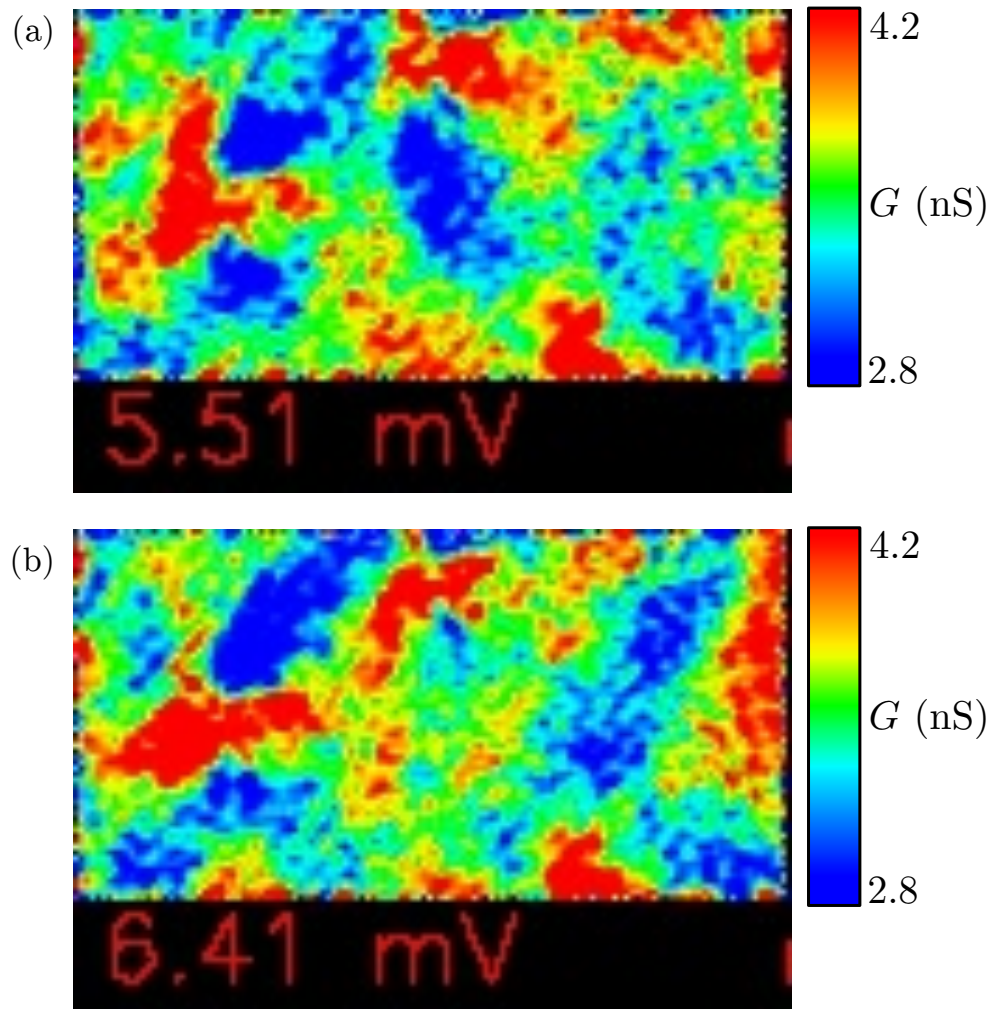


Figure 4.13: Slices of a conductance map at (a) $V = 5.51$ mV and (b) $V = 6.41$ mV of the region shown in Fig. 4.6(a).

locations on the sample. This behavior is consistent with $P(E)$ theory [131, 132] which predicts peaks at voltages where the pairs can radiate energy to electromagnetic modes of the environment. Both the theory and the data are described in more detail in Chapter 6. Here, the data is shown to attest to the mechanical stability of the tip, and to show that spectroscopic resolution of about $8 \mu\text{V}$ may be attained at ultra low temperatures.

Another interesting question I examined with the Nb tips that I fabricated was the effective temperature of the junction in our millikelvin STM. The temperature of the STM junction is a measure of the success of our noise filtering and heat sinking efforts, and is one factor in determining the spectroscopic energy resolution attainable by our instrument. In Chapter 5 I discuss this aspect of the tips and also how I characterized the STM performance in terms of stability and current noise. Finally, I note that the superconducting tips are of interest primarily because they offer the potential to directly probe a superconducting condensate via the tunneling of Cooper pairs in an S-I-S STM junction. Chapters 6 and 7 describe my effort at understanding the physics of ultra-small Josephson junctions, such as that formed by a superconducting STM tip and sample. There I show that the charge carriers at and near zero bias in such a junction are in fact Cooper pairs.

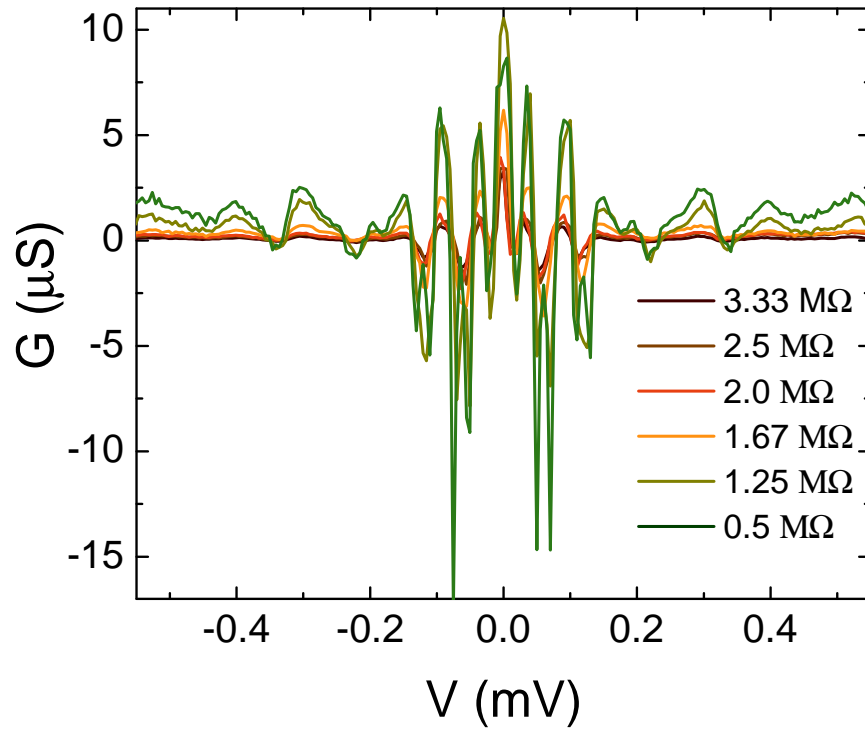


Figure 4.14: Conductance $G = dI/dV$ versus bias voltage V data taken on a Nb(100) single crystal with a Nb tip at 30 mK for different tunnel resistances. At the start of each curve, the bias voltage was set to 1 mV and the current was set to fix the tunnel resistance of the junction (see legend). The z -feedback loop was then turned off during the measurement. The successive traces show the evolution of the zero bias conductance peak and sub-gap excitations with tunnel resistance.

Chapter 5: Characterization and Performance of Dual Tip STM

5.1 Introduction

Having invested several years in designing, building and assembling the dual-tip mK STM system, it was important to carefully characterize its performance in terms of reliability, the effective temperature attained by the STM junction, the mechanical stability, and the system's resilience to noise.

The first major challenge I faced while testing the mK system involved operating the coarse approach mechanism, which was idiosyncratic and unreliable at sub-Kelvin temperatures due to a combination of factors. First, I found that the shear range of the piezos was reduced at cryogenic temperatures by a factor of 3 to 6 from the room temperature values. Although this could be addressed by using higher voltages on the piezo walkers, stressing the walker mechanism in this way increased the probability of arcing between the high voltage and ground connections on the piezos. A possible contributing factor to arcing was our use of an exchange gas (^3He) that resulted in a thin layer settling on all the surfaces in the STM, including the piezo walkers. Although the exchange gas was pumped out, a thin residual layer could have been left. The combination of high voltages (± 220 V) several times a second over 12 hour periods, and electrode to ground distances

< 0.5 mm, produced conditions that proved to be all too conducive to arcing and shorting out of these connections.

Another early problem I encountered involved the fact that our STM was designed with the large walker carrying the entire weight of the smaller walker assembly against gravity during coarse approach (see Chapter 3). Attaching the STM to the mixing chamber upright allowed for sample exchange while cold, and prevented the tip from crashing into the sample due to gravity. However, it meant that the large walker needed to be more powerful in order to carry the extra weight. Furthermore, although we chose materials with closely matched thermal expansion coefficients, it was difficult to accurately predict whether the friction between the aluminum pads (on the piezos) and the sapphire prism would increase or decrease when cold. Not only did this depend on whether the piezos tightened against the prism when cold, but also on other less predictable factors such as the extent of condensation of gas on the prism surface during cool-down providing either lubrication (when liquid) or increased friction (when solid). Finally, the tension of the wires attached to the tips also probably played a role in slowing down the walker at certain points during the approach. I tried to reduce the effect of the wires by using extremely springy and thin copper wires for the STM tip connections at the STM.

After several attempts at repairing the connections lost due to arcing on both large and small walkers, I decided to redesign both walkers to increase redundancy and ease repair. These modifications are discussed in detail in Chapter 3. Additional steps included testing the full range of the walker motors at 35-40% of its maximum power at room temperature 2-3 times before cool down, and ensuring that there is

no dust on the sapphire prism prior to cool down. Since we still used ^3He as an exchange gas, an additional precaution I took during operation was to ensure that the STM was the warmest part of the system during cool down so that any residual gas would tend to condense and adhere to the walls of the IVC rather than on the piezo stacks in the STM.

Ultimately, my effort at building a reliable coarse approach mechanisms for both STM tips was successful, as demonstrated by data we were able to obtain over the past ~ 1.5 years and 6-7 thermal cycles between room temperature and 30 mK. During this time (January 2013 to May 2014) we approached the sample with each of the tips over 30 times, without observing arcing between piezo stack connections.

Once the coarse approach mechanism could reliably move the STM tip within tunneling distance of the sample, the next major challenge involved achieving a temperature at the STM junction that was as close to that of the mixing chamber as possible, without sacrificing mechanical stability. Unlike pre-fabricated tunnel junctions, the STM junction has a variable tip-sample distance (and resistance) controlled by a voltage driven feedback loop. This makes the tip particularly vulnerable to mechanical and electrical noise.

The measures that we took to achieve both stability and a low effective temperature are described in detail in Chapter 3. In Section 5.2, I first present topographic images that demonstrate the success of our UHV sample preparation techniques. Next in Section 5.3, I describe our method for estimating the effective temperature of the sample, and present a simple model that incorporates the effect of voltage noise fluctuations. Data in the form of spectroscopy curves, and fits to theory are

also shown. In Section 5.4, I discuss the stability of each of our tips by analyzing unfiltered atomic resolution topographic images, line profiles, and current noise spectra. Since the simultaneous performance of the two tips is important for the ultimate goal of building a phase STM with coupled tips, I analyze the coupling between the two tips in Section 5.5. Finally in Section 5.6, I demonstrate the magnetic field capability of the system with a series of spectroscopy curves taken by a single-tip STM mounted on our refrigerator. The data shows the dependence of the superconducting gap of a $\text{Cu}_x\text{Bi}_2\text{Se}_3$ sample on magnetic field strength.

5.2 Topographic images taken with the STM

An STM can be thought of as a nano-scale tunnel junction that can be placed at specific locations on a sample with atomic precision to obtain position dependent tunneling characteristics on a sample. Atomic scale spatial resolution is the main capability that distinguishes the STM as an imaging tool for probing and characterizing materials. In order to take advantage of this in a millikelvin STM, it is crucial that the sample being studied have a surface that is free of impurities such as H_2O and N_2 molecules, oxides, or organic contaminants. For this reason it is preferable that samples can be prepared in UHV conditions and transferred into the cold STM once the exchange gas (^3He) has been pumped out of the inner vacuum can (IVC).

To test the sample preparation, we sputter-annealed a Au(100) single crystal [133] sample in the UHV chamber and transferred it into the STM at 1.5 K. Preparation of the crystal involved multiple sputter/heat cycles over 2-3 days with 1-2

keV Ar ions and 400-600° C heating. This was done to remove multiple 20-50 nm polishing grains that were embedded on the surface. Right before transferring the sample into the STM, we sputtered it for around 30 minutes with 750 eV Ar ions, followed by heating at 400-500° C for ~ 15 minutes.

Figure 5.1 shows topography and current images of the Au(100) single crystal, taken with our STM when cold. The raised dot like structures are individual atomic impurities on the surface. The striped atomic reconstruction [130] can be seen in the top right hand corner of the image, while the rest of the image is covered by atomic steps. The clarity of the atomic scale features in this topographic image, and in many others, indicate that we can successfully prepare samples by sputter-annealing in UHV conditions, and transfer them *in situ* into the STM.

5.3 Effective temperature of our mK STM

An important metric in characterizing our instrument was the effective temperature of the STM junction. As described in Chapter 2, the singularity in the gap edge in the BCS density of states of a superconductor can be used to probe the width of the Fermi function in a normal metal electrode of an S-I-N tunnel junction, and this width is directly related to the temperature of the electrons.

The quasiparticle tunnel current between an STM tip and sample [46] is given by

$$I(V) = \frac{4\pi e|M|^2}{\hbar} \int_{-\infty}^{\infty} [f_{\text{tip}}(E) - f_{\text{sample}}(E + eV)] \rho_{\text{tip}}(E) \rho_{\text{sample}}(E + eV) dE, \quad (5.1)$$

where $|M|$ is the average value of the tunneling matrix element, assumed to be

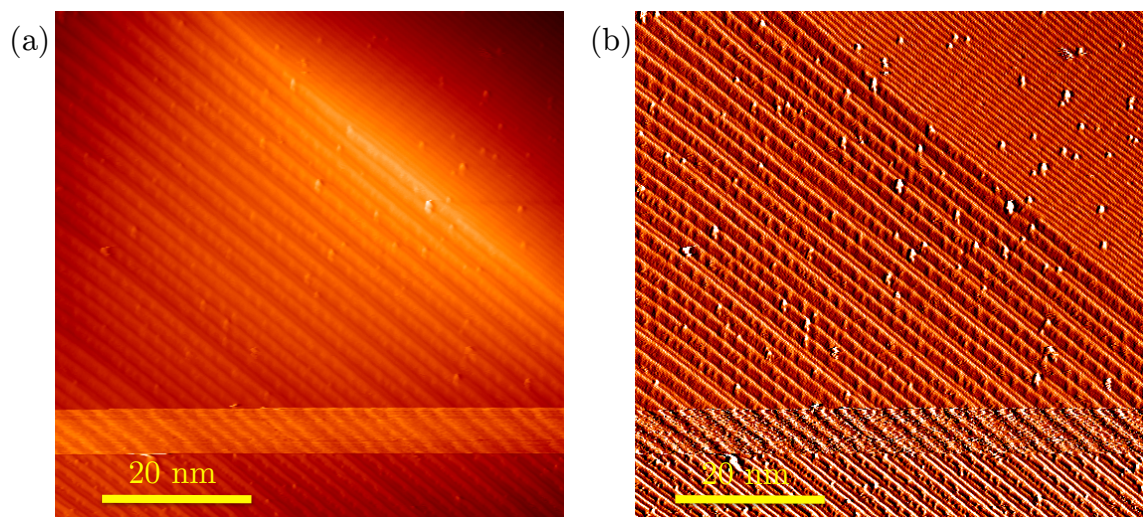


Figure 5.1: (a) Topography and (b) current images taken simultaneously with a Nb tip and an Au(100) sample at 30 mK. The scattered white dots are single atomic impurities adhering to the surface of the sample. The striped surface reconstruction can be seen in the top right hand corner of both images. The rest of the image shows atomic steps on the sample's surface.

independent of energy, f_{tip} and f_{sample} are the electron energy distribution functions in the electrodes which reduce to the Fermi distribution in thermal equilibrium, and ρ_{tip} and ρ_{sample} are the local electronic density of states (LDOS) of the tip and sample at the point of contact.

For a normal metal sample, we assume that the density of states of the sample is constant, and can write

$$I = \frac{G_n}{e\rho_{\text{tip,n}}(0)} \int_{-\infty}^{\infty} [f(E) - f(E + eV)] \rho_{\text{tip}}(E) dE, \quad (5.2)$$

where $\rho_{\text{tip,n}}(0)$ is the density of states of the tip at the Fermi energy when the tip is in the normal state, and $G_n = 4\pi e^2 |M|^2 \rho_{\text{sample}}(0) \rho_{\text{tip,n}}(0) / \hbar$ is the tunnel conductance in the normal state. Taking a derivative with respect to V , we obtain the conductance

$$G = \frac{dI}{dV} = \frac{-G_n}{e} \int_{-\infty}^{\infty} \frac{\partial}{\partial V} f(E + eV) \frac{\rho_{\text{tip}}(E)}{\rho_{\text{tip,n}}(0)} dE. \quad (5.3)$$

It is convenient to define $g(E) = -f'(E) = -df/dE$, in which case g will be positive everywhere and may be considered a probability distribution. For a superconducting tip this yields

$$\frac{dI}{dV} = G_n \int_{-\infty}^{\infty} g(E + eV) N_s(E) dE, \quad (5.4)$$

where the normalized density of states of the tip $N_s(E) = \rho_{\text{tip}}(E) / \rho_{\text{tip,n}}(0)$ is given by [49]

$$N_s(E) = \text{Re} \left[\frac{|E|}{\sqrt{E^2 - \Delta^2}} \right]. \quad (5.5)$$

Dynes incorporated finite quasiparticle lifetime effects into the density of states

by including broadening of the singularity at the gap edge [126]. Adding an imaginary term $i\Gamma$ to the energy, Eq. (5.5) becomes

$$N_s(E) = \text{Re} \left[\frac{|E - i\Gamma|}{\sqrt{(E - i\Gamma)^2 - \Delta^2}} \right] \quad (5.6)$$

Physically, the recombination rate Γ/\hbar is the rate at which a quasiparticle near the energy gap edge scatters inelastically or recombines into the superfluid condensate.

To obtain the effective temperature and energy resolution of our instrument, I measured the conductance (dI/dV) between a superconducting tip and a normal sample. The effective temperature was extracted by fitting the data to Eq. (5.4). The blue points in Fig. 5.2 show dI/dV measurements using a Nb inner tip and a Bi_2Se_3 sample at a nominal mixing chamber temperature of 35 mK. The measurements were taken by modulating the junction voltage with a small ($4 \mu\text{V}$) sinusoidal ac voltage at 1.9 kHz, and detecting the corresponding current response signal with a lock-in technique. Examining the plot, we see that the gap is $\Delta \approx 0.7 \text{ meV}$, which is about half that of bulk Nb, possibly due to this particular tip not being completely cleaned during field emission.

Figure 5.3(a) shows similar dI/dV curves measured as a function of the temperature of the mixing chamber from 35 mK to 500 mK, and Fig. 5.3(b) shows a closeup of the right conduction peak. We note that although the difference between the 35 mK curve and the 50 mK curve is negligible, there is a noticeable difference between the 50 mK curve and the 100 mK curve, as well as between subsequent curves. This suggests that our sample was able to cool to temperatures on the order of 100 mK.

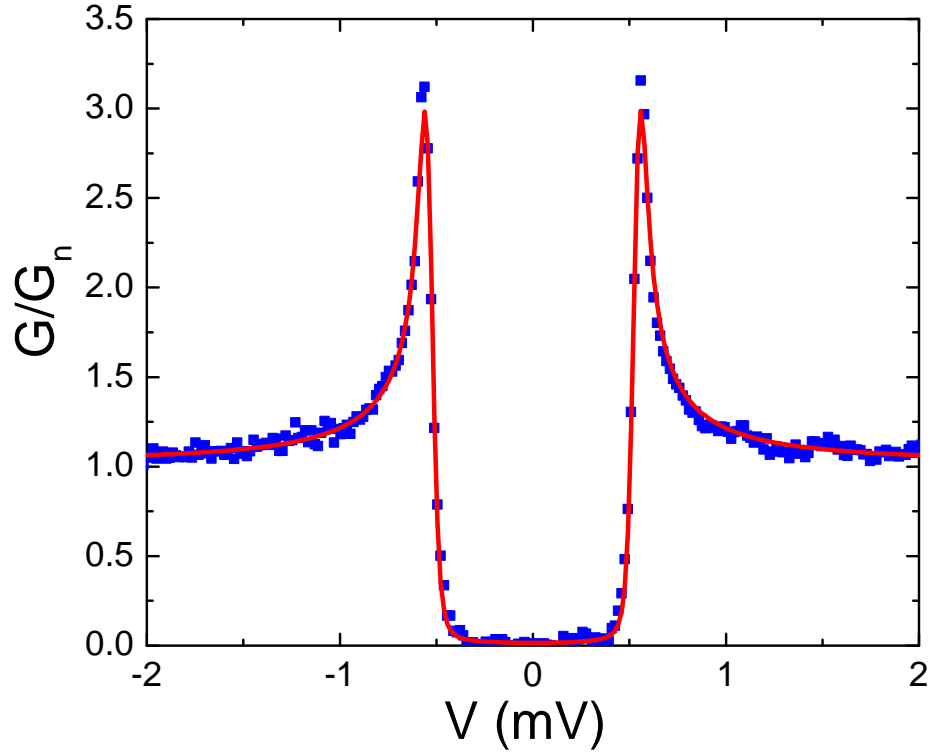


Figure 5.2: Plot of normalized conductance G/G_n versus tip-to-sample voltage V for a Nb tip and a Bi_2Se_3 sample at $T_{\text{mix}} = 35$ mK. Blue points are measured data and red curve is fit to Eq. (5.1) with energy gap $\Delta = 0.54$ meV, temperature $T_{\text{eff}} = 184$ mK, and $\Gamma \approx 10^{-5}$ meV.

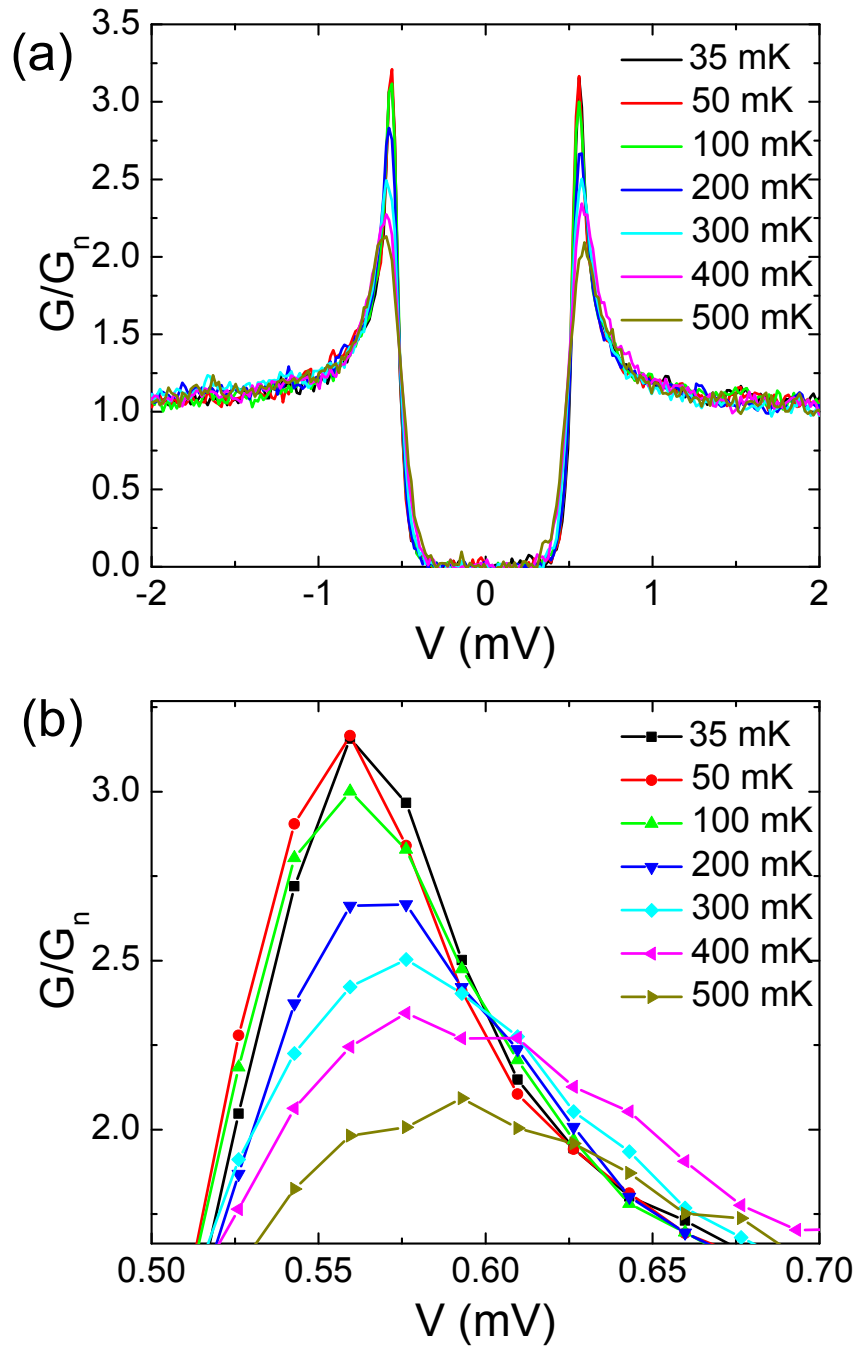


Figure 5.3: (a) Normalized conductance G/G_n versus tip voltage V measured from 35 mK to 500 mK using a Nb tip on a Bi_2Se_3 sample. (b) Detailed view of right conductance peaks near 0.6 mV reveals significant temperature dependence to the peak for temperatures above 50 mK.

In order to obtain an estimate for the effective temperature of our instrument, we fit each curve in Fig. 5.3(a) to Eq. (5.4). Since we used a superconducting tip made of Nb, we used

$$N_{s,\text{tip}}(E) = \text{Re} \left[\frac{|E - i\Gamma|}{\sqrt{(E - i\Gamma)^2 - \Delta^2}} \right], \quad (5.7)$$

where we assumed a BCS density of states for the tip and a finite quasiparticle relaxation time Γ [126]. Fitting our data using a weighted least-squares minimization via the Levenberg-Marquardt [134, 135] algorithm, we extract Δ , Γ , and the effective temperature T_{eff} , which enters through the Fermi function. The fit indicates that the effective temperature of our STM is $T_0 \approx 184$ mK, rather than 35 mK.

5.3.1 Voltage noise and effective temperature

In order to pin down the factors limiting our energy resolution, in this Section I describe a simple model below that incorporates the effect of voltage noise fluctuations.

Nyquist-Johnson voltage noise fluctuations can be characterized by a probability distribution function $P(V)$ that we assume to be a Gaussian with zero mean and standard deviation V_n . The experimentally observed conductance can then be written as

$$\begin{aligned} \left\langle \frac{dI}{dV}(V) \right\rangle &= \int P(V') \frac{dI}{dV}(V + V') dV' \\ &= G_n \int N_s(E) \int P(V') g(E + e(V + V')) dV' dE \\ &= G_n \int N_s(E) (P \star g)(E + eV) dE. \end{aligned} \quad (5.8)$$

where we have used Eq. (5.4) and used \star to represent the convolution of P and g .

Setting $F = P \star g$, we have

$$\left\langle \frac{dI}{dV} \right\rangle \propto \int N_{s,\text{tip}}(E)F(E)dE. \quad (5.9)$$

We note that $F(E)$ is a sharply peaked function of E with standard deviation σ_F that determines the sharpness of features such as the increase in conductance at the gap.

Because F is a convolution of P and g , which may both be considered as approximately Gaussian probability distributions with mean zero, their variances σ_P and σ_g add and we can write

$$\sigma_F^2 = e^2\sigma_P^2 + \sigma_g^2. \quad (5.10)$$

where the factor of e is necessary because σ_g has dimensions of energy and $\sigma_P = V_n$ has dimensions of voltage. For a Fermi distribution it can be shown that $\sigma_g^2 = \int_{-\infty}^{\infty} E^2 g(E)dE = k_B^2 T^2 \pi^2 / 3$. Since N_s is also a sharply peaked function, the total width of the measured coherence peak, $|\sigma_{dI/dV}|$, should scale as

$$\sigma_{dI/dV} \propto \sigma_g^2 + e^2\sigma_P^2 + \sigma_{N_s}^2 \quad (5.11)$$

where the standard deviation of the voltage noise is given by $\sigma_P = V_n$ and $\sigma_{N_s} = \Gamma$ is a measure of the width of ρ . This yields

$$\sigma_{dI/dV} \propto \left(\frac{k_B^2 T^2 \pi^2}{3} + e^2 V_n^2 + \Gamma^2 \right)^{1/2} \quad (5.12)$$

From Eq. (5.12), we see that the effect of voltage noise is indistinguishable from that of excess temperature when it comes to the broadening of I - V characteristics.

Assuming $\Gamma^2 \ll e^2 V_n^2$, and setting $k_B^2 T_{\text{eff}}^2 \pi^2 / 3 = k_B^2 T^2 \pi^2 / 3 + e^2 V_n^2$, we can define the effective temperature of the instrument as [136]

$$T_{\text{eff}} = \sqrt{T^2 + \frac{3e^2 V_n^2}{k_B^2 \pi^2}}. \quad (5.13)$$

The blue points in Fig. 5.4 show a plot of the effective temperature T_{eff} versus the temperature T_{mix} of the mixing chamber. The red solid curve in Fig. 5.4 shows that our data is well explained by a simple model of voltage noise [136]

$$T_{\text{eff}} = \sqrt{T_{\text{mix}}^2 + T_0^2}, \quad (5.14)$$

where the fitting parameter $T_0 = \sqrt{3e^2 V_n^2 / k_B^2 \pi^2}$ is the minimum effective sample temperature due to rms voltage noise V_n . From the fit, we find $T_0 = 184 \pm 6$ mK. This is equivalent to an energy resolution of $k_B T_0 / e \approx 16$ μeV . The good agreement between our data and Eq. (5.4) suggests that the sample is physically cooling to $T \sim T_{\text{mix}}$, but the energy resolution of our instrument is limited by voltage noise. This also suggests that additional cryogenic filtering on the scanner and walker wires might reduce the effective temperature.

Finally, additional evidence that voltage noise on the leads contributes to the effective temperature of our junction can be seen in Fig. 5.5, which shows a series of dI/dV curve taken with the outer Nb tip of our dual-tip STM and a Nb(100) sample, at temperatures ranging from 35 to 400 mK. A close up of the right peak in Fig. 5.6(a) shows that unlike the coherence peaks of the S-I-N junction in Fig. 5.3, the width of these peaks don't correlate as clearly with the temperature of the mixing chamber. However, a gaussian fit to the left 35 mK peak yields a width $\sigma_{\text{rms}} = 26$ μV . This is equivalent to ~ 300 mK when divided by k_B .

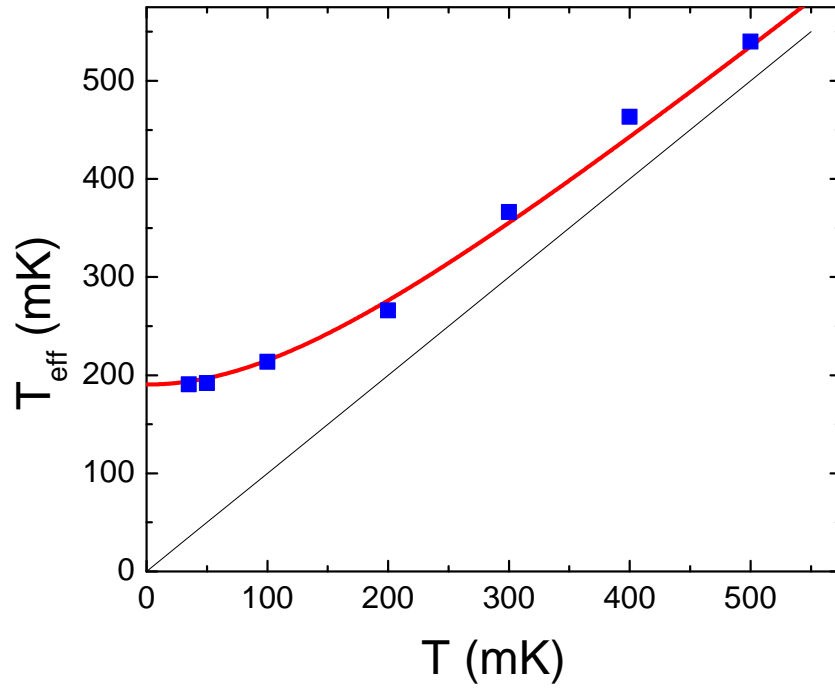


Figure 5.4: Plot of effective temperature T_{eff} vs. temperature T of the mixing chamber. Blue points were extracted from fitting BCS theory to the data shown in Fig. 5.3. The red curve is Eq. (5.13) with $T_{\text{mix}} = T$ and $T_0 = 184$ mK. The straight line shows $T_{\text{eff}} = T$.

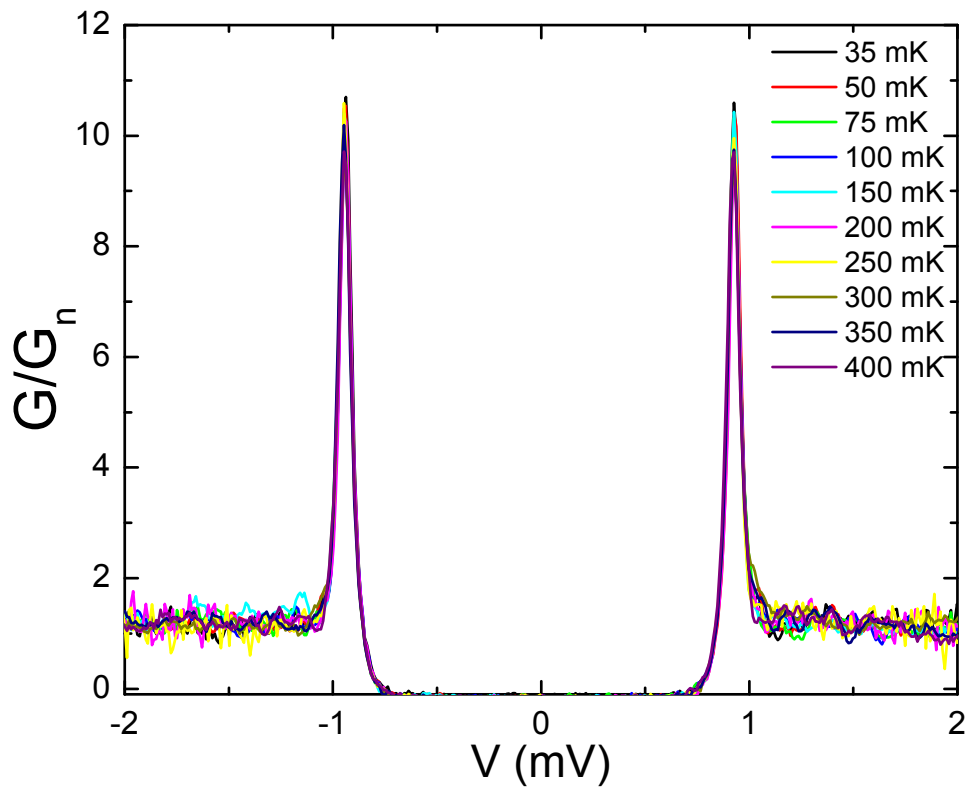


Figure 5.5: Normalized Conductance G/G_n versus tip voltage V measured from 35 mK to 400 mK for Nb tip and Nb sample.

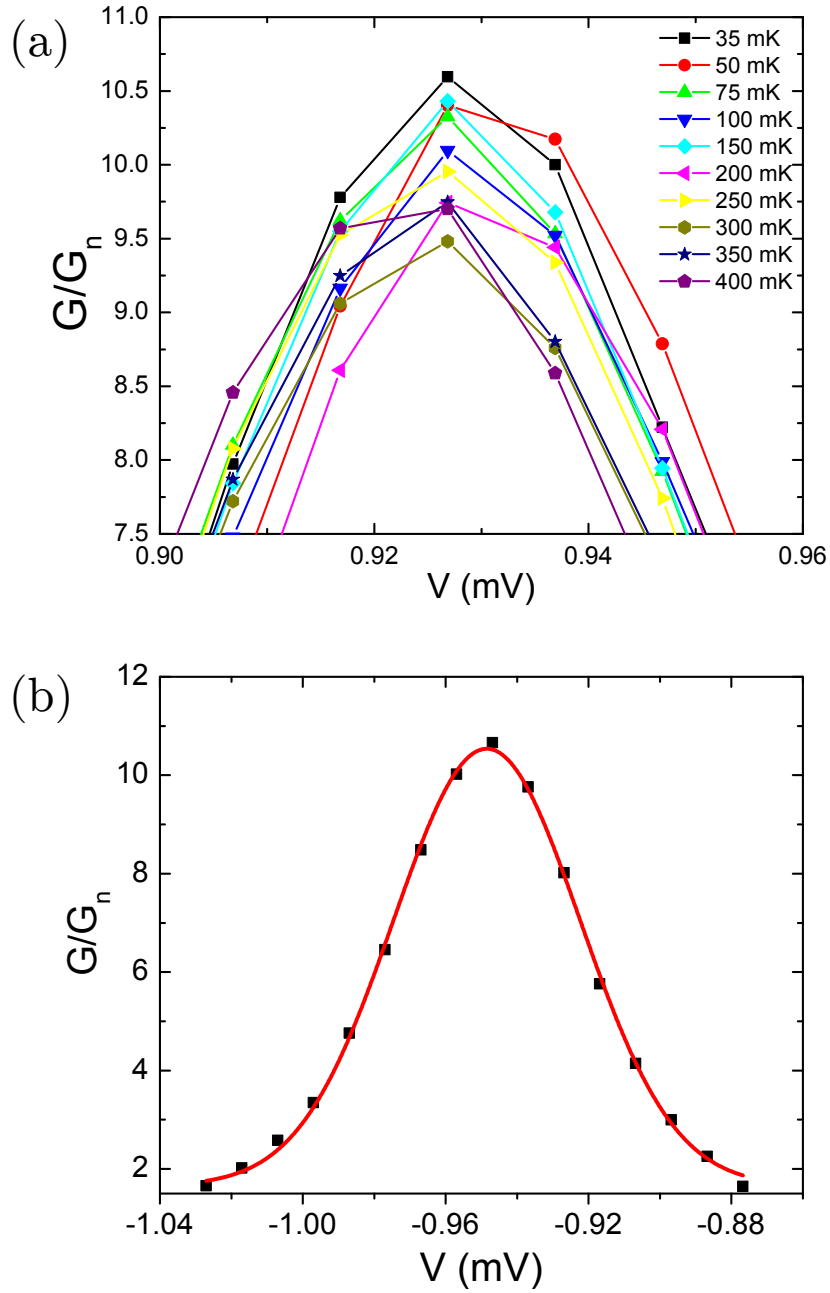


Figure 5.6: (a) Detailed view of right conductance peaks in Fig. 5.5 near 0.93 mV shows that the temperature dependence of the peaks is small in the measured temperature range. (c) Gaussian fit to one of the left peaks in Fig. 5.5 has a width of $\sigma_{\text{rms}} \approx 26 \mu\text{V}$ which yields an effective noise temperature of $\sim 300 \text{ mK}$ when divided by k_B .

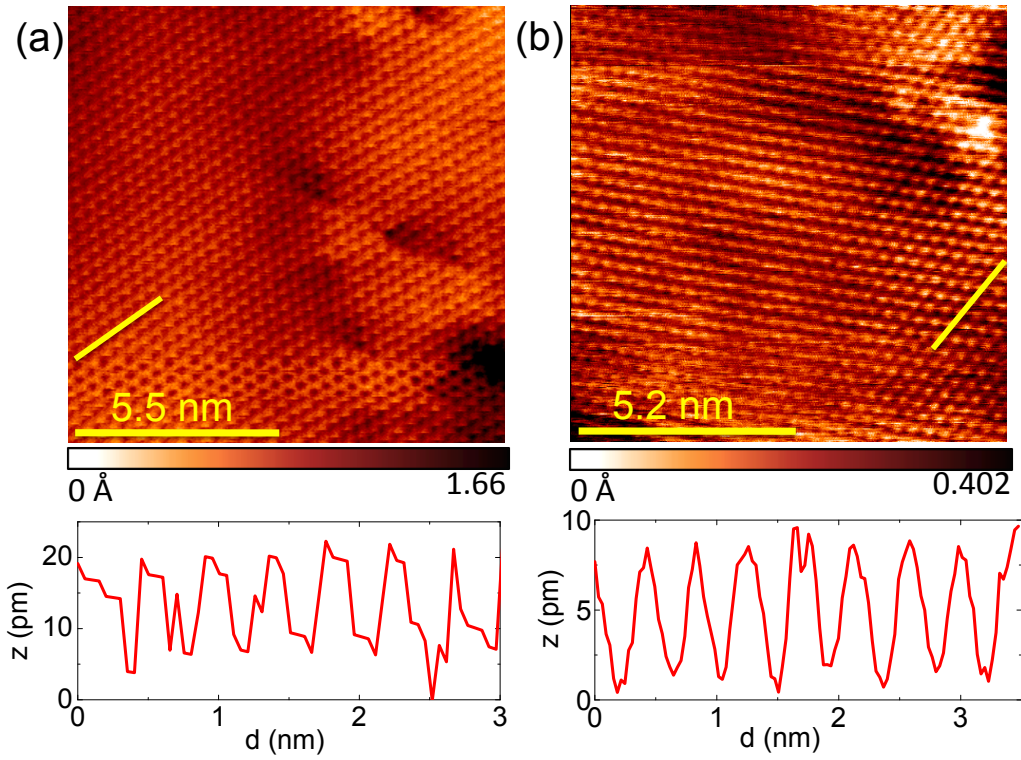


Figure 5.7: Unfiltered atomic resolution images of Bi_2Se_3 taken using Nb tips at 35 mK with (a) outer tip and (b) inner tip. Top: Topographic images. Bottom: Line scan plots of tip height z vs. distance scanned d , showing atomic corrugation with peak to valley heights of ~ 18 pm for the outer tip (a) and ~ 8 pm for the inner tip (b).

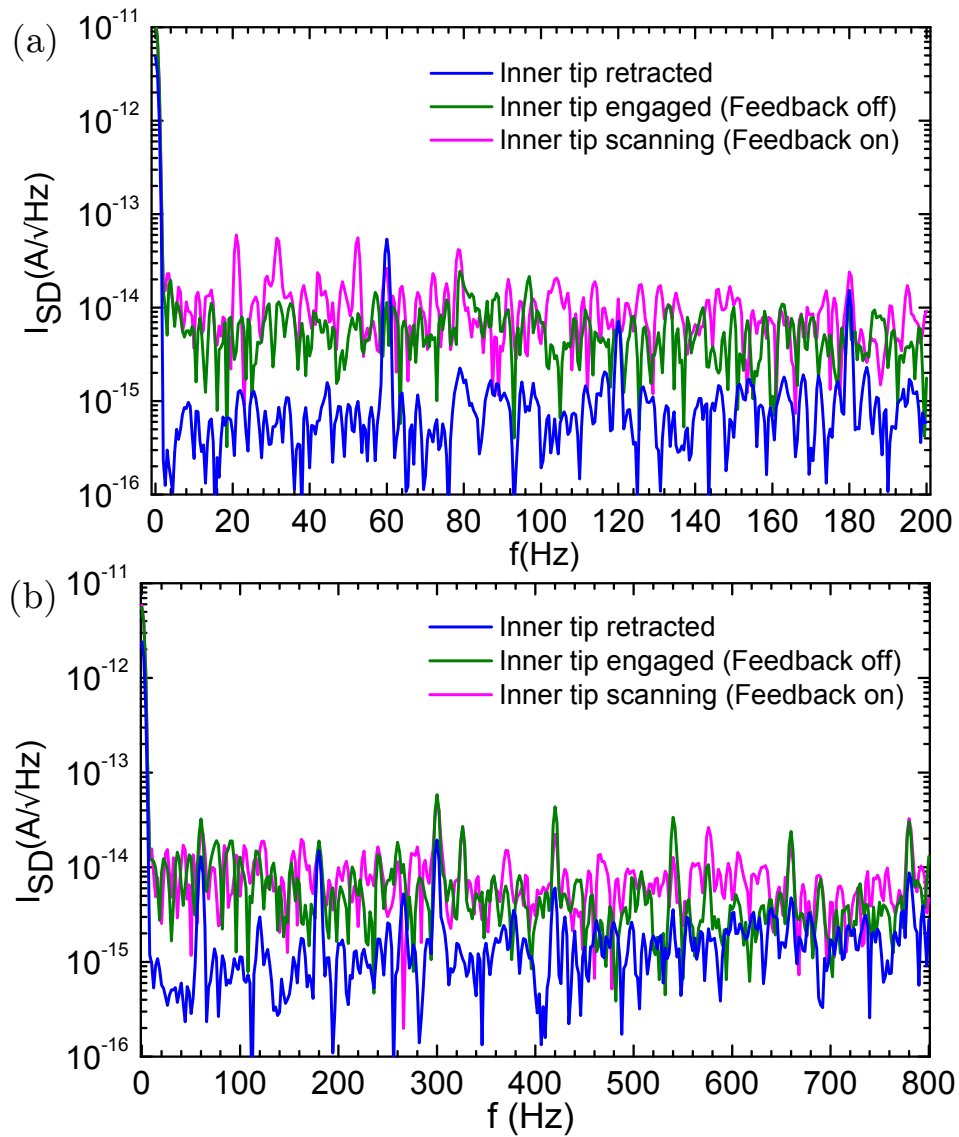


Figure 5.8: Root mean square noise power spectral density of the inner tip tunneling current with the tip retracted (blue), engaged (green), and scanning (pink) for the frequency ranges (a) 0-200 Hz and (b) 0-800 Hz.

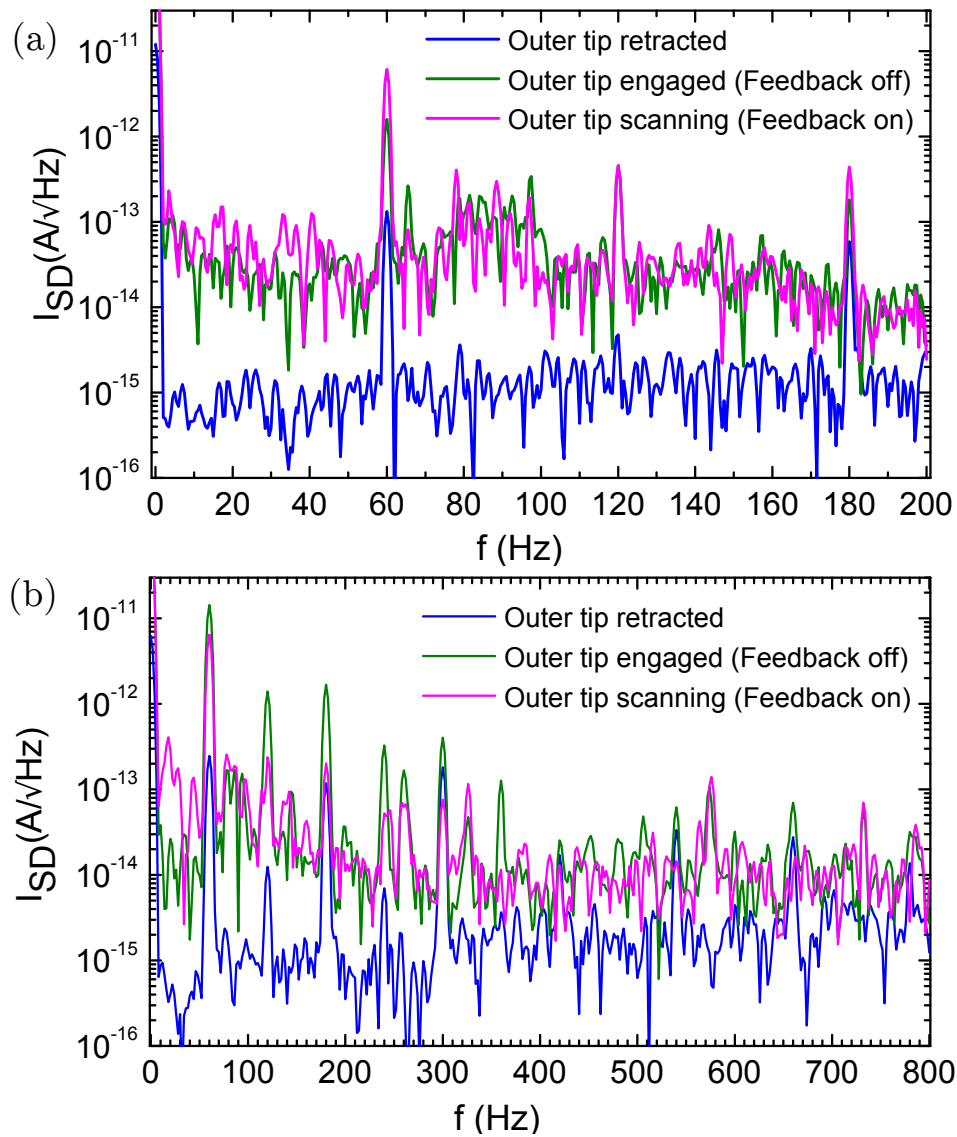


Figure 5.9: Root mean square noise power spectral density of the outer tip tunneling current with the tip retracted (blue), engaged (green), and scanning (pink) for the frequency ranges (a) 0-200 Hz and (b) 0-800 Hz.

5.4 Stability and noise characteristics

Figure 5.7 shows unfiltered atomic resolution images taken with the inner and outer Nb tips on a Bi_2Se_3 sample. The peak to valley atomic corrugation over the line sections shown of the outer and inner tips are ~ 18 pm and ~ 8 pm respectively. To characterize the noise, we Fourier transformed these images, filtered out the atomic lattice, and then analyzed the inverse Fourier transform. The rms roughness of the resulting background noise for the outer and inner tip images were 3.55 ± 0.03 pm and 1.75 ± 0.01 pm, respectively. The noise level for each tip was thus well below the signal for atomic scale features. We note that these measurements were taken with the 1K pot running. We calibrated the scanners in the x , y , and z directions from these images and images of mono-atomic steps on Au(100).

Low frequency noise is often the limiting factor in data obtained from STMs. Figures 5.8 and 5.9 show the RMS noise power spectral density of the current noise measured for inner and outer tips of our STM while the tip was retracted, in tunneling range, and scanning. The data was taken using typical operating conditions at 30 mK with the 1K pot running. In each case, the electronic noise floor—measured with the tip retracted—was between 10^{-16} and 10^{-15} A/ $\sqrt{\text{Hz}}$. When the tip was within tunneling distance, the mechanical noise results in the background level being raised to between 10^{-14} and 10^{-13} A/ $\sqrt{\text{Hz}}$ at low frequencies. The low current noise characteristics indicate that the instrument will yield a good signal to noise ratio for both topographic and spectroscopic data.

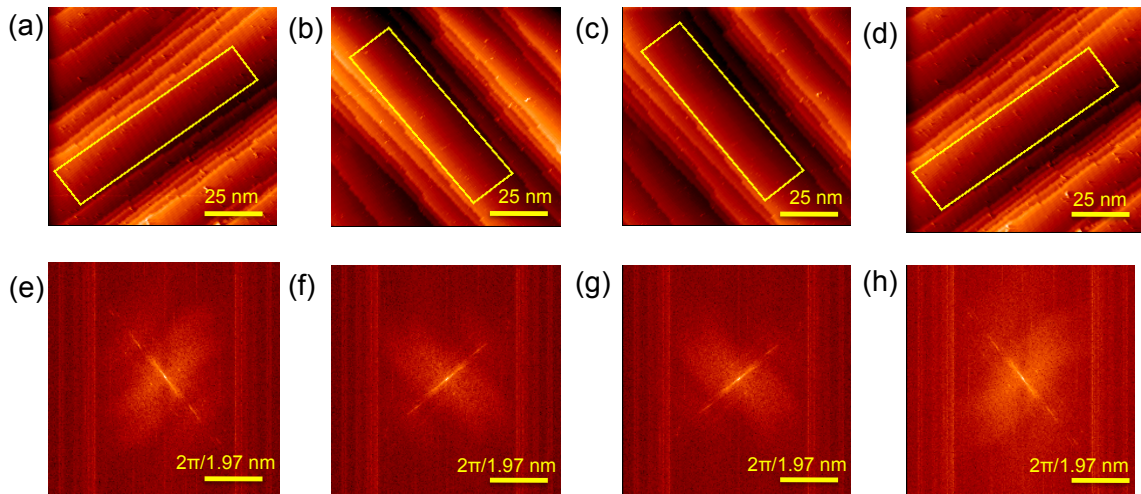


Figure 5.10: Topographic images of same region taken with outer Nb tip on Au(100), and corresponding Fourier transforms. The four different configurations and surface roughnesses are: (a) inner tip is retracted (scan angle of outer tip and $\sigma_{\text{rms}} = 14.2$ pm, (b) inner tip is in tunneling but not scanning and $\sigma_{\text{rms}} = 22.2$ pm, (c) inner tip is simultaneously scanning (scan angle of outer tip: 0°) and $\sigma_{\text{rms}} = 13.1$ pm, and (d) inner tip is simultaneously scanning (scan angle of outer tip: 90°) and $\sigma_{\text{rms}} = 12.3$ pm. The yellow boxes enclose regions on a single terrace where surface roughness σ_{rms} was computed. (e-h) Fourier transforms corresponding to images (a-d).

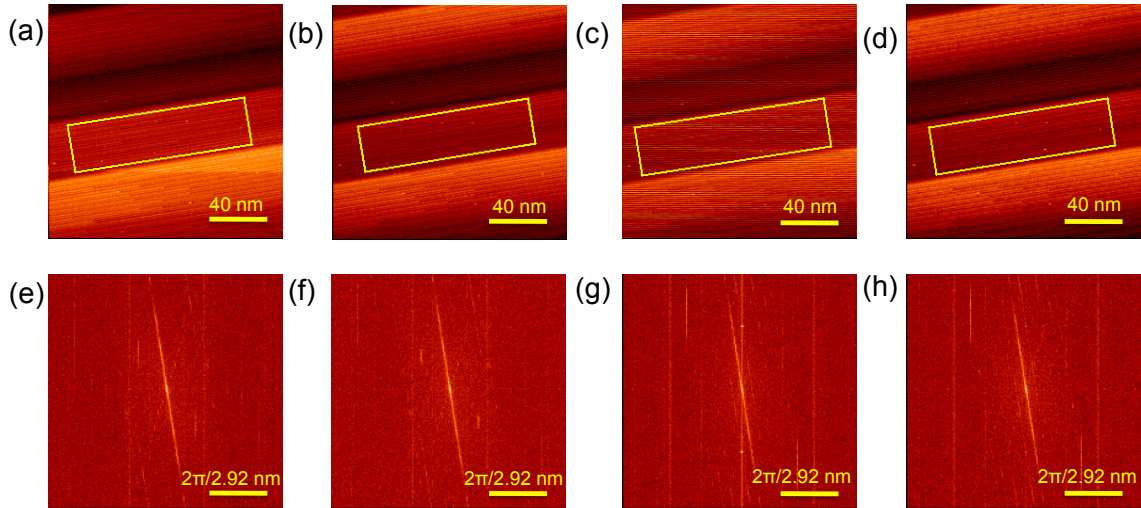


Figure 5.11: Topographic images taken with inner Nb tip on Au(100), and corresponding Fourier transforms. The four different configurations and surface roughnesses are: (a) outer tip is retracted: $\sigma_{\text{rms}} = 39.1$ pm (b) outer tip is in tunneling and $\sigma_{\text{rms}} = 39.2$ pm, (c) outer tip is scanning simultaneously with scan angle 0° and $\sigma_{\text{rms}} = 160$ pm, and (d) outer tip is scanning simultaneously with scan angle 90° and $\sigma_{\text{rms}} = 39.5$ pm. Yellow boxes show regions on a single terrace where surface roughness σ_{rms} was computed. (e-h) Fourier transforms corresponding to images (a-d); Comparing (e-f) to (g-h), note prominent vertical lines due to additional frequencies in (g) due to coupling to the outer tip.

5.5 Simultaneous imaging mode

Ultimately, to exploit the capability of an STM with two tips, the performance of each tip while the other tip is scanning simultaneously is important. Figures 5.10 and 5.11 show a series of topographic images of Au(100) taken with each Nb tip at 1.5 K. The images show the same area scanned with one tip for different configurations of the other tip. The r.m.s. roughness σ_{rms} of the points within the selected boxes was used to compare noise levels. Although these measurements were taken on atomically flat terraces, they include corrugation due to surface reconstruction. Hence the values for σ_{rms} obtained from these images is significantly higher than those obtained from the atomic resolution images above. By comparing σ_{rms} values in Figs. 5.11(c) (160 pm) and 5.11(d) (40 pm), we found that the angle at which the outer tip was scanned resulted in additional noise on the inner tip current signal. In contrast, Fig. 5.10 shows that there was no detectable effect on the outer tip due to the inner tip.

Further experimental study revealed that the effect of the outer tip on the inner tip is greatest for outer tip scan angles of 0° and 180° , increasing the σ_{rms} value to ≈ 120 pm. The cross talk was least at 90° and 270° , producing little additional noise at these angles. This can be understood from the geometry of the STM design, which involves over 3 dozen wires confined to an extremely limited space. The close proximity of the current wire for the inner tip and the x -piezo drive wire of the outer scanner produces capacitive coupling and results in cross talk in the inner tip signal. In contrast, the current wire for the outer tip is far from

scanner wires from the inner tip, and hence does not couple to them. Finally we note that while there is crosstalk present while simultaneously scanning both tips, it is insignificant in that it does not severely degrade the resolution of either tip, and atomic steps on Au(100) can still be clearly resolved, especially with proper choice of the tip scan angle.

5.6 Magnetic field

We also tested that our system could be used with a magnet. For this test, we used a standard single tip Pan-style STM mounted on the refrigerator, a tungsten tip, and a $\text{Cu}_x\text{Bi}_2\text{Se}_3$ superconducting sample. Figure 5.12 shows a series of spectroscopy curves measured at different field strengths. The superconducting gap and coherence peaks were predictably diminished with increasing magnetic field.

5.7 Conclusions

In this Chapter, I presented data that shows the stability and spectroscopic energy resolution of our dual-tip STM. The results are comparable to that of other single tip mK STMs [61, 62]. In addition, I analyzed the cross-talk between the two STM tips, and demonstrated the performance of a single-tip STM mounted on the refrigerator under applied magnetic field. The rest of this thesis is devoted to an analysis of data taken by this STM that exploits the millikelvin temperatures and μeV resolution that can be attained with the STM.

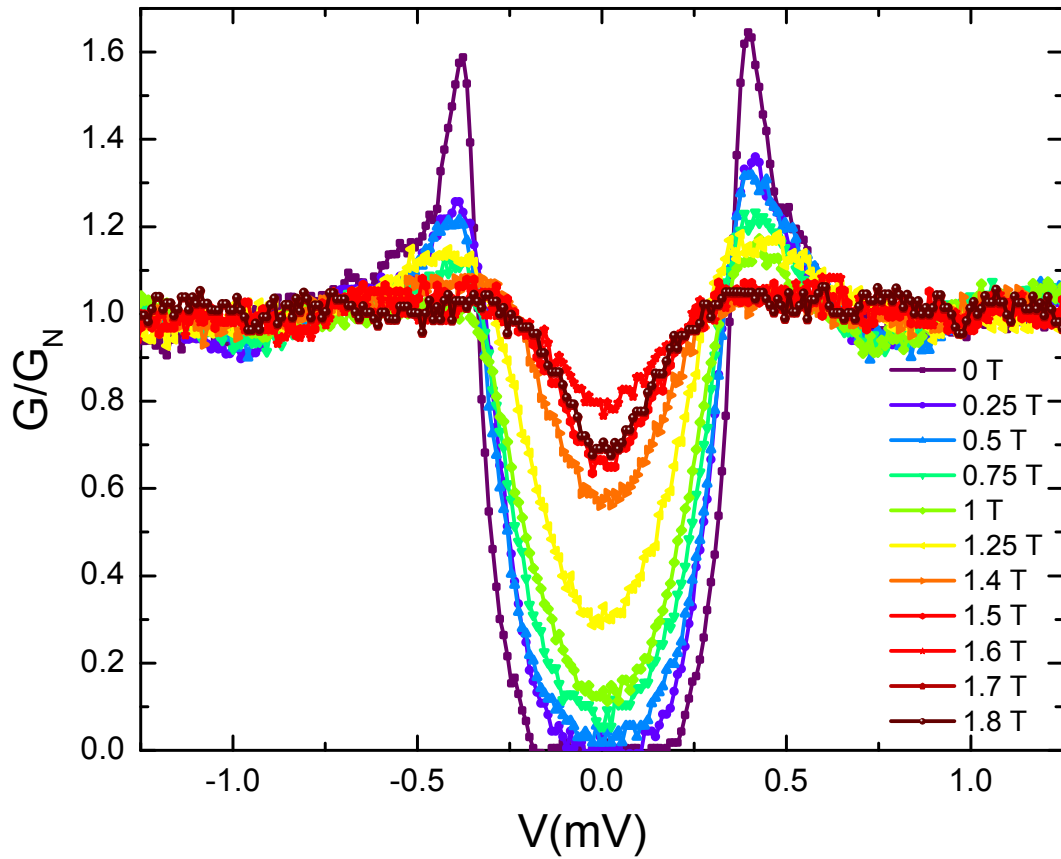


Figure 5.12: Plot of normalized conductance G/G_n versus tip-to-sample voltage V for a tungsten tip and copper-intercalated Bi_2Se_3 sample at $T_{\text{mix}} = 35$ mK for a series of applied magnetic fields. The superconducting gap is noticeably reduced as the magnetic field is increased to 1.8 T.

Chapter 6: Fluctuation-Dominated Tunneling in Ultra-Small Junctions

6.1 Introduction to Josephson junctions

Superconductors are characterized by a continuous phase transition at a critical temperature T_c , below which electrons combine to form a superconducting condensate composed of Cooper pairs with charge $2e$. The Cooper pairs in the condensate occupy a single state that can be described by a single macroscopic wave function $\psi = |\psi| \exp(i\phi)$ with a well defined phase ϕ .

A Josephson junction is formed when two superconducting electrodes are separated by a thin insulating layer. The overlap of the superconducting wave functions for each electrode allows the tunneling of Cooper pairs, as described in Chapter 2. The robustness of the phase coherence in conventional macroscopic Josephson junctions allows the junction dynamics to be modeled semi-classically. Brian Josephson predicted in a pioneering paper [50] that even in the absence of a voltage between the electrodes of a superconducting tunnel junction, there would exist a supercurrent given by

$$I = I_c \sin \phi. \tag{6.1}$$

Here, I_c is the critical current, the maximum supercurrent in the junction before it switches to its ohmic or normal conducting state, and ϕ is the gauge invariant phase difference between wave functions in the two electrodes. This counter-intuitive behavior of junctions is now called the dc Josephson effect. Josephson also predicted that in the presence of a voltage, V , the evolution of the gauge-invariant phase difference is given by

$$V = \frac{\hbar}{2e} \frac{d\phi}{dt}. \quad (6.2)$$

Integrating Eq. (6.2), the phase across a junction biased by a voltage V is

$$\phi = \int^t \frac{d\phi}{dt} = \frac{2eV}{\hbar} t \quad (6.3)$$

Substituting ϕ from Eq. (6.3) into Eq. (6.1), we see that an oscillating supercurrent develops across the junction, given by

$$I(t) = I_c \sin\left(\frac{2eV}{\hbar} t\right) \quad (6.4)$$

with frequency $f = 2eV/\hbar$. This is known as the ac Josephson effect, and relates voltage and frequency entirely through fundamental constants.

The dynamical variables that are natural choices to describe the physics of a Josephson junction are ϕ , the gauge invariant phase difference between the two electrodes, and Q , the total charge of the Cooper pairs that tunnel between them. The ac Josephson effect may be used to relate them via

$$V = \frac{\hbar}{2e} \frac{d\phi}{dt} = \frac{Q}{C}, \quad (6.5)$$

where C is the junction capacitance. In fact, the quantum operators corresponding to Q and ϕ are conjugate variables that obey the commutation relation $[\phi, Q] = 2ie$.

Since these operators do not commute, they obey an uncertainty relation $\Delta\phi\Delta Q \geq e$. Josephson junctions can thus display two limits of coherent behavior: one with a well defined phase, and the other with a well defined charge.

The Hamiltonian of an unbiased Josephson junction can be written as [137]

$$H(Q, \phi) = E_C \frac{Q^2}{e^2} - E_J \cos \phi, \quad (6.6)$$

where the first term is the kinetic or electrostatic energy of the junction, and the second term is the potential or Josephson coupling energy. In this expression the charging energy of the junction is $E_C = e^2/2C$, where C can be approximated by treating the junction as a parallel plate capacitor, in which case $C \propto \epsilon A/d$, where d is the separation between the electrodes, A is the plate area, and ϵ_0 is the permittivity of the material separating them. The potential energy stored in the junction can be calculated from

$$U = \int I_S V dt = \int_0^t I_S \left(\frac{\Phi_0}{2\pi} \frac{d\phi}{dt} \right) dt = \frac{\Phi_0}{2\pi} \int_{\phi(0)}^{\phi(t)} I_c \sin \phi d\phi = \frac{\Phi_0 I_c}{2\pi} (1 - \cos(\phi)) \quad (6.7)$$

The Josephson coupling energy, $E_J = \Phi_0 I_c / 2\pi$ sets the scale for the potential energy term of the Hamiltonian, where $\Phi_0 = h/2e$ is the flux quantum and we have chosen $\phi(0) = 0$.

The Ambegaokar-Baratoff relation for the critical current in a relatively opaque, symmetric junction composed of BCS superconductors is given by [138]

$$I_c = \frac{\pi \Delta(T)}{2eR_N} \tanh \left[\frac{\Delta(T)}{2k_B T} \right] \quad (6.8)$$

where $\Delta(T)$ is the superconducting energy gap, T is the temperature, and R_N is the

normal state tunneling resistance. The corresponding Josephson energy is

$$E_J = \frac{\pi\hbar}{4e^2} \frac{\Delta(T)}{R_N} \tanh \left[\frac{\Delta(T)}{2k_B T} \right] \quad (6.9)$$

At temperatures $T \ll \Delta/k_B$, this reduces to

$$E_J = \frac{h}{8e^2} \frac{\Delta}{R_N} \quad (6.10)$$

This expression is often used to estimate E_J in tunnel junctions because it relates the coupling energy to Δ and the normal tunneling resistance R_N , both of which are measurable. For an asymmetric junction with superconducting gaps Δ_1 and Δ_2 , an analytic result for E_J exists only at $T = 0$ and is given by [138]

$$E_J = \frac{\hbar}{e^2 R_N} \frac{\Delta_1 \Delta_2}{\Delta_1 + \Delta_2} K \left(\left| \frac{\Delta_1 - \Delta_2}{\Delta_1 + \Delta_2} \right| \right) \quad (6.11)$$

where K is a complete elliptic integral of the first kind.

6.2 Josephson junction dynamics

The dynamics of a Josephson Junction are generally determined by the ratios of the characteristic energy scales of the device (the charging energy E_C , the Josephson energy E_J , and the thermal energy $k_B T$) and coupling of the junction to the frequency dependent impedance $Z(\omega)$ due to the electromagnetic environment. This environment can generally be considered to have a low impedance when $\text{Re}[Z(\omega)] \ll R_Q$ and to have a high impedance when $\text{Re}[Z(\omega)] \gg R_Q$, where $R_Q = h/(2e)^2 \approx 6.4 \text{ k}\Omega$ is the quantum of resistance.

For typical experimental conditions, we can define a junction as being “macroscopic” or in the “phase limit” when $E_J \gg E_C$. In this case the superconducting

wave function is well localized in the minimum of the Josephson potential well, and ϕ may be treated as a sharply defined quantum variable. Provided the temperature is not too low, ϕ typically acts as a classical variable. In the limit $E_J \ll E_C$ on the other hand, the charge Q is not a good variable because it is subject to large quantum fluctuations. The device behavior in this regime is dominated by the dc and ac Josephson effects. The classical phase dynamics of a conventional Josephson junction are described in more detail in Section 6.3 below. In Section 6.4, I introduce Shapiro steps which describe the response of classical phase coherent Josephson junctions to microwave radiation.

As the charging energy increases from $E_C \ll E_J$ towards $E_C \sim E_J$, quantum fluctuations in the phase ϕ become increasingly important. Q now takes on the role of the well-defined variable that may be used to describe the system. In ultra-small junctions, one can easily achieve $E_C > E_J$, and the fluctuations in ϕ can be on the order of 2π . This leads to the junction's current-voltage characteristic showing a suppressed switching current because measurements of supercurrent involve averaging $\bar{I} = I_c \langle \sin \phi \rangle$.

A key point that is sometimes ignored, is that real junctions are not completely isolated but rather are always coupled to an external measurement circuit or other electromagnetic environment. This influences the junction dynamics significantly, especially in the ultra-small junction limit. The coupling between the junction and an external circuit may be treated quasi-classically or quantum mechanically. In Section 6.5, I present a classical description of the environment, followed in Section 6.6 by a quasi-classical treatment of the phase diffusive regime of ultra small

junctions. Junction dynamics are more comprehensively described by the quantum mechanical $P(E)$ theory [132, 139–141], which reduces to the classical case in the appropriate limit. For an ultra-small junction in a low impedance environment, *i.e.* $\text{Re}[Z(\omega)] \ll R_Q$, the $P(E)$ theory predicts that dissipation will occur via incoherently tunneling Cooper pairs that release energy to the environment. On the other hand, if an ultra-small junction is embedded in a high impedance circuit *i.e.* $\text{Re}[Z(\omega)] \gg R_Q$, the theory predicts that the fast discharge of the junction is prevented, and single charge effects such as Coulomb blockade [131, 139, 142] and Bloch oscillations [143, 144] will dominate. In Section 6.7, I briefly review the quantum mechanical description of the environment using the Caldeira-Legget model [145, 146]. Finally, in Section 6.8, I present the key ideas of the $P(E)$ theory, including a prediction for the supercurrent behavior of an ultra-small junction coupled to a finite transmission line, as well as the supercurrent response to microwave radiation.

6.3 The RCSJ model

A real Josephson junction not only has an ideal Josephson element, but some dissipation and some capacitance C . For simplicity, the dissipation is often modeled as a linear, frequency-independent resistor R that shunts the junction. For macroscopic junctions with $E_J/E_C \gg 1$, I will assume the wavefunction describing the system is localized in a minimum of a potential well, so there is a well defined phase ϕ . Furthermore, most real junctions that are connected to leads correspond to the case of a low impedance environment. Typically leads connected to a junction

may be approximated as a transmission line with an impedance on the order of the free-space impedance, $Z_0 \approx 377 \Omega$ [137, 147]. In this situation, the Resistively and Capacitively Shunted Junction (RCSJ) model [137, 148] described provides an accurate and intuitive description of the classical behavior of a real Josephson junction.

The RCSJ model [137, 148] describes a real Josephson junction as an ideal Josephson junction shunted by a resistor R and a capacitance C . Figure 6.1(a) shows an RCSJ junction biased by an ideal current source I_b . However, our STM has a voltage-biased configuration which may be modeled as shown in Fig. 6.1(b). I note that the results derived for the current-biased RCSJ model may be applied to a junction with bias voltage V_b when $V_b = I_b R$ [141].

Using Kirchhoff's laws, the circuit equation for the voltage-biased case can be written as

$$V_b = I_b R = R I_c \sin \phi + V + RC \frac{dV}{dt}. \quad (6.12)$$

The equation of motion for the phase difference ϕ between the two junction electrodes can then be obtained by substituting Eq. (6.5) for V in terms of ϕ from the AC Josephson effect,

$$I_b = I_c \sin \phi + \frac{\Phi_0}{2\pi R} \frac{d\phi}{dt} + \frac{\Phi_0 C}{2\pi} \frac{d^2\phi}{dt^2}. \quad (6.13)$$

This is recognizable as the differential equation for a driven damped harmonic oscillator. The Hamiltonian corresponding to this equation of motion, if dissipation is ignored, is

$$H(p_\phi, \phi) = \frac{1}{2C} \left(\frac{2\pi}{\Phi_0} \right)^2 p_\phi^2 - \frac{\Phi_0}{2\pi} (I_c \cos \phi + I_b \phi). \quad (6.14)$$

where ϕ is the generalized position coordinate, and p_ϕ is the the generalized mo-

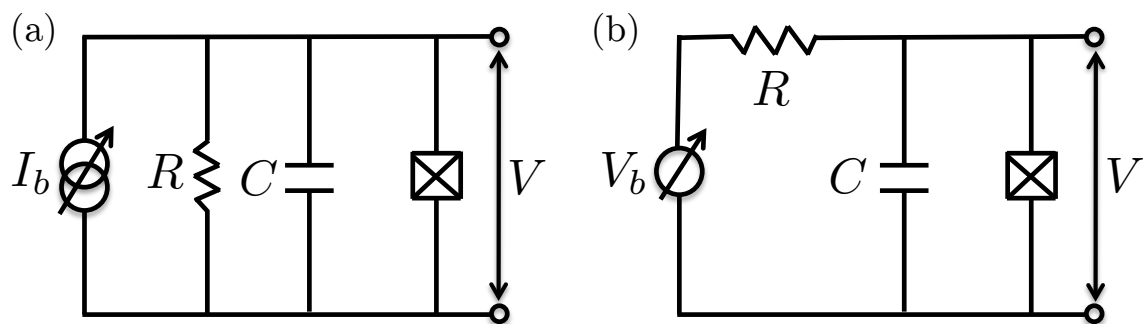


Figure 6.1: Schematic of RCSJ model with (a) current-biased configuration and (b) voltage-biased configuration. The two are equivalent if $V_b = RI_b$.

momentum coordinate, defined as $p_\phi = C(\Phi_0/2\pi)^2 d\phi/dt$. This Hamiltonian describes a ball of mass $m = C(\Phi_0/2\pi)^2$ in a tilted washboard potential

$$U(\gamma) = -\frac{\Phi_0}{2\pi}(I_c \cos \phi + I_b \phi) = -E_J \cos \phi - I_b \left(\frac{\hbar}{2e}\right) \phi \quad (6.15)$$

where the tilt is determined by the bias current. Although dissipation was ignored in formulating the Hamiltonian, the equation of motion Eq. (6.13) may be recovered by considering the ball to be subject to a viscous drag force $(\hbar/2e)^2(1/R)d\phi/dt$.

Figure 6.2 shows a sketch of the tilted washboard potential for various I_b/I_c ratios. When $I_b < I_c$, the particle is confined to a local minimum in the washboard potential, and a well-defined and non-zero supercurrent I_b flows. For $\phi \ll 1$, the potential may be approximated as harmonic, and a perturbation will cause the phase to oscillate in the minimum of the potential well with a plasma frequency

$$\omega_p = \sqrt{\frac{k}{m}} = \sqrt{\frac{2\pi I_c}{\Phi_0 C}}. \quad (6.16)$$

For $I_b > I_c$, the overall slope of the washboard is large enough that there are no local minima of the potential, leading to a current at finite voltage and a steady increase in ϕ at an average rate of $2eV/\hbar$. For $I_b = I_c$, the junction carries the maximum current I_c at zero voltage.

The dynamical behavior of a Josephson junction is strongly influenced by damping. Rescaling time by setting $\tau = \omega_p t = 2\pi R I_c t / \phi_0$, the equation of motion for a Josephson junction, Eq. (6.12), may be rewritten as

$$\frac{1}{I_c R} V_b = \sin \phi + \frac{d\phi}{d\tau} + Q^2 \frac{d^2 \phi}{d\tau^2} \quad (6.17)$$

where $Q = \omega_p R C$ is the quality factor, and $\beta_C = Q^2$ is the Stewart-McCumber

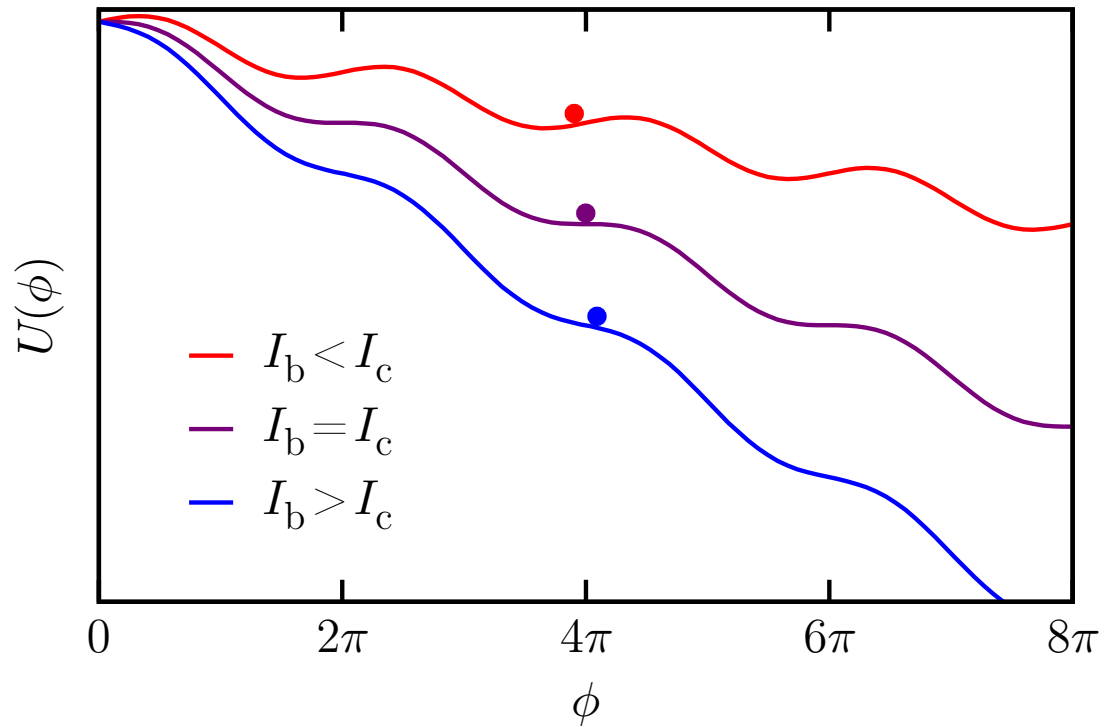


Figure 6.2: Sketch of the tilted washboard potential $U(\phi)$ vs. the phase ϕ . I_b is the bias current and I_c is the critical current of the junction. The three cases shown are for $I_b < I_c$ in red, $I_b = I_c$ in purple, and $I_b > I_c$ in blue.

damping parameter [149, 150]. Q may also be expressed as

$$Q = \pi \frac{R}{R_Q} \sqrt{\frac{E_J}{2E_C}} \quad (6.18)$$

Figure 6.3 shows I - V characteristics of a current-biased Josephson junction for $Q \ll 1$ and $Q \gg 1$, corresponding to the overdamped and underdamped limits, respectively. For $Q \ll 1$, the junction is in the overdamped regime. In the tilted washboard model, if the ball is in a local minimum (*i.e.*, $I < I_c$), it will remain stationary. When $I > I_c$, the ball rolls slowly down the washboard, giving rise to a voltage across the junction $V = (\hbar/2e)d\phi/dt$. The ball drops more quickly over the little potential hills, causing periodic voltage pulses at the Josephson frequency $f = 2e\langle V \rangle/h$. The I - V curve for overdamped junctions is non-hysteretic [137].

For $Q \gg 1$, on the other hand, the junction is in the underdamped regime, and the capacitance is large enough to play a significant role in the junction dynamics. In the washboard model, the capacitance may be thought of as giving the ball a large mass with significant inertia, and very little friction. The I - V curve of an underdamped junction is hysteretic (see Fig. 6.3). Once the junction is in the non-zero voltage state, the phase difference ϕ increases at the rate $2eV/\hbar$. If the bias current is reduced below its critical value, the voltage V will not drop back to 0 until a “re-trapping current” $I_r = 4I_c/\pi\beta_C^{1/2}$ is reached [137].

6.4 Shapiro steps

When a macroscopic Josephson junction is irradiated with microwaves of frequency ω , the Josephson frequency defined by Eq. (6.2) synchronizes with the ap-

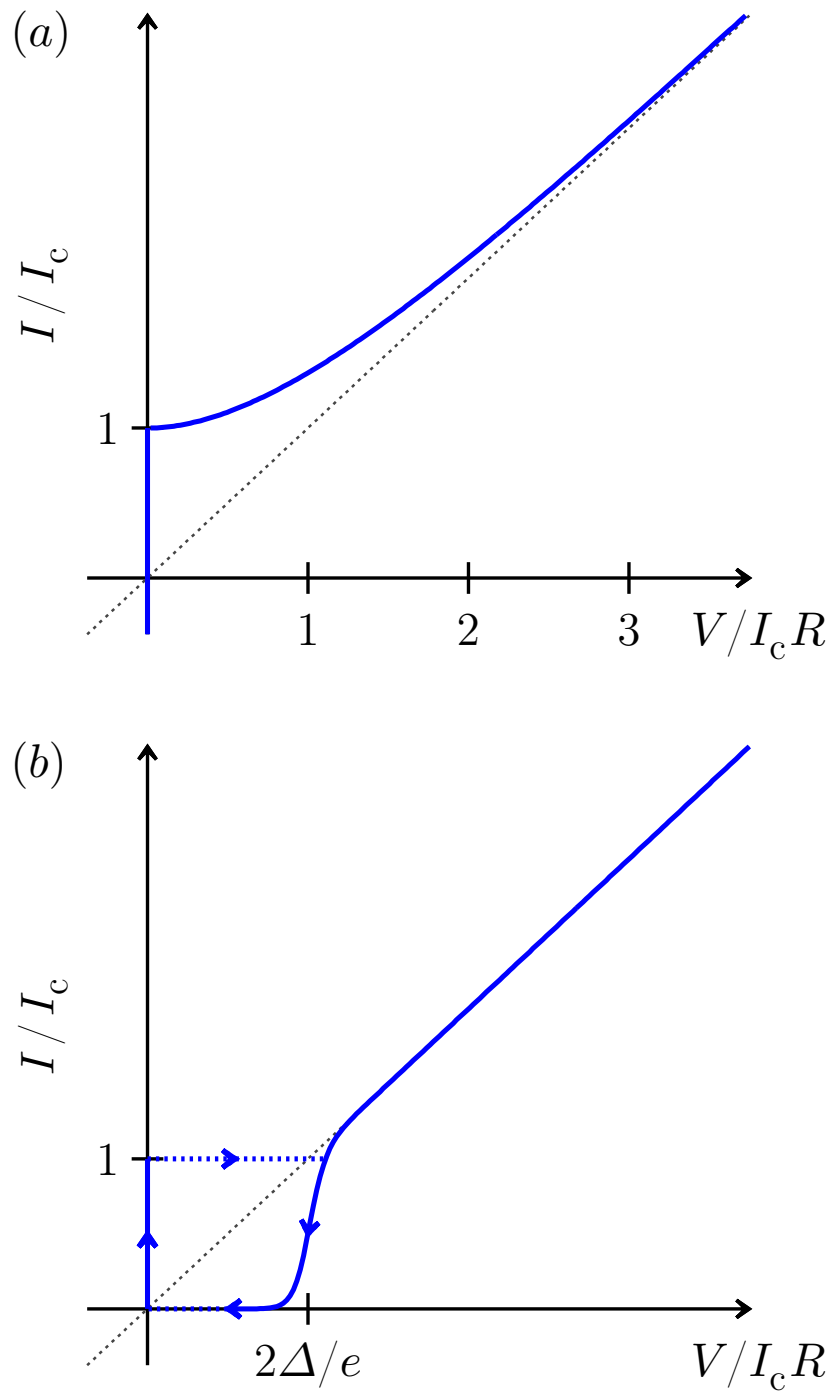


Figure 6.3: Sketch of the I - V curve of a classical macroscopic current-biased Josephson junction in the (a) overdamped limit ($Q \ll 1$) and (b) underdamped limit ($Q \gg 1$). The black dotted line corresponds to $I = V/R$.

plied microwaves frequency, and the supercurrent exhibits current steps at precisely defined voltages, $V_n = n\hbar\omega/2e$, where n is an integer [151]. This can be understood by treating the junction as having a bias voltage V with a dc voltage V_0 , and an ac voltage of amplitude V_1 at angular frequency ω created by the microwaves.

$$V = V_0 + V_1 \cos(\omega t) \quad (6.19)$$

Using the Josephson equation to replace V with $\hbar\phi/2e$ and integrating the resulting expression, I obtain the phase across the junction

$$\phi(t) = \phi_{\text{const}} + \omega_0 t + (2eV_1/\hbar\omega) \sin(\omega t), \quad (6.20)$$

where $\omega_0 = 2eV_0/\hbar$ and ϕ_{const} is the constant of integration. Inserting Eq. (6.18) into the dc Josephson equation, and expanding sine in terms of Bessel functions, one finds [137]

$$I_{\text{Shapiro}} = I_c \sum_{n=-\infty}^{\infty} (-1)^n J_n \left(\frac{2eV_1}{\hbar\omega_1} \right) \sin(\phi_0 + \omega_0 t - n\omega_1 t) \quad (6.21)$$

From this equation, we see that the time averaged current through the junction will be zero, except when when $\omega_0 = n\omega_1$, or $V_0 = n\hbar\omega_1/2e$. Thus Eq. (6.21) suggests that the measured I - V curve will display a discrete jump or rise in current at regularly spaced voltages. These features have come to be called Shapiro steps [151] and the effect is used to define the standard volt. It should be noted that this contribution to the total current is due to the response of the junction to microwaves, and that a calculation of the I - V characteristic of a real junction would need to include the effect of the shunting R and C components.

6.5 The electromagnetic environment

The electromagnetic environment that couples to a superconducting STM junction is important in understanding the dynamics of the junction. The environment in the case of our millikelvin STM consists of the leads connected to the tip and sample, that are filtered by bronze powder filters clamped to the mixing chamber of the dilution fridge. These wires ultimately connect to room temperature electronics. At the junction, the impedance of this external circuit can be written as

$$Z(\omega) = \frac{V(\omega)}{I(\omega)}. \quad (6.22)$$

where V is the voltage across the junction, and I is the current through the junction. The relevant frequency range for the junction dynamics is determined by its plasma frequency, $f_p = \sqrt{8E_J E_C}/h$, which is typically in the 1-100 GHz range. At these frequencies, the dc resistance of the remote current source is irrelevant because of attenuation in the lines and the shunting impedance of the circuit. At frequencies of 1-100 GHz, one expects that the junction damping is determined primarily by the last few centimeters of the leads connecting the junction to the external circuit. These leads are not matched or uniform and typically generate a capacitance that is much larger than the junction capacitance. Hence, even if we use a current source to bias the junction, it will charge this capacitor, creating an effective voltage source.

Taking the junction capacitance C into account but ignoring any internal

shunting resistance, the effective impedance seen by the junction is given by

$$Z_t = \frac{1}{i\omega C + Z^{-1}(\omega)} \quad (6.23)$$

where the junction capacitance is in parallel with the external impedance $Z(\omega)$. At GHz frequencies, capacitance in the leads will be much larger than the capacitance of an ultra-small junction, and radiation from the leads will tend to produce an impedance $Z_{\text{env}} \approx 377 \Omega$, instantaneously removing charge transferred through the junction [137, 142, 152]. Thus at high frequencies, we expect that an STM junction “sees” a low impedance environment with $Z_{\text{env}} \ll R_Q$, and is in the overdamped regime. However, it is important to note that the junction may be underdamped at low frequencies. This frequency-dependent damping is crucial to understanding the junction behavior, as it may display overdamped characteristics at some voltages or frequencies, and underdamped characteristics at others. It is also possible for the junction to be underdamped at its plasma frequency—the energy scale which determines the high-frequency phase dynamics, whereas it may be over-damped at lower frequencies.

6.6 Classical phase diffusion in ultra-small junctions

When the tunneling resistance of a junction is large and when the area of the junction is extremely small, it is easy to reach the limit $E_J/E_C \ll 1$. Since the typical STM tip radius is 10-100 nm, our STM junction is an ultra-small Josephson junction with $C \approx 1$ fF, corresponding to a charging energy $E_C/k_B \approx 1$ K. In this Section, I will review the classical dynamics of such an ultra-small, overdamped junction in

the presence of thermal noise [153–155]. Since this is a classical description, ϕ will be treated as a classical variable rather than an operator.

For a current-biased Josephson junction in the RCSJ model, the phase obeys the equation of motion

$$\frac{\hbar C}{2e} \frac{d^2\phi}{dt^2} + \frac{\hbar}{2eR} \frac{d\phi}{dt} + I_c \sin \phi = I_b. \quad (6.24)$$

Thermal fluctuations can be included as a stochastic Johnson current noise generated by the shunt resistor R at an effective noise temperature T_n . This can be modeled as arising from a random voltage source that satisfies the correlation function: $\langle \tilde{e}(t)\tilde{e}(0) \rangle = 2k_B T_n R \delta(t)$ [153, 156]. In the tilted washboard picture, this thermal current noise causes random fluctuations in the overall tilt of the washboard. These fluctuations cause the phase to diffuse between multiple metastable states, in what can be approximated as a discrete random walk [153]. I note that if the noise is sufficiently large, there will be a lack of phase coherence.

Ivanchenko and Zil'berman treated this case by arguing that they could ignore the second derivative term in Eq. (6.24) because $C \rightarrow 0$ [153, 157]. The circuit equation for a junction biased with a voltage V_b , including a fluctuation term to incorporate thermal noise, can then be written as

$$\frac{\hbar}{2e} \frac{d\phi}{dt} + RI_c \sin \phi = V_b + \tilde{e}(t), \quad (6.25)$$

where $I_c = 2\pi E_J/\Phi_0$ is the critical current. If we set $\tau = (2eRI_c/\hbar)t$, $\tilde{\epsilon} = \tilde{e}/RI_c$, $u = V_b/RI_c$. and $\gamma = k_B T_n/E_J$, Eq. (6.25) can be written as [153]

$$\frac{d\phi}{dt} + \sin \phi = u + \tilde{\epsilon}(\tau), \quad (6.26)$$

where $\langle \tilde{\epsilon}(\tau)\tilde{\epsilon}(0) \rangle = 2\gamma\delta(\tau)$. Equation (6.26) is the Langevin equation of the Josephson phase, with the corresponding Fokker-Planck equation given by

$$\frac{dW}{d\tau} = \gamma \frac{d^2W}{d\phi^2} + W \cos \phi + \frac{dW}{d\phi} (\sin \phi - u), \quad (6.27)$$

where W is the probability distribution of finding the junction at a given ϕ . W is a periodic function of ϕ , and I can write

$$W(\phi, \tau | \phi_0, 0) = \sum_{n=-\infty}^{+\infty} x_n e^{in\phi}. \quad (6.28)$$

Multiplying both sides by $e^{-im\phi}$ and integrating over ϕ gives

$$\int_0^{2\pi} e^{-im\phi} W(\phi, \tau | \phi_0, 0) d\phi = \sum_{n=-\infty}^{+\infty} x_n \int_0^{2\pi} e^{in\phi} e^{-im\phi} d\phi. \quad (6.29)$$

Since $\int_0^{2\pi} e^{in\phi} e^{-im\phi} d\phi = 2\pi\delta_{nm}$, we have $\int_0^{2\pi} e^{-im\phi} W(\phi, \tau | \phi_0, 0) d\phi = 2\pi x_m$. And, $x_n = \int_{-\infty}^{+\infty} e^{in\phi} W(\phi, \tau, \phi_0, 0) d\phi$. Multiplying Eq. (6.27) by $e^{in\phi}$ and integrating over ϕ gives

$$\frac{dx_n}{d\tau} = \int d\phi e^{in\phi} \left(\frac{1}{2}(in)^2 W + W \cos \phi + (\sin \phi - u) \right) \quad (6.30)$$

Substituting Eq. (6.28) for W one finds

$$\frac{dx_n}{d\tau} = -n \left((\gamma n - iu)x_n(\tau) + \frac{x_{n+1}(\tau) - x_{n-1}(\tau)}{2} \right) \quad (6.31)$$

This equation is easier to solve because we have converted a multi-variable differential equation to a single-variable differential equation. The solution can be written in terms of the modified Bessel function $I_\nu(z)$ which obeys a similar recursion relation:

$$\frac{2\nu}{z} I_\nu(z) = I_{\nu-1}(z) - I_{\nu+1}(z) \quad (6.32)$$

One can show that $x_n(\infty) = \frac{I_{n-iu/\gamma}(1/\gamma)}{I_{-iu/\gamma}(1/\gamma)}$ satisfies Eq. (6.31) for $\tau \rightarrow \infty$, and one can obtain the dc Josephson effect from this relation. To see this, note that as $\tau \rightarrow \infty$ the system approaches a steady state. Hence,

$$I = I_c \langle \sin \phi \rangle = I_c \lim_{\tau \rightarrow \infty} \int_{-\infty}^{+\infty} d\phi \sin \phi W(\phi, \tau | \phi_0, 0) = I_c \frac{x_1(\infty) - x_{-1}(\infty)}{2i} \quad (6.33)$$

Since the observed current is real, $I = I^*$, and $x_n^* = x_{-n}$. Then $\frac{x_1 - x_1^*}{2i} = \text{Im}(x_1)$. If we set $V_P = (2e/\hbar)Z_{\text{env}}k_B T_n$, we can write

$$I(V_b) = I_c \text{Im}[x_1(\infty)] = I_c \text{Im} \left[\frac{I_{1-i\frac{V_b}{V_P}}(E_J/k_B T_n)}{I_{-i\frac{V_b}{V_P}}(E_J/k_B T_n)} \right]. \quad (6.34)$$

The voltage across the junction is [153]:

$$V = \frac{\hbar}{2e} \frac{d}{dt} \langle \phi \rangle = V_b - I(V_b)Z_{\text{env}} \quad (6.35)$$

We note that Z_{env} is the generalized environmental impedance.

When $E_J/k_B T \ll 1$, Eqs. (6.34) and (6.35) yield [21, 153]

$$I(V) = \frac{I_c^2 Z_{\text{env}}}{2} \frac{V}{V^2 + V_P^2}. \quad (6.36)$$

Figure 6.4 shows a plot of $I(V)$ vs. V calculated using Eqs. (6.36) for three experimentally realistic tunnel resistances. Equation (6.36) may be rewritten in the form

$$I(V) = (I_c R_N)^2 \frac{Z_{\text{env}}}{2R_N^2} \frac{V}{V^2 + V_P^2}, \quad (6.37)$$

and the value of $I_c R_N$ can be determined using the Ambegaokar-Baratoff formula, Eq. (6.8). For this plot, I assumed we have a Nb-Nb STM junction (*i.e.*, $\Delta \approx 1.4$ meV), and chose $R_N = 1 \text{ M}\Omega$, $R_N = 2 \text{ M}\Omega$ and $R_N = 5 \text{ M}\Omega$. An environmental impedance of $Z_{\text{env}} = 377 \text{ }\Omega$ and temperature $T_n = 0.2 \text{ K}$ were also assumed.

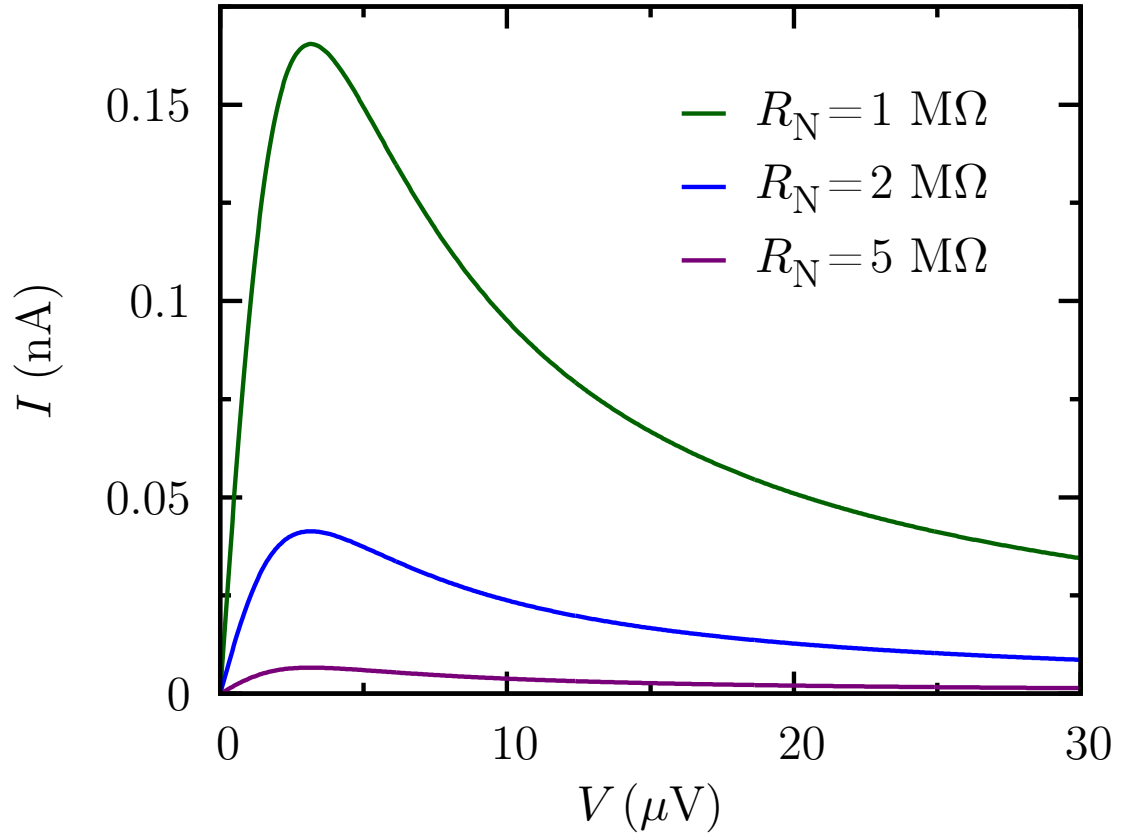


Figure 6.4: Plot of I vs. V calculated for tunnel resistances $R_N = 1 \text{ M}\Omega$ (green), $R_N = 2 \text{ M}\Omega$ (blue), and $R_N = 5 \text{ M}\Omega$ (purple), assuming $T = 200 \text{ mK}$ and $Z_{\text{env}} = 377 \Omega$.

As the plot shows, the thermal fluctuations of the phase suppress the observed critical current, transforming it into a peak with finite resistance rather than a branch with infinite resistance. This smooth s-shaped curve is extremely similar to the I - V characteristic observed by other STM groups at temperatures of 2.1 K and higher [27–29, 31, 114]. It also bears some resemblance to what I observed in our Nb-Nb STM junction at mK temperatures (see Chapter 7). However, we see additional spiked features in the phase diffusive supercurrent that cannot be explained by the quasi-classical picture presented here. In order to understand these features, it is necessary to consider a quantum description of the electromagnetic environment and the junction. In the next two Sections I provide a brief description of the aspects of the model that are relevant to my experiment.

6.7 The Caldeira-Leggett model

In order to fully describe the behavior of a tunnel junction that is coupled to a dissipative electromagnetic environment, a quantum mechanical treatment of the circuit is necessary. The basic idea for the Caldeira-Leggett model involves coupling the degrees of freedom of the tunnel junction, Q and ϕ , to the degrees of freedom of a circuit representing the environment [145, 146]. The starting point of this theory is recognizing that an L - C circuit is a harmonic oscillator, which may be shown as follows. If $V = Q/C$ is the voltage across a junction that is shunted by capacitance C , then a phase ϕ may be defined via

$$\phi(t) = \frac{e}{\hbar} \int_{-\infty}^t V(t') dt'. \quad (6.38)$$

This is essentially the ac Josephson equation, except that here the charge carriers are quasiparticles with charge e rather than Cooper pairs with charge $2e$. To develop a quantum mechanical description of this system, we consider ϕ , V and Q as operators which satisfy the commutation relation $[\phi, Q] = ie$. The Hamiltonian for this system may be written as

$$H = \frac{\tilde{Q}^2}{2C} + \frac{1}{2L} \left(\frac{\hbar}{e} \tilde{\phi} \right)^2. \quad (6.39)$$

Here, $\tilde{\phi}$ and \tilde{Q} describe phase and charge measured relative to their mean values, and are given by $\tilde{\phi}(t) = \phi(t) - e/\hbar Vt$, and $\tilde{Q} = Q - CV$. The first term in the Hamiltonian is the charging energy of the junction capacitor, and the second term is the potential energy stored in the inductor.

In the Caldeira-Leggett model, the environment is described as N such harmonic oscillators (L - C circuits) that have a distribution of resonant frequencies that all couple to the phase of the junction. The Hamiltonian for this environmental coupling is given by

$$H_{\text{env}} = \frac{\tilde{Q}^2}{2C} + \sum_{n=1}^N \left[\frac{q_n^2}{2C_n} + \left(\frac{\hbar}{e} \right)^2 \frac{1}{2L_n} (\tilde{\phi} - \phi_n)^2 \right] \quad (6.40)$$

The first term is the charging of the junction capacitor C and the second term sums over all the environmental degrees of freedom in the circuit, with $N \rightarrow \infty$.

This Hamiltonian formulation is essentially phenomenological rather than microscopic, and has to fulfill the requirement that the reduced dynamics are described correctly in the classical limit [141].

6.8 $P(E)$ theory

6.8.1 Overview

$P(E)$ theory is a quantum-mechanical treatment of phase fluctuations in ultra-small junctions. It was first introduced to describe single-electron charging effects such as the Coulomb blockade [131], and to calculate charge transfer rates in ultra-small normal junctions [139]. The formalism was later used to describe phase fluctuations in Josephson junctions [132, 140, 141, 158]. In this Section, I focus on the latter as it is directly relevant to my experiments, *i.e.*, a Nb-Nb STM junction at 30 mK, with a capacitance of ~ 1 fF, which gives a charging energy $E_C/k_B \approx 1$ K.

I first consider a system with normal metal junctions. The Hamiltonian for the junction electrodes and its electromagnetic environment is

$$H = H_0 + H_{\text{env}} + H_T, \quad (6.41)$$

where H_0 describes the quasiparticle Hamiltonian for the two electrodes, H_{env} describes the environment which can be modeled using the Caldeira-Leggett model described in Section 6.7, and H_T describes quasiparticle tunneling in the junction.

The quasiparticle Hamiltonian is given by

$$H_0 = \sum_{k\sigma} (\epsilon_k + eV) c_{k\sigma}^\dagger c_{k\sigma} + \sum_{q\sigma} \epsilon_q c_{q\sigma}^\dagger c_{q\sigma}, \quad (6.42)$$

where the quasiparticles with wave vectors k and q have energies ϵ_k and ϵ_q respectively. The first and second sum correspond to the left and right electrodes, with the energies shifted with respect to each other by eV to account for a voltage bias.

The tunneling Hamiltonian is the same as the conventional one, except for the additional operator $e^{-i\phi}$ [132, 141, 158]

$$H_T = \sum_{kq\sigma} T_{kq} c_{q\sigma}^\dagger c_{k\sigma} e^{-i\phi} + H.C. \quad (6.43)$$

I note that ϕ and $Q = (-ie)d/d\phi$ are conjugate variables that satisfy $[\phi, Q] = ie$, and that Q acts effectively as a “translation” operator changing the junction charge by e ,

$$e^{i\phi} Q e^{-i\phi} = Q - e. \quad (6.44)$$

In the limit of large tunnel resistance, *i.e.*, $R_T \gg h/4e^2$, we may assume that the states on the two electrodes mix weakly as the tunneling matrix element is inversely proportional to R_T . If we also assume that the system is in charge equilibrium, *i.e.*, that the time between tunneling processes is larger than the charge relaxation time, then the tunneling rate can be calculated perturbatively using Fermi’s Golden Rule,

$$\Gamma_{i \rightarrow f} = \frac{2\pi}{\hbar} |\langle f | H_T | i \rangle|^2 \delta(E_i - E_f), \quad (6.45)$$

where the initial state $|i\rangle$ and final state $|f\rangle$ are equilibrium states.

In a Josephson junction, we can replace the tunneling hamiltonian with the Josephson Hamiltonian, and ignore quasiparticle tunneling to lowest order. The Hamiltonian then reduces to [132]

$$H = H_{\text{env}} - E_J \cos(\phi), \quad (6.46)$$

where H_{env} in Eq. (6.46) describes a JJ coupled to environmental modes, and is

given by

$$H_{\text{env}} = \frac{Q^2}{2C} + \sum_{n=1}^N \left[\frac{q_n^2}{2C_n} + \left(\frac{\hbar}{e} \right)^2 \frac{1}{2L_n} \left(\frac{\phi}{2} - \frac{e}{\hbar} Vt - \phi_n \right)^2 \right]. \quad (6.47)$$

and

$$E_J \cos(\phi) = \frac{E_J}{2} e^{-i\phi} + H.C. \quad (6.48)$$

I note that the operator $e^{-i\phi}$ now changes the charge Q on the junction by $2e$ (rather than by e as in the quasiparticle case). Hence we may write $[\phi, Q] = 2ie$, and $e^{i\phi} Q e^{-i\phi} = Q - 2e$. This process is related to the tunneling of a Cooper pair across the junction, which is expressed in the Hamiltonian via the phase difference between the superconducting wave functions in each electrode. When $E_J \ll E_C$, this term can be treated perturbatively.

The tunneling rate Γ_{\uparrow} in the superconducting case can again be calculated from Fermi's golden rule, and one finds [141]

$$\Gamma_{\uparrow}(V) = \frac{E_J^2}{4\hbar^2} \int_{-\infty}^{+\infty} dt \exp\left(i \frac{2e}{\hbar} Vt\right) \left\langle e^{2i\phi(t)} e^{-2i\phi(t)} \right\rangle \quad (6.49)$$

where $\tilde{\phi}$ is the fluctuating part of the phase as previously defined. The thermal average is taken with respect to the environment partition function: $\text{Tr}[\exp(-H_{\text{env}}/k_B T)]$.

The correlation function may then be expressed as [141]

$$\left\langle e^{2i\phi(t)} e^{-2i\phi(t)} \right\rangle = J(t). \quad (6.50)$$

The tunneling rate may be written in terms of this correlation function [141]

$$\Gamma_{\uparrow}(V) = \left(\frac{\pi E_J^2}{2\hbar} \right) P(2eV) \quad (6.51)$$

where the probability that a tunneling Cooper pair emits energy E to the environment is given by

$$P(E) = \frac{1}{2\pi\hbar} \int_{-\infty}^{+\infty} \exp \left[J(t) + \frac{i}{\hbar} Et \right] dt. \quad (6.52)$$

The symmetry of the circuit demands that $\Gamma_{\uparrow}(V) = \Gamma_{\downarrow}(-V)$, where Γ_{\uparrow} is the tunneling from the electrode 1 to electrode 2, and Γ_{\downarrow} is the tunneling from electrode 2 to electrode 1. The total Cooper pair current is then given by

$$I_S(V) = 2e(\Gamma_{\uparrow}(V) - \Gamma_{\downarrow}(V)) = \frac{\pi e E_J^2}{\hbar} (P(2eV) - P(-2eV)) \quad (6.53)$$

Eq. (6.53) says that the supercurrent is directly related to $P(E)$. Thus measuring the I - V curve of an ultra-small Josephson junction can reveal frequency dependent dissipation to the junction's environment.

The $P(E)$ theory incorporates interactions between the junction and its environment in a natural way by building on the Caldeira-Leggett model. Furthermore, the $P(E)$ results are far more general than the classical phase diffusion case, which was restricted to overdamped junctions in an Ohmic environment. The theory can be used to calculate the supercurrent behavior of a junction for any E_J/E_C ratio, and for any model environment $Z(\omega)$. It reduces to the classical case for $Z_{\text{env}} = R$, and for $\rho^2 E_J \ll E_C$ [158].

6.8.2 Supercurrent peaks due to environmental resonances

Examples of electromagnetic environments are circuits with one or more lumped circuit elements ($Z_{\text{env}} = i\omega L$, $Z_{\text{env}} = 1/i\omega C$), or L - C or R - C transmission lines [141]. My own experimental setup however is perhaps more closely modeled as a finite L -

C transmission line terminated by a load resistance R_L [132]. A transmission line may be modeled as an L - C ladder with inductance per unit length given by L_0 , and capacitance per unit length given by C_0 (see Fig. 6.5).

The case of a junction connected to a transmission line has been presented in Ref. [132]. The treatment is complicated and here I will list only the important parameters used in the model, and present the resulting expression for $P(E)$ [132] calculated in the limit $T = 0$. The key parameters in the analysis are:

1. The characteristic resistance and wave velocity of an infinite transmission line are $R_\infty = (L_0/C_0)^{1/2}$ and $u = (L_0C_0)^{-1/2}$, respectively.
2. The load resistance R_L terminating the transmission line is described by the dimensionless ratio $\rho = R_L/R_\infty$
3. The ratio between the load resistance R_L and the impedance R_∞ of an infinite L - C transmission line $r = R_L/R_\infty$
4. The $\lambda/4$ resonance frequency can be written as $\omega_0 = (\pi/2)(u/l)$ where it is expressed in terms of the length l of the transmission line.
5. The ratio $\kappa = \omega_0/\omega_R$ where $\omega_R = 1/R_\infty C$ is the cutoff frequency due to the capacitance of the junction.
6. For a given frequency ω , ν is the dimensional frequency given by $\nu = \omega/\omega_0$.

The impedance of the transmission line has poles at $\nu = \nu_n$ and the residues of these poles are z_n given by

$$z_n = -\frac{i}{r} \frac{R_L}{\kappa + (\pi/2)(1 + \kappa^2 \nu_n^2)}. \quad (6.54)$$

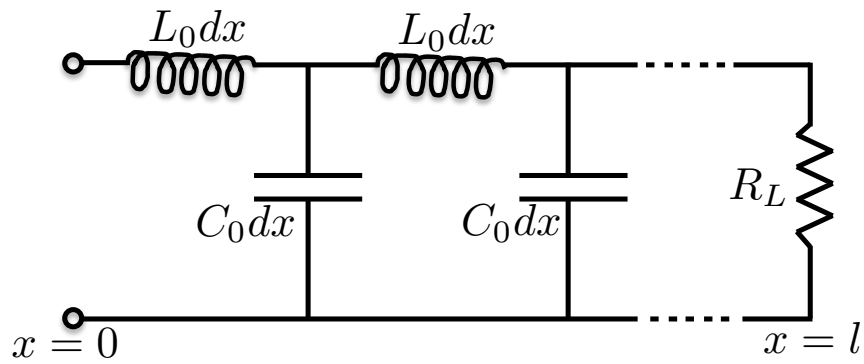


Figure 6.5: Schematic circuit model of a finite transmission line of length l terminated by a load resistance R_L . The inductance and capacitance per unit length are L_0 and C_0 , respectively.

The expression for $P(E)$ then becomes

$$P(E) = \frac{\rho}{E_C} (\pi\rho)^{2\rho-1} \Gamma(1-2\rho) e^{-2\rho\zeta} \times \text{Re} \left\{ i e^{-2i\pi\rho} \sum_{k=0}^{\infty} \frac{1}{k!} \sum_{n_1, \dots, n_k}^{\infty} \left[\prod_{j=1}^k \left(-\frac{2\pi i z_{n_j}^*}{R_Q \nu_{n_j}^*} \right) \left(\frac{E - \hbar\omega_0 \sum_{j=1}^k \nu_{n_j}^*}{E_C} \right)^{2\rho-1} \right] \right\}, \quad (6.55)$$

where the constant ζ contains details about the frequency dependence of the total impedance, and is given by

$$\zeta = \gamma + \int_0^{\infty} \frac{d\omega}{\omega} \left[\frac{\text{Re} Z_t(\omega)}{\rho R_Q} - \frac{1}{1 + (\pi\rho\hbar\omega/E_C)^2} \right]. \quad (6.56)$$

Here $\gamma \approx 0.5772$ is Euler's constant, and Z_t is the effective impedance of the junction capacitance in parallel with the external impedance given in Eq. (6.23). The first sum in Eq. (6.55) counts the total number k of excitations in a mode of the $\lambda/4$ resonance. The second sum denotes which of the modes, n_j are excited.

Although Eq. (6.55) for $P(E)$ is formidable, it nevertheless provides some intuition of the physics involved. The term within the product that is raised to the power $2\rho - 1$ describes energy exchanged between the junction and the environment via the emission of k quanta, *i.e.*, $\hbar\omega_0 \sum_{j=1}^k \nu_{n_j}^*$. The positions of the peaks in the I - V characteristic depend entirely on the poles within the product, as determined by the frequency ν . The probability of losing energy to a particular mode is given by the area under the peak at the mode frequency. This depends on the circuit parameters R_L and R_{∞} .

Although the circuit and junction parameters that correspond to our STM are not precisely known, the I - V curves generated using the model can be remark-

ably similar to those I observed in the Nb-Nb junction in our millikelvin STM. For example, Figs. 6.6-6.9 show calculated I - V curves for various circuit and junction parameters. For Fig. 6.6 and Fig. 6.7, I evaluated Eq. (6.55) for a transmission line with fundamental frequency $f = \omega_0/2\pi = 9$ GHz, 3 environmental modes coupled to an ultra-small junction with capacitance $C_J = 5 \times 10^{-14}$ F, and a critical current of $I_c = 1$ nA. The panels show I - V curves for various load resistances ranging from 1-75 Ω with transmission line impedances of $R_\infty = 50 \Omega$, $R_\infty = 75 \Omega$, $R_\infty = 100 \Omega$, and $R_\infty = 500 \Omega$ for Figs. 6.6(a), 6.6(b), 6.7(a) and 6.7(b) respectively. In each case, the supercurrent was clearly suppressed, with a peak current between 7 and 30 pA, depending on the ratio $r = R_L/R_\infty$.

In the model the excitations between the junction and the environmental modes may be denoted by $(a \ b \ c)$, where a, b , and c are the number of quanta emitted to each mode [132]. The junction is most likely to emit energy to the first mode, and so the first and highest peak on either side of 0 V in the I - V characteristic corresponds to emission denoted by $(1 \ 0 \ 0)$. This is typically followed by followed by $(2 \ 0 \ 0)$ and then $(0 \ 1 \ 0)$. The interplay between the junction and environmental parameters could make it more likely to emit two quanta to the first mode than 1 to the second, *etc.*

It is clear from comparing the peak current in plots 6.6(a), 6.6(b) and 6.7(a) that the smaller the value of r , the greater the supercurrent suppression. However, we can see from 6.7(b) that this effect is reversed for very large R_∞ , and conclude that the effect of this parameter is non-trivial. Additionally, I would like to note that Eq. (6.55) was calculated at $T = 0$. The width of the peaks at $T > 0$ is likely

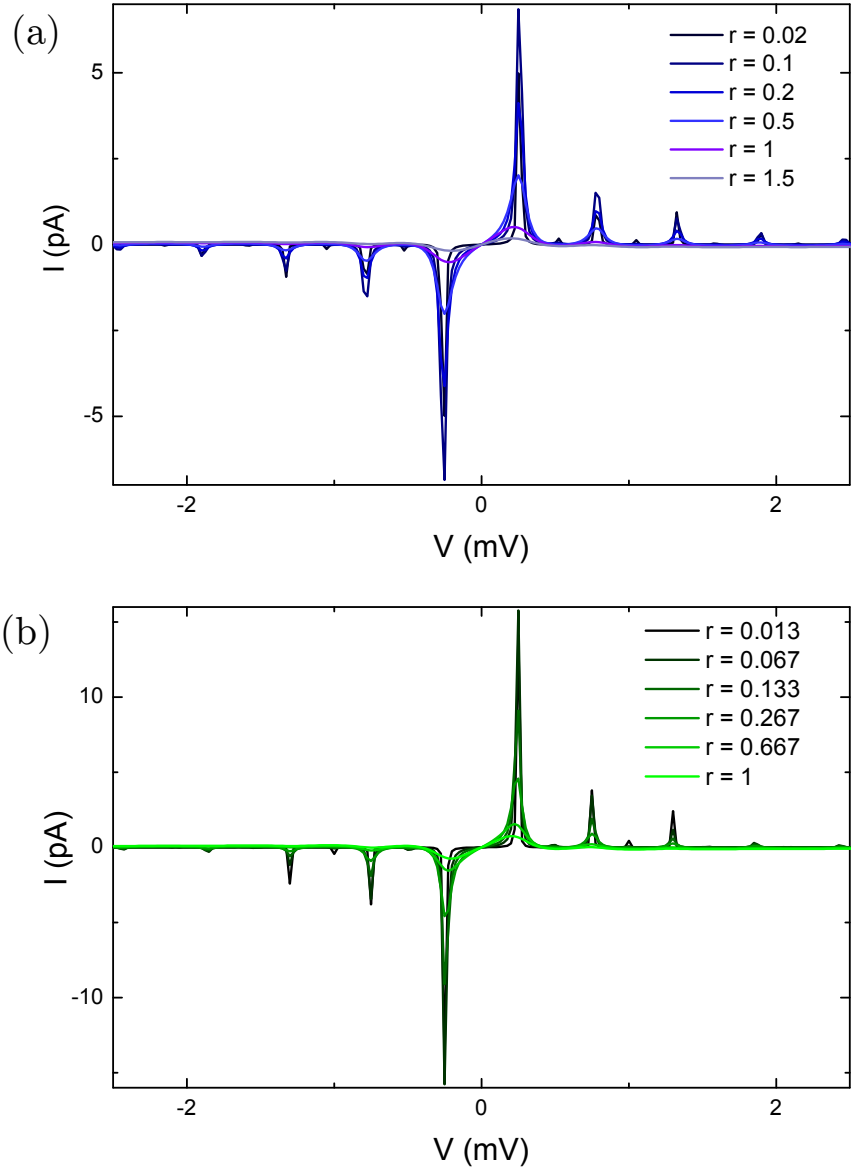


Figure 6.6: I - V curves generated by modeling the environment as a finite transmission line with 3 modes ($k = 3$) that couple to an ultra-small junction with capacitance 50 fF and non-phase-diffusive critical current $I_c = 1$ nA. The parameters used for the plots are (a) $R_\infty = 50 \Omega$, (b) $R_\infty = 75 \Omega$. Each graph shows plots for load resistances $R_L = 1, 5, 10, 40, 50$, and 75Ω . The $\lambda/4$ frequency used for the transmission line is 9 GHz.

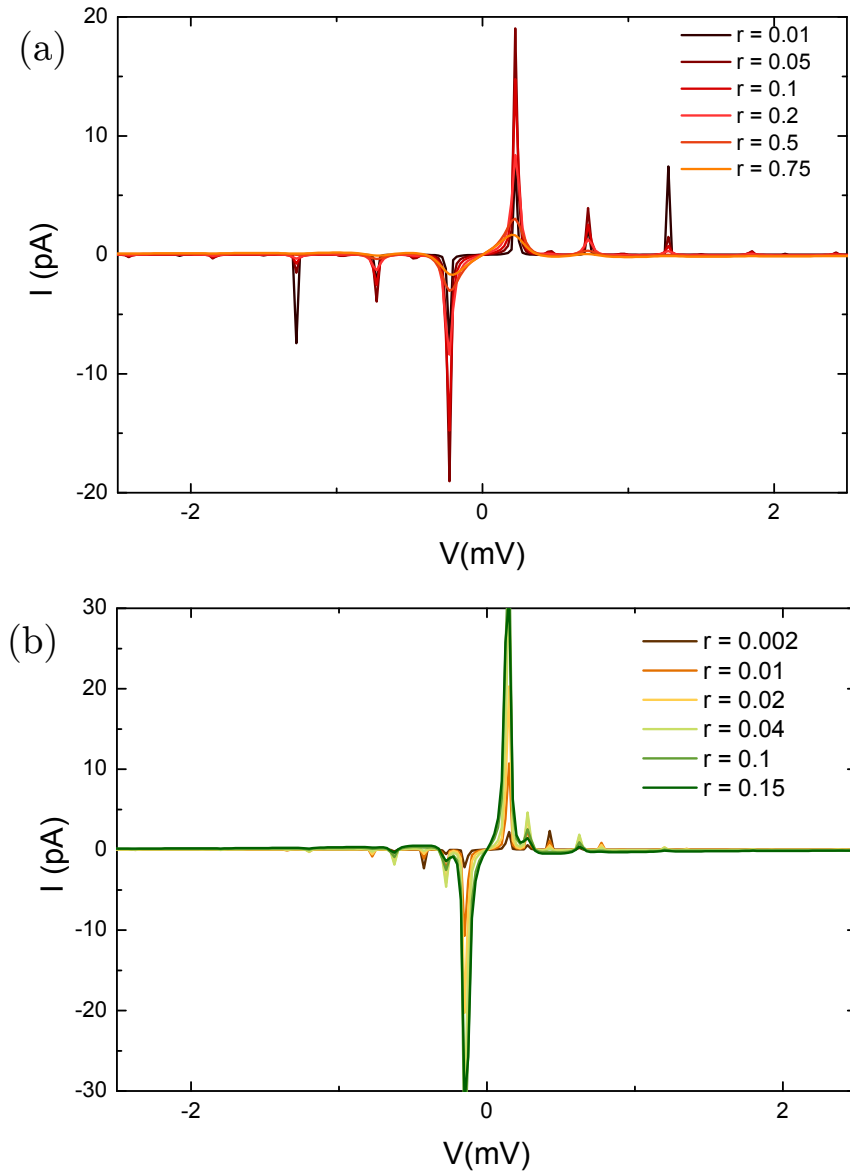


Figure 6.7: I - V curves generated by modeling the environment as a finite transmission line with 3 modes ($k = 3$) that couple to an ultra-small junction with capacitance 50 fF and non-phase-diffusive critical current $I_c = 1$ nA. The parameters used for the plots are (a) $R_\infty = 100 \Omega$, and (b) $R_\infty = 500 \Omega$. Each graph shows plots for load resistances $R_L = 1, 5, 10, 40, 50$, and 75Ω . The $\lambda/4$ frequency used for the transmission line is 9 GHz.

to be greater due to thermal smearing. Furthermore, a non-zero temperature might also affect the I - V characteristic in a non-trivial way if it additionally affects the probability that the junction will release energy into the various modes.

Figures 6.8 (a) and (b) show that the effect of doubling the resonant frequency of the transmission line doubles the spacing between the peaks in the I - V curve because the resonant frequency determines the dissipation channels in the system's environment. It should be noted that in general, a transmission line has multiple resonances, leading to a superposition of peaks in the I - V characteristics.

Finally, Figure 6.9 shows I - V curves generated by modeling the environment with (a) 3 modes and (b) 1 mode. Since the number of available dissipation channels depends on the number of modes in the transmission line, the peaks corresponding to dissipation to the 2nd and 3rd modes are absent in panel (b). The main peak in the I - V curve in panel (b) thus shows the probability of dissipating 1 quantum of energy to the single available mode, a far smaller peak corresponding to 2 quanta to the mode, and an extremely small peak representing the dissipation of 3 quanta to the mode. The spacing between the peaks reflects the difference in energy between 1, 2 and 3 quanta.

6.8.3 Photon-assisted incoherent tunneling of Cooper pairs

I now consider the response of an ultra-small junction in the phase diffusive regime to microwave photons. A macroscopic junction responds to microwaves in a phase coherent manner by exhibiting Shapiro steps [151]. The response of a

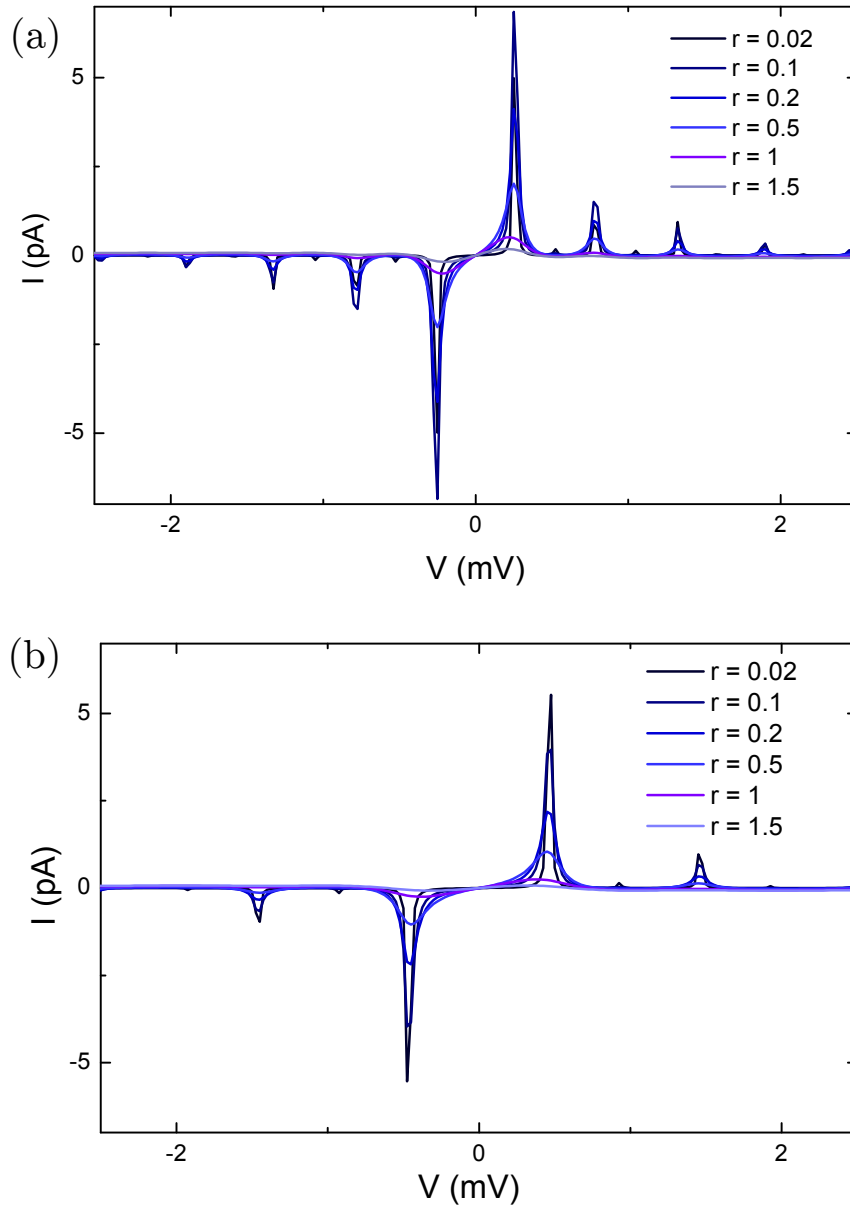


Figure 6.8: I - V curves generated by modeling the environment as a finite transmission line with 3 modes ($k = 3$) that couple to an ultra-small junction with capacitance of 50 fF, and non-phase-diffusive critical current $I_c = 1$ nA. The two panels differ only in the $\lambda/4$ frequency used for the transmission line: (a) $f = 9$ GHz, and (b) $f = 18$ GHz. The plots show that the mode frequency determines the energies at which the peaks appear.

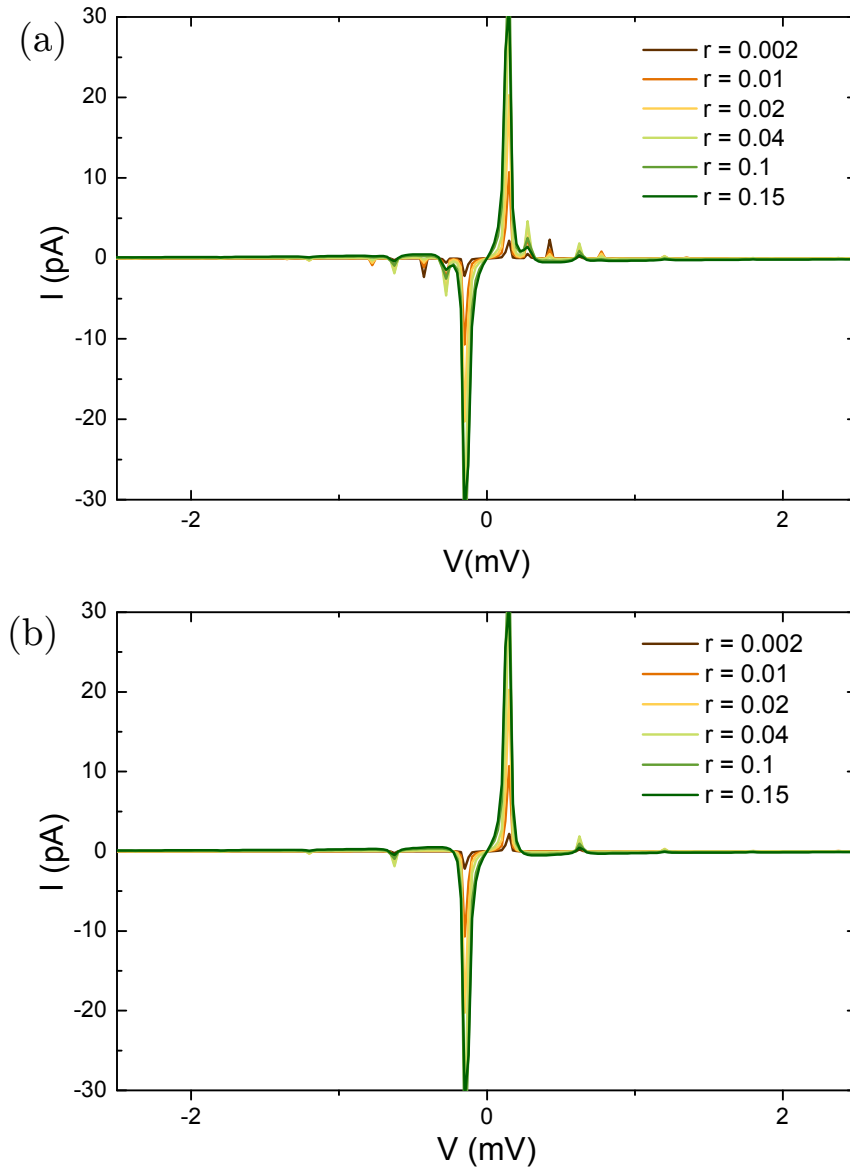


Figure 6.9: I - V curves generated by modeling the environment as a finite transmission line with a fundamental frequency $f = \lambda/4 = 9$ GHz, and $R_\infty = 500 \Omega$ that couples to an ultra-small junction with capacitance 50 fF, and non-phase-diffusive critical current $I_c = 1$ nA. The two panels differ in the number of modes k in the transmission line that couple to the junction. (a) Plots generated with $k = 3$ modes and (b) $k = 1$ mode.

Josephson junction to an ac voltage in the phase-diffusive limit was first considered by Falci *et al.* [140], as an extension of the $P(E)$ theory. The effect of microwaves was considered by setting the voltage across the junction to

$$V(t) = V_0 + V_1 \cos(\Omega t) \quad (6.57)$$

where V_0 is the dc bias voltage, $\Omega/2\pi$ is the frequency of the applied microwaves, and V_1 is the voltage amplitude of the microwaves across the junction. I omit Falci *et al.*'s derivation and simply quote the important result that there will be a net current or average dc current,

$$\bar{I}_s = \sum_{k=-\infty}^{\infty} J_k^2(2\nu) I_s \left[V_0 - \frac{k\hbar\Omega}{2e} \right], \quad (6.58)$$

where $\nu = eV_1/\hbar\Omega$, and J_k is the k^{th} Bessel function. The conductance can be calculated from Eq. (6.58) and is given by

$$G = \frac{d\bar{I}_s}{dV_0} = \sum_{k=-\infty}^{\infty} J_k^2(2\nu) \frac{dI_s}{dV} \left[V_0 - \frac{k\hbar\Omega}{2e} \right]. \quad (6.59)$$

The current in Eq. (6.58) is generated not by the Josephson effect (the coherent tunneling of Cooper pairs), but rather by the incoherent tunneling of Cooper pairs that have absorbed k photon(s) of energy $\hbar\Omega$. Figure 6.10 shows a grey-scale plot of the normalized conductance G/G_{rms} generated for increasing microwave amplitudes of frequency $\Omega/2\pi = 5.6$ GHz. Here G_{rms} for each line is the root mean square deviation of all the points in that line. The first line of the plot is the conductance curve generated in the absence of microwaves by the $P(E)$ theory. Figure 6.10(a) was generated for circuit parameters $R_\infty = 50 \Omega$, so that $r = 1$, while Fig. 6.10(b) has $R_\infty = 500 \Omega$, so that $r = 0.1$. The other parameters were $k = 3$, $C_J = 5 \times 10^{-15}$ F,

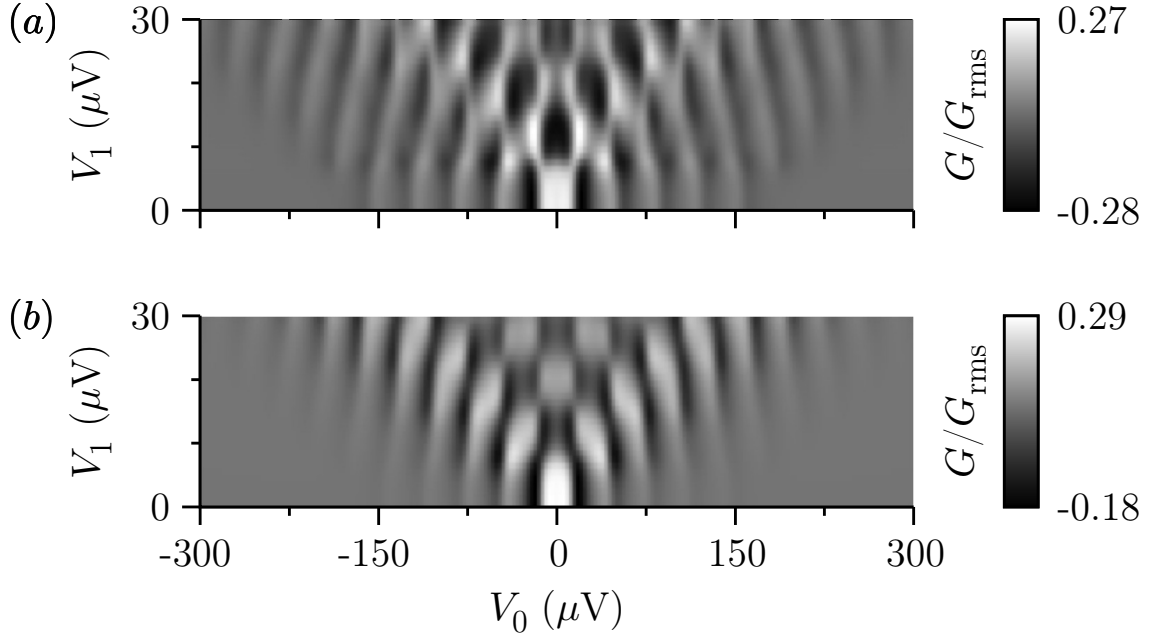


Figure 6.10: Gray scale plot of normalized conductance G/G_{rms} vs. V of the supercurrent response to increasing amplitudes (V_{ac}) of microwave radiation ($\Omega/2\pi = 5.6$ GHz), as predicted by Eq. (6.58). The circuit parameters chosen were resonant frequency $f = 9$ GHz, number of coupled modes $k = 3$, junction capacitance $C_J = 5$ fF, critical current $I_c = 1$ nA, and load resistance $R_L = 50 \Omega$. The parameters for each plot were (a) $R_\infty = 50 \Omega$ so that $r = 1$, and (b) $R_\infty = 500 \Omega$ so that $r = 0.1$. Bright spots are high conductance regions (peaks) and the dark spots are low conductance regions (dips) in the conductance curves.

$I_c = 1$ nA, and $R_L = 50$. The bright areas are high conductance regions (peaks) and the dark spots are negative conductance regions (dips) in the dI/dV curves. The bright spots are separated on the x -voltage scale by $\hbar\Omega/2e$, indicating that the Cooper pairs tunnel into distinct energy states.

6.9 Conclusions

In this Chapter, I have summarized the factors governing the dynamics of fluctuation-dominated tunneling in small capacitance Josephson junctions coupled to a low-impedance environment. In the next Chapter, I present data that was taken with our millikelvin STM in this regime and compare my results to the theory.

Chapter 7: Measurements of Photon-Assisted Incoherent Cooper Pair Tunneling in a Josephson STM

7.1 Introduction

STM studies with superconducting tips and samples are relatively rare, and all the studies reported to date have apparently been conducted at temperatures between 2.1 and 4 K [24, 113, 114]. At extremely low junction resistances these experiments have yielded minute zero bias conductance peaks that match the classical fluctuation dominated form theoretically predicted in the limit of small junction capacitance and critical current, as described in Section 6.6 [28, 29, 31, 114, 153]. These s-shaped I - V characteristics are smooth and display no evidence of resonant tunneling due to single charge effects as predicted by $P(E)$ theory at $T = 0$ (see Chapter 6). This is not surprising given that the instruments used in these studies operate in the 2-4 K range, and likely have significantly higher noise temperatures. Furthermore, direct proof that the charge carriers in these experiments are Cooper pairs rather than quasiparticles has not been demonstrated.

In this Chapter, I present measurements obtained with Nb tips and a Nb(100) sample in our millikelvin STM that are consistent with $P(E)$ theory as described

in Section 6.8.2. Our junction's effective temperature of ~ 185 mK corresponds to an energy resolution that is lower by at least a factor of 10 than previous superconducting STM studies. At these temperatures our STM displays dissipation due to resonant pair tunneling with loss due to the ultra-small STM junction exchanging energy with the electromagnetic environment it is embedded in. Furthermore, by irradiating the STM junction with microwaves, I observed photon assisted incoherent pair tunneling that shows that the charge carriers in an STM S-I-S junction at small biases are Cooper pairs with a charge of $2e$.

7.2 Resonant tunneling

Figure 7.1 shows a topographic image of a Nb(100) sample taken with a Nb tip. The sample was prepared by heating it to $\sim 600^\circ$ C for 10-12 hours at a time for 9 consecutive days with 2 keV Ar ions. Once most of the polishing grains had been removed, the sample was sputtered with 1keV Ar ions at a temperature of 600° C for a 2-3 hours before transferring it into the STM.

Figure 7.2 shows a series of I - V characteristics and corresponding conductance curves measured with a Nb tip on the Nb sample in Fig. 7.1 at 30 mK and at tunnel resistances ranging from 1.1 M Ω to 20 M Ω . The tunnel resistance for each curve was determined by setting the bias voltage to 2 mV, and fixing the set point tunnel current to a value, for example 0.1 nA to yield a tunnel resistance of 20 M Ω . The feed back was then disabled to keep the tip-to-sample distance fixed. The voltage was swept from -1 to 1 mV, and the I and dI/dV values recorded for points 5 μ V

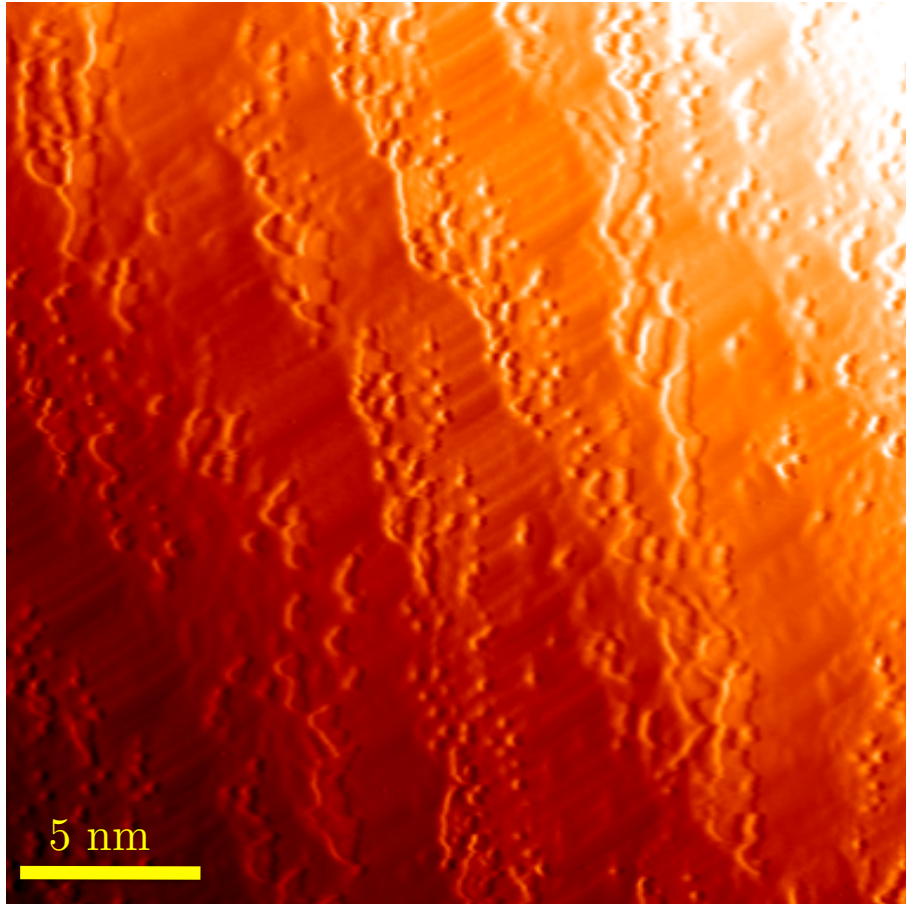


Figure 7.1: Topographic image of Nb(100) sample scanned with a Nb tip, at a bias voltage of $V = 100$ mV, and a tunnel current of $I = 100$ pA.

apart. The feedback was then turned on, the junction resistance changed by fixing a new current set point, and the process repeated for current values between 0.1 and 2 nA to get the corresponding tunnel resistances.

The data in Fig. 7.2 is in strong qualitative agreement with the curves generated using the $P(E)$ theory described in Section 6.8.2. In the theory, the positions of the peaks on the x -axis are determined by the resonant frequencies of the normal modes of the circuit that the junction is embedded in. We may think of these as dissipation channels, *i.e.*, tunneling Cooper pairs lose energy at these frequencies via the emission of microwave photons into resonant modes of the circuit. We measured similar I - V and dI/dV characteristics at a dozen or more locations on the sample shown in Fig. 7.1. The positions of the peaks on the x -axis—corresponding to the energies at which dissipation occurred—were remarkably consistent. This indicates that in this case the dissipation was independent of the sample, and is consistent with our analysis that our data is explained by coupling between the STM junction and resonant modes of the circuit.

Quantitative differences between the theory and the data are inevitable because the precise electrical nature of our circuit is unknown. Although the model described in Chapter 6 assumed a finite transmission line terminated by a load resistance R_L , our circuit could be better modeled by several transmission lines with load impedances Z_L that have reactive components. Furthermore, the theory was calculated for $T = 0$ K, whereas the temperature of our STM junction is between 30 and 180 mK. Nevertheless, our data appears to be well described by the $P(E)$ theory. In order to confirm this I performed an experiment to measure the junction's

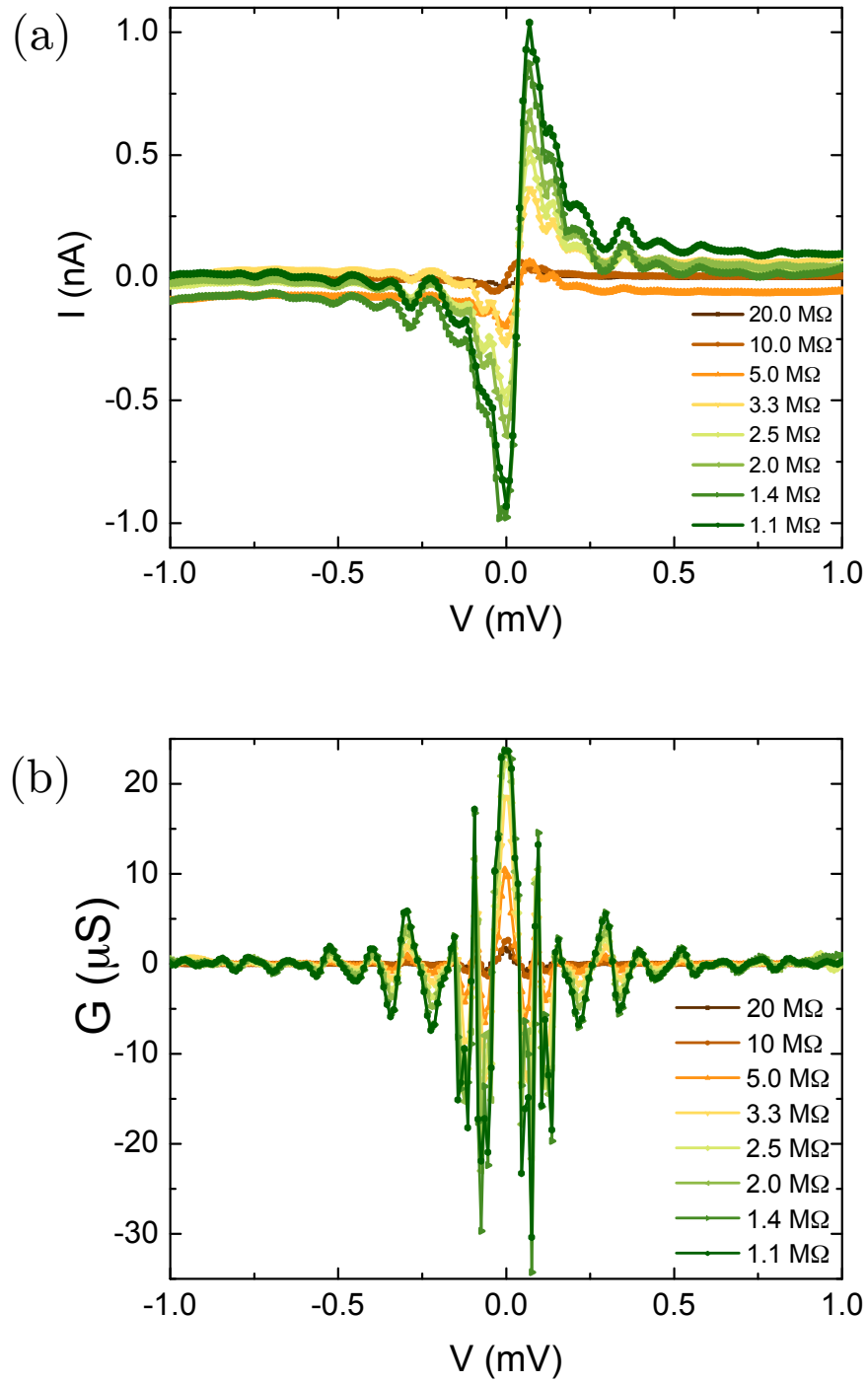


Figure 7.2: (a) I vs. V and (b) corresponding lock-in measurement of normalized conductance G/G_n measured at 30 mK with a Nb tip and Nb(100) sample at different tunnel resistances. The tunnel resistances were set at 2 mV.

response to microwave photons, as described in Sections 7.3 and 7.4.

7.3 Photon assisted quasiparticle tunneling

Photon assisted quasiparticle tunneling has been studied extensively in S-I-S junctions and in single electron transistors (SETs) over the last four decades [159–165]. In a junction driven by microwaves of frequency Ω the time averaged quasiparticle current is given by [140]

$$\bar{I}_{\text{qp}} = \sum_{k=-\infty}^{\infty} J_k^2 \left[\frac{eV_1}{\hbar\Omega} \right] I_{\text{qp}} \left[V_0 - \frac{k\hbar\Omega}{e} \right], \quad (7.1)$$

where V_1 is the amplitude of the ac voltage across the junction due to the microwaves, V_0 is the dc bias voltage, J_k is the k^{th} Bessel function, and I_{qp} is the quasiparticle current when no microwaves are applied. The effect of microwave radiation can be interpreted as causing a splitting of an unirradiated energy level with energy ϵ into levels $\epsilon \pm k\hbar\Omega$, that correspond to the absorption or emission of k photons. The probabilities of tunneling into each state is given by $J_k^2[eV_1/\hbar\Omega]$. While a smooth ohmic I - V curve will exhibit no features in response to microwave radiation, a non-ohmic I - V characteristic with sharp features will respond under microwave radiation by developing features shifted by $\pm k\hbar\Omega/e$ from the original positions along the voltage axis.

7.4 Photon assisted incoherent pair tunneling

Photon assisted Cooper pair tunneling is qualitatively similar to the quasiparticle case discussed in Section 7.3. However, for Cooper pairs, the sharp features

seen in the presence of microwaves will be shifted by $\pm k\hbar\Omega/2e$, which is one half the spacing of the quasiparticle case. The microwave response may thus be used to discern the charge of the carriers responsible for the tunneling current. The equation for the Cooper pair current through a junction driven by microwaves at frequency Ω is given by

$$\bar{I} = \sum_{k=-\infty}^{\infty} J_k^2 \left[\frac{2eV_1}{\hbar\Omega} \right] I_s \left[V_0 - \frac{k\hbar\Omega}{2e} \right], \quad (7.2)$$

where I_s is the Cooper pair current in the absence of microwaves, V_1 is the amplitude of the microwave voltage across the junction, V_0 is the dc bias voltage, and J_k is the k^{th} Bessel function. This lends itself to a physical interpretation similar to the quasiparticle case; peaks in the $I(V)$ characteristic are generated due to the absorption and stimulated emission by Cooper pairs of k photons with probability J_k^2 .

In order for an individual Cooper pair to emit or absorb microwave photons, charge coherence is required. This is relatively easily obtained in an ultra-small STM junction for $C \approx 1$ fF and $I_c < 1$ nA, and subject to voltage fluctuations that destroy phase coherence. If we want to apply Eq. (7.1) and (7.2) to distinguish pairs from quasiparticles, a second requirement is the presence of sharp features in the I - V curve, as well as the energy resolution necessary to resolve them. The former are expected from $P(E)$ theory if the junction is connected to bias leads that have transmission line resonances. If the bias circuit can be modeled, $P(E)$ theory can be used to calculate the probability of an ultra-small capacitance junction dissipating energy E via resonant coupling between the STM junction and electromagnetic

modes [131, 132].

7.4.1 The incoherent vs. coherent junction response to microwaves

I note that phase coherence present in macroscopic Josephson junctions prevents individual Cooper pairs from emitting and absorbing photons. For a classical macroscopic junction, the phase ϕ can be treated as a well-defined classical variable. In this limit a synchronization of the junction's Josephson frequency with the incident microwaves produces Shapiro steps, as described in Section 6.4 [151].

While the coherent supercurrent behavior of Shapiro steps has its roots in the ac Josephson effect, the junction dynamics captured by our STM are due to the absorption and stimulated emission of microwave photons by individual Cooper pairs. One way to distinguish the two phenomena experimentally, is by measuring variations in the current as a function of applied microwave power. The current in the case of incoherent pair tunneling is proportional to J_k^2 (see Eq. (7.2)), while the height of a Shapiro step varies as just J_k . This is a key point that allowed us to distinguish photon assisted incoherent pair tunneling in our STM from the more traditionally expected Shapiro steps. Also, it should be noted that Shapiro steps on an $I(V)$ curve appear only when microwaves are applied and are truly vertical, whereas the peak-features we see are present at zero power and have widths that are determined by the microwave resonances that cause them.

7.4.2 Incoherent pair tunneling: Microwave amplitude dependence

In this Section I present conductance measurements of the supercurrent response of a Nb-Nb STM junction as a function of microwave amplitude. Microwave radiation was generated by an Agilent N5183A microwave generator and transmitted to the STM cavity via an unfiltered dc thermometer line, which undoubtedly had several impedance mismatches. A Stanford Research SR830 lock-in amplifier was used to obtain conductance $G = dI/dV_0$ vs. V_0 data because they provide a better signal to noise ratio than the I - V_0 curves. The lock-in measurement consists of adding a small sinusoidal voltage $V_m \sin(\omega_m t)$ to V_0 and measuring the amplified current response to the modulation. The modulation frequency $f_m = \omega_m/2\pi$ was set to 1.9 kHz, so that it was much larger than that of the feedback loop, and much smaller than that of the microwaves applied, and thus would interfere with neither. For each set of measurements, the amplitude of the modulation V_m was typically chosen to be less than half the difference between two successive bias voltage measurements. For example, when I took a curve with 500 measurements at equally spaced voltages between $V_0 = 1$ mV and $V_0 = -1$ mV, the difference in bias voltage between any two successive points was $0.4 \mu\text{V}$. The amplitude V_m for such a data set was fixed at 0.1 or $0.2 \mu\text{V}$. Each measurement was typically averaged over 30-60 milliseconds, and the entire conductance curve typically took ~ 10 seconds to measure.

I found that the microwave amplitude “seen” by the junction was extremely frequency dependent, which was not surprising given the line we used. For the

most part, frequencies above 7.9 GHz did not result in a measurable change in the current through the STM junction, although I was able to obtain one data set at 8.5 GHz. The peaks at frequencies below 3.8 GHz were difficult to resolve because I was limited by the energy resolution of our STM. Furthermore, the power of the applied microwaves that produced a junction response had to be greater than 0 dBm at the source in order to produce a measurable effect at any frequency, suggesting a significant attenuation in our experimental setup.

Figure 7.3 shows a series of conductance curves taken with a Nb tip [98] and a Nb(100) sample. The STM junction was driven by 5.6 GHz microwaves. Starting with zero microwave power, each successive curve was measured at source microwave amplitudes (V_{ac}) that increased in steps of 25 mV from 0 to 3 V. The frequency and amplitude of the lock-in signal were carefully chosen so that they would not interfere with the measurement as described above. Figure 7.3 shows that as the microwave amplitude increased, additional peaks appear in the conductance curve separated by voltages of $V_0 = \hbar\Omega/2e$. Each horizontal line corresponds to a single conductance curve, divided by the standard deviation G_{rms} of that curve. The peaks are high conductance regions, and the dips are negative conductance regions. The zeros of the conductance in between the peaks and valleys correspond to peaks in the $I-V$ curve. According to $P(E)$ theory these are due to pair tunneling events with the absorption or stimulated emission of energy $n\hbar\Omega/2e$ that occur with probability proportional to $J_n^2(2eV_1/\hbar\Omega)$.

Figure 7.4 shows false color plot that illustrate the normalization and bias offset correction of the data. Figure 7.4(a) shows a false color plot of the raw con-

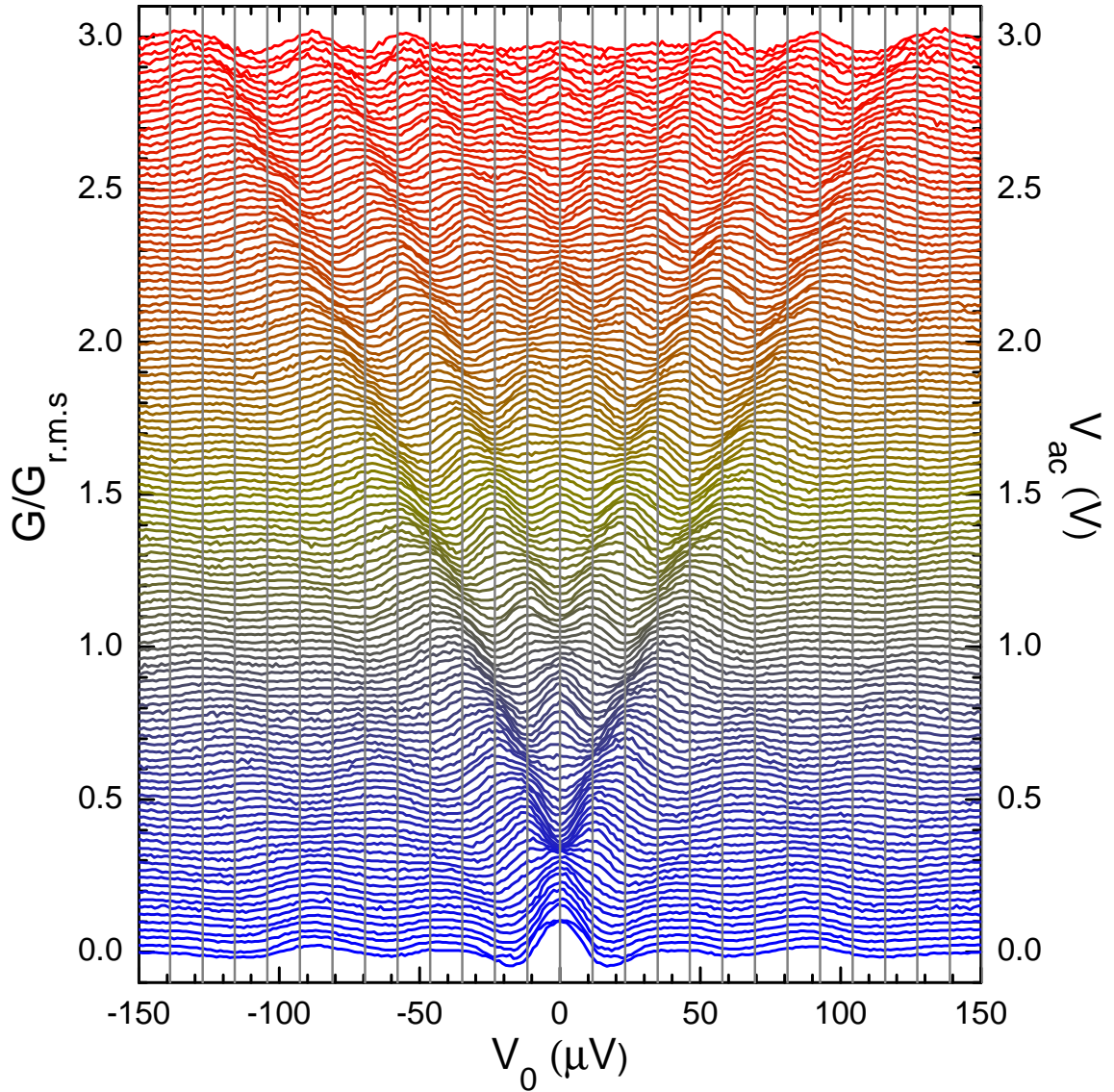


Figure 7.3: Measured conductance G divided by G_{rms} versus bias voltage V_0 taken at 30 mK with the outer tip Nb-Nb STM junction under irradiation by 5.6 GHz microwaves. The amplitude of the applied voltage V_{ac} varies from 0 V (blue) to 3.0 V (red) in steps of 0.1 V. Successive curves are offset by 0.025 V on the y -axis. Vertical grey lines are spaced $\Delta V_0 = \hbar\Omega/2e = 11.6 \mu\text{V}$ apart and coincide with emerging peaks in conductance, indicating that the charge of the carriers is $2e$.

ductance data corresponding to Fig. 7.3. The lightest yellow parts depicting peaks in conductance, and the darkest navy blue parts depicting dips. Figure 7.4(b) shows a false color plot of the same data, with each line divided by its standard deviation G_{rms} . By comparing Figs. 7.4(a) and 7.4(b), one can see that “normalizing” each curve in this way makes it easier to follow features from one curve to the next. Figure 7.4(c) shows a false color plot of the normalized data set with the offset in bias voltage on the x -axis removed for each line. Again, this was done to aid comparisons between curves.

Figure 7.5(a) is the false color plot shown in Fig. 7.4(c), presented again to allow comparison with Fig. 7.5(b), which shows the expected response of the STM junction based on Eq. (7.2). To generate the simulated plot in Fig. 7.5(b), I used the first line of conductance data, measured in the absence of microwaves, to generate each successive line by applying the derivative of Eq. (7.2) with respect to V_0 ,

$$G = \frac{d\bar{I}}{dV_0} = \sum_{k=-\infty}^{\infty} J_k^2 \left[\frac{2eV_1}{\hbar\Omega} \right] \frac{dI_s}{dV_0} \left[V_0 - \frac{k\hbar\Omega}{2e} \right]. \quad (7.3)$$

Notice that the Bessel functions in this expression are not a function of bias voltage. Once again, each simulated curve was divided by its standard deviation G_{rms} to allow direct comparison with the data in Fig. 7.5(a). I note that the only parameter that was adjusted to simulate the data was the overall scale factor for $A_\mu = V_1/V_{\text{ac}}$ that determines the ratio of the amplitude of the microwave voltage across the junction compared to the amplitude V_{ac} applied at the source. To generate Fig. 7.5(b), we set $A_\mu = 5.43 \times 10^{-5}$. Comparing Fig. 7.5(b) to the data in Fig. 7.5(a), we see excellent agreement, indicating that the current is due to incoherent pair tunneling

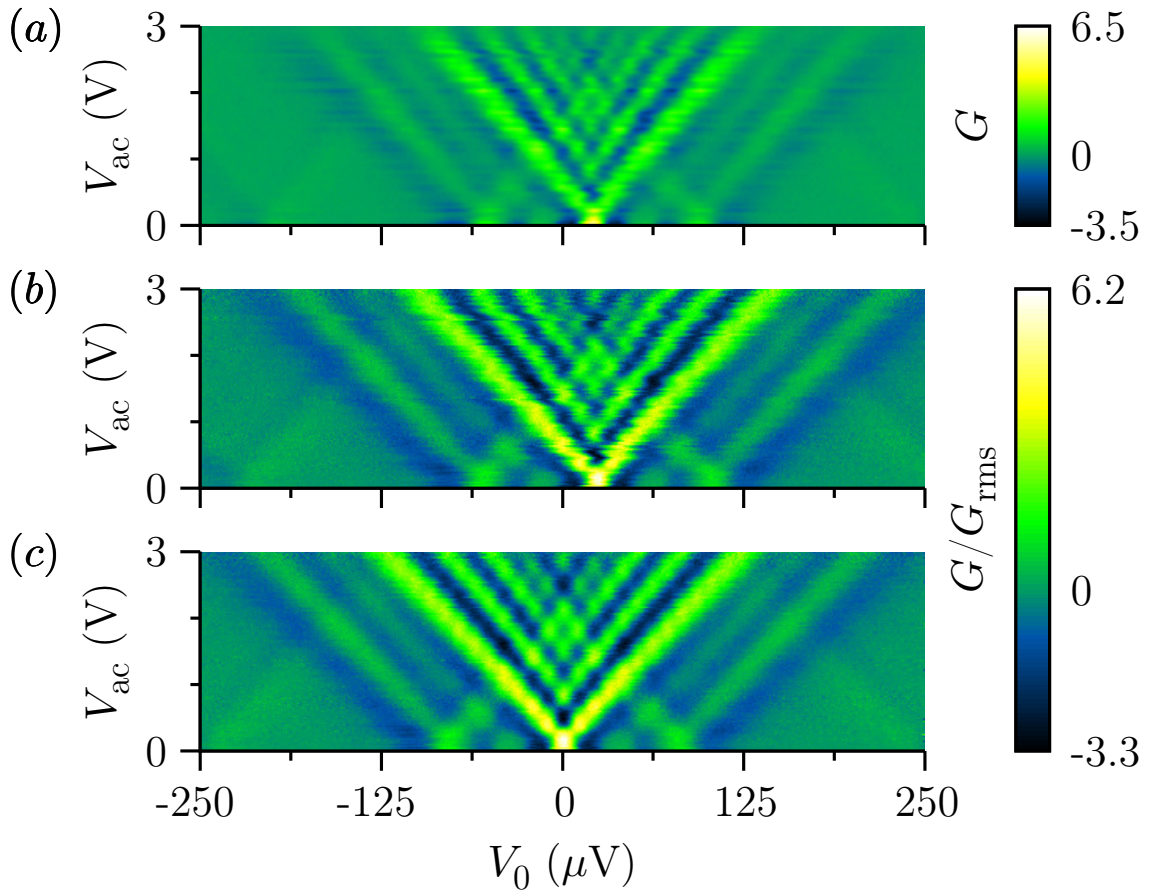


Figure 7.4: (a) False color plot of raw conductance data G versus dc bias voltage V_0 shown in Fig. 7.1. Microwave frequency is 5.6 GHz, and microwave amplitude V_{ac} ranges from 0 to 3 V. Each line corresponds to a conductance curve with yellow representing the positive peaks and dark blue representing the negative dips. (b) False color plot of data shown in (a) with each conductance curve G divided by G_{rms} of that line. (c) False color plot of normalized data shown in (b), with the bias offset corrected for each line.

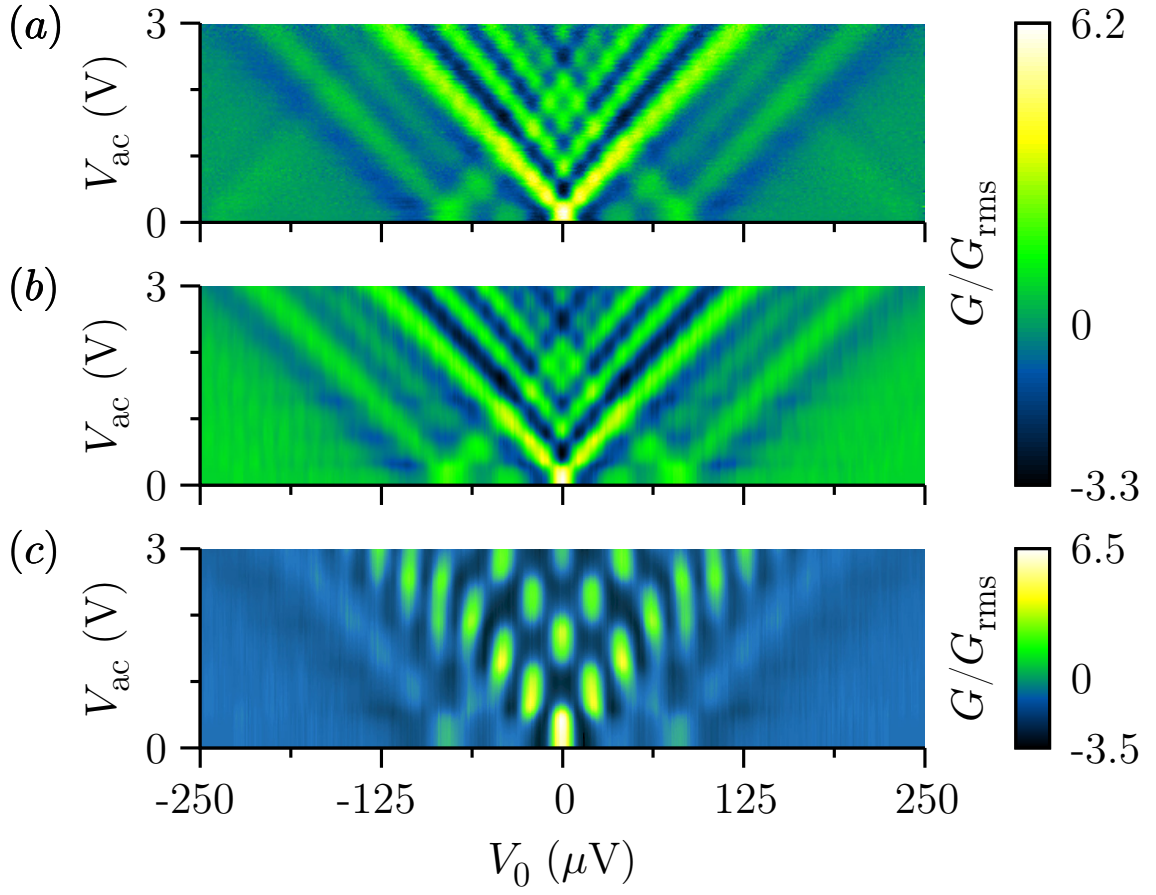


Figure 7.5: (a) False color plot of measured conductance G divided by G_{rms} versus dc bias voltage V_0 in Fig. 7.1. Microwave frequency is 5.6 GHz, and microwave amplitude V_{ac} ranges from 0 to 3 V. (b) Simulated false color plot assuming charge carriers are Cooper pairs. The measured conductance curve in the absence of microwaves and Eq. (7.2) were used to generate each successive curve with $A_\mu = V_1/V_{\text{ac}} = 5.43 \times 10^{-5}$. (c) Simulated false color plot assuming the charge carriers are quasiparticles with charge e . The measured conductance curve in the absence of microwaves and Eq. (7.1) were used to generate each successive curve with with $A_\mu = 5.43 \times 10^{-5}$. The data (a) strongly resembles (b) but not (c).

rather than coherent Shapiro steps. From the data we can also determine that the charge carriers are Cooper pairs because the voltage spacing between the peaks is $\hbar\Omega/2e$. In contrast, Fig. 7.5(c) shows the corresponding simulation assuming the charge carriers are quasiparticles with charge e . The voltage spacing in this case is twice that for Cooper pairs, and disagrees strongly with the data.

We also measured the STM junction's response to microwaves of a higher frequency. Since the voltage spacing between the conductance peaks is expected to scale with frequency, the steps should be easier to resolve provided sufficient power reaches the junction. Figure 7.6 shows a series of normalized conductance curves measured at 8.5 GHz as the applied microwave amplitude V_{ac} was increased from 0 V to 4.0 V at the source. Once again, each measured conductance curve was normalized by dividing it by its standard deviation. The gray lines spaced $\hbar\Omega/2e = 17 \mu\text{eV}$ apart can be seen once again to coincide with the peaks that appear as the microwave amplitude is increased. The corresponding false color map shown in Fig. 7.7(a), and the simulated false color map based on the curve measured at 0 microwave power and Eq. (7.2) is shown in Fig. 7.7(b). For this simulation, I used $A_\mu = 2.36 \times 10^{-5}$

To rule out the possibility of this being a junction specific phenomenon, I used the second Nb tip in our dual-tip STM to confirm the results. Figure 7.8(a) shows a false color plot of conductance measurements taken with the inner STM tip with 8.5 GHz applied microwave radiation, and Fig. 7.8(b) shows the false color plot generated using $A_\mu = 1.63 \times 10^{-5}$. Close comparison of Figs. 7.7(a) (outer tip) and 7.8(a) (inner tip) reveal small differences. Since each tip of our STM is connected

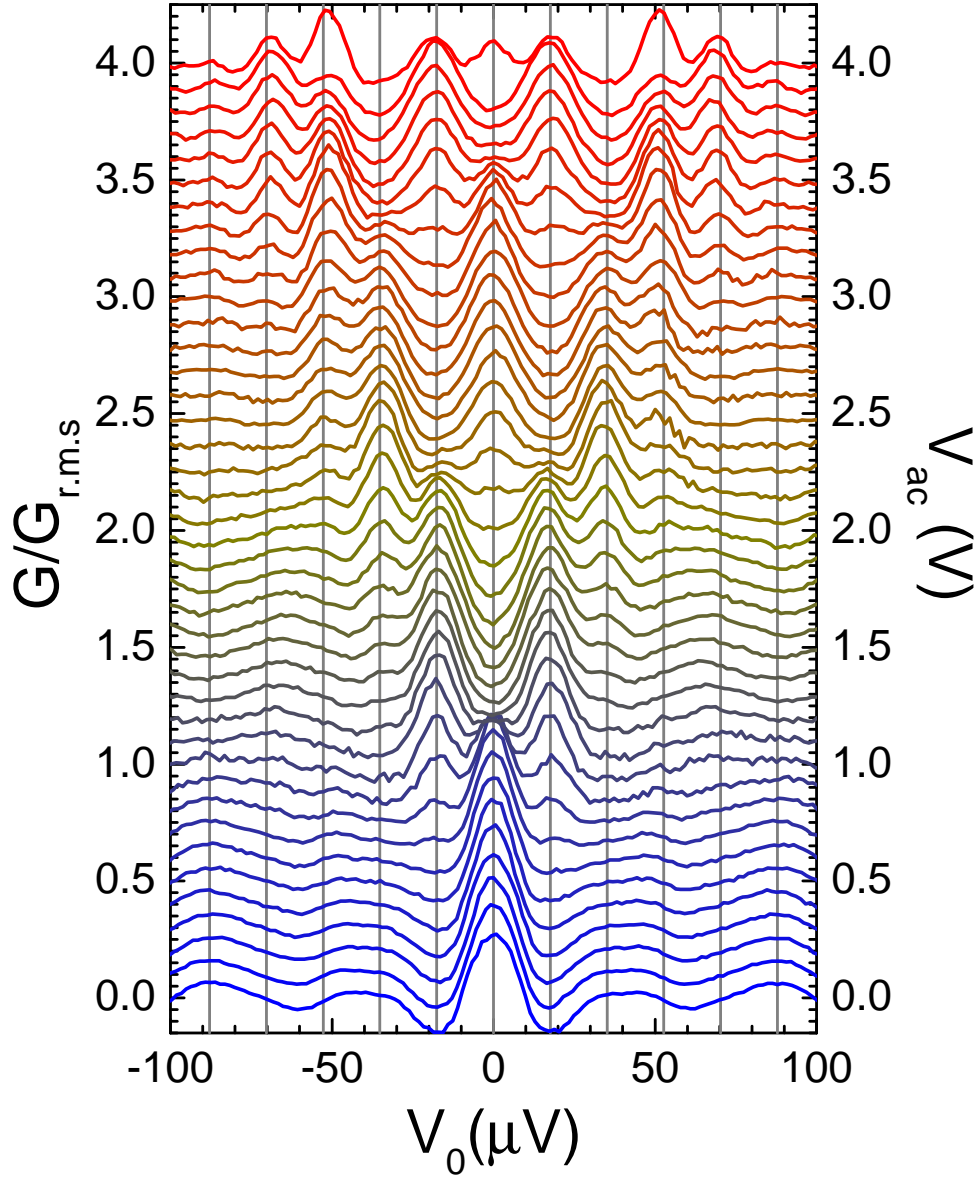


Figure 7.6: Measured conductance G divided by G_{rms} versus bias voltage V_0 taken at 30 mK with the outer tip Nb-Nb STM junction under irradiation by 8.5 GHz microwave radiation. The amplitude of the applied voltage V_{ac} is varied from 0 V (blue) to 4.0 V (red). Successive curves are offset by 0.1 V on the y -axis. Vertical grey lines are spaced $\Delta V_0 = \hbar\Omega/2e = 17 \mu\text{eV}$ apart. They coincide with high-power peaks in conductance, indicating that the charge of the carriers is $2e$.

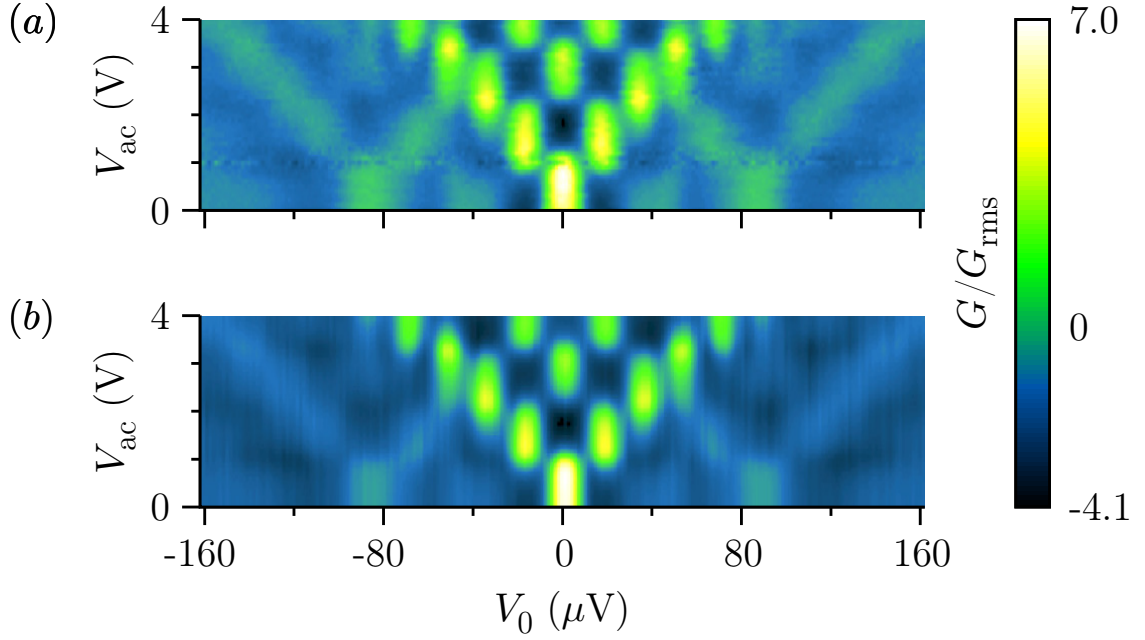


Figure 7.7: (a) False color plot of measured conductance curves G divided by G_{rms} versus bias voltage V_0 . This data is the same as in Fig. 7.4. Data was taken at 30 mK with outer Nb STM tip. Microwave frequency is 8.5 GHz, and microwave amplitude V_{ac} at the source ranges from 0 to 4 V. Each line corresponds to a conductance curve with yellow representing the positive peaks and dark blue representing the negative dips. (b) Simulated false color plot generated using the measured conductance curve in the absence of microwaves and Eq. (7.2) to generate each successive curve with $A_\mu = V_1/V_{ac} = 2.36 \times 10^{-5}$.

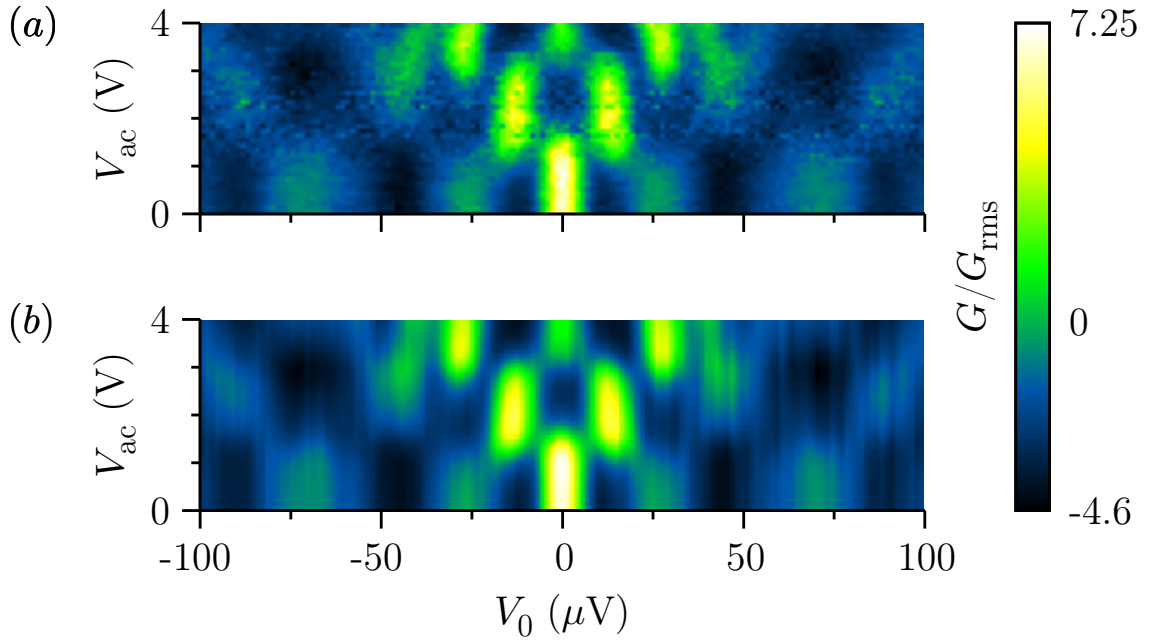


Figure 7.8: (a) False color plot of measured conductance curves G divided by G_{rms} versus bias voltage V_0 . Data was taken at 30 mK with inner STM tip. Microwave frequency is 8.5 GHz, and microwave amplitude V_{ac} ranges from 0 to 4 V. Each line corresponds to a conductance curve with yellow representing the positive peaks and dark blue representing the negative dips. (b) Simulation of false color plot generated using the measured conductance curve in the absence of microwaves and Eq. (7.2) to generate each successive curve with $A_{\mu} = V_1/V_{ac} = 1.63 \times 10^{-5}$

to its own set of current and piezo leads, the resonances and impedance seen by the tips are different, leading to minor differences in the conductance curve measured at zero microwave power. Nevertheless, the phenomenon was remarkably reproducible.

7.4.3 Incoherent pair tunneling: Microwave frequency dependence

In addition to the characterizing the response of the fluctuation-dominated supercurrent to microwave amplitude, I also measured the conductance versus bias voltage as a function of frequency. At most frequencies below 3.8 GHz, changes in conductance were difficult to resolve, and at frequencies above 7.8 GHz, I did not see any change in the conductance even at 25 dBm of applied microwave power. However, within this frequency range, the conductance curves indicated that the microwave amplitude across the junction V_1 varied significantly.

Figure 7.9 shows a gray scale plot of the conductance data, taken between 3.8 and 7.8 GHz. Figures 7.10-7.12 show measured data and fits to theory for some of the lines in the gray scale plot. The fits use Eq. (7.3) and the interpolated curve in the absence of microwaves shown in Fig. 7.10(a). The good agreement between the fit and the data is striking. The main fitting parameter for each curve is $A_\mu = V_1/V_{ac}$. Two other fitting parameters were also used – a small offset in V_0 to compensate for drifts in the bias voltage, and an overall scale factor (y -axis) to compensate for small variations in tunnel resistance from one data-set to the next. The fits yielded microwave amplitudes ranging from to 10-150 μ V at the junction, corresponding to attenuation ratios $A_\mu \sim 10 \times 10^{-6}$ to 35×10^{-6} .

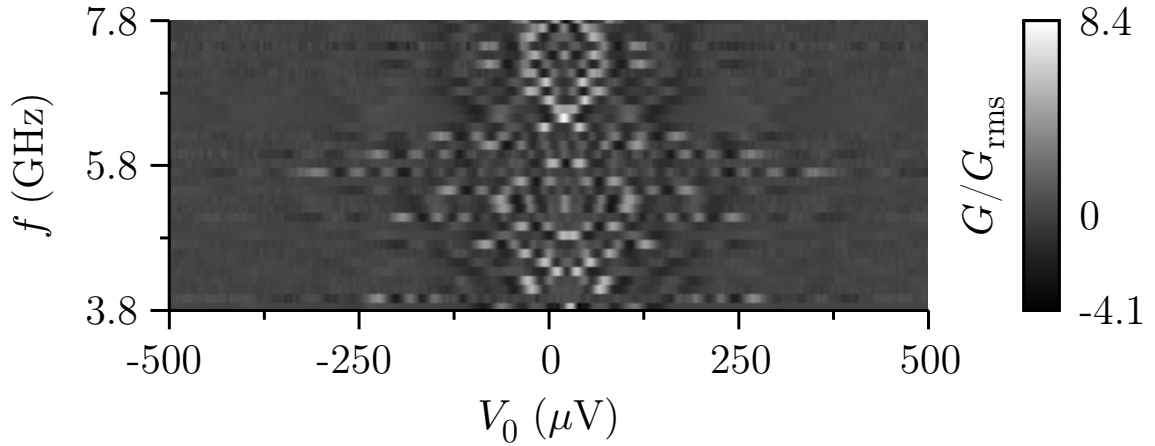


Figure 7.9: Gray scale plot of dI/dV_0 vs. V_0 measurements as a function of the microwave frequency f . Data was taken with the outer Nb tip and Nb(100) sample at 30 mK, and with a source microwave amplitude of $V_{\text{ac}} = 3.976$ V. Each line corresponds to a conductance curve measured at a different frequency with white representing the peaks and dark gray representing the dips. The large variation in peak features indicate that the transmission of microwaves varies greatly with frequency.

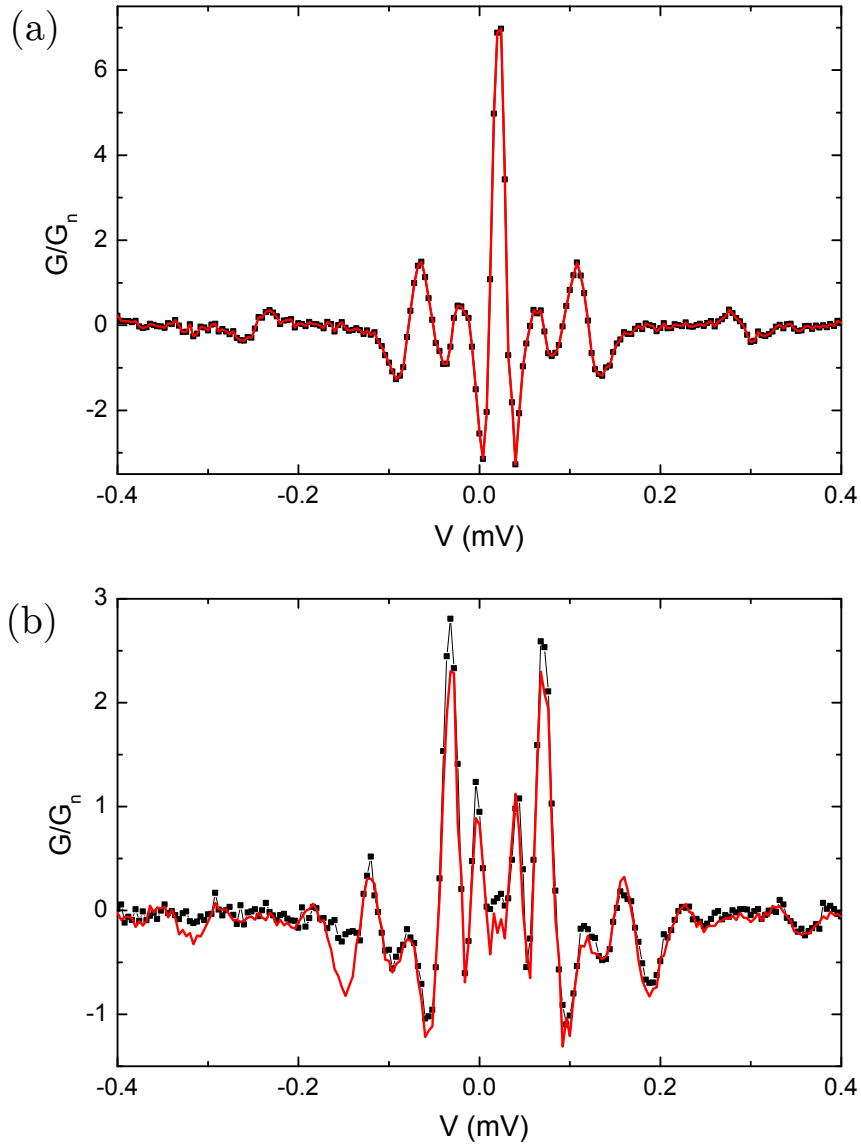


Figure 7.10: (a) Measured conductance G/G_n vs. bias voltage V (black dots) taken with outer Nb tip and Nb(100) sample at 30 mK in the absence of microwaves. The red curve was interpolated from the data. (b) Black points show conductance measurements taken with applied microwave power $P_{ac} = 25$ dBm ($V_{ac} \approx 3.97$ V), and microwave frequency $f = \Omega/2\pi = 4.3$ GHz. The red curve is fit to Eq. (7.3) using the interpolated curve from (a). The fit yielded $V_1 = 64.84 \mu\text{V}$ or equivalently $A_\mu = 16.3 \times 10^{-6}$.

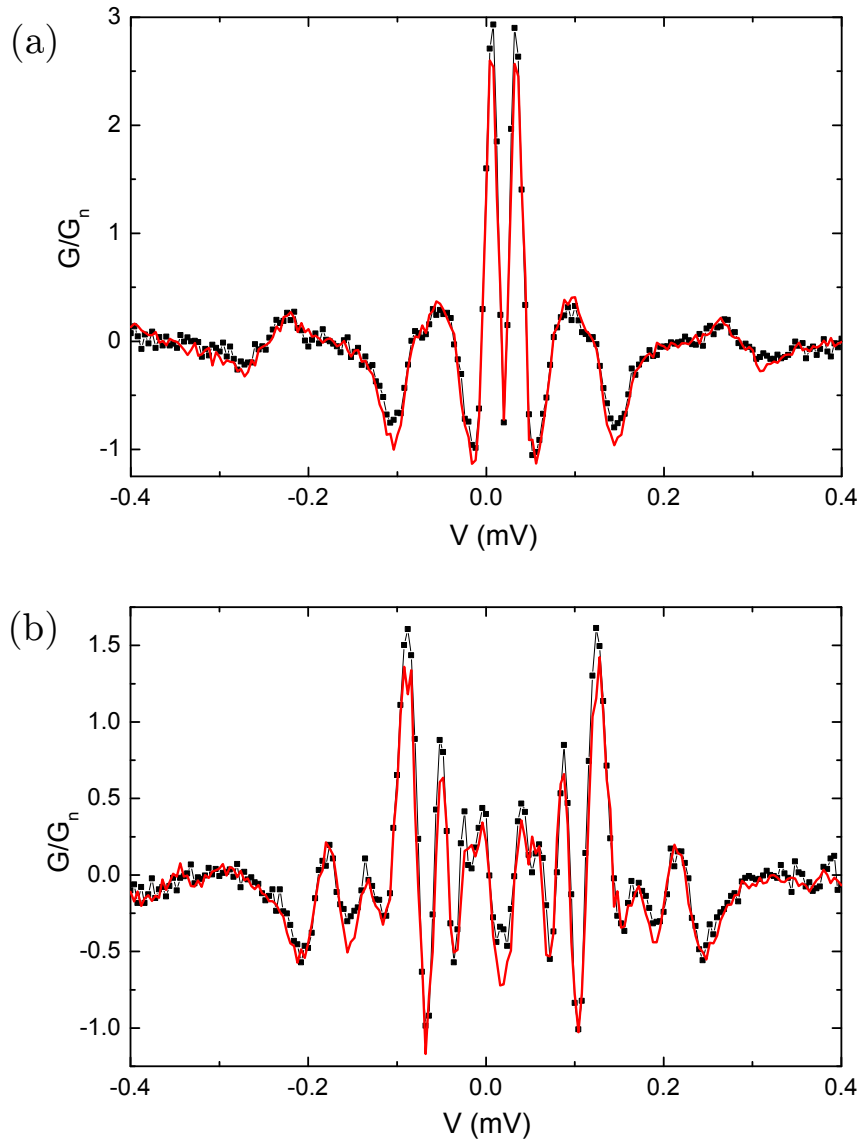


Figure 7.11: Black points show conductance measurements taken with outer Nb tip and Nb(100) sample at 30 mK, and with applied microwave power $P_{ac} = 25$ dBm ($V_{ac} \approx 3.97$ V). The applied microwave frequencies are (a) 4.4 GHz and (b) 4.5 GHz. The red curve is fit to Eq. (7.3) using the interpolated curve from Fig. 7.9(a). The fit yielded $V_1 = 20.78 \mu\text{V}$ ($A_\mu = 5.2 \times 10^{-6}$) and $V_1 = 40.55 \mu\text{V}$ ($A_\mu = 10.2 \times 10^{-6}$) respectively.

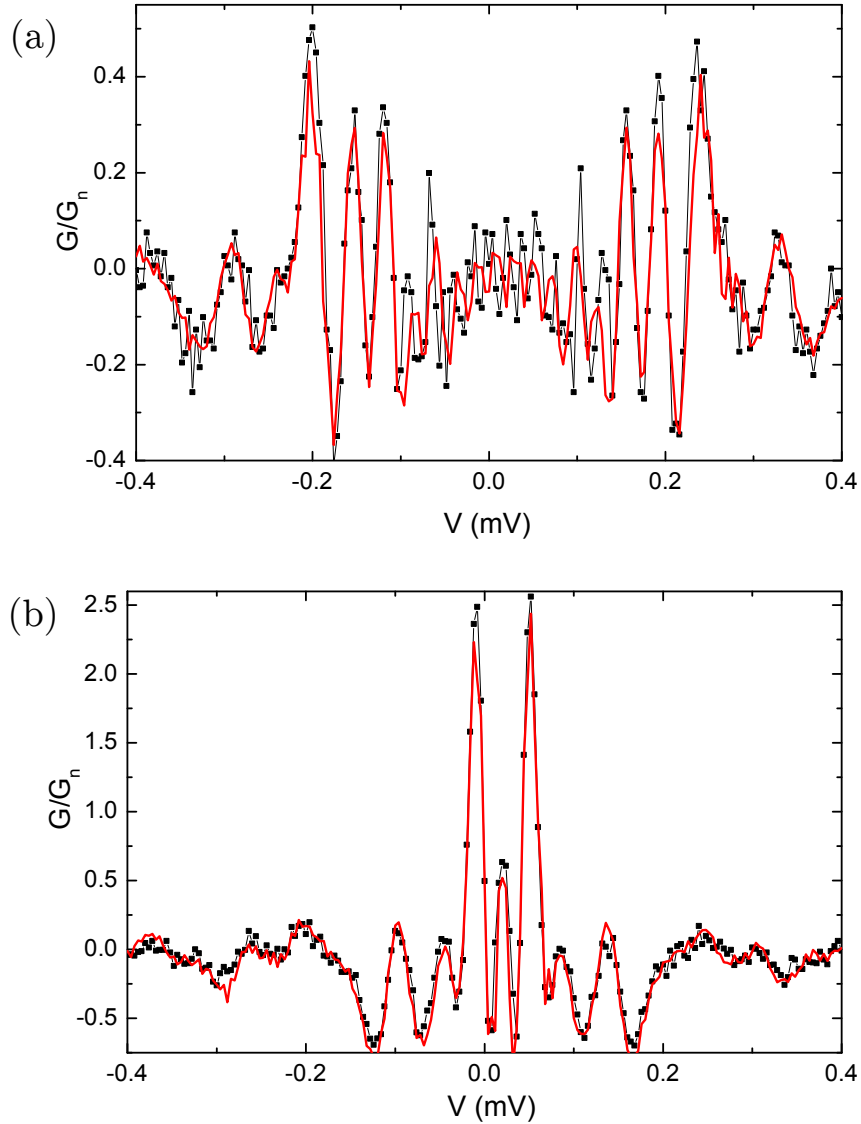


Figure 7.12: Black points show conductance measurements taken with outer Nb tip and Nb(100) sample at 30 mK, and with applied microwave power $P_{ac} = 25$ dBm ($V_{ac} \approx 3.97$ V). The applied microwave frequencies are (a) 4.7 GHz and (b) 5.0 GHz. The red curve is fit to Eq. (7.3) using the interpolated curve from Fig. 7.9(a). The fit yielded $V_1 = 125.91 \mu\text{V}$ ($A_\mu = 31.69 \times 10^{-6}$), and $V_1 = 15.6 \mu\text{V}$ ($A_\mu = 3.92 \times 10^{-6}$) respectively.

7.5 Conclusions

In conclusion, at ultra low temperatures I found that the charge carriers responsible for sharp sub-gap features observed in our superconducting STM were Cooper pairs. Our microwave technique offers the potential to directly identify the charge carriers responsible for specific features, as long as there are sharp voltage-dependent features present in the conductance data. With such sensitivity to the charge of the carriers, one could create novel images. For example, vortex cores, small normal regions, or the effects of single magnetic spins could be probed by mapping out normal and superconducting regions of samples via the presence of carriers with charge e .

My data also indicates that the microwave response of an ultra-small junction may be used to calibrate the microwave voltage V_1 across the junction. As the microwave amplitude is increased, the junction responds in a precise and predictable manner. The data sets measured above could be simulated by manipulating a single parameter $A_\mu = V_1/V_{ac}$. The measurement technique described could also provide a way to attain position-dependent local voltage measurements on a sample, and possibly allow imaging of frequency dependent loss. This could be of interest in studying the effect of molecules or defects that have sharp resonances [166].

Finally, the conductance curves measured in the absence of microwaves lend insight into dissipation channels associated with circuit resonances and other high frequency loss mechanisms. In particular, these results suggest that an ultra-small junction may be used to probe microwave loss and circuit resonances in cryogenic

circuits. When combined with the spatial resolution of an STM, this might pave the way to a novel technique of imaging local nano-scale sources of frequency dependent loss at ultra-low temperatures. Such a technique may be particularly interesting in superconducting qubit research.

Chapter 8: Conclusions

8.1 Summary

In this dissertation I described the design, realization and characterization of a dual tip STM that operates at temperatures as low as ~ 30 mK. I also described a novel plasma based Nb tip fabrication technique that yields STM tips that are superconducting, atomically sharp, and mechanically robust enough to take spectroscopic maps at low tunneling resistances. With these tips I tested the mechanical stability of our mK STM and took spectroscopy data that I used to estimate the effective temperature of the STM junction. Finally, with these Nb tips and a Nb(100) sample, I operated a Josephson STM—*i.e.*, an STM using tunneling Cooper pairs rather than quasiparticles to probe a superconducting sample.

In particular, in Chapter 7 I described how I used the enhanced spectroscopic resolution available at 30 mK to resolve peaks in the fluctuation-dominated supercurrent at sub-gap voltages. My analysis indicated that these peaks in the I - V characteristics are due to the incoherent tunneling of Cooper pairs at resonant frequencies determined by the electromagnetic environment that the junction is embedded in. Such I - V characteristics cannot be explained by the classical phase diffusion model, and it was necessary to use the quantum mechanical $P(E)$ theory

to understand our data.

Finally I was able to identify the charge carriers in this regime as Cooper pairs with charge $2e$, by measuring the response of the STM junction to microwaves. The current in this situation was due to the incoherent tunneling of Cooper pairs. The pairs individually absorb k photons of energy $\hbar\Omega$ where Ω is the frequency of the microwaves.

8.2 Future work

Having characterized the dynamics of fluctuation-dominated pair tunneling in an S-I-S STM junction at millikelvin temperatures, the next major step in the project is to explore how we might stabilize the phase to yield a true supercurrent in our STM. In fact, our instrument was designed to be compatible with modifications that would be necessary to map out the gauge invariant phase difference on the surface of a superconducting condensate. If two superconducting tips are connected via a flexible superconducting wire they form a SQUID loop with a superconducting sample. By coupling the two STM tips in this way, the phase of a single ultra-small Josephson junction (such as that formed by a single superconducting STM tip and sample) may be stabilized enough to produce a true supercurrent. Additionally the second STM tip would provide a reference point against which the gauge invariant phase difference may be measured as a function of position. In the remaining Sections, I discuss the feasibility and design parameters necessary to realize a Josephson phase STM.

8.3 Measuring the gauge-invariant phase difference on a superconducting sample

Ever since the debate over the underlying mechanism producing superconductivity in the high T_c superconductors began in the late 1980's, there has been an interest in phase sensitive experiments that can directly probe the pairing symmetry in these materials. Since then many experiments have probed the anisotropy of the gap by measuring the magnitude of the order parameter [167–171]. However, Van Harlingen *et al.* [172] were the first to probe the relative phase of the order parameter as a function of k -space direction, which unambiguously determined the symmetry of the pairing state in YBCO crystals.

The corner-SQUID experiment was first suggested in the late 1980's [173, 174], and relied on three key ideas. The first was that Josephson tunnel junctions can serve as directional probes of the gauge invariant phase inside the crystal (*i.e.*, they provide a measure of the order parameter perpendicular to the crystal face). The second was that YBCO was expected to display a sign change in the order parameter in the a and b lattice directions if it was a d -wave material. The third key idea was that the phase coherence of the order parameter in a SQUID with two junctions meant that the wave function of the superconducting condensate had to be single-valued. This leads to the phase constraint

$$\phi_a + \phi_b + 2\pi \left[\frac{\Phi}{\Phi_0} \right] + \delta_{ab} = 0, \quad (8.1)$$

where ϕ_a and ϕ_b are the gauge invariant phase differences across the junctions on the

a and b faces of the crystal. The magnetic flux in the loop is given by $\Phi = \Phi_{\text{ext}} + LJ$ where Φ_{ext} is the externally applied flux, and LJ is the flux induced due to the inductance L of the SQUID loop and the circulating current J . The term δ_{ab} is the intrinsic phase shift inside the crystal between the a and b directions. For an s -wave superconductor, $\delta_{ab} = 0$ whereas for a d -wave superconductor $\delta_{ab} = \pi$.

The experiments on YBCO described in references [172, 175, 176] revealed that $\delta_{ab} = \pi$, thus providing direct evidence for the d -wave pairing state in YBCO. Our proposal [33] to use a dual tip STM at millikelvin temperatures to map out the gauge invariant phase difference on superconducting samples built on the idea behind these phase-sensitive dc SQUID experiments. The main difference was that while a pre-fabricated corner dc SQUID is composed of fixed junctions, an STM with two independent tips offers the ability to position the junctions on the sample, and obtain phase data with atomic scale spatial resolution. An STM in which the two tips are connected to form a dc SQUID thus offers the potential for a novel atomic scale phase imaging technique that could be used to map out phase variations across grain boundaries, as well as near magnetic vortices, and single atom defects or other local perturbations.

8.4 Phase stabilization to produce a true supercurrent in a Josephson STM

One of the first questions that needs to be addressed while designing an STM to image atomic scale variations in the order parameter of superconducting samples,

is whether an ultra-small STM S-I-S junction can sustain a true phase-sensitive supercurrent rather than an incoherent supercurrent like feature. In this Section I discuss how the phase of an ultra-small superconducting STM junction at mK temperatures can be stabilized.

8.4.1 Reducing the quantum mechanical uncertainty in the phase

Our approach to reducing the uncertainty in the phase difference across the ultra-small STM junction involves connecting the junction to the second STM tip with a superconducting wire so that they form a SQUID with the sample.

Why this stabilizes the phase across the first tip can be seen by considering the Hamiltonian of the system. For an isolated current biased Josephson junction [33],

$$H = \frac{p^2}{2m} - E_J \cos(\gamma) - \frac{I\Phi_0}{2\pi} \gamma, \quad (8.2)$$

where $p = C(\Phi_0^2/2\pi)d\gamma/dt$, $m = C\Phi_0/4\pi^2$, and $E_J = \Phi_0 I_c/2\pi$. For zero bias, and small excursions of $\tilde{\gamma}$ around the minimum γ_0 in a potential well, the potential is approximately harmonic, and we can write

$$H \approx \frac{p^2}{2m} + \frac{E_J}{2} \tilde{\gamma}^2 \quad (8.3)$$

The energy states of this system are $E_n = (n + \frac{1}{2})\hbar\omega_p$. Here ω_p is the plasma frequency of the junction or 0 to 1 transition frequency and is given by

$$\omega_p = \frac{\sqrt{E_C E_J}}{\hbar} = \sqrt{\frac{2\pi I_c}{\Phi_0 C}} \quad (8.4)$$

At temperatures $T \ll \hbar\omega/k_B$, we expect the system to be in its ground state.

The ground state wave function for a harmonic oscillator is

$$\Psi_0(\gamma) = \frac{m\omega_p}{\pi\hbar} \exp\left(\frac{-m\omega_p\gamma^2}{2\hbar}\right). \quad (8.5)$$

Since p and γ are conjugate variables, they obey the uncertainty principle

$$\sigma_p\sigma_\gamma \geq \frac{\hbar}{2}. \quad (8.6)$$

where σ_p and σ_γ are the uncertainties in the canonical momentum and position, respectively. From Eq. (8.5), one can find that the uncertainty in γ in the ground state is

$$\sigma_\gamma \geq \sqrt{\frac{\hbar}{2m\omega}} = \left(\frac{2e^3}{I_c\hbar C}\right)^{1/4}. \quad (8.7)$$

We note that the uncertainty in γ is inversely proportional to the fourth root of the junction's critical current I_c and capacitance C . For an STM tip of radius 10 nm, at a tunneling distance of 1 nm, with a capacitance of 3×10^{-18} F, and an expected critical current of $I_c = 1$ nA, one finds that the minimum uncertainty is $\sigma_\gamma \approx 4\pi$. Such a large uncertainty in phase results in the supercurrent $I_c\langle\sin(\gamma)\rangle$ being almost completely suppressed.

In order to produce a measurable supercurrent in an STM junction, we need to reduce the uncertainty in γ . Equation (8.7) suggests that this could be done by increasing the capacitance C of the STM junction, the critical current I_c , or both. The STM junction may be approximated as a parallel plate capacitor with a capacitance $C \approx \epsilon_0 A/d$ where A is the area of the junction plates and d is the tip-sample separation. However in an STM setup there is a limited range over which A or d can be adjusted. STMs typically operate at relatively high tunnel resistances

of $\sim 1 \text{ M}\Omega$ – $1 \text{ G}\Omega$, with tip-sample separations of $\sim 1 \text{ nm}$. The tunnel resistance may be lowered by pushing the tip into the sample, but this can damage the sample surface or pick loose atoms off of it that remain on the tip. Since the operation of an STM relies on the STM tip being ultra-sharp with an ideal radius of curvature below 100 nm , it is not a good idea to push the tip into the sample. Increasing the radius of curvature of the STM tip would increase its capacitance, but typically results in reduced spatial resolution while scanning.

To increase the capacitance of the STM junction, one could consider attaching a shunting capacitance C_{shunt} across the ultra-small STM junction, so that the total capacitance of the junction is $C + C_{\text{shunt}}$. One way to do this is by shaping the parts of the tip that are not tunneling to give added capacitance to the sample. However, engineering this with the precision necessary is non-trivial. The junction is formed after the STM tip travels a distance of $\sim 1 \text{ mm}$ into tunneling distance, and one has little control over its final configuration. If the tip has a broad base with a small pointed cone of height $\sim 500 \text{ nm}$, then even slight deviations from a perfectly perpendicular approach will result in the blunter part of the tip (rather than the sharp apex) making tunneling contact with the sample first. Thus STM tips typically have a cone angle of 20 – 40° to ensure that only the very tip of the apex makes tunneling contact with the sample. This is a key requirement for obtaining atomic resolution topographic images with features that are not blurry or doubled. Furthermore, STM tips typically need to be cleaned via field emission before they are used to take data. Field emission is a fairly violent and uncontrolled process that blows off the apex of the tip, leaving behind a new and usually cleaner tip. An

STM tip design will need to take this into account.

An alternate approach that could be used is to effectively increase the critical current I_c through the junction to reduce the uncertainty in phase. One way to do this in effect is by connecting a large junction (the second tip) in parallel with the ultra-small STM junction and connecting them via a superconducting wire to form an asymmetric SQUID loop [19]. This configuration effectively couples the phase of the small junction to the phase of the large junction, much as if the small junction was part of a single junction with a larger critical current. The magnitude of the phase stabilization depends on the coupling strength (inversely proportional to the inductance) between the two junctions and the critical current of the large junction. I will omit the details of the derivation outlined in reference [19], and simply present the key result—the minimum uncertainty in the phase difference γ_1 across the small junction J_1 of the SQUID is [19, 33] is

$$\sigma_\gamma \approx \sqrt{\frac{2e^2}{\hbar}} \left(\frac{C}{L_{J_1}} + \frac{C}{L + L_{J_2}} \right)^{-1/4} = \left(\frac{2e^3}{\hbar I'_c C} \right)^{1/4} \quad (8.8)$$

where the effective critical current of the ultra-small STM junction is given by $I'_c = I_{c_1} + \Phi_0/2\pi L$ for $L_{J_1} \ll L$. Here L_{J_1} and L_{J_2} are the Josephson inductances of the two junctions, and L is the inductance of the circuit. For example, for an STM junction with $I_{c_2} = 1$ nA, increasing the junction capacitance to 6 fF and choosing a large junction with $I_c = 1$ μ A, and a loop inductance $L = 1$ nH, the effective critical current is $I'_c = 0.33$ μ A, and the uncertainty in phase is reduced to $\sigma_\gamma \approx 0.44$ radians, or 25° .

Considering a single ultra-small junction such as that of a single-tip STM, it

is important to note that the above discussion on reducing the quantum uncertainty in the phase γ assumes that the system is in its ground state, which is true if $\hbar\omega_p \gg k_B T$ and there is sufficiently small external noise. In general, the system will be in a superposition of the ground and excited states. Ignoring anharmonicity, the wave function of the n^{th} excited state is

$$\psi_n(x) = \frac{1}{\sqrt{2^n n!}} \left(\frac{m\omega_p}{\pi\hbar} \right)^{1/4} \exp\left(-\frac{m\omega_p x^2}{2\hbar}\right) H_n\left(\sqrt{\frac{m\omega_p}{\hbar}}x\right), \quad (8.9)$$

and $\sigma_\gamma \propto (I_c C)^{-1/4}$ which is the same dependence as the ground state. Thus, designing the system so that the capacitance, critical current, or both are increased still leads to a reduced width (or uncertainty) of γ in higher energy states that would be occupied at non-zero temperatures.

8.4.2 Proof of principle experiment

Before the dual tip mK STM described in this thesis was built, an experiment was done to see if the quantum mechanical uncertainty in the phase difference across a small junction could be reduced by coupling it to a large junction via an inductance. The experiment by Dan Sullivan *et al.* [19] was performed between 30 and 400 mK on the same dilution refrigerator subsequently modified and used for the mK STM. The I - V characteristics of an ultra-small 100 nm, thin-film Al-AlO_x-Al junction were first measured, and seen to exhibit phase diffusion and a greatly suppressed supercurrent. This junction was then connected in parallel with a much larger junction to form a SQUID as shown in Fig. 8.1(a). The switching current I_c versus applied bias flux Φ_a of the SQUID was then measured. To measure the switching

current, the flux in the SQUID was set by applying a fixed current I_Φ to a coil, the bias current I_b was ramped and the current I_c at which the device switched to the voltage state was recorded. This process was repeated $\sim 10^4$ times to yield a switching histogram for a given value of I_Φ . I_Φ was then set to a new value, and the entire process repeated.

Figure 8.1(b) shows the change in the average measured switching current ΔI_c versus the current I_{Φ_a} used to apply flux Φ_a at 50 mK. The modulation in the switching current indicates that the full ~ 1 nA supercurrent through the small junction is adding to or subtracting from the ~ 1 μ A current of the large junction. The data confirmed that while the supercurrent in an ultra-small junction is in fact suppressed due to phase diffusion, it is fully measurable when the junction is part of a SQUID designed with suitable parameters. Even more importantly, the experiment also confirms that the relative phase of the currents through the junctions is measurable, *i.e.* the total current depends on the flux in the SQUID loop.

8.4.3 Reducing thermally induced phase diffusion

Consider again an individual ultra-small junction. Section 8.4.1 addressed the problem of phase diffusion in ultra-small junctions due to the fundamental uncertainty in the phase γ arising from Heisenberg's uncertainty principle. The quantum mechanical uncertainty in phase is present at $T = 0$ as well as at higher temperatures. However, in an experimental setup, the STM junction is not isolated, nor

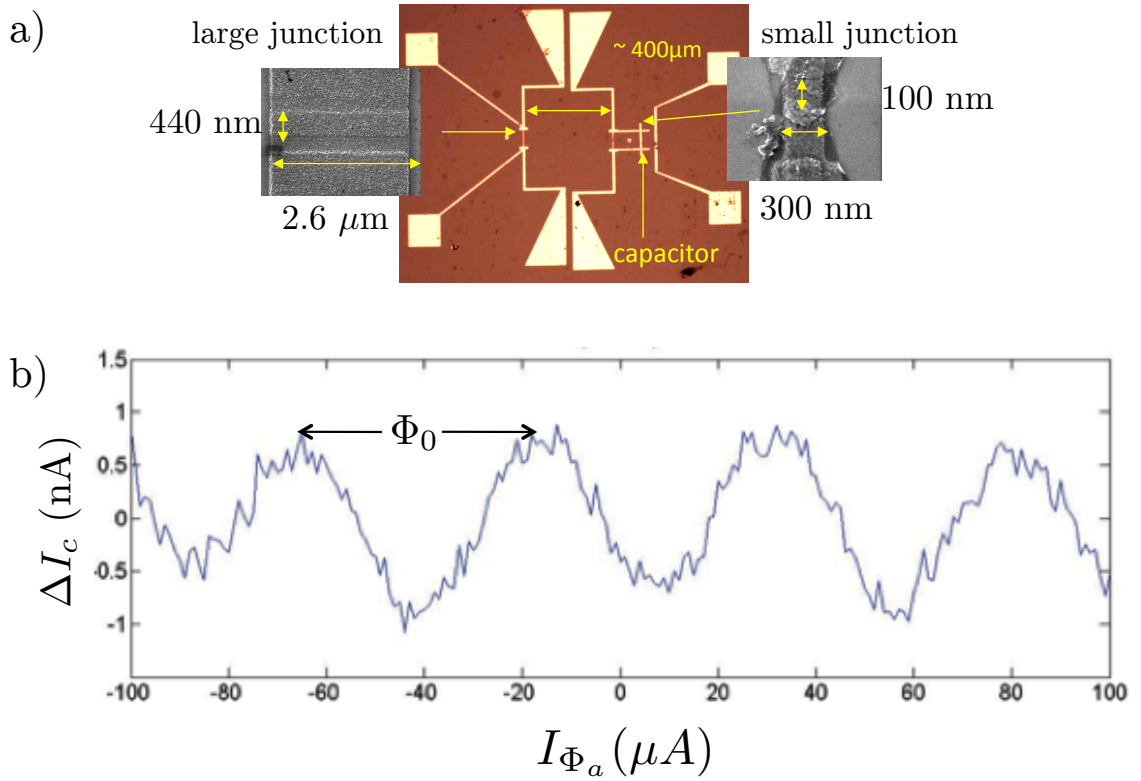


Figure 8.1: (a) SEM image of asymmetric dc SQUID used in the experiment by Dan Sullivan *et al.* [19]. (b) change in the switching current ΔI_c versus applied flux Φ_a measured at 50 mK. A true supercurrent of $\sim 1 \mu\text{A}$ was present, and the data shows a clear modulation of $\sim \pm 1 \text{ nA}$ as the flux varied, indicating phase stabilization across the small junction.

is it at $T = 0$ K. Rather, it is coupled to a heat bath as well as to an external circuit. Thus in addition to quantum uncertainty in the phase, it will be subject to thermally induced phase-diffusion, as described in Chapter 6. The classical phase diffusion model is based on the premise that thermal fluctuations in the environment cause the phase to undergo a random walk. This results in fluctuation-dominated tunneling and a highly suppressed “supercurrent” with a finite slope.

All of the Josephson STM studies to date have apparently been implemented at temperatures between 2-4 K, and they were uncontroversially in the thermally phase diffusive regime [25–29, 31, 113, 114]. Although it has been suggested that a millikelvin Josephson STM might circumvent this problem [21], we are (to the best of my knowledge) the first group to have attempted to implement one. The STM junction temperature is crucial in determining the junction dynamics because lower temperatures allow the observation of pair tunneling at higher junction resistances. This may be demonstrated by considering the conditions for which thermal effects dominate the other energy scales (E_J and E_C) in the system.

For a symmetric superconducting junction, the Ambegaokar-Baratoff formula gives [138]

$$I_c R_N = \frac{2e}{\hbar} E_J R_N = \frac{\pi}{2e} \Delta(T) \tanh \left[\frac{\Delta(T)}{2k_B T} \right], \quad (8.10)$$

where R_N is the tunneling resistance of the junction in the normal state. Ideally, the Josephson coupling energy, $E_J = \hbar I_c / 2e$, is much greater than $k_B T$. Otherwise, thermal effects might dominate if there are no other important energy scales. From

this and Eq. (8.10), we deduce the condition

$$\frac{\hbar}{e^2} \frac{\pi}{4} \Delta(T) > (k_B T) R_N, \quad (8.11)$$

or equivalently,

$$R_n < \frac{\Delta}{k_B T} R_Q \quad (8.12)$$

where $R_Q = \hbar/e^2$ is the quantum resistance. In order for thermal effects not to dominate in a single ultra-small Nb-Nb junction at 2.1 K, Eq. (8.12) yields a requirement that $R_N < 31.8 \text{ k}\Omega$. At 50 mK, we require a junction resistance of $R_N < 1.33 \text{ M}\Omega$. For a typical STM, the tunnel resistance is $\sim 100 \text{ M}\Omega$, two orders of magnitude above this. However, for spectroscopy (rather than scanning), we have shown we can use tunnel resistance down to $\sim 1 \text{ M}\Omega$. It is important to consider that in order to obtain a tunnel resistance of $1 \text{ M}\Omega$, we set the bias voltage to 1 mV and obtain a critical current of 1 nA. This requires pushing the STM tip into the sample, possibly to the point of destruction. Topographic images, in particular, are impossible to obtain with these parameters.

From these considerations, we expect it to be challenging to operate a single-tipped STM in a regime in which phase fluctuations do not dominate. Furthermore, data taken with our mK STM with a Nb tip and Nb(100) sample at R_N down to $1 \text{ M}\Omega$ are consistent with the classical phase diffusion model with the finer features better described by $P(E)$ theory. Since our strategy to reduce uncertainty in the phase involves increasing both the junction capacitance C and the effective critical current I_c by coupling an ultra-sharp tip to a much larger tip, a question that remains is whether this will also reduce phase diffusion induced by fluctuations in

the junction's environment.

In order to address this, we again consider the classical circuit equation for an ultra-small junction biased with voltage U , and a fluctuation term $\tilde{e}(t)$,

$$\frac{\hbar RC}{2e} \frac{d^2\phi}{dt^2} + \frac{\hbar}{2e} \frac{d\phi}{dt} + RI_c \sin \phi = U + \tilde{e}(t). \quad (8.13)$$

The voltage fluctuations can be modeled as Johnson noise generated by the shunt resistor R at an effective noise temperature T_n . The voltage noise has correlation: $\langle \tilde{e}(t)\tilde{e}(0) \rangle = 2k_B T_n R \delta(t)$. This is the starting point for the derivation outlined in Chapter 6 that describe the effects of thermal fluctuations on a small capacitance junction [153]. Since C is small, the classical phase diffusion model disregards the first term, which may be interpreted in the tilted washboard analogy as the inertia of the ball in the washboard potential. A small-capacitance junction thus corresponds to a ball of negligible mass, subject to thermally-induced fluctuations.

If we increase C , the the contribution of the inertial term can become significant. In the tilted washboard analogy, a more massive ball is less vulnerable to fluctuations imposed by the environment. Phase diffusion is also reduced when the effective critical current I_c is increased, as suggested in Section 8.4.1. In this case, we are directly modifying the amplitude of the sine term in Eq. (8.13). In the tilted-washboard model, this corresponds to increasing the depth of the potential well, which increases the energetic cost of moving away from the minimum in the potential well. This, in turn, reduces σ_γ . This suggests that our two-pronged approach of adjusting C and I_c of the ultra-small STM junction in order to reduce quantum uncertainty in the phase also reduces phase diffusion due to thermal fluctuations at

finite temperatures.

8.5 Implementation of the phase STM

Although a millikelvin STM is an extremely powerful tool in itself, my work described in this thesis sets the foundation for the realization of a phase STM. The millikelvin system has been designed and built with great care. Vibration isolation is critical to ensure mechanical stability and resilience to noise. Filtering and heat sinking of the wires and the STM are critical to ensure that the junction reaches as low a temperature as possible. The UHV sample preparation chamber and *in situ* transfer system ensures that we will be able to study a wide variety of samples that are prepared under ideal conditions. The dual tip STM is built and each tip's coarse approach mechanism and scanner has been tested on a variety of samples.

The next step is clearly to couple the two tips via a superconducting wire. Although I developed a fabrication process to make superconducting Nb tips, it should not be underestimated how challenging this next step may be. For example, after I developed the fabrication process for superconducting Nb tips, I attempted to wire-bond a 10 μm Al wire between two Nb tips. I found that although it is possible to connect the tips in this way, the bond is very delicate and could not withstand relative motion between the two tips, which is unavoidable during operation in order to bring the tips into tunneling range of the sample. I also tried to spot-weld a thin strip of tantalum foil to the two tips. I found that it was necessary to sand each of the wires down to create flat surfaces; spot-welding the foil to flat surfaces created

a more robust weld. Although I didn't pursue this aspect of the project any farther, this method of connecting the tips seemed promising. Another critical step will be to arrange the second tip to give a SQUID circuit that has parameters such that the system avoids the phase diffusion regime and achieves a full supercurrent across the ultra-small STM junction. The project did not progress to this stage while I was working on it.

Yet another key step that will be necessary in order for the phase STM to operate, is that modifications will need to be made to the feedback circuit. The feedback indicates when the tip has approached the sample (during coarse approach), and it is also used to maintain a constant current while scanning. The circuits for each tip are currently independent. However, if the two tips are connected, one will need to distinguish between the signals from each tip so that we can determine which tip has approached the sample. One way in which this may be done is to modulate the z of each tip by a small amount $\sim 1 \text{ \AA}$, but use different frequencies for each tip. Two lock-in amplifiers might then be used to detect the respective modulations in a net current signal, and the measured amplitudes used to generate two feedback signals.

Finally, as described in Chapter 3, the mK STM system currently only has cryogenic microwave powder filters on the bias, current and thermometer lines. The elevated noise temperature of $T_n \sim 185 \text{ mK}$ that we observe is likely due to pick up of noise from the two dozen other high voltage wires that are in close proximity to the junction. If a lower noise temperature is a priority, cryogenic filters for these other lines could be added. However the space available on the dilution refrigerator is too

small to accommodate conventional powder filters for all of these lines. Cryogenic micro-fabricated R - C filters with dimensions of ~ 1 cm have been developed by other groups, and display excellent attenuation characteristics at microwave frequencies [136, 177]. I would suggest that the filters for our system be designed and built based on this approach, with close attention to the work described in Refs. [136, 177] in particular.

8.6 Conclusions

Few groups have successfully built STMs that operate in the 10-30 mK range, with reported junction noise temperatures between 80 and 250 mK [61, 62, 178]. Other groups with STMs that operate at higher cryogenic temperatures have successfully fabricated superconducting tips. Some of these tips are sharp and robust enough to yield atomic resolution images and spectroscopic maps on superconducting samples [24, 113, 114]. Our Josephson STM that operates at millikelvin temperatures is therefore a unique instrument that could be used to probe the condensate of a wide variety of superconducting samples at energy scales that have so far not been explored. Some samples that might be studied include NbN [179], NbSe₂ [3, 4, 21, 23, 180], the cuprates (BSSCO, YBCO) [11–13, 16] the pnictides [31, 34], and heavy fermion systems such as UPt₃ [181]. The STM could also be used to probe the superconducting behavior of doped topological insulators such as Cu_{*x*}Bi₂Se₃, currently of great interest due to the possibility of Majorana bound states and potential applications in topological quantum computing [35, 37, 109–

112].

When the dual tip STM is successfully modified to provide phase-sensitive data, we will have built a radically new instrument and developed a novel imaging technique. An instrument that can map out atomic scale variations of the gauge invariant phase difference will undoubtedly provide new insight into superconductivity.

Bibliography

- [1] G. Binnig and H. Rohrer, "Scanning tunneling microscopy," *Surface Science* **126**, 236 (1983).
- [2] H. F. Hess, R. B. Robinson, and J. V. Waszczak, "Vortex-core structure observed with a scanning tunneling microscope," *Physical Review Letters* **64**, 2711 (1990).
- [3] K. Iwaya, T. Hanaguri, A. Koizumi, K. Takaki, A. Maeda, and K. Kitazawa, "Electronic state of NbSe₂ investigated by STM/STS," *Physica B: Condensed Matter* Proceedings of the 23rd International Conference on Low Temperature Physics, **329333**, Part 2, 1598 (2003).
- [4] H. Wang, J. Lee, M. Dreyer, and B. I. Barker, "A scanning tunneling microscopy study of a new superstructure around defects created by tip/sample interaction on 2H-NbSe₂," *Journal of Physics: Condensed Matter* **21**, 265005 (2009).
- [5] F. Giubileo, D. Roditchev, W. Sacks, R. Lamy, D. X. Thanh, J. Klein, S. Miraglia, D. Fruchart, J. Marcus, and P. Monod, "Two-gap state density in MgB₂: A true bulk property or a proximity effect?" *Physical Review Letters* **87**, 177008 (2001).
- [6] G. Rubio-Bollinger, H. Suderow, and S. Vieira, "Tunneling spectroscopy in small grains of superconducting MgB₂," *Physical Review Letters* **86**, 5582 (2001).
- [7] M. Iavarone, G. Karapetrov, A. E. Koshelev, W. K. Kwok, G. W. Crabtree, W. N. Kang, E.-M. Choi, H. J. Kim, and S.-I. Lee, "STM tunneling spectroscopy in MgB₂ thin films: the role of band structure in tunneling spectra," *Superconductor Science and Technology* **17** (2004).
- [8] H. Murakami and R. Aoki, "Observation of multi-stage superconducting gap states in Bi₂Sr₂CaCu₂O_x crystal surface by LT-STM/STS," *Journal of the Physical Society of Japan* **64**, 1287 (1995).

- [9] T. Hasegawa, M. Nantoh, M. Ogino, H. Sugawara, M. Kawasaki, H. Koinuma, and K. Kitazawa, “STM tunneling spectroscopy on high T_c superconductors,” *Journal of Superconductivity* **8**, 467 (1995).
- [10] M. Oda, K. Hoya, R. Kubota, C. Manabe, N. Momono, T. Nakano, and M. Ido, “STM/STS studies for doping effects on the symmetry and magnitude of superconducting gap in $\text{Bi}_2\text{Sr}_2\text{CaCu}_2\text{O}_{8+\delta}$,” *Physica C: Superconductivity* **282287**, Part 3, 1499 (1997).
- [11] S. H. Pan, E. W. Hudson, K. M. Lang, H. Eisaki, S. Uchida, and J. C. Davis, “Imaging the effects of individual zinc impurity atoms on superconductivity in $\text{Bi}_2\text{Sr}_2\text{CaCu}_2\text{O}_{8+\delta}$,” *Nature* **403**, 746 (2000).
- [12] S. H. Pan, J. P. O’Neal, R. L. Badzey, C. Chamon, H. Ding, J. R. Engelbrecht, Z. Wang, H. Eisaki, S. Uchida, A. K. Gupta, K.-W. Ng, E. W. Hudson, K. M. Lang, and J. C. Davis, “Microscopic electronic inhomogeneity in the high- T_c superconductor $\text{Bi}_2\text{Sr}_2\text{CaCu}_2\text{O}_{8+x}$,” *Nature* **413**, 282 (2001).
- [13] E. W. Hudson, V. Madhavan, K. McElroy, J. E. Hoffman, K. M. Lang, H. Eisaki, S. Uchida, and J. C. Davis, “STM study of novel resonances in $\text{Bi}_2\text{Sr}_2\text{CaCu}_2\text{O}_{8+\delta}$,” *Physica B: Condensed Matter* Proceedings of the 23rd International Conference on Low Temperature Physics, **329333**, Part 2, 1365 (2003).
- [14] A. Yazdani, B. A. Jones, C. P. Lutz, M. F. Crommie, and D. M. Eigler, “Probing the local effects of magnetic impurities on superconductivity,” *Science* **275**, 1767 (1997).
- [15] J. Li, W.-D. Schneider, R. Berndt, and B. Delley, “Kondo scattering observed at a single magnetic impurity,” *Physical Review Letters* **80**, 2893 (1998).
- [16] A. Yazdani, C. M. Howald, C. P. Lutz, A. Kapitulnik, and D. M. Eigler, “Impurity-induced bound excitations on the surface of $\text{Bi}_2\text{Sr}_2\text{CaCu}_2\text{O}_8$,” *Physical Review Letters* **83**, 176 (1999).
- [17] J. Šmakov, I. Martin, and A. V. Balatsky, “Josephson scanning tunneling microscopy,” *Physical Review B* **64**, 212506 (2001).
- [18] A. V. Balatsky, J. Šmakov, and I. Martin, “Potential applications of a scanning tunneling microscope with a superconducting tip,” *Superconductor Science and Technology* **15**, 446 (2002).
- [19] D. Sullivan, S. Dutta, M. Dreyer, M. Gubrud, A. Roychowdhury, J. Anderson, C. Lobb, and F. Wellstood, “Asymmetric superconducting quantum interference devices for suppression of phase diffusion in small Josephson junctions,” *Journal of Applied Physics* **113**, 183905 (2013).

- [20] S. H. Pan, E. W. Hudson, and J. C. Davis, “Vacuum tunneling of superconducting quasiparticles from atomically sharp scanning tunneling microscope tips,” *Applied Physics Letters* **73**, 2992 (1998).
- [21] O. Naaman, *Josephson scanning tunneling microscope: a local probe of the superconducting pair amplitude*, Ph.D. thesis, University of California, Berkeley (2003).
- [22] M. Xu, Y. Takano, T. Hatano, M. Kitahara, and D. Fujita, “The fabrication of MgB₂ superconducting STM tips,” *Physica C: Superconductivity* **388**, 117 (2003).
- [23] J. G. Rodrigo, H. Suderow, and S. Vieira, “On the use of STM superconducting tips at very low temperatures,” *The European Physical Journal B - Condensed Matter and Complex Systems* **40**, 483 (2004).
- [24] A. Kohen, Y. Noat, T. Proslie, E. Lacaze, M. Aprili, W. Sacks, and D. Roditchev, “Fabrication and characterization of scanning tunneling microscopy superconducting Nb tips having highly enhanced critical fields,” *Physica C: Superconductivity* **419**, 18 (2005).
- [25] A. Kohen, T. Cren, Y. Noat, T. Proslie, F. Giubileo, F. Bobba, A. Cucolo, N. Zhigadlo, S. Kazakov, J. Karpinski, W. Sacks, and D. Roditchev, “Recent progress in vortex studies by tunneling spectroscopy,” *Physica C: Superconductivity* **437438**, 145 (2006).
- [26] T. Proslie, A. Kohen, Y. Noat, T. Cren, D. Roditchev, and W. Sacks, “Probing the superconducting condensate on a nanometer scale,” *Europhysics Letters* **73**, 962 (2006).
- [27] N. Bergeal, V. Dubost, Y. Noat, W. Sacks, D. Roditchev, N. Emery, C. Hérold, J.-F. Maréché, P. Lagrange, and G. Loupiau, “Scanning tunneling spectroscopy on the novel superconductor CaC₆,” *Physical Review Letters* **97**, 077003 (2006).
- [28] H. Kimura, R. P. Barber, S. Ono, Y. Ando, and R. C. Dynes, “Scanning Josephson tunneling microscopy of single-crystal Bi₂Sr₂CaCu₂O_{8+δ} with a conventional superconducting tip,” *Physical Review Letters* **101**, 037002 (2008).
- [29] N. Bergeal, Y. Noat, T. Cren, T. Proslie, V. Dubost, F. Debontridder, A. Zimmers, D. Roditchev, W. Sacks, and J. Marcus, “Mapping the superconducting condensate surrounding a vortex in superconducting V₃Si using a superconducting MgB₂ tip in a scanning tunneling microscope,” *Physical Review B* **78**, 140507 (2008).
- [30] H. Kimura, R. P. Barber, S. Ono, Y. Ando, and R. C. Dynes, “Josephson scanning tunneling microscopy: A local and direct probe of the superconducting order parameter,” *Physical Review B* **80**, 144506 (2009).

- [31] Y. Noat, T. Cren, V. Dubost, S. Lange, F. Debontridder, P. Toulemonde, J. Marcus, A. Sulpice, W. Sacks, and D. Roditchev, "Disorder effects in pnictides: a tunneling spectroscopy study," *Journal of Physics: Condensed Matter* **22**, 465701 (2010).
- [32] O. Naaman, W. Teizer, and R. C. Dynes, "Fluctuation dominated Josephson tunneling with a scanning tunneling microscope," *Physical Review Letters* **87**, 097004 (2001).
- [33] J. R. Anderson, C. J. Lobb, and F. C. Wellstood, "Imaging the gauge-invariant phase difference of superconductors at the atomic scale," (2005), NSF DMR-0605763.
- [34] Y. Yin, M. Zech, T. L. Williams, X. F. Wang, G. Wu, X. H. Chen, and J. E. Hoffman, "Scanning tunneling spectroscopy and vortex imaging in the iron pnictide superconductor $\text{BaFe}_{1.8}\text{Co}_{0.2}\text{As}_2$," *Physical Review Letters* **102**, 097002 (2009).
- [35] Y. S. Hor, A. J. Williams, J. G. Checkelsky, P. Roushan, J. Seo, Q. Xu, H. W. Zandbergen, A. Yazdani, N. P. Ong, and R. J. Cava, "Superconductivity in $\text{Cu}_x\text{Bi}_2\text{Se}_3$ and its implications for pairing in the undoped topological insulator," *Physical Review Letters* **104**, 057001 (2010).
- [36] M.-X. Wang, C. Liu, J.-P. Xu, F. Yang, L. Miao, M.-Y. Yao, C. L. Gao, C. Shen, X. Ma, X. Chen, Z.-A. Xu, Y. Liu, S.-C. Zhang, D. Qian, J.-F. Jia, and Q.-K. Xue, "The coexistence of superconductivity and topological order in the Bi_2Se_3 thin films," *Science* **336**, 52 (2012).
- [37] N. Levy, T. Zhang, J. Ha, F. Sharifi, A. A. Talin, Y. Kuk, and J. A. Stroscio, "Experimental evidence for *s*-wave pairing symmetry in superconducting $\text{Cu}_x\text{Bi}_2\text{Se}_3$ single crystals using a scanning tunneling microscope," *Physical Review Letters* **110**, 117001 (2013).
- [38] C.-L. Song, Y.-L. Wang, Y.-P. Jiang, Z. Li, L. Wang, K. He, X. Chen, J. E. Hoffman, X.-C. Ma, and Q.-K. Xue, "Imaging the electron-boson coupling in superconducting FeSe films using a scanning tunneling microscope," *Physical Review Letters* **112**, 057002 (2014).
- [39] G. Binnig, H. Rohrer, C. Gerber, and E. Weibel, "Surface studies by scanning tunneling microscopy," *Physical Review Letters* **49**, 57 (1982).
- [40] G. Binnig, C. F. Quate, and C. Gerber, "Atomic force microscope," *Physical Review Letters* **56**, 930 (1986).
- [41] E.-L. Florin, M. Radmacher, B. Fleck, and H. E. Gaub, "Atomic force microscope with magnetic force modulation," *Review of Scientific Instruments* **65**, 639 (1994).

- [42] D. W. Pohl, W. Denk, and M. Lanz, “Optical stethoscopy: Image recording with resolution $\lambda/20$,” *Applied Physics Letters* **44**, 651 (1984).
- [43] R. Crook, C. G. Smith, M. Y. Simmons, and D. A. Ritchie, “One-dimensional probability density observed using scanned gate microscopy,” *Journal of Physics: Condensed Matter* **12**, L735 (2000).
- [44] R. Wiesendanger, H.-J. Güntherodt, G. Güntherodt, R. J. Gambino, and R. Ruf, “Observation of vacuum tunneling of spin-polarized electrons with the scanning tunneling microscope,” *Physical Review Letters* **65**, 247 (1990).
- [45] S. H. Pan, E. W. Hudson, and J. C. Davis, “ ^3He refrigerator based very low temperature scanning tunneling microscope,” *Review of Scientific Instruments* **70**, 1459 (1999).
- [46] J. Bardeen, “Tunneling from a many-particle point of view,” *Physical Review Letters* **6**, 57 (1961).
- [47] J. Tersoff and D. R. Hamann, “Theory of the scanning tunneling microscope,” *Physical Review B* **31**, 805 (1985).
- [48] I. Giaever, “Electron tunneling between two superconductors,” *Physical Review Letters* **5**, 464 (1960).
- [49] J. Bardeen, L. N. Cooper, and J. R. Schrieffer, “Theory of superconductivity,” *Physical Review* **108**, 1175 (1957).
- [50] B. D. Josephson, “Possible new effects in superconductive tunneling,” *Physics Letters* **1**, 251253 (1962).
- [51] A. F. Andreev, “Thermal conductivity of the intermediate state of superconductors,” *Soviet Physics JETP* **20** (1965).
- [52] S. Loth, C. P. Lutz, and A. J. Heinrich, “Spin-polarized spin excitation spectroscopy,” *New Journal of Physics* **12**, 125021 (2010).
- [53] S. Loth, S. Baumann, C. P. Lutz, D. M. Eigler, and A. J. Heinrich, “Bistability in atomic-scale antiferromagnets,” *Science* **335**, 196 (2012).
- [54] S. R. Schofield, N. J. Curson, M. Y. Simmons, F. J. Rue, T. Hallam, L. Oberbeck, and R. G. Clark, “Atomically precise placement of single dopants in Si,” *Physical Review Letters* **91**, 136104 (2003).
- [55] M. B. Haider, J. L. Pitters, G. A. DiLabio, L. Livadaru, J. Y. Mutus, and R. A. Wolkow, “Controlled coupling and occupation of Silicon atomic quantum dots at room temperature,” *Physical Review Letters* **102**, 046805 (2009).
- [56] S. A. Elrod, A. L. de Lozanne, and C. F. Quate, “Low-temperature vacuum tunneling microscopy,” *Applied Physics Letters* **45**, 1240 (1984).

- [57] O. Marti, G. Binnig, H. Rohrer, and H. Salemink, “Low-temperature scanning tunneling microscope,” *Surface Science* **181**, 230 (1987).
- [58] A. P. Fein, J. R. Kirtley, and R. M. Feenstra, “Scanning tunneling microscope for low temperature, high magnetic field, and spatially resolved spectroscopy,” *Review of Scientific Instruments* **58**, 1806 (1987).
- [59] S. H. Tessmer, D. J. V. Harlingen, and J. W. Lyding, “Integrated cryogenic scanning tunneling microscopy and sample preparation system,” *Review of Scientific Instruments* **65**, 2855 (1994).
- [60] H. Suderow, M. Crespo, P. Martinez-Samper, J. Rodrigo, G. Rubio-Bollinger, S. Vieira, N. Luchier, J. Brison, and P. Canfield, “Scanning tunneling microscopy and spectroscopy at very low temperatures,” *Physica C: Superconductivity* **369**, 106 (2002).
- [61] Y. J. Song, A. F. Otte, V. Shvarts, Z. Zhao, Y. Kuk, S. R. Blankenship, A. Band, F. M. Hess, and J. A. Stroscio, “Invited review article: A 10 mK scanning probe microscopy facility,” *Review of Scientific Instruments* **81**, 121101 (2010).
- [62] M. Assig, M. Etzkorn, A. Enders, W. Stiepany, C. R. Ast, and K. Kern, “A 10mK scanning tunneling microscope operating in ultra high vacuum and high magnetic fields,” *Review of Scientific Instruments* **84**, 033903 (2013).
- [63] J. W. G. Wildöer, A. J. A. van Roy, H. van Kempen, and C. J. P. M. Harmans, “Low-temperature scanning tunneling microscope for use on artificially fabricated nanostructures,” *Review of Scientific Instruments* **65**, 2849 (1994).
- [64] G. Meyer, “A simple low-temperature ultrahigh-vacuum scanning tunneling microscope capable of atomic manipulation,” *Review of Scientific Instruments* **67**, 2960 (1996).
- [65] C. Wittneven, R. Dombrowski, S. H. Pan, and R. Wiesendanger, “A low-temperature ultrahigh-vacuum scanning tunneling microscope with rotatable magnetic field,” *Review of Scientific Instruments* **68**, 3806 (1997).
- [66] J. H. Ferris, J. G. Kushmerick, J. A. Johnson, M. G. Yoshikawa Youngquist, R. B. Kessinger, H. F. Kingsbury, and P. S. Weiss, “Design, operation, and housing of an ultrastable, low temperature, ultrahigh vacuum scanning tunneling microscope,” *Review of Scientific Instruments* **69**, 2691 (1998).
- [67] M. Kugler, C. Renner, Ø. Fischer, V. Mikheev, and G. Batey, “A ^3He refrigerated scanning tunneling microscope in high magnetic fields and ultrahigh vacuum,” *Review of Scientific Instruments* **71**, 1475 (2000).
- [68] A. J. Heinrich, C. P. Lutz, J. A. Gupta, and D. M. Eigler, “Molecule cascades,” *Science* **298**, 1381 (2002).

- [69] J. Wiebe, A. Wachowiak, F. Meier, D. Haude, T. Foster, M. Morgenstern, and R. Wiesendanger, "A 300mK ultra-high vacuum scanning tunneling microscope for spin-resolved spectroscopy at high energy resolution," *Review of Scientific Instruments* **75**, 4871 (2004).
- [70] P. Davidsson, H. Olin, M. Persson, and S. Pehrson, "Design and operation of a low-temperature scanning tunneling microscope suitable for operation below 1 K," *Ultramicroscopy* **4244**, Part 2, 1470 (1992).
- [71] N. Moussy, H. Courtois, and B. Pannetier, "A very low temperature scanning tunneling microscope for the local spectroscopy of mesoscopic structures," *Review of Scientific Instruments* **72**, 128 (2001).
- [72] M. D. Upward, J. W. Janssen, L. Gurevich, A. F. Morpurgo, and L. P. Kouwenhoven, "An ultralow-temperature scanning tunneling microscope," *Applied Physics A* **72**, S253 (2001).
- [73] H. Kambara, T. Matsui, Y. Niimi, and H. Fukuyama, "Construction of a versatile ultralow temperature scanning tunneling microscope," *Review of Scientific Instruments* **78**, 073703 (2007).
- [74] Kadel Engineering, Danville IN.
- [75] American Magnetics, Inc.
- [76] Andeen-Hagerling Inc., Model AH 2700A.
- [77] M. A. Gubrud, *Scanning Tunneling Microscopy at milliKelvin Temperatures: Design and Construction*, Ph.D. thesis, University of Maryland, College Park (2010).
- [78] SPM 1000 Scanning Probe Microscope Control System.
- [79] DL Instrument Model 1211.
- [80] Technical Manufacturing Corporation.,TMC Model 71-473-spl.
- [81] TMC Model 71-473-SPL; Technical Manufacturing Corporation, Peabody, MA.
- [82] Varian Models Starcell 75 and 300, respectively.
- [83] Vacuum Generators Model ST2 and Varian Model 929-022.
- [84] VG Scienta Model VIG18/Arun Microelectronics Ltd. PGC1.
- [85] Varian TModel V551 Navigator/VT 1000HT.
- [86] Varian Model TriScroll600.
- [87] Extorr Model XT200.

- [88] Omicron Model EFM3/EVC 100.
- [89] Specs Model IQE 10.
- [90] VG Scienta Model HPT.
- [91] M. Dreyer, J. Lee, H. Wang, and B. Barker, “A low temperature scanning tunneling microscopy system for measuring Si at 4.2 K,” *Review of Scientific Instruments* **81**, 053703 (2010).
- [92] SC-040/50-CN-CN Coax Co., Lt., Kanagawa, Japan.
- [93] Britannia House, Cambridge, UK.
- [94] Microstock Inc., Westpoint, PA, USA.
- [95] Rami Ceramic Industries, Nazareth, Palestine.
- [96] F. P. Milliken, J. R. Rozen, G. A. Keefe, and R. H. Koch, “ 50Ω characteristic impedance low-pass metal powder filters,” *Review of Scientific Instruments* **78**, 024701 (2007).
- [97] J. M. Martinis, M. H. Devoret, and J. Clarke, “Experimental tests for the quantum behavior of a macroscopic degree of freedom: The phase difference across a Josephson junction,” *Physical Review B* **35**, 4682 (1987).
- [98] A. Roychowdhury, R. Dana, M. Dreyer, J. R. Anderson, C. J. Lobb, and F. C. Wellstood, “Plasma etching of superconducting Niobium tips,” *arXiv:cond-mat/1404.5370* (2014).
- [99] Y. W. Zhu, H. Z. Zhang, X. C. Sun, S. Q. Feng, J. Xu, Q. Zhao, B. Xiang, R. M. Wang, and D. P. Yu, “Efficient field emission from ZnO nanoneedle arrays,” *Applied Physics Letters* **83**, 144 (2003).
- [100] E. I. Givargizov, “Ultrasharp tips for field emission applications prepared by the vaporliquid-solid growth technique,” *Journal of Vacuum Science & Technology B* **11**, 449 (1993).
- [101] J. N. Randall, J. W. Lyding, S. Schmucker, J. R. V. Ehr, J. Ballard, R. Saini, H. Xu, and Y. Ding, “Atomic precision lithography on Si,” *Journal of Vacuum Science & Technology B* **27**, 2764 (2009).
- [102] D. Pires, J. L. Hedrick, A. D. Silva, J. Frommer, B. Gotsmann, H. Wolf, M. Despont, U. Duerig, and A. W. Knoll, “Nanoscale three-dimensional patterning of molecular resists by scanning probes,” *Science* **328**, 732 (2010).
- [103] M. Kaestner and I. W. Rangelow, “Multi-step scanning probe lithography (SPL) on calixarene with overlay alignment,” *Proc. SPIE 8323* , 83231G (2012).

- [104] Z. Durrani, M. Kaestner, M. Hofer, T. Ivanov, and I. Rangelow, “Scanning probe lithography for electronics at the 5 nm scale,” *SPIE Newsroom* (2013).
- [105] A. I. Oliva, A. R. G, J. L. Peña, E. Anguiano, and M. Aguilar, “Electrochemical preparation of tungsten tips for a scanning tunneling microscope,” *Review of Scientific Instruments* **67**, 1917 (1996).
- [106] I. H. Musselman and P. E. Russell, “Platinum/Iridium tips with controlled geometry for scanning tunneling microscopy,” *Journal of Vacuum Science & Technology A* **8**, 3558 (1990).
- [107] I. Guillamon, H. Suderow, S. Vieira, and P. Rodiere, “Scanning tunneling spectroscopy with superconducting tips of Al,” *Physica C: Superconductivity* **468**, 537 (2008).
- [108] J. Rodrigo, V. Crespo, and S. Vieira, “Josephson current at atomic scale: Tunneling and nanocontacts using a STM,” *Physica C: Superconductivity* **437**, 270 (2006).
- [109] M. Z. Hasan and C. L. Kane, “Colloquium: Topological insulators,” *Reviews of Modern Physics* **82**, 3045 (2010).
- [110] L. Fu and C. L. Kane, “Superconducting proximity effect and Majorana fermions at the surface of a topological insulator,” *Physical Review Letters* **100**, 096407 (2008).
- [111] T. D. Stanescu, J. D. Sau, R. M. Lutchyn, and S. Das Sarma, “Proximity effect at the superconductor/topological insulator interface,” *Physical Review B* **81**, 241310 (2010).
- [112] J. Linder, Y. Tanaka, T. Yokoyama, A. Sudbø, and N. Nagaosa, “Unconventional superconductivity on a topological insulator,” *Physical Review Letters* **104**, 067001 (2010).
- [113] M. Ternes, W.-D. Schneider, J.-C. Cuevas, C. P. Lutz, C. F. Hirjibehedin, and A. J. Heinrich, “Subgap structure in asymmetric superconducting tunnel junctions,” *Physical Review B* **74**, 132501 (2006).
- [114] O. Naaman, W. Teizer, and R. C. Dynes, “The fabrication of reproducible superconducting scanning tunneling microscope tips,” *Review of Scientific Instruments* **72**, 1688 (2001).
- [115] A. Lichtenberger, D. Lea, and F. Lloyd, “Investigation of etching techniques for superconductive Nb/Al-Al₂O₃/Nb fabrication processes,” *IEEE Transactions on Applied Superconductivity* **3**, 2191 (1993).
- [116] Q. Zhong, W. Cao, J. Li, Y. Zhong, and X. Wang, “Study of dry etching process using SF₆ and CF₄/O₂ for Nb/Nb_xSi_{1-x}/Nb Josephson-junction fabrication,” *2012 Conference on Precision Electromagnetic Measurements (CPEM)*, 46 (2012).

- [117] J. P. Ibe, P. P. Bey, Jr, S. L. Brandow, R. A. Brizzolara, N. A. Burnham, D. P. DiLella, K. P. Lee, C. R. K. Marrian, and R. J. Colton, "On the electrochemical etching of tips for scanning tunneling microscopy," *Journal of Vacuum Science & Technology A* **8**, 3570 (1990).
- [118] Plasma-Therm 790 series: <http://www.plasmatherm.com/790-rie.html>.
- [119] C. D. Child, "Discharge from hot CaO," *Physical Review (Series I)* **32**, 492 (1911).
- [120] I. Langmuir, "The effect of space charge and residual gases on thermionic currents in high vacuum," *Physical Review* **2**, 450 (1913).
- [121] M. J. Madou, *Fundamentals of Microfabrication: The Science of Miniaturization*, 2nd ed. (CRC Press, 2002).
- [122] P. A. Watterson, "Child-Langmuir sheath structure around wedge-shaped cathodes," *Journal of Physics D: Applied Physics* **22**, 1300 (1989).
- [123] I. J. Donnelly and P. A. Watterson, "Ion-matrix sheath structure around cathodes of complex shape," *Journal of Physics D: Applied Physics* **22**, 90 (1989).
- [124] T. E. Sheridan, "Analytical expression for sheath edge around corner cathodes," *Journal of Physics D: Applied Physics* **42**, 015212 (2009).
- [125] K. Sokhey, S. Rai, and G. Lodha, "Oxidation studies of niobium thin films at room temperature by X-ray reflectivity," *Applied Surface Science* **257**, 222 (2010).
- [126] R. C. Dynes, V. Narayanamurti, and J. P. Garno, "Direct measurement of quasiparticle-lifetime broadening in a strong-coupled superconductor," *Physical Review Letters* **41**, 1509 (1978).
- [127] A. Roychowdhury, M. A. Gubrud, R. Dana, J. R. Anderson, C. J. Lobb, F. C. Wellstood, and M. Dreyer, "A 30 mK, 13.5 T scanning tunneling microscope with two independent tips," *Review of Scientific Instruments* **85**, 043706 (2014).
- [128] J. V. Barth, H. Brune, G. Ertl, and R. J. Behm, "Scanning tunneling microscopy observations on the reconstructed Au(111) surface: Atomic structure, long-range superstructure, rotational domains, and surface defects," *Physical Review B* **42**, 9307 (1990).
- [129] S. Narasimhan and D. Vanderbilt, "Elastic stress domains and the herringbone reconstruction on Au(111)," *Physical Review Letters* **69**, 1564 (1992).
- [130] O. K. Binnig, H. Rohrer, C. Gerber, and E. Stoll, "Real-space observation of the reconstruction of Au(100)," *Surface Science* **144**, 321 (1984).

- [131] D. V. Averin and K. K. Likharev, “Coulomb blockade of single-electron tunneling, and coherent oscillations in small tunnel junctions,” *Journal of Low Temperature Physics* **62**, 345 (1986).
- [132] G.-L. Ingold, H. Grabert, and U. Eberhardt, “Cooper-pair current through ultrasmall Josephson junctions,” *Physical Review B* **50**, 395 (1994).
- [133] Accumet Materials Co. (L), Ossining, NY.
- [134] K. Levenberg, “A method for the solution of certain problems in least squares,” *Quarterly of Applied Mathematics* **2**, 164168 (1944).
- [135] D. W. Marquardt, “An algorithm for least-squares estimation of nonlinear parameters,” *Journal of the Society for Industrial & Applied Mathematics* **11**, 431441 (1963).
- [136] H. le Sueur and P. Joyez, “Microfabricated electromagnetic filters for millikelvin experiments,” *Review of Scientific Instruments* **77**, 115102 (2006).
- [137] M. Tinkham, *Introduction to Superconductivity: Second Edition* (Dover Publications, 2004).
- [138] V. Ambegaokar and A. Baratoff, “Tunneling between superconductors,” *Physical Review Letters* **10** (1963).
- [139] M. H. Devoret, D. Esteve, H. Grabert, G.-L. Ingold, H. Pothier, and C. Urbina, “Effect of the electromagnetic environment on the Coulomb blockade in ultrasmall tunnel junctions,” *Physical Review Letters* **64**, 1824 (1990).
- [140] G. Falci, V. Bubanja, and G. Schön, “Quantum tunneling in small-capacitance Josephson junctions in a general electromagnetic environment,” *Europhysics Letters* **16**, 109 (1991).
- [141] G.-L. Ingold and Y. V. Nazarov, “Charge tunneling rates in ultrasmall junctions,” in *Single Charge Tunneling*, NATO ASI Series B No. 294 (Plenum Press, New York, 1992) pp. 21–107.
- [142] H. Grabert and M. H. Devoret, *Single charge tunneling: Coulomb blockade phenomena in nanostructures*, Vol. 294 (Plenum Pub Corp, 1992).
- [143] D. V. Averin, A. B. Zorin, and K. K. Likharev, “Bloch oscillations in small Josephson junctions,” *Sov. Phys. JETP* **61:2** (1985).
- [144] K. K. Likharev and A. B. Zorin, “Theory of the Bloch-wave oscillations in small Josephson junctions,” *Journal of Low Temperature Physics* **59**, 347 (1985).
- [145] A. O. Caldeira and A. J. Leggett, “Influence of dissipation on quantum tunneling in macroscopic systems,” *Physical Review Letters* **46**, 211 (1981).

- [146] A. O. Caldeira and A. J. Leggett, “Quantum tunneling in a dissipative system,” *Annals of Physics* **149**, 374456 (1983).
- [147] P. Joyez, D. Vion, M. Götz, M. H. Devoret, and D. Esteve, “The Josephson effect in nanoscale tunnel junctions,” *Journal of Superconductivity* **12**, 757 (1999).
- [148] T. P. Orlando and K. A. Delin, *Foundations of Applied Superconductivity* (Addison-Wesley, 1991).
- [149] W. C. Stewart, “Current-voltage characteristics of Josephson junctions,” *Applied Physics Letters* **12**, 277 (1968).
- [150] D. E. McCumber, “Effect of ac impedance on dc voltage-current characteristics of superconductor weak-link junctions,” *Journal of Applied Physics* **39**, 3113 (1968).
- [151] S. Shapiro, “Josephson currents in superconducting tunneling: The effect of microwaves and other observations,” *Physical Review Letters* **11**, 80 (1963).
- [152] Y. Nakamura, Y. A. Pashkin, and J. S. Tsai, “Coherent control of macroscopic quantum states in a single-Cooper-pair box,” *Nature* **398**, 786 (1999).
- [153] Y. M. I. Anchenko and L. A. Zil’berman, “The Josephson effect in small tunnel contacts,” *Soviet Physics JETP* **28** (1969).
- [154] J. M. Martinis and R. L. Kautz, “Classical phase diffusion in small hysteretic Josephson junctions,” *Physical Review Letters* **63**, 1507 (1989).
- [155] R. L. Kautz and J. M. Martinis, “Noise-affected I - V curves in small hysteretic Josephson junctions,” *Physical Review B* **42**, 9903 (1990).
- [156] V. Ambegaokar and B. I. Halperin, “Voltage due to thermal noise in the dc Josephson effect.” *Physical Review Letters* **23**, 274 (1969).
- [157] The current biased case was treated soon after by Ambegaokar and Halperin [156].
- [158] H. Grabert, G.-L. Ingold, and B. Paul, “Phase diffusion and charging effects in Josephson junctions,” *Europhysics Letters* **44**, 360 (1998).
- [159] P. K. Tien and J. P. Gordon, “Multiphoton process observed in the interaction of microwave fields with the tunneling between superconductor films,” *Physical Review* **129**, 647 (1963).
- [160] J. N. Sweet and G. I. Rochlin, “Microwave-photon-assisted tunneling in Sn-I-Sn superconducting tunnel junctions,” *Physical Review B* **2**, 656 (1970).

- [161] L. P. Kouwenhoven, S. Jauhar, K. McCormick, D. Dixon, P. L. McEuen, Y. V. Nazarov, N. C. van der Vaart, and C. T. Foxon, “Photon-assisted tunneling through a quantum dot,” *Physical Review B* **50**, 2019 (1994).
- [162] J. M. Hergenrother, M. T. Tuominen, J. G. Lu, D. C. Ralph, and M. Tinkham, “Charge transport and photon-assisted tunneling in the NSN single-electron transistor,” *Physica B: Condensed Matter* **203**, 327 (1994).
- [163] Y. Nakamura, C. D. Chen, and J. S. Tsai, “Observation of photon-assisted Josephson-quasiparticle current,” *Czechoslovak Journal of Physics* **46**, 2301 (1996).
- [164] R. J. Fitzgerald, J. M. Hergenrother, S. L. Pohlen, and M. Tinkham, “Crossover from photon-assisted tunneling to classical behavior in single-electron transistors,” *Physical Review B* **57**, 9893 (1998).
- [165] S. E. de Graaf, J. Leppäkangas, A. Adamyan, A. V. Danilov, T. Lindström, M. Fogelström, T. Bauch, G. Johansson, and S. E. Kubatkin, “Charge qubit coupled to an intense microwave electromagnetic field in a superconducting Nb device: Evidence for photon-assisted quasiparticle tunneling,” *Physical Review Letters* **111**, 137002 (2013).
- [166] B. Sarabi, A. N. Ramanayaka, A. L. Burin, F. C. Wellstood, and K. D. Osborn, “Cavity quantum electrodynamics of nanoscale two-level systems,” *arXiv:cond-mat/1405.0264* (2014).
- [167] Z.-X. Shen, D. S. Dessau, B. O. Wells, D. M. King, W. E. Spicer, A. J. Arko, D. Marshall, L. W. Lombardo, A. Kapitulnik, P. Dickinson, S. Doniach, J. DiCarlo, T. Loeser, and C. H. Park, “Anomalously large gap anisotropy in the a - b plane of $\text{Bi}_2\text{Sr}_2\text{CaCu}_2\text{O}_{8+\delta}$,” *Physical Review Letters* **70**, 1553 (1993).
- [168] J. A. Martindale, S. E. Barrett, K. E. OHara, C. P. Slichter, W. C. Lee, and D. M. Ginsberg, “Magnetic-field dependence of planar copper and oxygen spin-lattice relaxation rates in the superconducting state of $\text{YBa}_2\text{Cu}_3\text{O}_7$,” *Physical Review B* **47**, 9155 (1993).
- [169] J. Kane, Q. Chen, K.-W. Ng, and H.-J. Tao, “Observation of a - b plane gap anisotropy in $\text{Bi}_2\text{Sr}_2\text{CaCu}_2\text{O}_8$ with a low temperature scanning tunneling microscope,” *Physical Review Letters* **72**, 128 (1994).
- [170] T. P. Devereaux, D. Einzel, B. Stadlober, R. Hackl, D. H. Leach, and J. J. Neumeier, “Electronic Raman scattering in high- T_c superconductors: A probe of $d_{x^2-y^2}$ pairing,” *Physical Review Letters* **72**, 396 (1994).
- [171] F. Yu, M. B. Salamon, A. J. Leggett, W. C. Lee, and D. M. Ginsberg, “Tensor magnetothermal resistance in $\text{YBa}_2\text{Cu}_3\text{O}_{7-x}$ via Andreev scattering of quasiparticles,” *Physical Review Letters* **74**, 5136 (1995).

- [172] D. A. Wollman, D. J. Van Harlingen, W. C. Lee, D. M. Ginsberg, and A. J. Leggett, “Experimental determination of the superconducting pairing state in YBCO from the phase coherence of YBCO-Pb dc SQUIDS,” *Physical Review Letters* **71**, 2134 (1993).
- [173] V. Geshkenbein, A. Larkin, and A. Barone, “Vortices with half magnetic flux quanta in ‘heavy-fermion’ superconductors,” *Physical Review B* **36**, 235 (1987).
- [174] M. Sigrist and T. M. Rice, “Paramagnetic effect in high T_c superconductors— a hint for d -wave superconductivity,” *Journal of the Physical Society of Japan* **61**, 4283 (1992).
- [175] D. A. Wollman, D. J. Van Harlingen, J. Giapintzakis, and D. M. Ginsberg, “Evidence for $d_{x^2-y^2}$ pairing from the magnetic field modulation of YBa₂Cu₃O₇-Pb Josephson junctions,” *Physical Review Letters* **74**, 797 (1995).
- [176] A. Mathai, Y. Gim, R. C. Black, A. Amar, and F. C. Wellstood, “Experimental proof of a time-reversal-invariant order parameter with a π shift in YBa₂Cu₃O_{7- δ} ,” *Physical Review Letters* **74**, 4523 (1995).
- [177] D. Vion, P. F. Orfila, P. Joyez, D. Esteve, and M. H. Devoret, “Miniature electrical filters for single electron devices,” *Journal of Applied Physics* **77**, 2519 (1995).
- [178] S. Misra, B. B. Zhou, I. K. Drozdov, J. Seo, L. Urban, A. Gyenis, S. C. J. Kingsley, H. Jones, and A. Yazdani, “Design and performance of an ultra-high vacuum scanning tunneling microscope operating at dilution refrigerator temperatures and high magnetic fields,” *Review of Scientific Instruments* **84**, 103903 (2013).
- [179] Y. Noat, V. Cherkez, C. Brun, T. Cren, C. Carbillet, F. Debontridder, K. Ilin, M. Siegel, A. Semenov, H.-W. Hübers, and D. Roditchev, “Unconventional superconductivity in ultrathin superconducting NbN films studied by scanning tunneling spectroscopy,” *Physical Review B* **88**, 014503 (2013).
- [180] J. Rodrigo, V. Crespo, and S. Vieira, “Scanning tunneling spectroscopy of the vortex state in NbSe₂ using a superconducting tip,” *Physica C: Superconductivity* **468**, 547 (2008).
- [181] R. Joynt and L. Taillefer, “The superconducting phases of UPt₃,” *Reviews of Modern Physics* **74**, 235 (2002).